The Dissertation Committee for Richelle Czarina Thomas Certifies that this is the approved version of the following dissertation:

NOVEL TEMPLATING OF THREE-DIMENSIONAL HYALURONIC ACID SOFT TISSUE SCAFFOLDS

Committee:

Isaac Sanchez, Supervisor

Christine E. Schmidt, Co-Supervisor

Jennifer Maynard

Hal Alper

Laura Suggs

NOVEL TEMPLATING OF THREE-DIMENSIONAL HYALURONIC ACID SOFT TISSUE SCAFFOLDS

by

Richelle Czarina Thomas, B.S. Ch.E.

Dissertation

Presented to the Faculty of the Graduate School of

The University of Texas at Austin

in Partial Fulfillment

of the Requirements

for the Degree of

Doctor of Philosophy

The University of Texas at Austin

December 2013

Dedication

It is not the critic who counts; not the man who points out how the strong man stumbles, or where the doer of deeds could have done them better. The credit belongs to the man who is actually in the arena, whose face is marred by dust and sweat and blood, who strives valiantly; who errs and comes short again and again; because there is not effort without error and shortcomings; but who does actually strive to do the deed; who knows the great enthusiasm, the great devotion, who spends himself in a worthy cause, who at the best knows in the end the triumph of high achievement and who at the worst, if he fails, at least he fails while daring greatly. So that his place shall never be with those cold and timid souls who know neither victory nor defeat." ~ Theodore Roosevelt

Acknowledgements

I would like to thank my beloved family and friends who have stood by me as I completed my studies. The small victories, times of self-doubt and defeat, you all have been there all along. I especially thank my parents. Together, you two have been the constant presence of love and encouragement I needed throughout this journey. You know more than anyone, my insecurities, fears and challenges. I thank you for being ears when I needed to vent and being willing to give a kind word or a hug when I did not know to ask. You two are model parents that any child would be grateful for. I am so thankful and blessed that I "got you babe". I love you both, forever and ever.

I would also like to thank the friends I've made along the way. To "the girlies", I could not imagine Austin without you! Joyce Olushola, Megan Watson and Celina Dozier: I will always look back at this time in my life and smile over the good times (and good cries) we've had together. Thank you for being the friends I needed. I can only hope that I was half as good a friend to each of you, as you have been to me.

To my labmates, I love our times together. I could not imagine being with a livelier, more intelligent group of colleagues to scientifically mature with. To Dr. Leandro Forciniti, Dr. Jon Nickels, Dr. Sarah Mayes, Dr. Ryan Nagao, Derek Hernandez, Chase Cornelison, and Sydney Geissler, thank you for making the lab such a great place to work and also for being my scientific family. Your friendship, encouragement and thought-provoking feedback has been invaluable. Thank you.

Finally, and most of all, I would like to give thanks to God. I know He called me to graduate school and to do this work. I can only hope that He is pleased with the work I have done and the preparation I have had for what He has next for me. Praise be to God, forever and ever, Amen.

Novel Templating of Three-Dimensional Hyaluronic Acid Soft Tissue Scaffolds

Richelle Czarina Thomas, Ph.D.

The University of Texas at Austin, 2013

Supervisor: Isaac Sanchez

Co-Supervisor: Christine E. Schmidt

Effective tissue engineering scaffolds should mimic the physical and chemical attributes of native tissue. Native tissues have intricate patterns, a multitude of porosities, and large water contents that are each directly associated with their ability to regulate and support life function. Therefore, the physical architecture of scaffolds intended to mimic these tissues for engineering applications plays an important role in scaffold performance both *in vitro* and *in vivo*. Self-assembling molecules organize into intricate patterns with a complexity that resembles that of native tissue. Hyaluronic acid (HA) hydrogels are widely used in tissue engineering for a variety of applications but fail to offer physical architecture beyond the inherent hydrogel porosity.

To address this issue, a novel method to impose architecture within thin HA-based films using crystal nucleation was developed in the Schmidt lab [1]. The work described herein extends this method for use in three-dimensional matrices, with the main

goal being the creation of hydrogels with a complex macroarchitecture. Four *in situ* self-assembling molecules were used: glycine, guanidine, urea and potassium dihydrogen phosphate. The crystallization of each molecule creates a specific porous network within the hydrogel that is the negative imprint of the crystalline geometry. The novel restriction of aqueous polymer into the molecule interstitial crystalline space allows hydrogels to embody complex geometric lumen architectures. The hydrogels were characterized in terms of their internal architectures, swelling, bulk moduli, biodegradability, cytotoxicity and *in vitro* cellular response. The unique structure-property relationships displayed by hydrogels templated by each of the crystallizing molecules were characterized in regards to mechanical properties.

The need for complex microscopic architecture is conserved over many tissue engineering applications and templated scaffolds were evaluated for two unique applications. Crystal-templated hydrogels were investigated for use as an artificial stem cell niche environment to expand undifferentiated neural progenitor cells. Additionally, the templated hydrogels were evaluated for the *in vitro* study of myelin expression from Schwann cells. A hydrogel that combines the biocompatible properties of HA and the architectural complexity of native tissue may prove beneficial for biomedical applications.

Table of Contents

List of Tables

List of Figures

Chapter One. Introduction

1.1 Hydrogels and Tissue Engineering

A current challenge in tissue engineering accurately recreating the native biological microenvironment as accurately as possible, while also correctly inducing the desired *in vitro* response [2, 3]. To this end, researchers have developed various methods to synthesize scaffolds that mimic natural tissue. The intrinsic large water content and mechanical integrity achieved using simple synthesis techniques make hydrogels a premier technology applicable to address this biomedical research need. Hydrogel systems in their swollen state can serve as wound dressings [4], provide controlled drug release [5, 6], and encourage *in vitro* cellular behavior more indicative of the *in vivo* response [7, 8].

Hydrogels are typically amorphous and only possess porosities intrinsic to the aqueous polymer. Ideal, natural biological scaffolds have macroscopic, geometric porous structure which amorphous hydrogels currently cannot achieve. Amorphous hydrogels neglect an opportunity to mimic the physical intricacies of natural tissues. Instilling hydrogels with an internal geometry similar to native tissue present a viable means to combine chemical and physical stimuli in three-dimensions (3D). Experiments conducted in biomimetic 3D environments allow for more representative *in vitro* cell culture than those carried out in two-dimensions (2D) [3]. The purpose of this thesis is to elucidate the

role 3D physical architecture within hydrogels plays in maintaining or directing cell behavior and the implications for tissue engineering in the central and peripheral nervous systems.

The creation of complex architecture within extracellular matrix soft scaffolds is where the novelty lies in this project. In an effort to promote maximum biocompatibility, natural polymers are used in this work. The biopolymer of choice in this work, hyaluronic acid, is a ubiquitous component of the extracellular matrix and provides advantageous chemical cues for *in vitro* cell culture. Weaving biologically relevant architecture within chemically advantageous substrata makes this project uniquely positioned to address one of the major challenges in neural tissue engineering today. By examining the engineering of biologically relevant architectures in soft tissue scaffolds, this project directly addresses concerns about the impact large void volumes has on mechanical properties and their utility as three-dimensional culture environments.

1.2 Ideal 3D Culture Substrate

An ideal tissue engineering scaffold combines durable mechanical characteristics of synthetic polymers with biomimetic properties of natural materials. It is important to realize that the body requires the coordination of a multitude of stimuli when developing biomaterials. These stimuli may be characterized into three primary genres: chemical, topographical (physical) and electrical [9]. Studies herein have focused on the combination of chemical and physical cues. The primary challenge for tissue engineering is combining the expertise of the field into one biomaterial that serves multiple functions at the site of interest [3]. Ideally this biomaterial should coordinate cell-substrate interactions on the nano-, micro- and macro-scales to be most effective [10]. Ideal

artificial scaffolds should support cell growth and maintenance, serve as a topographical mimic, and provide adjustable mechanical stiffness that is biomechanically similar to native extracellular matrix [3].

1.3 Properties of Hydrogels

Hydrogels are hydrophilic polymer matrices with linkages that allow the scaffold to equilibrate with an aqueous environment but not dissolve [11]. Hydrogels have physical properties similar to living tissue: high water content, soft rubbery consistency, and low interfacial tension in both water and biological fluids [6]. These materials offer precise tailoring of chemical and physical properties which can complement the microenvironment of many potential tissues of interest. Hydrogels may be of various charges (anionic, cationic, neutral, ionic, ampholytic), morphologies (crystalline, semicrystalline, amorphous), and physical dimensions by employing different methods of crosslinking (chemical, physical, ionic) and a variety of polymer categories (biopolymer, biocompatible, synthetic, copolymer) [12]. Polymers used in hydrogels are typically chosen to be biocompatible or bio-inert and tend to allow fictionalization to further enhance compatibility, if desired.

A scaffold that is biodegradable or bioresorable via the body's metabolic pathways is particularly advantageous in tissue engineering. These scaffolds do not require a second surgery for removal. A debate exists in scientific community over whether natural or synthetic polymers are better suited for biodegradable scaffolds [12]. Naturally-derived polymers often have complimentary biological degradation enzymes whose products are typically found to be systemically present in healthy, normal bodies [4, 12]. Natural polymers are derived from a biological source and often provide

chemical modalities that cells are accustomed to interacting with *in vivo*. Biopolymers that are commonly used for tissue engineering include collagen, laminin, hyaluronic acid, cellulose, chitosan and gelatin. These polymers are synthesized easily, allow chemical functionalization on their backbone and permit scaffold formation with simple control over physical and mechanical properties in scaffolds [13]. Natural polymers are not mechanically robust enough for all applications because they may undergo mechanical deformation prior to or during the implantation process [14]. The primary drawbacks of natural materials include the batch to batch variability, mechanical properties and limited process ability. The advantages of natural polymers are the degradability, biocompatibility, low cost and wide availability [2]. The reduced potential for an immune rejection upon implantation is an additional attribute of natural polymers.

Synthetic materials, however, may have hydrolysable bonds incorporated into the polymer backbone to facilitate degradation. While this method does ensure scaffold breakdown, it may leave uncertainty in regards to the degradation byproducts and the long-term effects thereof. Synthetic polymer subunits could potentially lead to a myriad of adverse biological responses upon implantation. These polymers, however, are advantageous for applications that require mechanical deformation, excellent consistencies, reproducibility and a complete blank state devoid of any biological moieties [15].

1.3.1 Mechanical Properties There is an interrelated relationship between hydrogel mechanical properties, synthesis parameters, and scaffold success [15]. The polymer attributes, crosslink degree and surrounding or environmental conditions are each pertinent to the properties a hydrogel displays. The relationship between

composition choices and hydrogel behavior creates a codependent dynamic for the scaffold and its environment. Synthesis parameters have a direct influence on hydrogel mechanical behavior [4, 5, 12, 13, 16, 17]. Hydrogels are able to be tailored to suit the bulk properties of the site of interest, which makes these three-dimensional hydrophilic systems highly desirable. Furthermore, because hydrogels readily adapt to external stimuli such as temperature, pH, and solvent, the surrounding area of interest must be considered [11]. Hydrogel efficacy in application is also related to its water content The water content allows free diffusion of solute molecules and influences the mechanical properties, permeability, biocompatibility, surface properties and mesh size of the polymer network [4, 11].

Crosslinks are bonds or linkages that occur between the polymer network chains that help the hydrogel resist dissolution. Hydrogels can be crosslinked by forming covalent bonds, physical crosslinks, hydrogen bonds, strong Van der Waals interactions and crystalline associations [10]. Ideally hydrogels would exhibit a homogeneous distribution of crosslinks and therefore mechanical properties, however, clusters of molecular entanglements can create local heterogeneities [11]. Truthfully, most materials demonstrate similar variations; therefore, hydrogel inhomogenities do not detract from their ability to serve as a robust mimic to natural tissue bulk mechanical behavior.

1.4 Three-Dimensional Hydrogels

Gathering tissue engineering data that is representative of how the experimental sample would behave in the physiological environment is an on-going challenge in the field. There is evidence to suggest that 3D hydrogels may serve as better scaffolds for cell culture than traditional 2D techniques [12, 18, 19]; because they more closely imitate the

native local environment. The cellular signaling, gene expression and morphology that results from 2D culture holds little to no correlation to what is found *in vivo* [3, 20]. Nutrients and growth factors diffuse through a hydrogel much like they would in native tissues Therefore 3D culture within hydrogels is a better representation of the *in vivo* environment. The shortcoming of 3D hydrogels is that with increased thickness, the transport properties of the scaffold may be hampered. It is difficult for vascularization to occur within the inner most regions of thick samples if sufficient porosity is not present. Additionally, seeding cells on 3D matrices is a challenge. There are a limited number of methods to encourage cells to readily infiltrate a swollen polymer matrix. Non-even cell seeding and poor cell integration coupled with a lack of vasculature account for the majority of the cell-scaffold integration difficulties [3].

In vitro cell studies do provide an idea of cell behavior but fall short of the complexities of an organism [19, 20]. The 2D culture system may influence the individual cell behavior. Ideally, hydrogel scaffolds should facilitate spatial cellular organization in the tissue of interest [21-24]. Using hydrogels as 3D culture substrates instead of 2D culture dishes *in vitro* present an opportunity to gather useful data from *in vitro* experiments.

1.4.1 Porous Architecture of Hydrogels Matrices with microscopic architectures have been used for vascular [25], bone [26], cartilage [27], and neural[28] applications, among others. The internal morphology of a regenerative scaffold plays a significant role in its success upon implantation or *in vitro* culture. Scaffolds must mimic and modulate the cellular microenvironment both *in vivo* and *in vitro* to improve patient outcome and progress technology development. Isotropic hydrogels have an inherent porosity related

to the polymer but the ability to control the internal organization of hydrogel scaffolds is expected to prove beneficial in increasing the efficacy of experimental data enhancing tissue regeneration [3].

Biomimetic scaffolds that closely replicate the complex physical diversity apparent in natural tissue are expected to lead to more representative *in vitro* culture. The extracellular matrix-like components of the scaffolds help regulate intercellular signals and direct cells via well-defined spatial domains [29]. Regardless of the specific architecture, materials that resemble the tissue of interest have been shown to be the most successful [15]. *In vivo,* tissue architecture is directly related to the role that the tissue performs. Each biological tissue has a precise topographical landscape and hierarchical organization that complements its function. Therefore it is imperative that scaffolds attempt to mimic the geometrical complexity of natural tissues. Unfortunately, isotropic hydrogel scaffolds used in tissue engineering do not have any quantifiable, geometric physical architecture within their matrix. The isotropic hydrogel porous network largely manifests to high water contents and handling properties similar to that of native tissue. This project is a step in the direction towards recreating architectures that artificially resemble native tissue.

The cross-sections of various native tissues shown in **Figure 1.1** display a hierarchical patterning, which is consistent among tissue types regardless of specific tissue or origin. In each of the examples presented, there is a porous network surrounded by a dense continuous phase. Similarly, methods to create macroscopic architecture with microscopic detail restrict the polymer component into a compact geometry. Imposing

macroscopic structure within hydrogel scaffolds allow us to mimic tissue architectures within the customarily random cell environment [19].

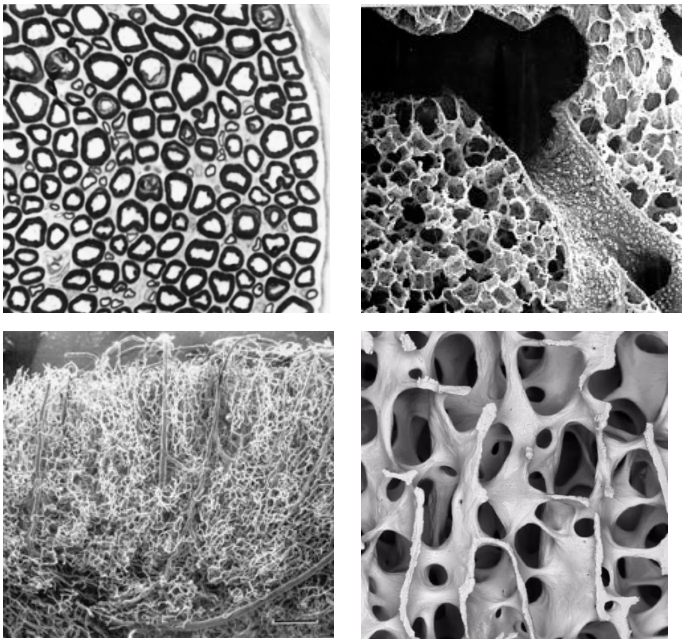

Figure 1.1: Cross-section of natural tissues displaying hierarchical patterning. The top left image is of adult rat sciatic nerve with toluidine blue stain [30]. Top right, scanning electron micrograph of mouse lung [31]. Bottom left, vascular bed of brain [32]. Bottom right, scanning electron micrograph of human bone [33].

1.4.2 Current Technologies for 3D Macroporous Hydrogels In an effort to harness the utility and promise of isotropic hydrogels and address the need to recreate the complex architecture of native tissues in polymer environments, numerous approaches have been explored to impose structural complexities within hydrogels [34]. The current work uses self-assembling small molecule crystals as a sacrificial template to impart architecture within hyaluronic acid-based hydrogels. The methodology is similar to other two-phase hydrogel templating techniques as illustrated in **Figure 1.2**. The desired bulk polymer is loaded with a secondary agent (chemical, microspheres, etc) and the two phases separate to maximize thermodynamic stability [12, 34, 35]. The bulk polymer is fixed into a continuous network around the geometrically organized porogen. The porogen is then selectively removed, leaving an organized imprint within the bulk polymer. Phase separation must occur during the network formation process so the two phase structure formed is preserved by the addition of crosslinks. When the porogen is removed after crosslinking and leaves porous structure within a highly crosslinked network [11].

In this work, crystallizing molecules are thermally dissolved in the polymer solution to act as the sacrificial secondary agent. The polymer-small molecule mixture was injected into molds and cooled on ice to promote spontaneous crystal nucleation. The polymer was crosslinked around the crystalline network and the crystals selectively removed from the hydrogel. The resulting scaffold retained the architectural imprint of the crystalline network.

The other techniques for creating macroporous hydrogels include porogen leaching, gas foaming, photolithography, and microsphere templating. **Figure 1.3** visually summarizes the 3D templating techniques. In porogen leaching, the bulk polymer is dissolved in organic solvent and mixed with a water-soluble porogen. The solvent is slowly evaporated over the course of hours to days to concentrate the polymer and the porogen is subsequently rinsed away [26, 36, 37]. The pore size is directly controlled by the porogen particle size but the potential negative impact on cell viability from harsh organic solvents and long process time are significant limitations of this technique [38, 39]. Gas foaming, in comparison, does not require organic solvents and can be used with biopolymers. Pores are created using high pressure carbon dioxide that forces the polymer into a continuous phase around carbon dioxide bubbles. However, because of the small size of carbon dioxide bubbles, the majority of pore sizes are not suitable for cell infiltration. The long processing time required is also a limitation of this technique [40].

Photolithography is a technique that uses masks to physically demarcate where the photopolymerization reaction occurs. This technique yields precise control over the synthesis of 3D objects from 2D slices. Hydrogels made via photolithography, however, are restricted to geometry of the mask and may lack consistency between layers of more complex structures [12, 41]. A uniquely sophisticated conduit design scheme was fabricated by Sannino et al. to investigate conduits with both radially oriented pores and cylindrical matrices with axially oriented pores using a freeze drying process [35].

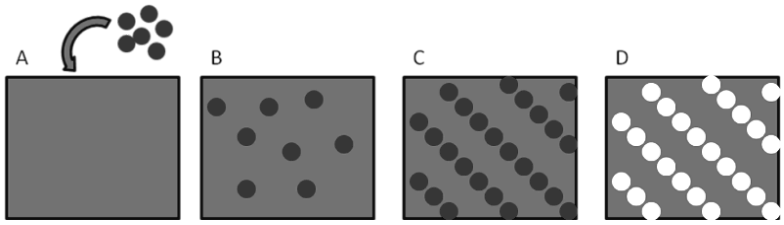

Figure 1.2: Schematic description of two-phase polymer templating techniques.

(A) First the secondary agent is incorporated into the bulk polymer and (B) allow to disperse. (C) The two phases separate and/or organize and the bulk, desired polymer is fixed into place. (D) The secondary agent is selectively removed from the polymer and the imprint of its pattern remains in the bulk polymer.

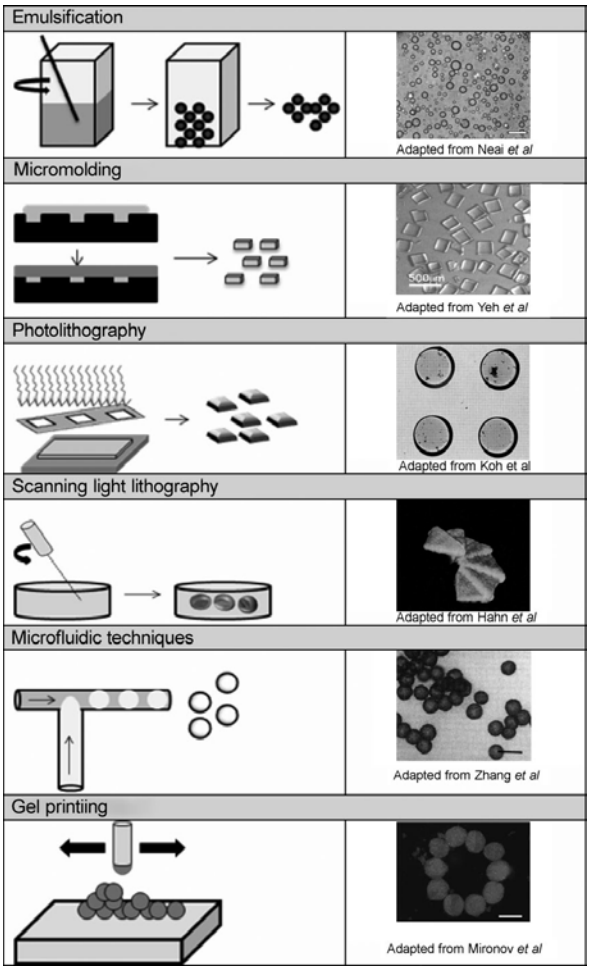

Figure 1.3: Schematic of various methods to create macroscopic pores within hydrogel scaffolds. Image courtesy of [12].

1.4.3 Cell-Substrate Interactions. Flat, artificial substrates have been shown to skew cellular behavior [42]. Three-dimensional culture systems are thought to be more advantageous than two-dimensional systems because they are able to provide both cell-cell and cell-substrate interactions. These interactions completely surround the cell and imitate the *in vivo* environment more closely than a two-dimensional substrate. Flat, artificial substrates have been shown to skew cellular behavior [42]. The increase in hydrogel porous volume from templating is expected to improve not only the cellular behavior because of organization but also nutrient transport into and out of the scaffold. Cellular interactions with a substrate are an important component to consider when designing biomaterials. It has been well established that cells respond to physical stimuli but the extent this influences large scale cell behavior and potentially impacts therapies is yet to be explored. Fibroblasts have shown alignment based on contact guidance from topographical substrates and topographical depressions have guided cell growth [16, 30]. Ceballos et al. used magnetically-oriented collagen fibrillar gels to enhance peripheral nerve regeneration in 4-6mm gaps in mouse sciatic nerve. Axonal elongation was attributed to the aligned fibers within the gel [8].

Integrin structures known as focal adhesions allow information delivery between extracellular matrix molecules and cells [42]. This interplay of communication is altered in 2D culture. For example, culture on 2D substrates has been shown to induce polarity in normally nonpolar cell types. 3D matrix interactions have been shown to display enhanced cell biological activities and narrowed integrin usage as compared to 2D

substrates [43]. Within this work, the influence of 3D geometric culture conditions on *in vitro* cell behavior are explored.

1.4.4 Crystal Templating of Hydrogels. The crystal templating technique used in this work is a simple, scalable method for imparting macroscopic architecture in polymer scaffolds. The technique is compatible with biologically-derived polymers, yet robust enough to form stable scaffolds that can withstand mild mechanical deformation without the loss of imposed geometry. The technique has shown consistent repeatability in 2D films, however 3D scaffolds are more geometrically appropriate for tissue engineering scaffolds [1]. The top-down approach of creating macroarchitectures within scaffolds has shown large scale repeatability in 3D which involves phase or component separation [12]. The *in vitro* study of 3D hydrogels allows cells to more closely mimic their in vivo behavior. Experiments conducted using 3D hydrogels yield information that is pertinent to translation *in vivo* and may therefore also improve the potential for clinical application [12, 18-20, 44]. The current system involves a secondary agent removes volume in such a way that the remaining polymer network retains the negative imprint of the crystalline network.

The self-assembling nature of crystal growth is used to replicate some of the complexity found in native tissue. The hydrogel solution gets loaded with a secondary agent such as a crystallizing small molecule which causes separation within the bulk solution. The molecule is allowed to nucleate and propagate crystals in the polymer solution. The surrounding polymer solution is polymerized around the crystalline pattern. The crystalline lattice is subsequently selectively removed from the scaffold leaving an imprint within the polymer network. The scaffold can then be used for experiments in

which the internal architecture would be advantageous. For this work, the self-assembling property of small molecule colloidal crystals is used to impose architectural detail within soft polymer scaffolds.

1.5 Hyaluronic Acid as Suitable Material

Hyaluronic acid (HA) is the most widely studied extracellular matrix biopolymer for use as a biomaterial scaffold because of its abundance and ease of purification [23]. HA is found in animal tissues such as the rooster comb, synovial fluid, umbilical cord and vitreous humor and is produced on large scale which adds to its relatively low price and sustained supply [10, 12, 13, 24, 45]. Hyaluronic acid exists *in vivo* as the polyanion hyaluronan, which is highly hydrophobic. The viscoelastic polymer works as a lubricant and shock absorber in the synovial fluid. HA is particularly well suited for neural applications because it is a large component of the developing central nervous system. Crosslinks may be incorporated in hyaluronic acid using standard bioconjugation chemistry, typically targeting the carboxyl and hydroxyl residues on the backbone of the polymer as shown in **Figure 1.4**. HA-based hydrogels are commonly used to support cell growth and organization because the structural integrity and rate of degradation can be easily adjusted via the extent of crosslinking [4, 46, 47]. HA is highly susceptible to temperature and pH degradation, but its high molecular weight makes its aqueous solutions viscous.

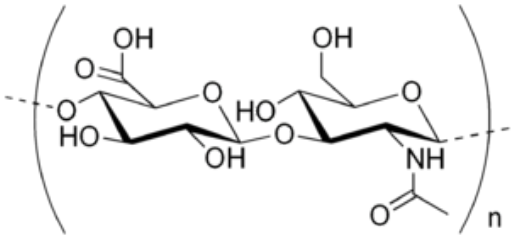

Figure 1.4: Chemical structure of hyaluronic acid consisting of the D-glucuronic acid and D-N-acetylglucosamine subunits.

1.6 Summary and Outline

The goal of this work is to create soft tissue scaffolds that have internal architectures relevant to the intricacies of *in vivo* tissue and retain advantageous hydrogel physical properties. A simple, scalable scaffold fabrication process to address the challenge of imparting strategic geometry within soft tissue hydrogels is the ultimate deliverable. We are not the first to attempt to develop a tailored *in vitro* cell culture environment that mimics the intricate and organized nanoscale meshwork of native extracellular matrix [3]. However, we are the first to our knowledge to do so using small molecules as a means to create intricate organization. Scaffolds with geometrically complex internal architecture have been developed, characterized, and used for three-dimensional culture of neural progenitor and Schwann cells in the study of two medically relevant applications. Geometric matching is a larger goal for the development of tissue engineering scaffolds; this project aims to explore the possibility of creating organization within soft, hydrated polymer scaffolds with internal geometry mimicking native tissue and assessing the utility for improved *in vitro* cellular responses. The novelty of the project lies in leveraging crystalline self-assembly in a unique manner to address a major challenge in the field. Creating architecture within hydrogels addresses the issue of

having scaffolds of the desired chemical properties but that lack the ability to induce cellular response using physical cues. Researchers are interested in determining the role physical cues play in cell culture and cellular behavior. Hyaluronic acid was chosen in this work as it is a natural, biodegradable polymer present in the extracellular matrix and is actively involved in the body's natural wound healing activities.

This work incorporates complex three-dimensional architecture into what are otherwise isotropic hydrogels and evaluates the benefit of macroscopic geometry to aid in counteracting inflammation derived peripheral nerve degeneration and expanding neural progenitor cell (NPC) population sizes. My original contribution to knowledge is the development of a simple, robust method for marrying cell-directing substrate morphology with extracellular matrix polymers for three-dimensional *in vitro* experimentation of potential therapies. This dissertation is comprised of seven chapters, including this introduction. Chapter two targets the development of soft tissue scaffolds with templated interiors in regards to raw materials, polymer synthesis and sample preparation. Chapter three discusses the geometric features of the scaffolds while chapter four characterizes the bulk hydrogel mechanical behavior. The broad utility of the material for tissue engineering was investigated in parallel in chapters five and six.

Chapter six recreated the architectural complexity of a NPC niche environment within hydrogel scaffolds. Progenitor cells reside in localized regions called niches *in vivo* where they are able to self-renew and proliferate while retaining their ability to differentiate into neurons, astrocytes, and oligodendrocytes. As the niche environment provides specific yet complex interplay of chemical and physical geometry to direct cell behavior. We hypothesized that the templated hydrogel architecture would maintain NPC

viability and permit undifferentiated expansion in three-dimensional *in vitro* culture. Chapter six also focuses on improving *in vitro* cell response using scaffolds with complex internal architecture. Diabetic wounds have inflammatory agents that persist long after injury and cause a reduction in myelin production from Schwann cells. The effect of the harsh diabetic environment has on Schwann cell myelination *in vitro* and the ability to maintain or recover myelin production had not been thoroughly investigated. Templated scaffolds were used to create an *in vitro* model of a diabetic wound to support Schwann cell culture and monitor the cellular response to anti-inflammatory therapy. The goal was to gain insight into the effect of the inflammatory diabetic wound environment on myelinating Schwann cell marker secretion using a cell adhesive version of the templated hydrogels as a three-dimensional culture environment. Chapter seven summarizes the findings of each of the previous chapters and provides comments on potential areas of further study.

Chapter Two. Templated Hyaluronic Acid Soft Tissue Scaffolds

Soft tissue scaffolds are a premier tool for tissue engineering repair and regenerative techniques. The pursuit of scaffolds that can mimic both the mechanical and physiological attributes of native tissue drives the field. That being said, it is imperative that such scaffolds present the highest potential for preserving cellular characteristics while engineering the surrounding tissue of interest. Polymer selection for this application is critical to scaffold success both *in vitro* and *in vivo*. Hyaluronic acid (HA) is a ubiquitous polymer with favorable viscoelastic properties and wide range applicability. Methacrylate addition to HA facilitates simple, photocrosslinked scaffold formation. Small molecules with molecular weights below 300 Daltons crystallize to create geometric detail within the polymer matrix while maintaining the ability to readily diffuse from the samples. The molecules were incorporated as sacrificial components that readily organize at 4˚C into intricate crystalline lattices. The crystallization generates interesting mechanical properties, polymer organization and the geometry it produces potentially mediates cell-material interaction. In this chapter we present characteristic descriptions of each of the hydrogel components and comment on their potential role in the scaffold.

2.1 Hyaluronic Acid (HA)

The extracellular matrix is comprised of many proteins and a mixture of glycosaminoglycans that bind growth factors and cytokines. Hyaluronic acid (HA) is one of the primary components of the extracellular matrix that plays an active role in wound healing and contributes to cell migration and proliferation [15]. In the body, HA exists as hyaluronan, not in its protonated form. The stereochemistry of the two subunits, D-

glucuronic acid and D-N-acetyl glucosamine, leads to its energetic stability [45]. Anionic HA is highly conserved across species; commercially, HA is harvested from rooster comb, bovine testes and *Streptococci* bacteria [48]. This implies its wide range of applicability and status as a sustainable source for extracellular matrix proteins and viscoelastic properties. The main attributes of HA are derived from its viscoelastic properties which allow it to serve as a lubricant [49, 50].

Hyaluronic acid has viscoelastic properties that make it widely applicable in tissue engineering. Depending on the application, the compressive modulus of HA scaffolds can range from 20-60 kPa [51]. Normal adults have about 15 g of the 1.6 kDa polymer in their body that is primarily located in the synovial fluid, vitreous humor of the eye and umbilical cords and is turned over every 24-72 hours [48]. Indeed, it is HA that gives the synovial fluid its viscoelastic nature, existing at a concentration of 2-3 mg/mL [49, 52]. In order to decrease the *in vivo* degradation rate, implanted HA should be crosslinked to be suitable for longer term applications. Photopolymerization allows spatial and temporal control of the degree to which samples are polymerized by modulating the time of exposure [51]. HA is particularly well-suited for tissue engineering applications because it can be covalently modified via either its carboxylic acid or hydroxyl functional groups [4, 45, 51]. It is common to add methacrylates to HA to form chemically crosslinked scaffolds [4, 10]. HA is reacted with excess triethylamine to act as an intermediate and pH buffer to facilitate reaction with glycidyl methacrylate [4, 51]. ^{1}HNMR results show methacrylate peaks at approximately 6.1, 5.6 and 1.85 ppm, the HA polymer methyl peaks are at 1.9 ppm as shown in **Figure 6.15** [51]. Furthermore,

controlling the crosslink density is a common method to modulate hydrogel mechanical properties.

Hyaluronic acid is particularly advantageous because it is angiogenic when degraded by the enzyme hyaluronidase [51]. Having a natural route of degradation makes HA a flagship polymer for tissue engineering. HA may also be degraded chemically using hydrogen peroxide, however for tissue engineering applications enzymatic degradation is more relevant [53]. The family of hyaluronidases hydrolyzes HA, chondroitin sulfate, synovial fluid, and vitreous humor in eye. It is beneficial to have a naturally occurring enzyme manage the polymer clearance from the body [15]. Besides HA hydrolysis, hyaluronidase has structural roles as a stabilizer, lubricant and shock absorber. Its viscoelastic properties are dependent on the concentration and molecular weight of hyaluronic acid [54]. HA has been used in films, hydrogels and electrospun networks and has been chemically crosslinked with both photopolymerization and thiol chemistries. Each hyaluronic acid disaccharide unit is approximately 1 nm in length. This equates to persistence length of 8 monomer subunits which is a high level of polymer chain flexibility [55].

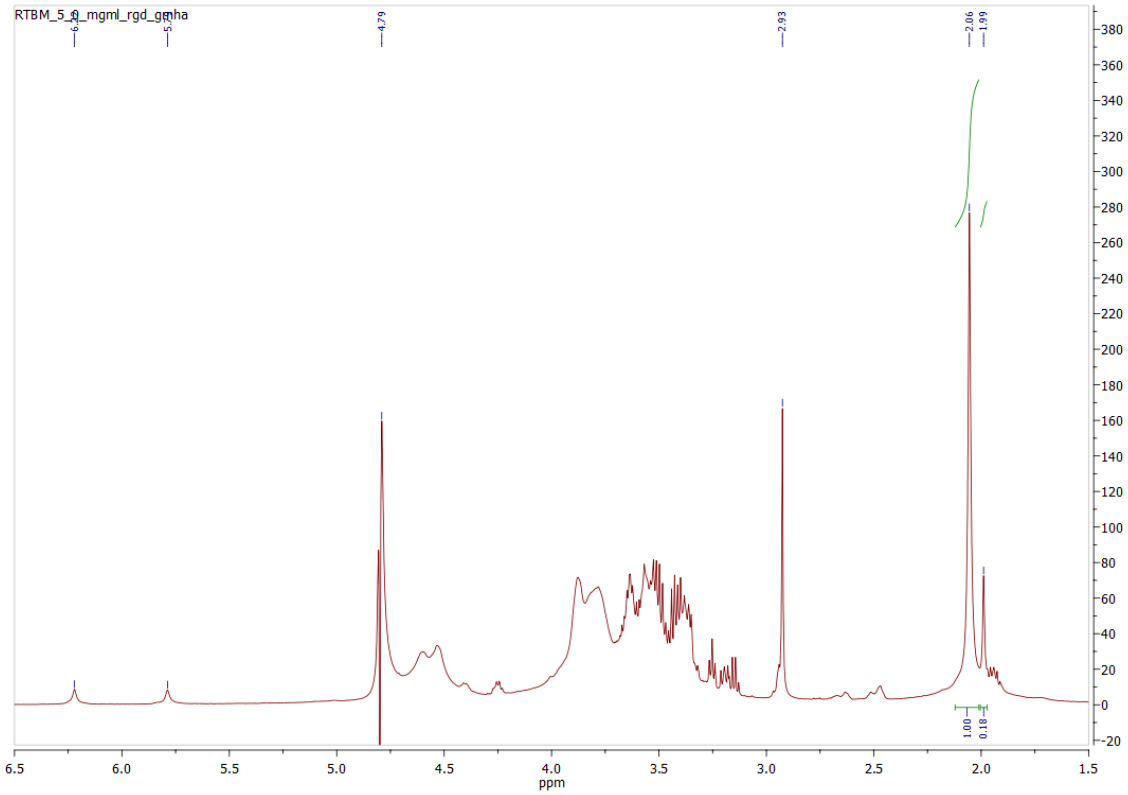

Figure 2.1: ^{1}HNMR of methacrylated hyaluronic acid. The plot shows peaks at approximately 6.1, 5.6, and 1.85 ppm from methacrylate groups and at 1.9ppm from the methyl group on HA. The areas under the curve suggest an approximately 18-20% methacrylation on hyaluronic acid.

2.2 Small Molecules

Macromolecules have the length and flexibility of nanometers to micrometers and therefore possess unique control of hierarchical organization and long range interactions. Phase separation can be a beneficial means to create void regions in a continuous phase. The relative concentrations of each component typically dictate the organization into a continuous phase with void spaces or with increasing degrees of homogeneity and organization. Thermally induced phase separation is used to encourage phases to separate. To date, most research has focused on 3D porous polymer scaffolds with controlled morphology and microarchitecture (fiber bonding, freeze drying and phase separation incompatible with injection materials) [56].

Liu 1995 et al presents a theory that crystal growth in aqueous solutions occurs via screw dislocations on crystal structure. According to the theory, the growth occurs by depositing and incorporating solute molecules from the bulk media which leads to advancement of crystal growth. The diffusion of solute molecules to the growth interface governs the process [57]. They suggest that the equilibrium shape a crystal takes on is a product of the surface free energies of the crystal faces, whereas the growth morphology is determined by kinetic factors [57]. It is known in the field of crystallography that crystal macroscopic shape is subject to the growth conditions because kinetic forces dominate the crystal propagation [58]. Furthermore, the polymer viscosity is largely a product of the molecular weight and the mobility of the polymer chains and is not directly related to the crystallization kinetics [59].

Small molecules are typically characterized by their low molecular weight, less than 900 Da and a size on order of 10^{-9}m. The majority of small molecules are less than 300

Da [60]. Typical drug molecular weights fall below 550 Da and most oral antibacterial agents, for example, fall between 350-450 Da [60, 61]. Solubility is a measure of how much solute can dissolve in a known amount of solvent. Small molecules that readily form crystals were used as the means to template the hydrogel lumen. Molecules were selected based on their ability to spontaneously nucleate crystals in a highly viscous aqueous environment. It was important that they were on a similar size order to small therapeutics for potential drug delivery applications. Small molecules needed to be soluble in water to ensure homogeneity prior to phase separation and to allow crude control over the temperature at which the phase separation would occur. The porogens were also selected based on their lack of large functional moieties in an effort to reduce the interaction, if any, between the small molecule and HA bulk polymer.

As stated in Chapter One, biological tissues can be viewed as dense networks with highly complex void regions. Even the brain and spinal cord consist of highly specific regions and intricate architecture. The hippocampus and subventricular zones in the brain as well white and gray matter of the spinal cord are examples of geometrically complex structures [62]. Many fundamental studies using cultured cells have shown that creating a complex topographical landscape [63] with submicron and nanoscale features[63] have been shown beneficial in directing direct neural cell behavior. It is not entirely clear if having a consistent pore size is a critical requirement for successful cell-biomaterial compatibility, however it is important to determine the method to create pores and the optimum pore size for a particular application [64]. Some argue that specific scaffold geometry does not play a significant role in scaffold integration or cell penetration in the brain; instead it is likely that the overall porosity plays the largest role [65, 66]. However,

scaffold with pore sizes that are larger than 100 μm and have complex architectures such as fiber-like struts and sheet-like features, for example, showed successful integration with host tissue, endothelialization and new ECM formation [67].

Macroarchitecture that mimics the natural tissue is thought to encourage regeneration. Friedman et al. theorized that creating architecture with specific features to mimic spinal cord tracts would encourage regeneration [68]. Other studies suggest that natural ECM cues are required for optimal neural cell behavior [69]. Hydrogel scaffolds with slightly more complex architecture have been explored recently to repair the spinal cord. Scaffolds with the structure-mimicking designs also encouraged more axonal infiltration, astrocyte migration and myelinated axon growth into the material compared to the other designs [70]. This study, did not assess meaningful functional recovery, but it provided a strong argument in support of anatomically relevant architectural cues for improving cell-material interaction. In summary, when it comes to incorporating structure into hydrogel scaffolds, researchers must determine the most relevant biological features and how to create similar architectures within biomaterials. Future work in this area needs to focus on fine-tuning the optimal morphological layout, length scales, and feature sizes. To this end, four sacrificial porogens were explored in this work: urea, potassium dihydrogen phosphate, glycine and guanidine. The templating protocol was optimized for each porogen to allow spontaneous crystal nucleation within the viscous polymer solution.

2.3.1 Urea. Urea is the main final product of protein metabolism. Urea concentration is most often used as an indicator of liver and kidney function. The concentration of urea in blood for normal, healthy individual is estimated as 29.3 mg urea per 100cc blood [71].Techniques to detect urea concentration are particularly useful for clinical

laboratories. Annual world production of urea exceeds 100 million metric tons and most of it is dedicated to fertilizer. Urea has a molecular weight of 60.06 g/mol and a density of 1.32g/cm^3. It is highly soluble in water with a solubility of 1.079 g/mL at 20 ˚C. Urea has a pk_b of 0.18 meaning it is basic. Urea is a resonance structure and at least one of the nitrogen's has a lone pair of electrons on it, which makes urea a good proton acceptor. Urea has a high crystallographic symmetry with a tetragonal scalenohedral crystal structure [72]. Liu et al predicts urea crystals in aqueous media to take on a needle-like geometry [57, 58] which does match experimental results [73]. The axial ratio for urea is a:c =1:0.8333 [72] and has unit structure dimensions of d_{001}=4.7Å, d_{001}=5.63 Å. Femtolasers can be used to cause perpendicular branching on urea crystals and urea crystals propagate from seeds [73]. We expect the polymer void spaces to reflect evidence of needle-shaped crystals within the scaffolds. Ideally, there would be some interconnectivity of pores resulting from overlapping or intersecting crystals.

Urea amounts can be determined directly or indirectly. Direct urea detection results in a product that does not include prior degradation but also includes methods like UV absorbance. Indirect urea measurement requires enzymatic degradation of urea prior to detection. Enzyme urease hydrolytically degrades urea into ammonia and carbon dioxide; the amount of ammonia can be subsequently quantified. Typically in indirect measurements, colormetric or fluorometric detection is applied to ammonia produced by enzymatic degradation [74]. Koncki et al. used a flow-injection system to analyze the concentration of removed urea in the effluent liquid. Urease at 75 U/mg was used to convert urea to ammonia and an ammonia selective electrode determined the ammonia concentration [75]. The challenge with this method is that the reagents can be relatively

unstable (short shelf life) and there can be a loss of ammonia during the procedure [76]. Acid urease is effective in the pH region 30.-4.0.

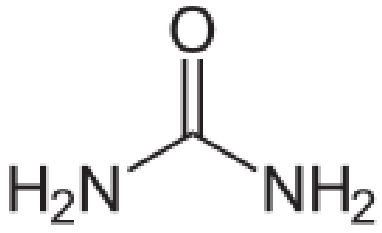

Figure 2.2: Molecular formula of urea. Urea is characterized by two amine groups and a double bonded oxygen. This small molecule is the most common product of protein metabolism and is therefore often targeted for detection in aqueous media. The molecular weight of urea is 60.06 g/mol. Urea crystallizes into spindle or needle-like struts in aqueous media.

2.3.2 Potassium Dihydrogen Phosphate. Potassium dihydrogen phosphate is a soluble salt that is commonly used as fertilizer, food additive and fungicide. Phosphate is an integral compound of biomolecules, it serves as a buffering agent by providing a source of both phosphorous and potassium. Clinically, potassium dihydrogen phosphate is administered at pH 4.5 as a phosphate supplement to treat hypokalemia in patients with a concentration that it does not exceed 40mmol per 1000mL [77]. Potassium dihydrogen phosphate has a molecular weight of 136.086 g/mol and a density of 2.338 g/cm^3. It is soluble in water at 0.22 g/mL at 25 ˚C. It has a pk_a of 7.2 and pk_b of 11.9. The crystal structure is tetragonal. Wang et al. used phosphate specific labeling under aqueous conditions using EDC [78]. This is an alternative technique for phosphate detection.

Potassium dihydrogen phosphate crystals are frequently used in light modulation. Crystals of this molecule can grow solutions whose pH ranges from 2.3-5.5 and in

temperatures up to 55 ˚C [79]. The transmittance of potassium dihydrogen phosphate crystals in 200-400 nm range was investigated in terms of how it was affected by inorganic impurities [79]. Trivalent cation impurities such as Fe^{3+} and Cr^{3+} increase the solution absorption of potassium dihydrogen phosphate crystals in the UV range [79, 80]. Solutions of pH 4.0 had the highest crystal transmittance and boric acid can be used to raise crystal transmittance because it combines with the impurities [79].

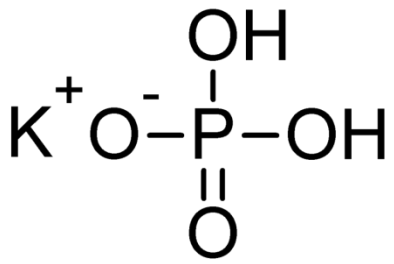

Figure 2.3: Molecular formula of potassium dihydrogen phosphate. Potassium dihydrogen phosphate readily disassociates into its ionic components in aqueous solutions. This small molecule serves as a buffering agent by providing both phosphorous and potassium. The molecular weight of potassium dihydrogen phosphate is 136.086 g/mol. Potassium dihydrogen phosphate crystallizes into a tetrahedral structure aqueous solutions.

2.3.3 Glycine. Glycine is a colorless crystalline solid that is the smallest of the 20 amino acids. The monoclinic crystalline molecule is well suited for both hydrophilic and hydrophobic environments because it has only one hydrogen atom. [81]. Glycine has a pka that ranges between 2.35-9.78, therefore at pH above 9.78 glycine exists as anionic amine. Below pH 2.35, glycine contains mostly cationic carboxylic acid.

It is commonly known that amino acids exist as zwitterions in solution. A zwitterion is a dipole ion that simultaneously has both anionic and cationic states within the molecule. In the case of glycine, the amine deprotonates the carboxylic acid. The glycine molecules are flat and held together by hydrogen bonds. Glycine molecules have zwitterionic form within the crystal. In crystalline form, the glycine crystal consists of double layers of molecules held together by hydrogen bonds [81]. Glycine molecules form discrete layers parallel to the xyz plane. Monoclinic unit cell. Albrecht discovered the crystal structure of glycine in 1939. A0=5.1A, b0=11.96A, c0=5.45A, beta=111˚38' [82]. Glycine can form small needle geometries if ethyl alcohol is added to concentrated aqueous solutions. The beta form of glycine is unstable, the alpha form is the normal form. Molecular structure is sheets of glycine. Two single sheets of glycine are held together by hydrogen bonds to form a double sheet which is packed by van der Waals forces throughout the crystal [82]. Glycine has a molecular weight of 75.07 g/mol and a density of 1.607g/cm^3. It is in water at 0.2499 g/mL at 25C. It has a pka of 2.34 and a pkB of 9.6.

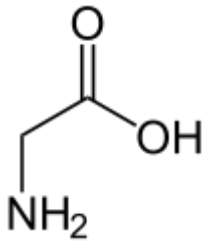

Figure 2.4: Molecular structure of glycine salt. Glycine is the smallest of the twenty amino acids. As an amino acid, glycine readily forms a zwitterion in aqueous media. The molecular weight of glycine is 75.07 g/mol. Glycine crystals are held together by hydrogen bonds and the molecule exists in zwitterionic form within the crystal.

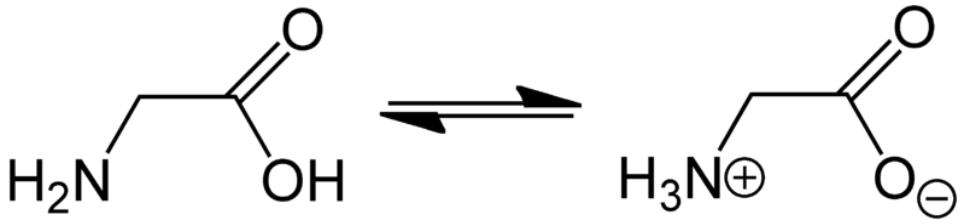

Figure 2.5: Glycine in its zwitterionic form on the right and at neutral pH on the left.

2.3.4 Guanidine crystalline compound. Guanidine is a strongly alkaline crystalline compound formed by oxidation of guanine. It is found in urine as a product of protein metabolism and exists in its protonated form at physiological conditions. The guanidium cation has a positive one charge. The guanidine resonance structure provides efficient stabilization of the cation in aqueous conditions. The molecular weight of guanidine is 59.07 g/mol and a density of 1.35 g/cm^3.Guanidine has a pka of 13.6 which means it is a very strong base at aqueous conditions. Guanidine has a solubility of 2.15 g/mL in water at 25˚C. It was incorporated at this concentration experimentally. Guanidine is normally supplied as guanidium chloride or guanidine hydrochloride. It exists as guanidine cations and chloride anions in solution.

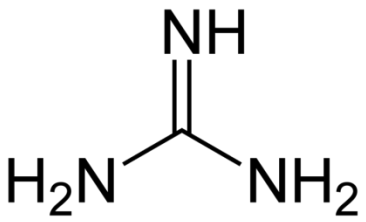

Figure 2.6: Molecular structure of guanidine. Like urea, guanidine is a product of protein metabolism found in urine. This nitrogen rich small molecule forms a resonance structure that stabilizes the cation in aqueous solutions. The molecular weight of guanidine is 59.07 g/mol.

2.4 Issues and resolutions

Hyaluronic acid is a weak polyelectrolyte. Electrostatic polyelectrolyte binding sites on proteins are areas where electrostatic potential that arises from the protein linkage is large enough to significantly constrain the motion of the polyelectrolyte segments [83]. Stiff polyelectrolytes bind micelles and dendrimers more weakly than flexible ones as the same charge density. That being said, there were concerns of anionic interactions with the different charged molecules. Urea is neutral so little to no interaction is anticipated. Potassium dihydrogen phosphate has an overall negative charge like HA, therefore there is a potential for repelling forces to contribute to phase separation behavior between the two. There could be some charged interactions between HA and guanidine and glycine since they both have positive charges at low pH. The opposite charge with HA could potentially impact behavior.

Urea and guanidine are chaotropic agents, meaning they are normally used to denature proteins [84, 85]. Guanidine is a much stronger denaturing agent than urea. The

ability of urea to denature proteins originates from its ability to bind to the protein, however, since it is a neutral molecule, no significant interactions are expected between the HA and urea. The guanidine cation, however, is ionic and therefore has a different mode of denaturation [86]. Guanidine has been shown to cause unfolding in a proteins secondary structure above 1M [85], however small angle neutron scattering results suggest that interactions between polyelectrolyte chains and surrounding monovalent cations are negligible [87].

Additionally, high concentrations of water leachable porogens have been shown to lead to concerns [56]. Specifically, handling difficulty, decreased injectability, nonuniform porogen distribution, compromised scaffold mechanical strength after porogen leach out, and potential local toxicity because of high osmolarity from leached salt were potential causes for concern. Because the hydrogel samples were pre-formed and rinsed to allow the porogen to diffuse out of the scaffold before cell culture, the majority of these issues were not applicable to this project.

2.5 Conclusions

The colloidal crystals were thermally dissolved in the hydrogel solution in excess of their individual room temperature saturation concentrations. The concentration at saturation was the minimum concentration at which we were able to induce crystallization within the hydrogel solution and was roughly associated with the porogen solubility at 25°C in water. The crystalline network pushes the polymer volume into the interstitial void space resulting in polymeric architectures resembling the negative imprint of the crystal pattern. With this technique the size of the final crystal-induced pores may be modulated by the media the hydrogel is allowed to equilibrate within, as well as the concentration of porogen and/or crosslink density by changing the amount of pohotoinitiator or ultra-violet light exposure.

Chapter Three. Hydrogel Network Structure

The network structure of a hydrogel dictates its behavior as a scaffold. The geometry of the continuous polymer phase has implications for the role a scaffold may play and its suitability for specific applications. It is important to evaluate both pore structure and polymer structure to acquire a representative picture of the scaffold in its entirety. Hydrogel structure may be visualized using confocal microscopy, cryopreservation scanning electron microscopy (cryoSEM), and magnetic resonance imaging (MRI). We have chosen a combination of confocal microscopy and cryoSEM to generate images of the internal and surface geometries within the polymer networks. We observed differences in the voided geometry for each of the crystal-templated hydrogels. Results indicate that there is agreement between the polymer and void space morphology in the needle-like voids for urea-templated hydrogels, and roughly so for potassium dihydrogen phosphate-templated samples. Guanidine-templated hydrogels exhibited flattened cubic-like voided areas that presented as surface undulations for the polymer component. Glycine crystal templating lead to fibrous polymer strands on the two micron length scale but no overall organization was visible either in the polymer or in the voided space on longer length scales.

3.1 Background: Hydrogel Structure

Hydrogels may promote regeneration or the differentiation of resident cells toward a functional tissue when designed to mimic the mechanical properties [88], adhesive properties [89], and chemical microenvironment of native ECM [90]. The polymer and solvent components each contribute to scaffold behavior. The polymer

component is responsible for the mechanical properties, viscoelasticity, and any architectural features of the scaffold. The hydrogel porosity is also an attribute of the polymer component, but may also depend on solvent. The higher the concentration of the polymer portion of the hydrogel, the more tightly packed the polymer chains and the lower the effective porosity. The geometry of the voided region is an artifact of the polymer organization, and influences the diffusion of other molecules into and out of the scaffold. Logically, the larger the pores, the more effectively biological fluids, water, and small molecules will diffuse through the hydrogel.

3.2 Cross Linked Structure

Covalently crosslinked hydrogels have the ability to uptake and retain copious amounts of water or solvent without dissolving [6, 91]. Hydrophilic polymer matrices may be rendered insoluble by forming either physical or covalent crosslinks between the polymer chains. The density of crosslinks within a sample controls the elasticity, bulk properties and degradation rate of the hydrogel. Physical crosslinks rely on polymer chain entanglements, fiber formation, or ionic secondary forces [11, 92, 93]. Physical hydrogels can also result from non-covalent interactions like dipole-dipole, hydrogen bonding and van der Waals interactions. For example, polymers such as alginate can be combined with a multivalent cation, and the two components form an ionic physical gel. The dissolution or stability of this type of gel depends on the surrounding ionic environment [15, 94]. Physical hydrogels are particularly susceptible to inhomogeneities because of molecular entanglement clustering [93]. Chemical hydrogels are covalently crosslinked water soluble polymers where the degree of crosslinking affects the mechanical properties between polymer chains [15]. Water soluble polymers form irreversible

hydrophilic networks after covalent crosslinking. Chemical gels also have spatial inhomogeneties that may be the result of hydrophobic aggregation or inhomogeneous distribution of crosslinking agents [91, 94].

Both physical and chemical hydrogels have the propensity for free polymer chain ends, chain loops, or entanglements to create defects in the polymer network [93, 95]. These defects in homogeneous domains have a significant impact on the mechanical and transport properties of the hydrogels. Degree of opacity is typically used as a qualitative indication of inhomogeneity, consequently transparent samples are considered to be homogeneous [91]. Covalently cross-liked hydrogels are used in this work because it is important that the hyaluronic acid (HA) based hydrogels are able to resist dissolution, if implanted. As stated previously, the polymer has a high turnover rate; therefore, it would be advantageous in any future application to have a relatively insoluble polymer network to prolong their residence *in vivo*.

3.3 Significance of Effective Porosity

The effective porosity of a hydrogel is a measure of the voided region within the scaffold, which affects diffusion, tortuosity and swelling of the hydrogel. Hydrogels inherently have void spaces filled with solvent, and these voids are known as pores. These pores exist on a variety of length scales and may be isolated or interconnected [91]. The porosity determines hydrogel characteristics and dictates the applications for which they would be best suited. Calvino-Casilda et al. refer to them as effective reservoirs for solvent uptake [91]. There are crude designations for different pore sizes as described by Calvino-Casilda et al. Micropores are less than 2 nm in diameter, mesopores are 2-50 nm,

macropores are 0.05-10 μm and superpores are 10-100 μm [91]. They go on to argue that the elastic modulus is not affected until the pores become interconnected [91]. Intuitively, the larger the pore size the more efficiently solute molecules can diffuse and the more permeable the scaffold. In the case of macro and superporous hydrogels, there is rapid swelling or shrinkage in response to external stimuli. The equilibrium swelling of crosslinked gels depends on the crosslink density which is estimated by the molecular weight between crosslinks, $\overline{M_C}$. It is in light of effective porosity that we discuss templated hydrogels [91].

The templating technique presented in this thesis increases the effective porosity of the scaffolds by creating larger void regions within the hydrogels. It is expected that this geometry would create scaffolds that have a level of intricate organization applicable for tissue engineering applications. Depending on a combination of the crosslinker concentration, polymer, and the existence of a porogen, the effective porosity will be affected, and the pores can also take on a variety of geometries [91].

3.4 Templated Hydrogel Physical Characterization

3.4.1 Templated Hydrogel Porous Geometry

Following synthesis, the void space geometry of templated hydrogels was evaluated. The crystalline molecules effectively created complex architectures within the hydrogel matrices for several different porogens. Each of the small molecules were encouraged to thermally nucleate within the pre-polymer solution. Urea, potassium dihydrogen phosphate, glycine and guanidine were each dissolved in the polymer solution at their 25˚C solubility. The temperature was reduced to approximately 4˚C to encourage nucleation in each of the polymer solutions. Representative images of glycidyl

methacrylate functionalized hyaluronic acid hydrogels templated using the porogens are shown below in **Figure 3.1**. The crystallization pattern and any changes to pore structure are inherent properties of the crystallizing molecule. The organization of the porogen network was expected to be influenced by the non-Newtonian polymer solution; however these interactions have not been investigated. The porogens selected are small molecules that have small likelihood of chemical interaction between the crystallizing molecules, polymer and solvent based on their chemical structure. To this end, polymer-porogen interaction was assumed to be largely negligible.

Urea crystals are described to have a needle-like geometry. The urea crystal-induced pattern is somewhat lamellar showing alignment in the x-y dimension of the top-down projection. The void regions appear to be largely aligned in the x-y dimension and are shown in **Figure 3.1**. The pattern appears to be present throughout the z-dimension in excess of 2 mm. No effort was made to orient the crystal direction. It should be noted that when samples were placed on ice to encourage nucleation that the crystals tended to propagate from one of the glass slide faces through the hydrogel samples. However, the nucleation is still largely spontaneous as many crystals nucleate throughout the hydrogel. There is no way to isolate the nucleation to only the glass face so nucleation therefore relies on relative clusters of molecules that accumulate once the pre-polymer mixture falls below a critical crystallization temperature. The urea crystals appear to have effectively spatially-restricted the polymer into a geometry representative of the crystal-induced void space. Urea crystals are an effective method for creating needle-like voided geometric regions within hydrogels.

Potassium dihydrogen phosphate crystals bisect the three-dimensional space to create starburst-like voided areas within hydrogel samples. **Figure 3.2** is an x-z projection of the void region in a representative sample. The organization appears to traverse all three-dimensions of the sample and not be restricted to any specific two-dimensional plane. The full crystal orientation can be seen. The orientation of the voided volume suggests a central nucleation point in the scaffold and compact regions radiate out from that central location. The starburst-like voided areas within the hydrogel are 50-100 μm wide in the x-y plane as shown. We hypothesize that the polymer component of the potassium dihydrogen phosphate-templated hydrogels is more tightly packed because of ionic crystal organization. This could explain the low background or infiltration of dextran-FITC into the polymer region as compared to the confocal images for the other samples.

Guanidine crystal-templated hydrogels show alignment in the x-y plane as illustrated in **Figure 3.3**. The pattern appears to traverse a large portion of the z-dimension. The images are confocal projections of two-dimensional images. The full cube-like geometries formed are evident. The void spaces appear as pockets of crystal nucleation rather than an interconnected network of pores.

Experiments to capture the porous geometry of glycine-templated hydrogels were not successful. The images from cryoSEM suggest that a significant voided region geometry was not produced as a result of crystal templating.

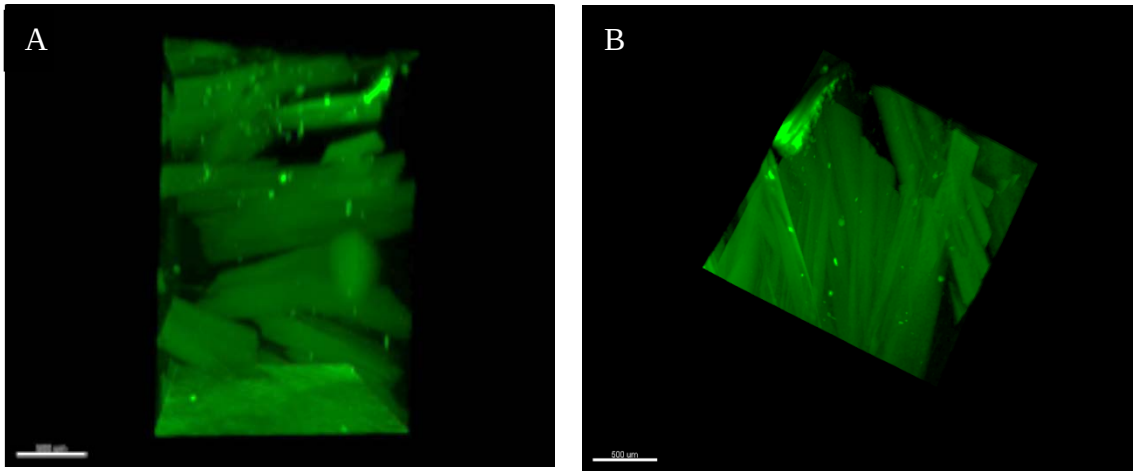

Figure 3.1: Confocal stack of voided space in urea-templated hydrogels. Samples were crosslinked for 5 minutes then exhaustively rinsed in water to remove the crystalline portion. They were then incubated with Dextran-FITC overnight and exhaustively rinsed for 3-5days prior to imaging. Templating is in excess of 2 mm in the z direction (A) and 1.5 mm in the x-y direction (B). Scaffolds show spindle or needle-like void spaces in the x-z image (A). There appears to be bulk alignment of crystal-induced voids from the top view x-y image (B). Scale bars are 500μm in each image. The urea crystals effectively spatially restricted the hydrogel polymer and appear to have occupied a large volume portion of the hydrogel. It is clear from the images that urea crystals are an effective method for creating spindle-like geometry within soft polymer scaffolds.

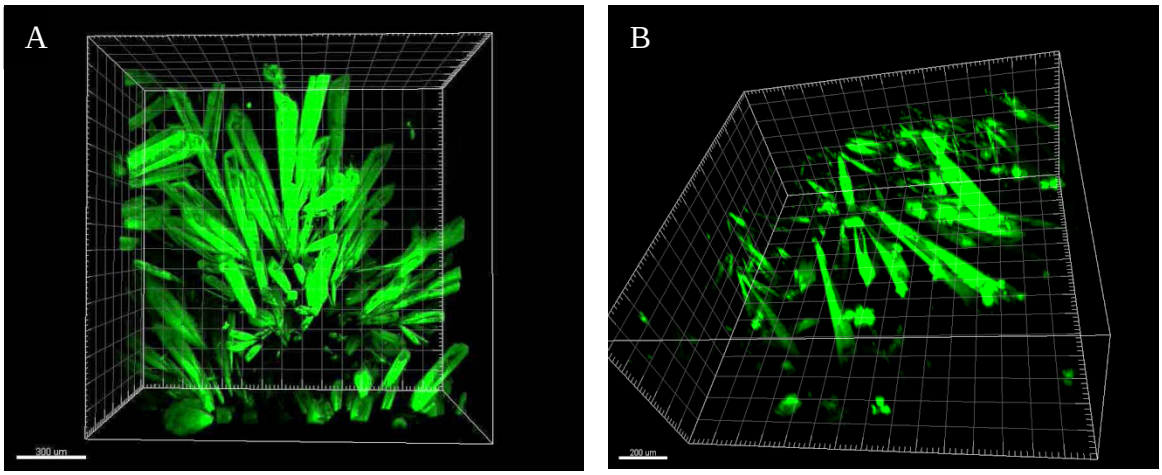

Figure 3.2: Confocal stack of voided space in potassium dihydrogen phosphate-templated hydrogels. Samples were crosslinked for 5 minutes then exhaustively rinsed in water to remove the crystalline portion. They were then incubated with Dextran-FITC overnight and exhaustively rinsed for 3-5 days prior to imaging. Templating is in excess of 1 mm in the z direction and 1.5 mm in the x-y direction. Scaffolds show crystal organization into starburst-like geometries. The potassium dihydrogen phosphate crystals effectively spatially restricted the hydrogel polymer. Scaffolds show voids that suggest the majority of nucleation began in a central location within the sample. Scale bars (A) 300 μm (B) 200 μm.

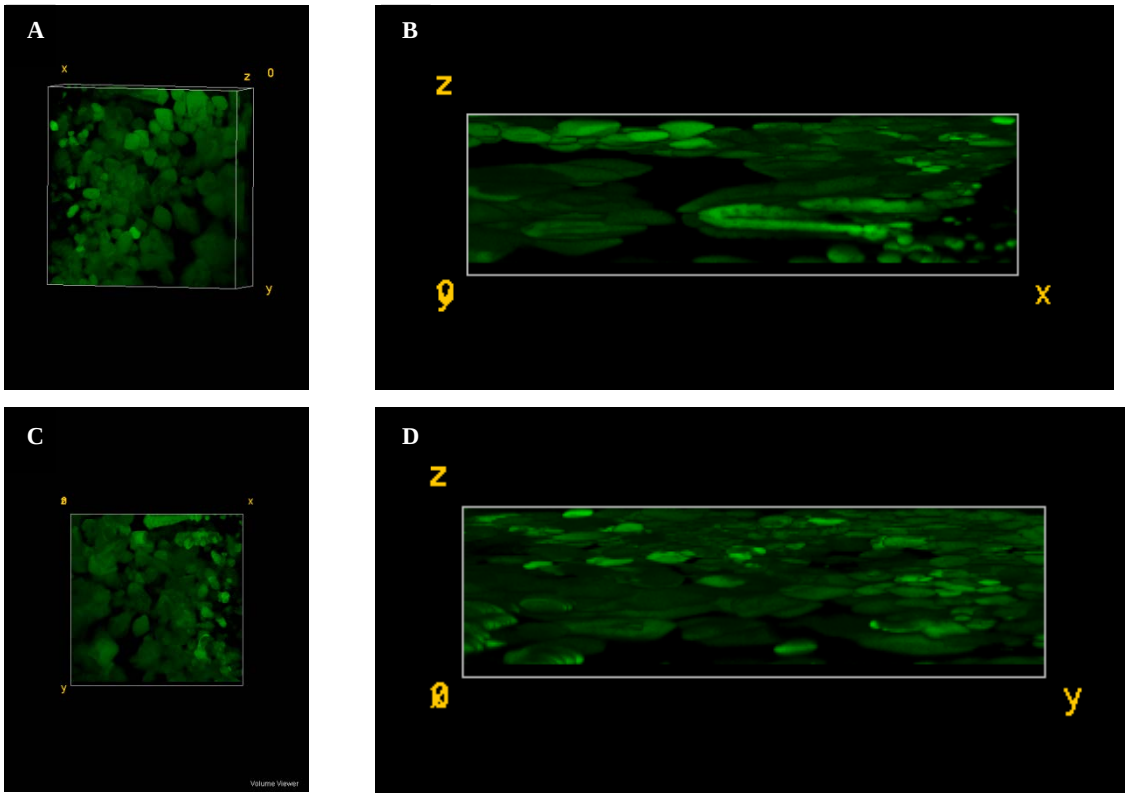

Figure 3.3: Confocal stack of void space in guanidine-templated hydrogels. Samples were crosslinked for 5 minutes then exhaustively rinsed in water to remove the crystalline portion. Samples were then incubated with Dextran-FITC overnight and exhaustively rinsed for 3-5 days prior to imaging. Templating is in excess of 1.5 mm in the x-y direction. Guanidine-templated hydrogel void space as a 3D volume projection (A), and x-z view (B), an x-y view (C) and an y-z view (D). The crystal templating lead to cubic disc-like void spaces within the hydrogel matrix.

3.4.2 Templated Hydrogel Polymer Geometry The microstructure of the hydrogel polymer component is critical to mimicking the complexity of *in vivo* extracellular matrix architecture. Much like *in vivo* tissue, the polymer component of a hydrogel provides dense structural scaffolding for cells to attach to and interact with. Mechanically, the polymer component is the primary contributor to behaviors of modulus, swelling and environmental response. Indeed, these rheological and scaffold behavior measurements reveal polymer characteristics. The polymer swells and shrinks in response to the media the scaffold is in and is therefore critically important to the attributes it presents. The polymer component was characterized with cryopreservation and scanning electron microscopy (cryoSEM) to evaluate the polymer reaction to nucleation of each of the different crystal templating molecules. Images presented in **Figure 3.4** allow broad comparison of the polymer component of the templated hydrogels versus the not templated control samples. The images suggest that crystal templating is an effective method to impose geometric features into otherwise amorphous hydrogels. In each case there is a dense, continuous phase that surrounds the void regions. The extent or pronunciation of voids varies from each crystallizing molecule used. Nevertheless, interesting architectures have been revealed that are not present in standard amorphous hyaluronic acid hydrogels.

A more in-depth look is taken in the following images to identify distinguishing characteristics between the not templated samples and each of the crystal templated hydrogels. The polymer component of not templated hydrogels is presented in **Figure 3.5**. A pattern of randomness is apparent on the surface of these scaffolds. The morphology of samples at 1, 10 and 100 μm are presented in the figure. At 1 μm, there

appear to be multiple layers of polymer, interspersed with particles and aggregated fibers. There are inhomogenieites in the polymer morphology (sheet, aggregate, fiber) and in their geometric layout. Similarly, at 10 μm the aggregates are no longer very visible; however the layers of polymer sheets are readily visualized. These results are supported by other hydrogel images where similar dense polymer layers were evident [96]. This suggests that while particulate aggregates exist, they do not comprise a significant portion of the not templated sample. At 100 μm, small peaks or "bumps" emerge on the sample surface.

The polymer component of urea-templated hydrogels resembles stacked sheets reminiscent of the crystal imprint. **Figure 3.6** shows the polymer component of urea-templated hydrogels. The urea-templated images suggest that crystal nucleation lead to polymer organization at the one micron, ten micron and hundred micron scales. While confocal imaging showed large spindle-like remnants, the polymer shows evidence of more intimate polymer-crystal interaction. Indeed, on the 5 micron scale, faces of polymer layers appear to have dense bundles of polymer as opposed to the sheets present in not templated control samples. The layers comprised of dense polymer phases are connected by fibrous polymers. The layers are an artifact of templating, but the faces of each layer have intricate patterns that suggest complete polymer interaction with the crystalline organization. At 20 μm, it is apparent that the sheets are interconnected by fibrous polymer and perpendicular thin polymer layers. The cross-sectional image at 200 μm confirms the geometry is not solely on the top layer that was presented in **Figure 3.4(B)** but also within the hydrogel.

Similar to what was shown in the urea-templated hydrogels, potassium dihydrogen phosphate-templated hydrogels show a strong resemblance to the imprint found in the confocal images for **Figure 3.2**. In **Figure 3.7**, the hydrogel surface shows evidence of crystal presence on a similar scale as **Figure 3.2**. The cryoSEM images show the effect of templating is evident on as small as the micron scale. In potassium dihydrogen phosphate-templated hydrogels, the polymer takes on a starburst-like morphology on the one micron scale. The polymer is confined to struts that together geometrically resemble a single nucleation point and propagation from that original point. At lower magnification, however, sheet-like layers become evident. The images suggest that crystals cut into a largely homogeneous polymer plane leaving remnants of layered or stacked polymer sheets at 20μm length scale. At still lower magnifications, the sheet-like architecture on hydrogel surface remains evident. The surface appears as if the crystals sharply cut or pierced the polymer. The collection of cryoSEM images indicate an intimate organization and interplay between the potassium dihydrogen phosphate crystals and the HA polymer.

Glycine-templated hydrogels have less organized micron-level architecture as compared to the others. The polymer domains qualitatively appear to be more widely spaced with a significant void fraction at the micron scale. **Figure 3.8** shows the surface topography of hydrogels that were templated with glycine at a series of magnifications. Glycine-templated hydrogels exhibit a web-like morphology on the micron level that was not conserved at lower magnifications. Additionally, some areas of the samples consisted of fibrous polymer strands (B) while others show the presence of craters (A) in addition

to the fibrous morphology. The compact fibers remain visible at the 10 μm scale but any organization the fibers may have becomes less apparent [1].

Figure 3.9 highlights the surface structure of a hydrogel templated by guanidine. The crystalline solid appears to have a significant impact on the surface morphology on the 20 μm level and higher. The surface topography of guanidine- templated hydrogels on the 20 μm level show undulations throughout the x-y space. The bulk polymer undulations instead of clear voided areas are likely to have contributed to the difficulties achieving confocal images of the void volume.

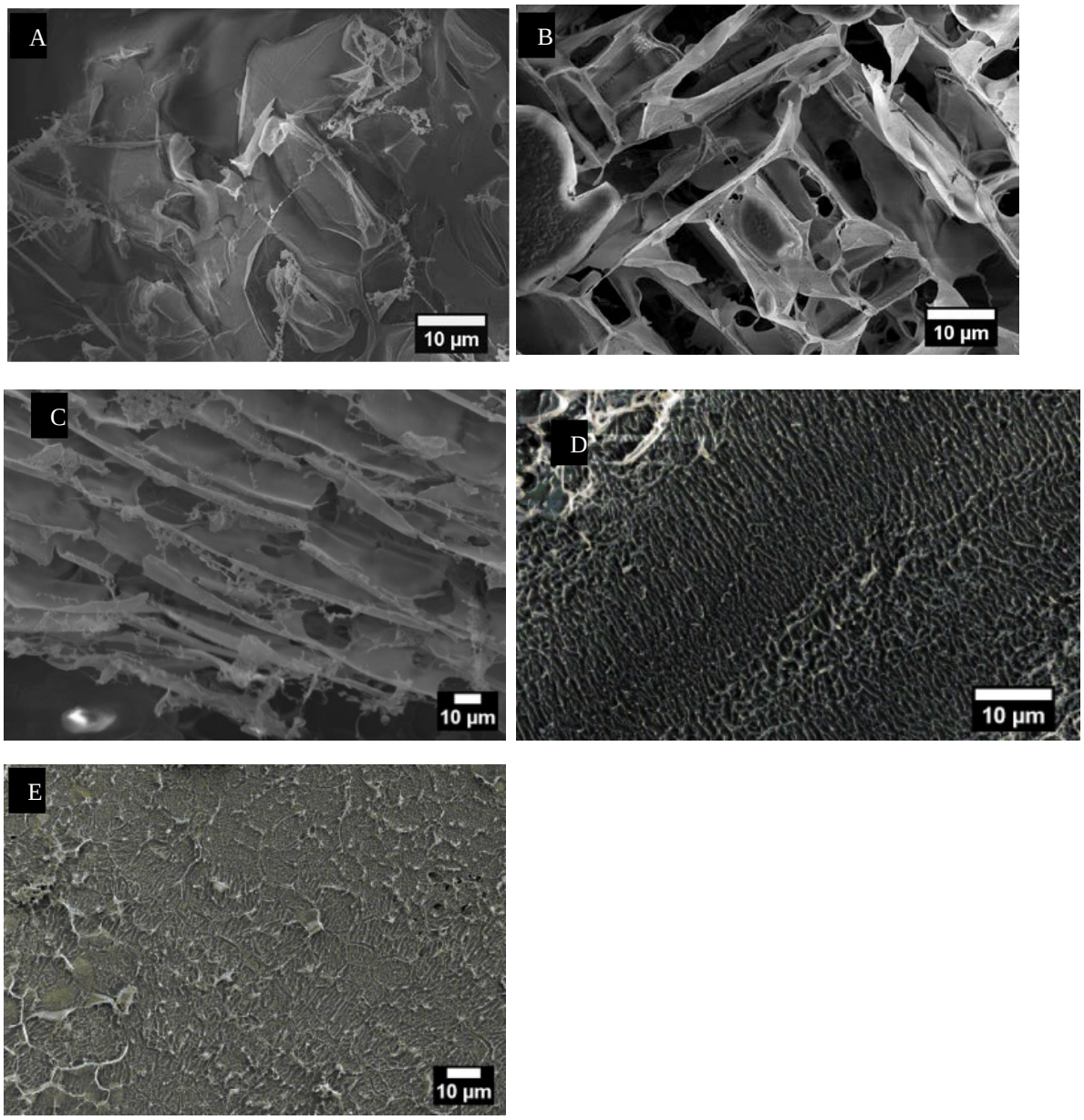

Figure 3.4: Polymer architecture of not templated and templated hydrogels with cryoSEM. Each of the samples were rinsed in water to remove the crystalline component, where applicable, and swollen in PBS prior to imaging. Samples were mounted and flash frozen to facilitate visualization of surface morphology. (A) Not templated hydrogels that show no organization among the polymer. (B) Urea-templated hydrogels show polymer morphology indicative of rectangular spindle-like crystal presence. (C) Potassium dihydrogen phosphate patterned hydrogels also show spatial restriction of the polymer for sheet-like structure. (D) The guanidine-templated hydrogels appear to organize in ribbed patterns and (E) glycine-templated hydrogels have a pattern that is the least defined. The templated samples show clearly different surface morphologies as compared to the not templated control on the same 10 µm length scale.

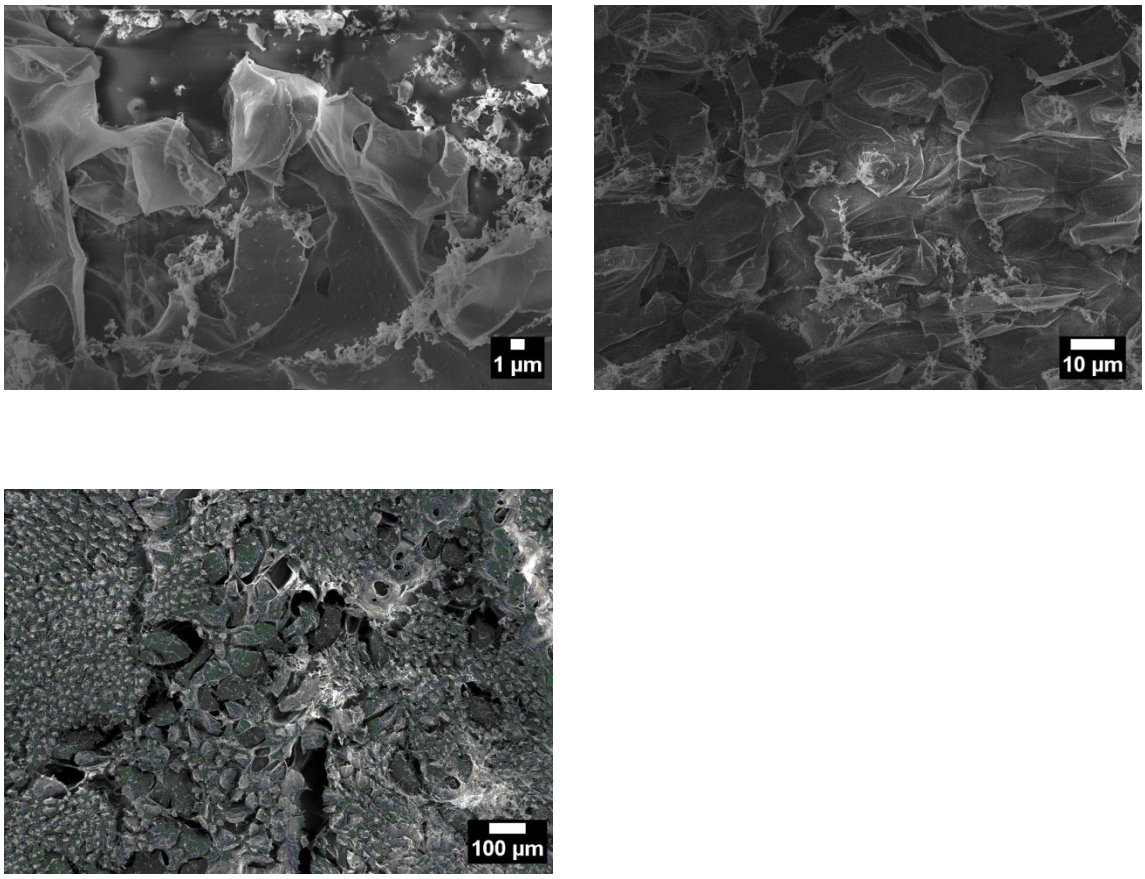

Figure 3.5: Polymer architecture of not templated hydrogels as characterized by cryoSEM. Each of the samples were rinsed in water, as consistent with the templated samples then swollen in PBS. Samples were mounted and flash frozen to facilitate visualization of surface morphology. The surface morphology of samples at the (A) 1 µm, (B) 10 µm, and (C) 100 µm length scales is presented. In each case, there is not apparent overall surface organization. At 1 µm multiple layers of polymer appear and are interspersed with aggregated fiber. At 10 µm the surface is dominated by polymer sheets, which suggests that the aggregates may not contribute significantly to scaffold behavior. At 100 µm some small peaks are visible in various regions but is not apparent on the smaller length scales.

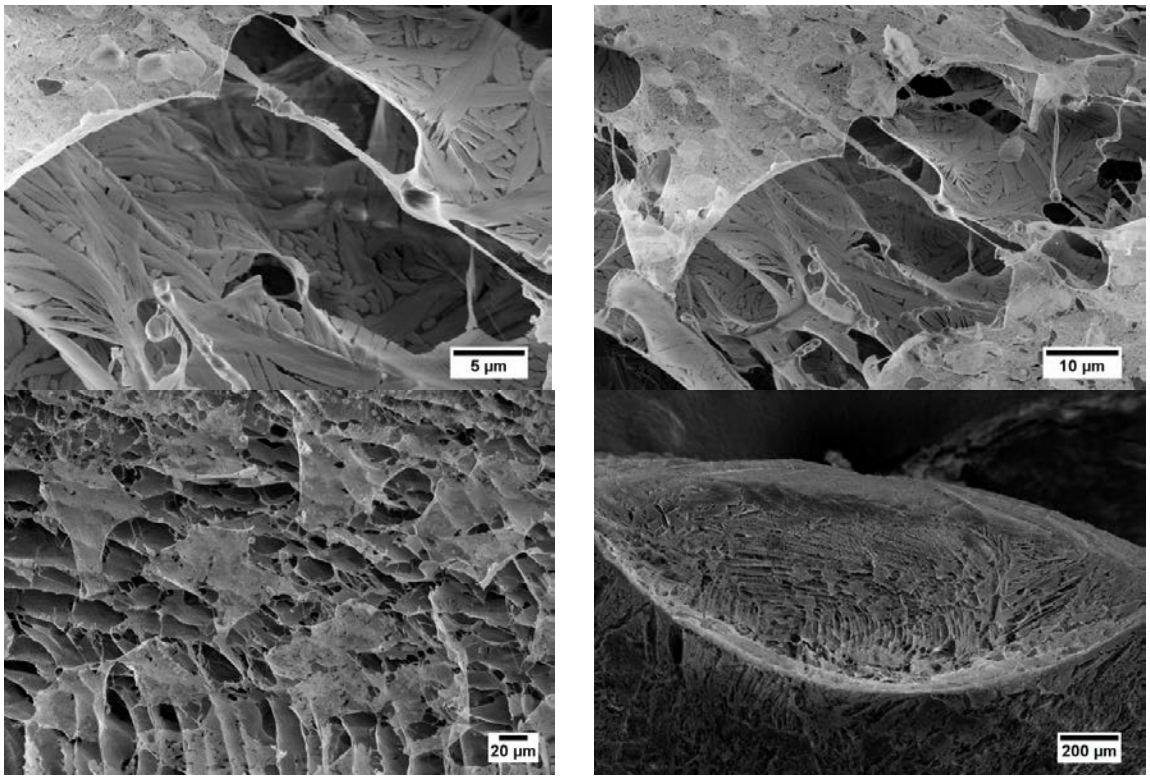

Figure 3.6: Polymer architecture of urea-templated hydrogel samples as characterized by cryoSEM. Hydrogel samples were exhaustively rinsed in water to remove the crystalline component then swollen in PBS. Samples were then mounted and flash frozen to facilitate visualization of the morphology and cross-sectional organization. Polymer organization is shown (A) on the 5µm and (B) 10µm length scales where the lumen of the hydrogel appears to have a stacked sheet-type structure with distinct organization on each plane. There is an overall stacked planar structure that is visible in the (C) 100µm range and (D) is a 200µm cross-sectional broad view.

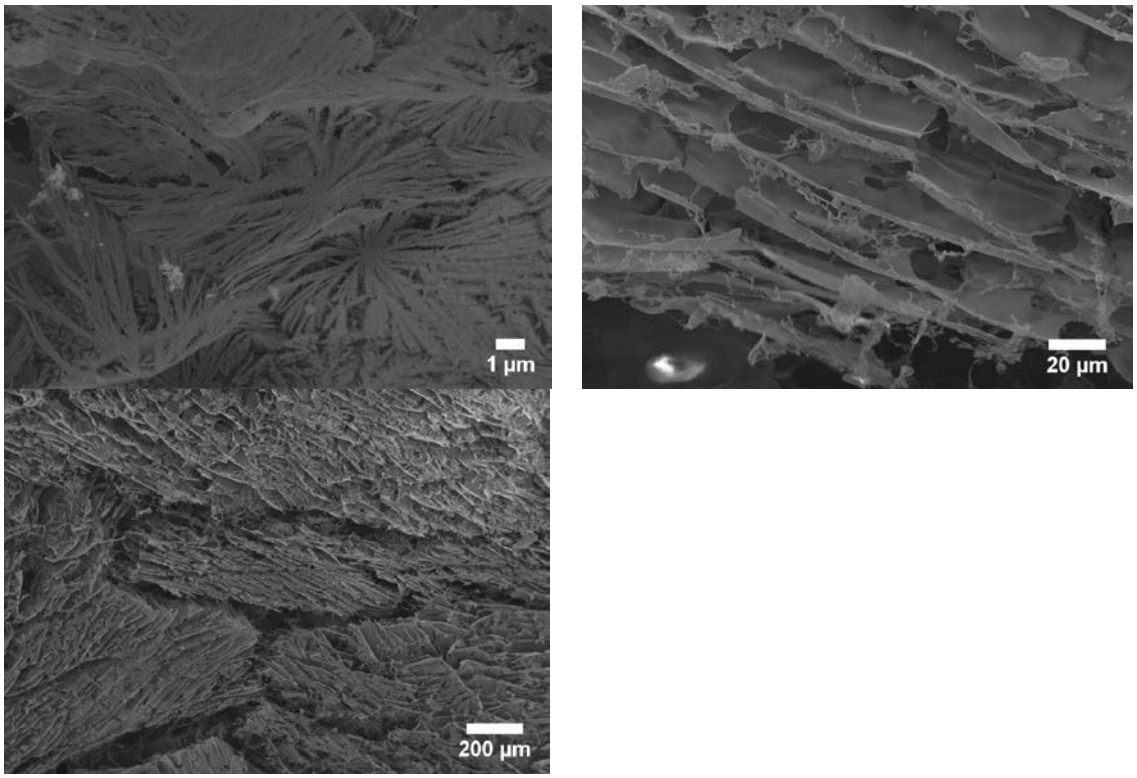

Figure 3.7: Polymer architecture of potassium dihydrogen phosphate templated hydrogel samples as characterized by cryoSEM. Hydrogel samples were exhaustively rinsed in water to remove the crystalline component then swollen in PBS. Samples were then mounted and flash frozen to facilitate visualization of the morphology. The surface morphologies evident at (A) 1 µm, (B) 20 µm and (C) 200 µm are presented. The template left by the crystalline structure is apparent on the 2 µm scale and stacked planar morphology is viewed on the (B) 10µm and (C) 200µm length scales. In each case, a clear overall organization emerges. At 1 µm a starburst-like polymer geometry is evident. At 20 µm, the starburst polymer planes clearly have a stacked organization. The densely packed polymer sheets collectively contribute to the slightly raised morphology visible at 200 µm.

A

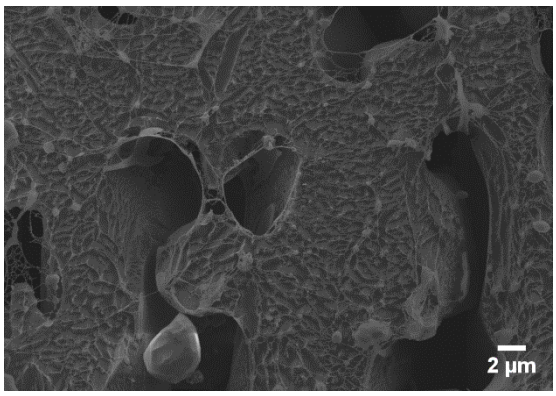

B

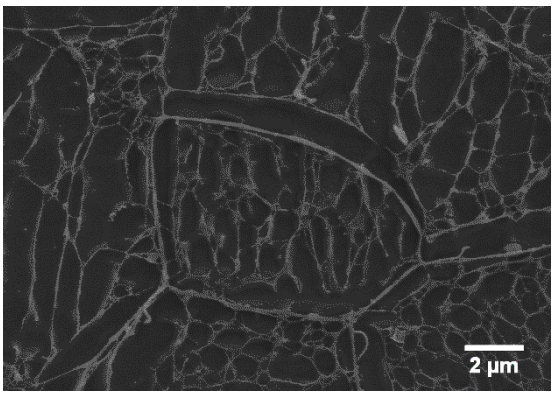

C

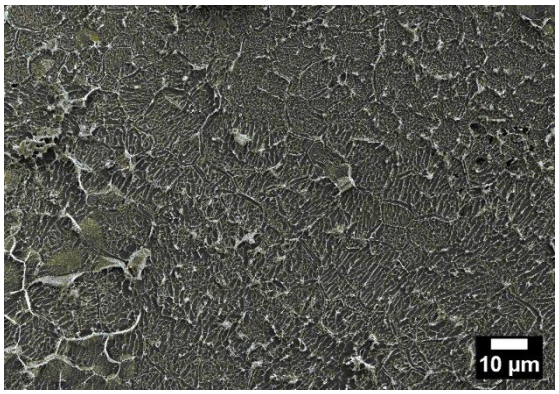

D

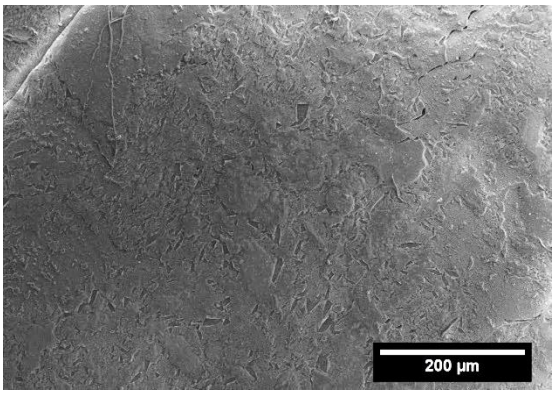

Figure 3.8 : Polymer architecture of glycine-templated hydrogels as characterized by cryoSEM. Hydrogel samples were exhaustively rinsed in water to remove the crystalline component then swollen in PBS. Samples were then mounted and flash frozen to facilitate visualization of the morphology. The surface morphologies at (A, B) 2 µm, (C) 10 µm, and (D) 200 µm are presented. Some spatial differences exist where on the same length scale (A) craters are visible, while in other locations the morphology consists of (B) fibrous polymer strands. Compacted polymer fibers are evident at 2 µm but the bulk organization is less visible at longer length scales.

A

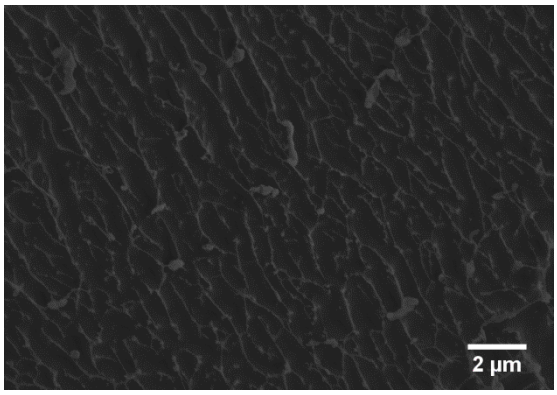

B

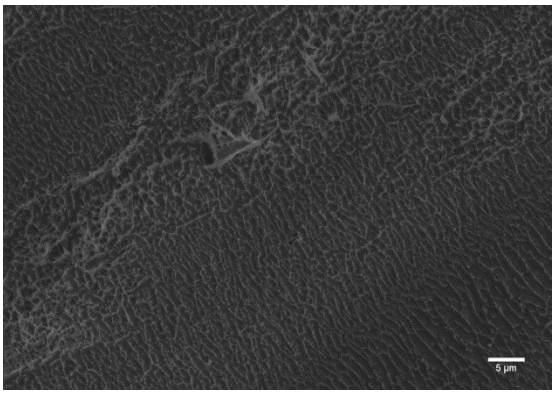

C

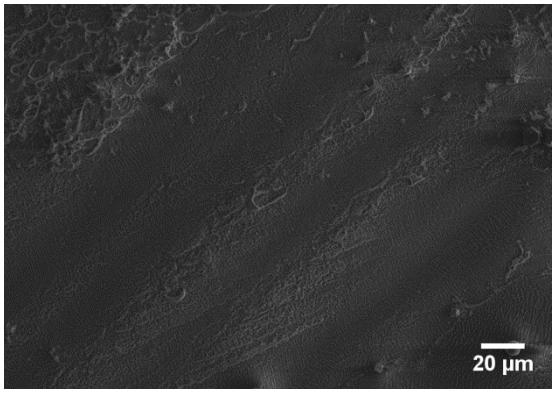

Figure 3.9: Polymer architecture of guanidine-templated hydrogel samples as characterized by cryoSEM. Hydrogel samples were exhaustively rinsed in water to remove the crystalline component then swollen in PBS. Samples were then mounted and flash frozen to facilitate visualization of the morphology. The surface morphologies evident at (A) 2 µm, (B) 5 µm and (C) 20 µm are presented. The molecule crystallization appears to have had significant impact on the surface morphology at 20 µm. Surface undulations are present throughout the x-y plane.

3.5 Conclusions

The self-assembled organization of a porogen is an inherent property of the molecule and was conserved throughout experimental samples. The crystalline network pushes the polymer volume into the interstitial void space. The polymeric architectures that result resemble the negative imprint of the crystal pattern in the cases of urea and potassium. Guanidine and glycine-templated hydrogels, however, only show minor evidence of polymer-crystal interaction. The void spaces for glycine-templated samples proved difficult to capture as evidenced by vaguely visible fiber morphology as opposed to distinct void regions from the cryoSEM images. With this technique the size of the final crystal-induced pores may be modulated by the media the hydrogel is allowed to equilibrate within, as well as the concentration of porogen and/or crosslink density.

The void space confocal images taken in context of cryoSEM images help paint a picture of hydrogel organization on the micro and millimeter length scales. It is interesting that in some cases the void space and polymer images relate very closely as in the case of urea-templating. In the case of potassium dihydrogen phosphate-templated samples, for example, the two show different perspectives. The self-assembled organization of the porogen is an inherent property of the molecule and was conserved throughout experimental samples.

3.6 Materials and Methods

3.6.1 Materials. High molecular weight sodium hyaluronate from *Streptococcus equi* of molecular weight 1.6 x 10^6 Da (53747-10G), Glycidyl Methacrylate (779342-500ML), Triethylamine (T0886-1L), Urea (U5378), Potassium Phosphate Monobasic (P5655-500G) and dextran-FITC were all purchased from Sigma Aldrich (St Louis, Mo).

Irgacure 2959 was purchased from Ciba Specialty Chemicals/ BASF (Basel, Switzerland). Guanidine hydrochloride (BP178-500), Glycine (BP381-500), Acetone (A181), BD PrecisionGlide 25 gauge needles (305122), and Luer-Lok syringes (2018-06) were all purchased from Fisher Scientific.

3.6.2 Hydrogel synthesis. Photocrosslinkable three-dimensionally patterned hyaluronic acid hydrogels were synthesized by preparing 2-5% (w/v) solution of glycidyl methacrylated hyaluronic acid with photoinitiator concentration varied between 0.3-1% Irgacure 2959. A 1% stock photoinitiator solution was prepared in 10 mM phosphate-buffered saline and added accordingly to the hydrogel solution to obtain the desired final concentration. The photoinitiator was heat sonicated for 30-45 minutes to facilitate solubilization.

3.6.3 Confocal microscopy sample preparation. Confocal microscopy was used to visualize the restricted hydrogel volume to give an account of the size dimensions of the voided volume. Hydrogels were soaked in deionized water overnight to remove the porogen, then swollen in 10 mM phosphate-buffered saline. The samples were then incubated in a 1 mg/mL dextran-FITC (Sigma) solution in water overnight and subsequently rinsed in deionized water for 2-5 days to reduce background signal for any unlocalized dextran. The aggregation of dextran-FITC molecules in the void domains allowed for the visualization of the porous domains. Confocal images were taken on Leica SP2 AOBS Microscope in z-stack. The acquired images were compiled using IMARIS software or ImageJ with Volume Viewer 2.0 plug-in to create three-dimensional renderings of the void area.

3.6.4 Cryopreservation scanning electron microscopy sample preparation. To examine the microstructure of the polymer component of the hydrogel after templating, environmental scanning electron microscopy was performed. After rinsing with deionized water, samples were allowed to reach equilibrium swelling in 10 mM phosphate-buffered saline. The hydrated samples were fixed to a mounting stage with carbon tape and carbon paint. The samples were then flash frozen to retain their hydrated morphology, sputter coated with platinum, and imaged under vacuum with the SEM. A vacuum was pulled to allow sublimation to occur before sputter coating. In order to examine the microstructure of the remaining hydrogel after templating. A Zeiss Supra 40VP was used.

Chapter Four. Mechanical Properties of Templated Hyaluronic Acid Hydrogels

Hydrogel mechanical properties directly dictate end behavior and performance yet are heavily dependent on the scaffold's porous attributes. Biomimetic hierarchically structured void spaces in methacrylated hyaluronic acid (GMHA) hydrogels can be created using small molecule crystallization that acts as a sacrificial template. The polymer (HA) is pushed into the interstitial crystalline space when the small molecules crystallize in the polymer solution. Within the bulk polymer solution, on the micron scale the polymer chains are organized around a crystalline network and therefore leave the crystals taking up the majority of solution surface area. The increase in void fraction that results from crystal nucleation was visible via confocal and cryo-scanning electron microscopy (cryoSEM) which indicate significant changes in hydrogel surface morphology after crystal templating. Therefore, changes in the mechanical properties of the hydrogels also likely occur. Data suggests that the increase in the hydrogel void volume reduces the bulk storage modulus under consistent synthesis parameters yet has little effect on the equilibrium water content. Differences in the crystal structure of individual porogens and the resulting swelling, rheological and degradation properties were explored. The bulk properties of crystal-templated hydrogels were compared to those of not templated hydrogels at consistent GMHA polymer concentrations, UV exposures and photoinitiator (PI) concentrations.

4.1 Small Molecules

Four molecules that crystallize in aqueous environments were explored in this work: urea, potassium dihydrogen phosphate, glycine, and guanidine. Each of these molecules are capable of crystallizing in aqueous methacrylated hyaluronic acid (GMHA) solutions [97-99]. The crystal nucleation pushes the polymer into the interstitial crystalline space and, in some cases, leads to a significant increase in hydrogel void space. Each molecule creates a unique geometry within the hydrogel and the differences that manifest between them are elucidated through swelling, rheological, and degradation experiments.

Small molecules may be incorporated into polymer networks by either of two methods. The additive can be mixed into the pre-hydrogel solution with polymer, porogen, cross linker (if needed) and solvent. When the polymer is polymerized around the additive, it traps the additive inside its matrix. This can be an attractive option for cases where little interaction between the molecule and polymer take place or if the configuration of the molecules or additives is critical to the final product. Alternatively, the preformed hydrogel can swell to equilibrium in an aqueous solution of the additive. Some optimization experiments would be necessary to ensure sufficient uptake by the hydrogel. Depending on the chemical composition of the swelling media, additional chemistry could be performed to bind the two components. The first method is preferred for this application because we are interested in the organization properties of the small molecules, not solely their chemical functionalities. With the second method the molecule would be incorporated within the hydrogel matrix but would not allow the scaffold to leverage its organization as a means to create architecture within the scaffold.

Because the purpose of this thesis is to explore the necessity (or lack thereof) of complex geometries in 3D scaffolds, the spatial organization and resulting polymer behavior take precedence.

4.2 Templated Hydrogel Bulk Characterization

Using a top-down approach to scaffold construction, this project focused on controlling macroscale features such as shape of relatively large pores. This thesis evaluates the effect of colloidal crystal templating on bulk hydrogel properties using complementary materials characterization techniques to assess hydrogel behavior characteristics [4]. The purpose is to develop and optimize crystalline porogen nucleation in hydrogels and elucidate the specific mechanical attributes that arise from this macroporous templating method. Mechanical properties are typically evaluated using swelling, oscillatory and compressive strain experiments whereas physiochemical information is derived using measures of porosity and interconnectivity [3]. To this end, swelling and rheological experiments were conducted and used to calculate porosity parameters. The bulk properties of each type of the templated hydrogels were compared to that of not templated hydrogel controls. Thus, the polymer concentration, photoinitiator concentration, and extent of UV exposure had to be optimized to recreate the robust character of amorphous hydrogels in this system. Each of the parameters and calculations presented must be considered in light of the media they are allowed to equilibrate in because that also has a direct effect on scaffold behavior.

4.2.1 Equilibrium Water Content. Scaffold water content largely influences the scaffold characteristics and mechanical properties as well as its potential effectiveness as

a cell culture environment [100]. The amount of water within a hydrogel is instrumental in the permeation and transport of nutrients and cells into and out of the scaffold [93]. Theory suggests crude characterization for the different roles of water within a hydrogel. When water enters the scaffold, the molecules that hydrate the most hydrophilic groups are considered primary bound water. The secondary bound water molecules then interact with the less hydrophillic groups within the polymer. Combined, the primary and secondary bound water account for the total bound water in the hydrogel [93]. After the bound water has properly interacted with the polymer, the osmotic driving forces allow the hydrogel to take in additional water until it reaches an elastic network retraction force or the equilibrium swelling amount [93]. The free water describes the molecules that were taken in after the polymer groups have been saturated [93]. The volume fraction of water and the free and bound water characteristics of a hydrogel determine the diffusion of solutes through the hydrogel. The equilibrium water content (EWC) is the weight percentage of water that is in the hydrogel when allowed to equilibrate in water. The hydrogel is dried in order to calculate this quantity, therefore, the EWC takes both the free and bound water into consideration. The EWC was calculated as follows:

$$EWC\ (\%) = \frac{W_e - W_D}{W_e} \times 100 \qquad (1)$$

$\mathbf{W_e}$ is the swollen weight of the sample at equilibrium, and $\mathbf{W_D}$ is the dried weight of the sample. The swelling and EWC experiments were conducted with a minimum of 6 samples per genre of hydrogel [5, 13].

The experimental results indicate an equilibrium water content of approximately 99% for not templated control hydrogels, glycine-templated, potassium dihydrogen phosphate-templated and urea-templated samples. Guanidine-templated hydrogels were

approximately 96% water. These results suggest that the overall water in a hydrogel is not significantly affected by crystal templating, with the exception of guanidine-templated hydrogels. It is intuitive to expect that an increased void space would lead to an increased amount of free water. The results indicate that the amount of water in a hydrogel is dominated by the polymer and not by its effective porosity. However, the guanidine-templated samples expel water as a result of crystal-templating. The overall hydrogen size does not increase as the crystals nucleate because they are synthesized between clamped glass slides which restrict any potential expansion. It is possible that water is expelled as the guanidine crystals propagate through the polymer solution because the polymer is spatially restricted by the interstitial crystal space.

	EWC (%)	Std. Error
Not Templated	99.555	0.156
Urea-Templated	99.627	0.201
Potassium Dihydrogen Phosphate-Templated	99.389	0.201
Guanidine-Templated	96.476	1.186
Glycine-Templated	99.513	0.0140

Table 1: Equilibrium water contents of not templated and small molecule templated hydrogel samples. Hydrogel samples were first rinsed in water overnight then swollen in deionized water to determine the maximum water content at equilibrium. The EWCs were found to be 99.56% for not templated, 99.62% for urea-templated, 99.39% for potassium dihydrogen phosphate-templated, 99.51% for glycine-templated and 96.5% for guanidine-templated hydrogels. Interestingly, the EWC did not change significantly between the not templated control and the crystal templated samples with the exception of guanidine-templated samples. This suggests that the effective voided area of a hydrogel may not significantly impact its water content. Guanidine-templated samples expel water as a result of the crystal templating process.

4.2.2 Swelling Behavior. Swelling is a powerful experimental technique because it provides a clear depiction of the scaffold's bulk reaction to various environmental conditions. The reaction to changes in temperature or ionic properties of surrounding media, for example, can provide valuable information about the scaffold. Furthermore, the experimental results typically match theory sufficiently to allow calculations of quantitative hydrogel characteristics. Swelling behavior of neutral polymers described by Flory and Rehner is a result of mixing pure solvent with initially pure, unstrained polymer networks [101]. The most important parameters used to characterize network structure are the average molecular weight of polymer chains between neighboring crosslinks ($\overline{M_C}$), the corresponding mesh size (ξ), and the effective network density υ_e [10, 91]. These relationships are described by the Flory-Rehner equilibrium swelling theory. The mesh size is a particularly important parameter because it indicates the size of the solute molecules that are able to pass into and out of the hydrogel. Topographical barriers such as the number of crosslinks/junctions, branches, and crystallites in network exist in hydrogels and effect these calculated parameters [102]. Van Vlierburghe et al. approximated the mesh size to be directly related to the polymer volume fraction in the swollen state by $\upsilon_{2s}^{-3/4 \text{ or } -1/2}$, using the buoyancy method. Hydrogel swelling has a dependence on temperature therefore swelling measurements were conducted isothermally at 25˚C [103].

Kim et al created 3D porous poly(caprolactone fumarate) (PCLF) hydrogel scaffolds using microparticles to template or pattern PCLF scaffolds with pore sizes between 100-500 μm [56]. Intuitively they found that a lower porosity yielded a greater

scaffold compressive modulus. It should be noted that a decrease in weight can occur as a result of water outflow when mechanical pressure is applied to swollen gels [103]. To circumvent the issues associated with water leachable porogens, they opted to use porogens that degrade at physiological conditions. By using hydrogel microparticles as the porogens, they were able to obtain better rheological properties during injection. They were able to eliminate the salt leaching step, and retain the ability to load and deliver cells, bioactive molecules, or both within the hydrogel phase [56].

The swell ratio of a hydrogel is a useful method to determine relative amounts of crosslinking and/or void area within a polymer matrix. It provides an indirect approximation of the crosslink density within a hydrogel. The swell ratio was calculated from the dry and swollen hydrogel weights as follows:

$$Swell\ Ratio = \frac{W_S - W_D}{W_D} \quad (2)$$

$\mathbf{W_s}$ is the swollen weight of the sample, and $\mathbf{W_D}$ is the weight of the dried sample. The swell ratio, also known as the equilibrium degree of swelling, may also be calculated as a function of time [5, 13, 17, 91, 103, 104]. The swell ratio was used to determine the increase in swelling of the templated hydrogels by recording the dried and saline-swollen hydrogel weights. Ideally, scaffolds would be tailored to the optimal conditions for the site of interest [15].

Hydrogels are subject to a number of different parameters that can affect their behavior. In an effort to remove some of the variables and standardize the experimental results, parameters were investigated with consistent design variables. The photoinitiator concentration, UV exposures, and polymer concentration were examined independent of other parameters so that only the porogen or crystallizing molecule was different between

them. The swelling behavior has been characterized for each of the four crystal-templated hydrogels. Data acquired suggests that each crystallizing molecule creates a void space that correlates to the swelling ratio. The swelling ratio follows this order (smallest to largest): urea-templated, potassium dihydrogen phosphate-templated, glycine-templated, guanidine-templated, then not templated as shown in **Figure 4.1**. The characteristic swell ratio experiments gave insight into the effective degree of crosslinking in the hydrogels. From this we are able to hypothesize that urea-templated hydrogels have the highest effective crosslink density and not templated hydrogels have the lowest. This trend is plausible because the crystal templating could bring the polymer chains closer together and result in a higher degree of effective crosslinking results.

The relative amount of swelling a hydrogel experiences may be described by the percent swell. This percentage describes the relative amount the sample swells in phosphate buffered saline as compared to its initial weight immediately after synthesis.

$$\%\, Swell = \frac{W_s - W_i}{W_i} x\ 100\%$$

The combination of swell ratio and percent swell provide a representation of the hydrogel bulk behavior for the not templated controls and templated hydrogel samples. The swell ratio may be artificially inflated as a result of swelling in PBS prior to oven drying. Any residual salts in the matrix would remain in the dry phase and contribute to the recorded dry weight. With this in mind a shortcoming of the procedure is achieving an accurate representation of the swelling capacity of the samples as a result of the potential residual salt content.

The amount that a hydrogel swells is indicative of the void space in the polymer and the extent of crosslinking within the network. Therefore, the swell ratio (SR) of a

hydrogel is a useful method to determine relative amounts of crosslinking and/or void area within a polymer matrix. The trend of EWC did not mirror that of swelling in PBS. The EWCs for the hydrogels were roughly 99%, except for guanidine-templated hydrogels. While all the hydrogels hold comparable amounts of water, the polymer behavior is uniquely different. This is thought to be indicative of the saline interacting with any residual crystalline molecules and therefore influencing the ionic balance in solution and thus the amount the hydrogel swells.

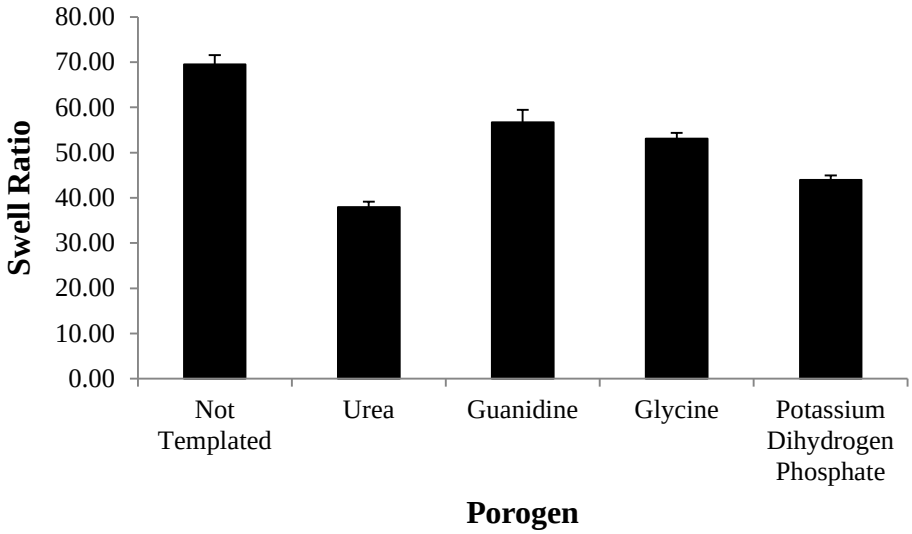

Figure 4.1: Characteristic swell ratio as function of crystallizing molecule at 5 minutes of UV exposure. The characteristic swelling ratio found for hydrogels templated by each crystallizing molecule is shown. Hydrogels were templated using each of the four crystallizing molecules and exposure to 5 minutes of UV, then equilibrated in 10 mM PBS. Samples were analyzed by weight to calculate the characteristic swell ratio attributed to each porogen. Not templated samples presented a higher swell ratio than any of the crystal-templated samples. In order of swelling from lowest to highest are urea-templated, potassium dihydrogen phosphate-templated samples, glycine-templated, guanidine-templated, then not templated samples. The urea-templated samples have the highest effective crosslink density and not templated hydrogels have the lowest.

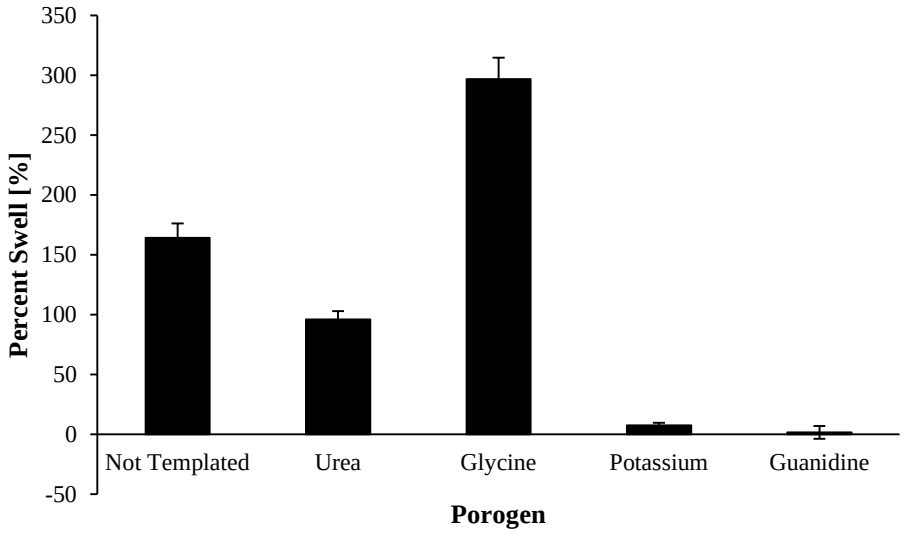

Figure 4.2: Characteristic percent swell as function of crystallizing molecule at 5 minutes of UV exposure. The characteristic swelling ratio found for hydrogels templated by each crystallizing molecule is shown. Hydrogels were templated using each of the four crystallizing molecules and exposure to 5 minutes of UV, then equilibrated in 10 mM PBS. Samples were analyzed by weight to calculate the characteristic percent swell attributed to each porogen. In order of swelling from lowest to highest are guanidine-templated, potassium dihydrogen phosphate-templated, urea-templated, not template then glycine-templated samples.

Porogen	SR at 5 min	Std. Error
Not Templated	69.49	2.08
Urea	37.97	1.17
Guanidine	56.67	2.80
Glycine	53.11	1.29
Potassium Dihydrogen Phosphate	43.99	0.99

Table 2: Swell ratio of 20 mg/mL hydrogels with 0.3% I2959 and 5 minutes of UV exposure templated by each of the crystallizing porogens compared to not templated control group. The table presents corresponding values to the bar plot in Figure 4.1. The swelling order suggests that templated samples lead to a higher effective degree of crosslinking than the not templated control samples.

4.2.2.1 Swelling Calculations. The degree of swelling can be measured by conventional Flory-Huggins swelling theory which is a result of the polymer synthesis conditions. The equilibrium swelling theory is robust; however, the presence of the crystalline molecule can affect the swelling [6]. Therefore, we hypothesize increased swelling in crystal-templated hydrogels. In 1989, Canal and Peppas established correlations between mesh size and equilibrium volume fraction for hydrogels isothermally swollen until equilibrium [102]. Crosslink density controls hydrogel elasticity, and bulk properties and determines permissible routes for polymer clearance from the body. The theory of solute diffusion suggests that ξ (mesh size) indicates a maximum solute size that can pass through the network [102]. The mesh size and other quantitative hydrogel characteristics may be determined through calculations from experimental results. In swollen, crosslinked structures the equilibrium polymer volume fraction, υ_{2s}, is inversely proportional to equilibrium volume degree of swelling, Q_v [10, 102]. Briefly, the initial sample weight is recorded to capture the sample in the relaxed state according to the theory of rubber elasticity. This is the state where the polymer chains are relaxed, meaning they are not expanded or swollen. Polymer volume fraction in "relaxed" state, $\upsilon_{2,}$ is recorded immediately after crosslinking but before equilibrium swelling υ_{2s} [102].

The samples are swollen in pure water to record the swollen weight. After swelling, samples are extensively dried to obtain a weight of the polymer component of the gel. The ratio of the swollen mass in pure water to the dried mass is the degree of mass swelling Q_M.

$$Q_M = \frac{M_{Swollen}}{M_{Dry}} \quad (3)$$

The degree of mass swelling relates to the volumetric swelling ratio, Q_v, through the densities of the polymer and solvent [4, 105].

$$Q_v = 1 + \frac{\rho_p}{\rho_s}(Q_M - 1) \quad (4)$$

The dry polymer density, ρ_p, for HA is 1.229 g/cm^3 [4] and the density of the solvent (water) is 1 g/cm^3. The volumetric swelling ratio is related to the molecular weight between crosslinks via the molar volume of the solvent, the Flory interaction parameter of the polymer, and the solvent. According to Leach et al, the interaction parameter, χ, for HA-water is 0.473 [4]. The molar volume of water, V_1, is 18.1 cm^3/mol. Therefore the molecular weight between crosslinks can be calculated using:

$$Q_v^{5/3} \approx \frac{\bar{\upsilon}\overline{M_C}}{V_1}\left(\frac{1}{2} - X\right) \quad (2)$$

The product of the third root of the volumetric swelling ratio with the root initial square radius $\overline{r_o^2}$ is the swollen hydrogel mesh size.

$$\xi = Q_V^{1/3}\sqrt{\overline{r_o^2}} \quad (6)$$

Cleland et al found that $\frac{\overline{r_o^2}}{2n} = 2.4nm$ [4, 106] which allows simplification of **Equation 6** to:

$$\xi = 0.1748\sqrt{\overline{M_c}}\, Q_V^{1/3} \quad (7)$$

Equation 7 relates the $\overline{M_C}$ to the mesh size and allows the prediction of mesh size without knowing the unperturbed distance. The mesh size can be determined under physiological conditions for a more realistic representation of how ions and salts may affect the sample behavior. The effective crosslink density, υ_e, is the ratio of the polymer density to the molecular weight between crosslinks.

$$\upsilon_e = \frac{\rho_p}{\overline{M}_C} \quad (3)$$

It is interesting that the degree of mass swelling presented a different trend than the SR for the hydrogel samples at 5 minutes of UV exposure. The differences lie in the fact that the SR is essentially the mass ratio of the weight of water in the samples relative to the dry polymer weight, whereas the Q_M takes both the polymer and water components into account. Kim et al. used micro computed tomography (microCT) to get tomographic reconstruction of a sample thereby demonstrating pore interconnectivity. MicroCT techniques could give more accurate assessment of scaffold porosity because mercury instruction porosimetry only measures pores accessible to the pressurized mercury. Results showed that calculated porosity was different than initial porogen amounts, particularly for salt porogens. Salt porogens likely have poor porogen interconnectivity because the particles can be cubic [56].

	Q_M	Q_v	$\overline{M_C}$ (g/mol)	ξ (nm)	υ_e (mol/cm^3)
Not Templated	140.16	172.0297	6997872	2571.73	1.76E-07

Table 3: Mass swelling ratio, volumetric swelling ratio, mesh size and crosslink density for 5 minute not templated hydrogel samples. The degree of mass swelling, Q_M, was calculated and along with the volumetric degree of swelling, $\mathbf{Q_v}$ and used to determine the mesh size of the hydrogel. The control not templated hydrogels displayed a mesh size of 2571.73 nm.

4.2.3 Viscoelastic Behavior

Semi-solid materials fall into the category of structured fluids. The rheological properties of structured fluids are dominated by the interactions of the constituent parts. In general, structured fluids do not behave in a Newtonian manner, meaning that the relationship between applied stress and modulus is more complex than the simple, linear Newtonian relationship. Any fluid that does not follow a Newtonian relationship is classified as non-Newtonian. A strain sweep must be conducted because a viscoelastic material's behavior is independent of strain until a critical strain level, g_c. A strain sweep is an experiment where the sample is exposed to a range of strains at a constant frequency. A typical strain sweep is conducted at 1 Hertz or 6.28 radians per second. After the critical strain level, the behavior is no longer linear and the storage modulus declines [107]. The strain sweep determines the linear range for the material where the frequency sweep should occur. When strain is less than critical strain, material is solid-like, and the storage modulus is greater than the loss modulus which suggests that the material is highly structured. The parameter tan δ, the ratio of the loss modulus to the storage modulus, reflects the strength of colloidal forces. If tan δ is less than 1, the particles are highly associated. A large tan δ, where loss modulus is larger than the storage modulus, suggests that the particles have become unassociated.

After the linear viscoelastic region is identified in the strain sweep, a frequency sweep at a strain less than critical strain, γ_c, can be used to further describe the structure. Beyond the critical strain, the storage modulus is no longer independent of the strain. Frequency sweeps conduct measurements over a range of oscillatory frequencies at constant oscillation amplitude and temperature. Similar to a strain sweep, a frequency

sweep is an experiment where the sample's storage modulus is determined in response to a range of oscillatory frequencies at a constant strain. Below the critical strain, the elastic modulus is practically independent of frequency. This is expected for structured materials [107]. The more frequency-dependent the sample, the more fluid-like or liquid-like the material. For rheological experiments, the deformation force is expressed as stress per unit area. The degree of deformation is quantified as the strain [108]. Hooke's law describes mechanical behavior of an ideal solid. It states that if shear strain, τ, is applied to an ideal solid, a shear stress, ɣ, develops in proportion to the strain. The relationship $\tau = G\gamma$ describes interplay of the modulus G and the strain. This modulus is a measure of stiffness or how much the material is able to resist deformation. Linear stress-strain behavior is observed when the modulus remains unchanged in response to changes in strain. This linear region is also known as the Hookean region. Newton's law relates the shear stress to the strain rate through the apparent viscosity.

A plot of the viscosity, η, versus the shear rate, $\dot{\gamma}$, gives an appreciation for the shear thinning characteristics of the material, if any. Shear thinning occurs when the viscosity drops at high rates of shear stress. This behavior is common among polymer solutions and occurs when the material becomes less resistant to flow. Induced flow shear thickening occurs when some materials show an increased rate of stress after the shear thinning region. Shear thinning occurs when viscosity decreases until a plateau [107]. When viscosity increases as the shear increases, is called shear thickening. Shear thinning materials are known as pseudoplastic. The relationship between shear stress and shear rate is $\tau=\eta\dot{\gamma}$. When the apparent viscosity is plot against the shear rate for shear-thinning fluids, the plot experiences a drop, then a plateau.

The bulk mechanical properties of hydrogel scaffolds are important to scaffold performance. Scaffolds must be mechanically robust to withstand mechanical loading and stresses that occur in the body. Rheological experiments were performed under oscillatory shear stress to characterize the mechanical integrity of the templated hydrogels. The effective crosslinking relates to the stiffness of the hydrogel, which correlates to the storage modulus, G'. Studies displayed in **Figure 4.3** suggest a decrease in the storage modulus occurs upon crystal templating. The extent of the decrease is a function of the crystallizing molecule.

The not templated samples display the highest modulus. This is intuitive because we would expect crosslinking around crystalline structures to increase the effective void space within hydrogel samples. The hydrogels, in order of highest to lowest modulus are not templated, potassium dihydrogen phosphate-templated, urea-templated, guanidine-templated then glycine-templated. Based on these results, we conclude that glycine crystallization has the largest impact on the storage modulus of all the molecules investigated. Furthermore, we would expect that the effective void region of glycine-templated samples to be the largest. Interestingly, the not templated samples retained the largest calculated swell ratio. Because the elastic modulus is affected by crystal templating, the crystallization could have caused the pores to become sufficiently interconnected, as suggested by Calvino-Casilda et al. [91].

It is important to recognize that rheology does not take wave propagation [109], frequency dependence of the sample [109], or the dynamic properties into account [110]. Time and rate dependent behavior is normally explained by viscoelasticity whereas dynamic properties are in response to periodic impact loading. Dynamic material

properties have not been investigated as thoroughly as the static properties of soft tissue scaffolds. This is a shortcoming because soft tissues have complex nonlinear, anisotropic, nonhomogeneous time and rate-dependent behavior. There are many open questions about the dynamic material and mechanical properties of human and animal tissue (both healthy and diseased). It is important to address dynamic sample behavior to achieve a complete picture, but access to *in vivo* samples is limited [110]. Teller et al performed rheology on porcine and human vocal folds. While they found that rheology is incapable of accounting for the frequency dependence of their samples, they did extract valuable information. They speculate that an autologous, injectable construct that would regenerate vocal folds and allow normal vibratory function in patients would be beneficial [109]. For vocal applications the frequency is directly related to speech quality and characteristics, therefore being able to account for sample behavior under various frequency conditions would allow for more pertinent material characterization. This is an interesting challenge that does not directly translate to experimental capabilities because rheological frequency experiments are conducted in the linear viscoelastic range and therefore are mostly independent of frequency. Dynamic properties of hydrogels are beyond the scope of this work, however nanoindentation would be a potential candidate for techniques to address this issue [111].

There are 3 categories of stimuli/cues: topographical, chemical and mechanical [9]. From an applications standpoint, Wong et al. focus on how elastic modulus (mechanical stimulus) can affect cell behavior. The need exists to measure local mechanical properties both on the microscopic and mesoscopic scale for length scales ranging from individual cells to whole tissues. Bulk measures of elastic modulus are not

sensitive to local variations in the mechanical properties. It is well known that hydrogels often have heterogeneities on the micron scale, which is the length scale relevant to cells. Synthetic polymers can be useful for decoupling chemistry from mechanical properties because the polymer does not necessarily have naturally cell-adhesive functionalities like fibrin or collagen [9]. Wong et al. developed a combination of photopolymerization with microfluidics or micropatterning to develop hydrogels that have microgradient level features. Structure and property relationships are very dependent on preparation state of hydrogels, particularly with the goal of creating synthetic polymer networks that mimic key features of natural ECMs. Lutolf et al focused on the crosslinking kinetics and rheology [104]. They used the Archimedes buoyancy principal to calculate hydrogel volumes after crosslinking and after swelling. They plot the relationship between the swelling ratio and elastic modulus on a double logarithmic plot [104]. If the data for multiple parameters fall along the same curve then the same parameters dominate both the swelling and elastic network behaviors [104]. They produced a scatter plot of data from individual hydrogel samples to determine if the Flory interaction parameters were consistent among the sample populations.

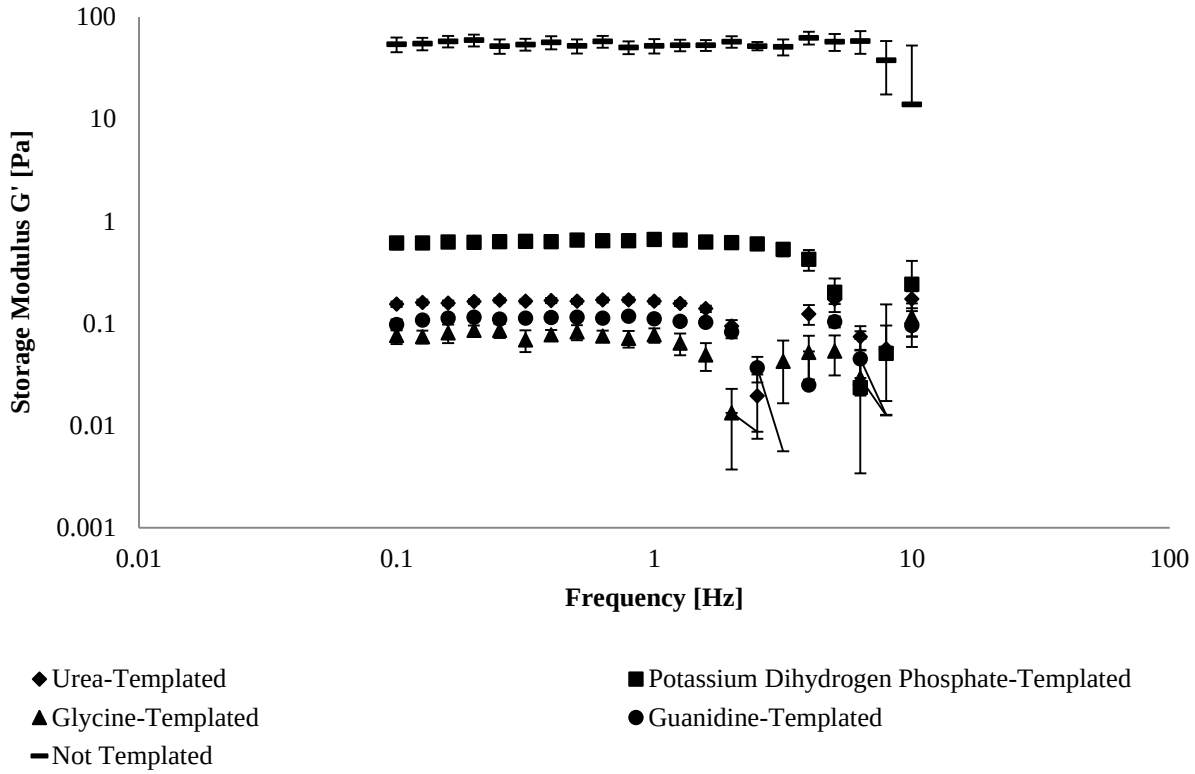

Figure 4.3: Storage modulus of hydrogel samples as a function of crystallizing small molecule. An oscillatory frequency sweep was performed on 20 mg/ml GMHA, 0.3% I2959, 5 minutes UV hydrogels from 0.1-10 Hz. Not templated samples presented the highest storage modulus. In order of highest to lowest the storage moduli were: not templated, potassium dihydrogen phosphate-templated, urea-templated, guanidine-templated, and glycine-templated. These results for crystal-templated samples are consistent with the calculated swell ratio measurements in section 4.2.2. Also, as the storage modulus decreased so did the frequency range where the modulus was stable and independent of frequency. The results indicate that the not templated hydrogels are the most solid-like or resistant to mechanical deformation.

4.2.4 Degradation Behavior. Hydrogels may degrade by mechanisms of hydrolysis, enzymatic degradation or dissolution [15]. Synthetic polymers are often degraded by hydrolysis, natural polymers enzymatically and ionic gels by dissolution [15]. It is possible for ionic gels to undergo hydrolysis as well. Biopolymers are widely used in tissue engineering because of their ability to be degraded *in vivo* by biologically prevalent enzymes. To verify the ability of templated hydrogels to be enzymatically degraded and the relative rate at which degradation may occur after crystal templating, degradation experiments were conducted by incubating the hydrogels in 50 U/mL hyaluronidase and recording the weight hourly for 12 hours, or until complete disintegration. The higher the swell ratio, the higher the propensity for the hydrogel to absorb media; this characteristics may, in turn, influence degradation rate. Hyaluronidase describes the family of enzymes that degrade HA [112]. Hyaluronidase is primarily extracted from bovine testes and bacteria. Testicular hyaluronidases randomly cleave β-N-acetyl-hexosamine (1->4) glycosidic bonds resulting in even numbered oligosaccharides with tetrasaccharides as the smallest fragments; S and N-acetyglucosamine at the reducing end. The molecular weight of this type of hyaluronidase is 61kDa [112]. The *in vitro* degradation profile of hydrogels with various amounts of photoinitiator and UV exposure attests to the malleability of hydrogels and the method of imposing macroscopic architecture within a soft matrix. Experimental results are presented in **Figure 4.4** as the mean degradation normalized to the initial weight with error bars for standard error. Experiments were conducted 3 times for each combination of photoinitiator concentration and UV exposure, each with a minimum of

12 samples. The hydrogel weights were recorded after swelling in saline (W_o) and hourly during enzymatic degradation (W_t) [4]:

$$Degradation = \frac{W_o - W_t}{W_o} \quad (9)$$

Hydrogels at 20 mg/mL methacrylated hyaluronic acid with 0.3% photoinitiator were templated with each of the porogens. Urea and glycine templated hydrogels were the most susceptible to enzymatic degradation, whereas potassium dihydrogen phosphate templated samples resisted degradation the most efficiently. Degradation rates from slowest to fastest were as follows: potassium dihydrogen phosphate-templated, not templated, guanidine-templated, glycine-templated and urea-templated. It should be noted that both the not templated and guanidine-templated samples experienced slight swelling before degradation began. This is within normal hydrogel behavior because as some of the polymer bonds are cleaved, the hydrogel has the ability to swell more before it reaches its elastic retraction force.

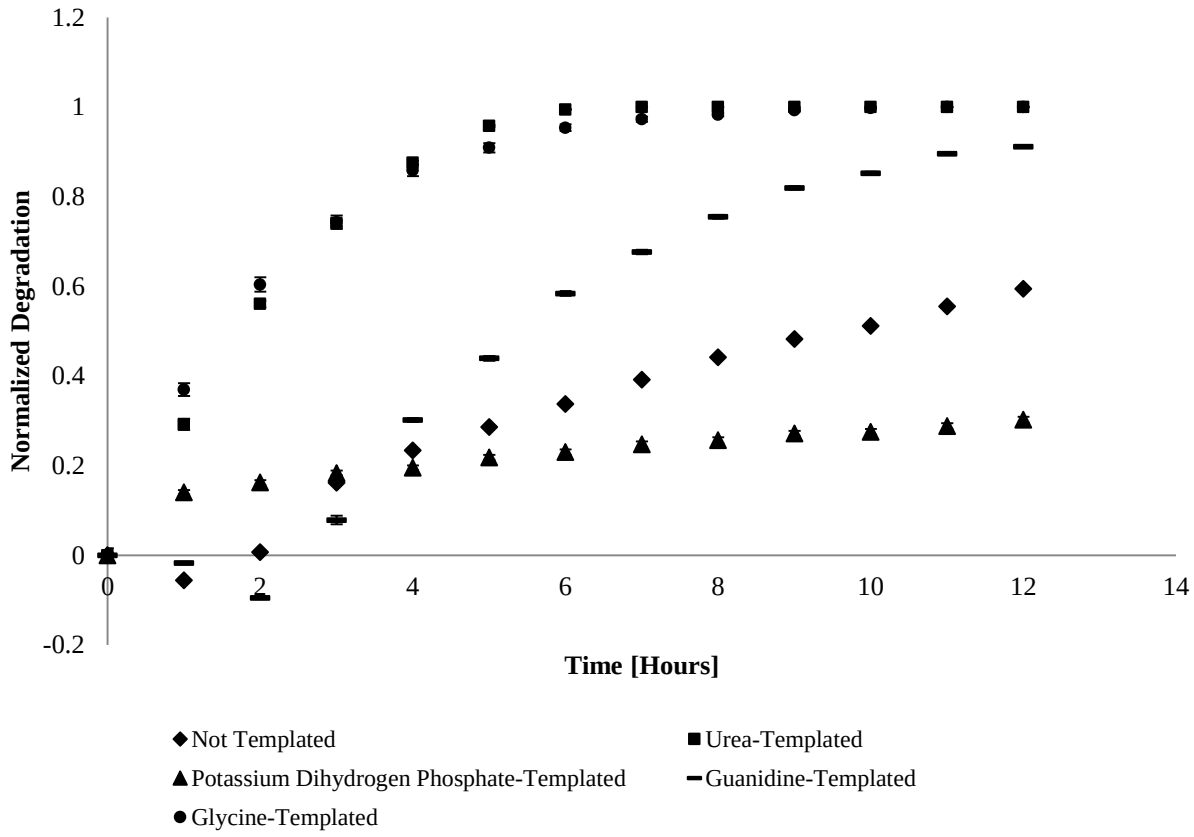

Figure 4.4: Degradation behavior of methacrylated hyaluronic acid hydrogels as a function of crystallizing molecule. Hydrogel samples synthesized at 20 mg/ml GMHA, 0.3% PI, 5 min UV were enzymatically degraded over 12 hours. In order of degradation from slowest to fastest: potassium dihydrogen phosphate-templated, not templated, guanidine-templated, glycine-templated and urea-templated. Both the not templated and guanidine-templated samples experienced some slight swelling before they degraded.

4.3 Conclusions

The equilibrium water contents for not templated controls and the crystal templated samples were not significantly different, with the exception of guanidine. This suggests that the amount of water a hydrogel holds is largely independent of the size of void spaces within its matrix. The swelling results showed that templated samples exhibited a smaller swell ratio than the control samples. This indicates that the polymer chains are potentially compacted after crystal nucleation within the pre-hydrogel solution, which could allow for more effective crosslinking [1]. The mesh size measurements indicate how effectively molecules can pass through the polymeric portion of the sample, not the bulk hydrogel. The results suggest that template hydrogels swell to a greater degree than the not template samples while their swell ratio suggests that the proximity of the polymer chains in crystal-templated samples may lead to a smaller size [1]. A caveat to consider for the swelling experiments is the potential for residual salt presence from equilibration in PBS artificially inflating the dried hydrogel weight. In order to address this concern both the swell ratio, percent swell and raw data were included to offer a more holistic view of the hydrogel behavior. Furthermore, potential charge interactions between the polymer and the molecules likely have an impact on the mechanical properties. Viscoelastic experiments showed a reduction in the storage modulus when hydrogels are crystal-templated. Because this is a bulk measurement, the results are intuitive because as the amount of voided region increases within a sample the overall behavior is less resistant to flow and therefore displays a lower storage modulus. Finally, degradation results displayed hydrogel degradation from slowest to fastest as follows:

potassium dihydrogen phosphate-templated, not templated, guanidine-templated, glycine-templated and urea-templated.

4.4 Materials and Methods

4.3.1 Materials. High molecular weight sodium hyaluronate from *Streptococcus equi* of molecular weight 1.6 x 10^6 Da (53747-10G), Glycidyl Methacrylate (779342-500ML), Triethylamine (T0886-1L), Urea (U5378), Potassium Phosphate Monobasic (P5655-500G) and dextran-FITC were all purchased from Sigma Aldrich (St Louis, Mo). Irgacure 2959 was purchased from Ciba Specialty Chemicals/ BASF (Basel, Switzerland). Guanidine hydrochloride (BP178-500), Glycine (BP381-500), Acetone (A181), BD PrecisionGlide 25 gauge needles (305122), Luer-Lok syringes (2018-06) were all purchased from Fisher Scientific.

4.3.2 Hydrogel synthesis. Photocrosslinkable three-dimensionally patterned hyaluronic acid hydrogels were synthesized by preparing 2-5 w/v% solution of glycidyl methacrylated hyaluronic acid with photoinitiator concentration variing between 0.3-1 % Irgacure 2959. A 1% stock photoinitiator solution was prepared in 10 mM phosphate-buffered saline and added accordingly to the hydrogel solution to obtain the desired final concentration. The photoinitaitor was heat sonicated for 30-45 minutes to facilitate solubilzation.

4.3.3 Equilibrium Water Content Experiments. The templated hydrogels were first rinsed in deionized water overnight to remove the crystalline molecules. The hydrogel was transferred to fresh deionized water and allowed to reach equilibrium and

the weight recorded. The samples were then dried overnight in an oven to achieve the weight of the polymer component in the hydrogel samples. The dried weight was recorded and used to calculate the equilibrium water content for each templated hydrogel.

4.3.4 Swelling. The crystal template was rinsed away in deionized water, and the hydrogel was then swollen overnight in 10 mM phosphate-buffered saline (PBS) to complete swelling studies. The equilibrium weight in pH 7.4 PBS at room temperature was recorded. The equilibrium hydrogels were subsequently dried at 40 ^{o}C for 48 hours to obtain the dry weight of the polymer.

4.3.5 Rheology. An Anton Paar rheometer with 25 mm parallel plates was used over a frequency sweep of 0.1-10 Hz at constant strain and 2 mm gap size [104]. Two rheometers were used in this thesis. The ARES LS1 allows more functionality however the Anton Paar is more user-friendly. The ARES displays the force whereas the Anton Paar only shows contact with the sample. Samples evaluated on the ARES LS1 with an air pressure of approximately 80 psi on a thermocouple heated stage to maintain 25˚C and 8mm parallel plate. The plate was attached using a balanced pin. The gap was calibrated automatically using normal force, and then measurements were taken at approximately 0.1N force to exert minimal force on the sample but to ensure contact. Even though different sizes and machines were used, the data can still be compared because the sample sizes were scaled as appropriate to the plates available.

4.3.6 Degradation. For degradation experiments a solution of 50 units per milliliter hyaluronidase in 10mM PBS was prepared. The PBS swollen hydrogels were placed in 1 mL of hyaluronidase solution and incubated at 40 ˚C. The initial hydrogel

weight was recorded with weights subsequently recorded every hour for 12 hours. The *in vitro* degradation profile of templated hydrogels was evaluated by recording the hydrogel weights after swelling in saline (W_o) and at specific times during hyaluronidase enzymatic degradation (W_t) [4]:

$$\%\ Degradation = \frac{W_o - W_t}{W_o} \times 100\% \qquad (10)$$

Chapter Five. Mechanical Properties of Templated Hydrogel as Function of Synthesis Parameters

Polymers have defined molecular architecture that is predetermined by the structures of their precursor components [104]. The synthesis parameters directly influence hydrogel bulk property behaviors. We hypothesize that the effect of synthesis parameters is more evident in hydrogels with large porous volumes than in normal control samples. Thus, a screen of synthesis parameters at designated set points was carried out in samples whose void space was increased using small molecule crystal nucleation. Hydrogel experiments were completed using approximately 18-20% methacrylated hyaluronic acid at a concentration of 20 mg/mL, unless otherwise noted. In the crystal-templated hydrogels, experiments were conducted to determine the hydrogel swelling in response to the extent of UV exposure, photoinitiator concentration, and porogen concentration, among others. Hydrogel network properties are very sensitive to the preparation and synthesis conditions [104].

5.1 Importance of Synthesis Parameters on Swelling Behavior

Swelling remains one of the most useful techniques to determine how a hydrogel behaves as well as quantitative characteristics such as mesh size, molecular weight between crosslinks and crosslink density. These quantitative measures provide insight into the sizes of molecules that can effectively diffuse into and out of the polymeric scaffold as well as potential *in vivo* application areas.

Not templated control samples were swollen in PBS until equilibrium to determine the swell ratio (SR). This dimensionless ratio of the swollen weight to dry weight of the hydrogel provides information on the extent samples swell in a given media. Not templated samples were photocrosslinked for 2, 5, 10 and 20 minutes of ultra-violet (UV) light exposure and the data is presented in **Figure 5.1**. The swell ratio decreased with increased duration of UV exposure until 10 minutes. At 20 minutes of exposure, the SR increased to 72.14 which is not significantly different than the value after 2 minutes of UV exposure. It is likely that at 20 minutes of exposure the UV light begins to degrade polymer, counteracting the potentially high crosslink density. These results suggest a correlation between the extent of UV exposure and the swell ratio for 2, 5, and 10 minutes of UV exposure. The correlation does not remain true for 20 minutes of crosslinking.

The samples were swollen in water to obtain the degree of mass swelling, Q_M, before they were swollen in PBS to calculate the SR. As stated in chapter 4, Q_M is the ratio of the mass of the swollen sample in pure water to the mass of the dry samples or the dry polymer weight. The experimentally determined Q_M can be used to calculate the quantitative hydrogel characteristics. The degree of mass swelling, unlike the SR, saw little to no correlation based on the extent of UV exposure. The Q_M did increase at 20 minutes, however. The molecular weight between crosslinks for not templated hydrogels was found to be $6.5*10^6$ Da at 2 minutes, $7.0*10^6$ Da at 5 minutes, $5.7*10^6$ Da at 10 minutes and $11.49*10^6$ Da at 20 minutes as summarized in **Table 4**. This translates into mesh sizes ranging from 2.2-3.6 mm. The crosslink densities range from $1.07*10^{-7}$ to $2.14*10^{-7}$ mol/cm^3. This information highlights the differences in hydrogel behavior in

different media (water vs. PBS) as well as the effects of UV exposure. In PBS, the not templated samples had SRs that followed a correlation for three consecutive time points. Additionally, the percent swell for not templated hydrogels mirrored that of the swell ratio (**Figure 5.2**). In water, these same samples showed no clear relationship.

Urea crystals nucleated in the presence of 20 mg/mL GMHA, 0.3% I2959 mixture and the polymer was crosslinked with 2, 5, 10, and 20 minutes of UV exposure. The swell ratio of urea-templated samples decreased as the time of UV exposure increased until 10 minutes (**Figure 5.3**). The data suggests that the swell ratio was approximately the same for 5 and 10 minutes of UV exposure. Similar to the not templated control samples, the swell ratio at 20 minutes UV exposure was similar to that at 2 minutes. The data suggests that urea-templated samples roughly maintained the same SR trend as the not templated control population. Urea templating did not affect the SR relationship with UV exposure for 2, 5, and 10 minutes. The percent swell, on the other hand, decreased with increasing lengths of UV exposure. The swell ratio results were similar to those found for the not templated samples, however the percent swell results showed a relationship with UV exposure which suggests higher effective crosslinking (**Figure 5.4**).

The degree of mass swelling for urea-templated hydrogels did not follow any correlation to the time of UV exposure. However, Q_M varied in a manner that appeared to be independent of the duration of photopolymerization, which is interesting considering the large void regions shown in the confocal and cryoSEM images.

The potassium dihydrogen phosphate-templated hydrogel samples display a swell ratio that decreases with increasing durations of photocrosslinking. There is a strong

relationship between extent of UV exposure (**Figure 5.5**) and the swell ratio for these samples. The swell ratios were 53.39 ± 3.01 for 2 minutes, 43.99 ±0.99 for 5 minutes, 41.63 ± 1.67 for 10 minutes and 39.69 ± 1.98 for 20 minutes of UV exposure. The swell ratio decreased as the extent of UV exposure increased. The potassium dihydrogen phosphate-templated samples also did not experience the increase in swell ratio at 20 minutes that was evident in the urea-templated and control groups. These data are presented as the mean with standard error **Figure 5.5.** Percent swell results for potassium dihydrogen phosphate-templated hydrogels displayed a decrease as the length of UV exposure increased as was found in the swell ratio results (**Figure 5.6**). After 20 minutes of UV exposure percent swell data show that the samples swell to a lesser extent than the initial sample.

The degree of mass swelling for potassium dihydrogen phosphate-templated hydrogels also followed a trend with the extent of UV exposure. The Q_M was found to be 47.74 for 2 minute hydrogels, 37.39 for 5 minute, 34.94 for 10 minute and 34.26 for 20 minute UV exposure durations **Table 6**. This suggests a strong relationship between the swelling mass of the samples and the duration of photopolymerization. For the potassium dihydrogen phosphate-templated samples both SR and Q_M had a relationship with the duration of UV exposure. This suggests that UV exposure plays a dominant role in scaffold behavior regardless of whether or not the water component is taken into account for calculations.

For guanidine-templated hydrogels, the SR was 54.68 ± 2.23 for 2 minutes, 56.67 ± 2.80 for 5 minutes, 60.50 ± 3.5 for 10 minutes and 40.4 ± 6.78 for 20 minutes UV exposure (**Figure 5.7**). There was not a significant difference in the swell ratio for

samples photopolymerized from 2, 5 and 10 minutes. At 20 minutes, the swell ratio was reduced. This relationship is unique from the other porogens where a relationship between SR and UV exposure could be identified until 10 minutes. In the case of guanidine-templated samples, the SR appears to be independent of UV exposure. The same conclusion holds true for percent swell results. The percent swell data suggest that the guanidine-templated hydrogels are independent of UV exposure for each of the time points (**Figure 5.8**). The mean values did mirror the trend found for the not templated control samples by decreasing until 10 minutes of UV exposure, then increasing after 20 minutes. The counter-intuitive relationship between duration of UV exposure and SR could result from guanidine denaturing the HA. Both guanidine hydrochloride and urea are chaotropic agents meaning they denature proteins. Guanidine specifically has some ionic properties. Because it has a much higher ionic strength than urea it is a much stronger denaturant than urea [85, 86]. Alternatively, the guanidine crystals could have interfered with the ability to modulate the hydrogel behavior using UV exposure. Furthermore, HA and guanidine ion has a positive charge which is the opposite of anionic HA so that could play a role as well.

The guanidine-templated hydrogel degree of mass swelling did not present a trend with the extent of UV exposure. The degree of mass swelling ranged from 42.89 to 82.68 as shown in **Table 7**. The Q_M in order from lowest to highest were 20 minutes of UV exposure, 2 minutes, 10 minutes then 5 minutes. The mass swelling did not follow a trend related to the extent of UV exposure nor any relationship to the SR behavior. The related crosslink densities ranged from $1.27*10^{-5}$to $9.99*10^{-7}$ mol/cm^3 **Table 7**. When the

amount of water in the hydrogel is taken into consideration for Q_M, no correlation can be made with the photocrosslinking durations.

Glycine-templated samples had a strong relationship between the SR and the time of UV exposure. The swell ratio decreased as the extent of UV exposure increased. The SR at 2 minutes UV exposure was 55.33 ± 2.33, 53.11 ± 1.29 at 5 minutes, 48.44 ±1.31 at 10 minutes and 48.12 ± 1.4 at 20 minutes (**Figure 5.9**). The relationship is intuitive and mirrors the trend found in potassium dihydrogen phosphate-templated samples. Interestingly, the samples did not experience the large increase in SR following 20 minutes of UV exposure that was evident for urea-templated and not templated control groups. The glycine-templated samples appear to have formed the maximum number of crosslinks at 10 minutes of UV exposure and no additional effective crosslinks were formed in the additional 10 minutes. The percent swell results concur with that of swell ratio, however the trend is more pronounced (**Figure 5.10**). Glycine-crystal templating could have provided some shielding effect that prevented polymer degradation by UV because it is the smallest of the molecules.

The glycine-templated hydrogel degree of mass swelling ranged from 98.29 to 109.42. The Q_M in order from lowest to highest were 2 minutes of UV exposure, 10 minutes, 5 minutes then 20 minutes (**Table 8**). The calculated swelling amounts did not follow a trend related to the extent of UV exposure. The related crosslink densities ranged from $2.66*10^{-7}$ to $3.18*10^{-7}$ mol/cm^3 (**Table 8**). Again, Q_M takes the water weight into account and therefore may display different trends than the SR which is measured in PBS. In water, the glycine-templated samples behave largely independent of UV exposure.

To further investigate the impact of templating on the hydrogel properties, the remaining characterization studies were completed with urea as a representative porogen. Both urea-templated and not templated hydrogels were compared for the effective swell ratio at two photoinitiator concentrations. Increased amounts of photoinitiator resulted in more effective crosslinking as measured by swell ratio. Templated hydrogels were swollen overnight in deionized water to remove the colloidal crystal after UV exposure. The hydrogels were subsequently allowed to equilibrate in phosphate-buffered saline (PBS) overnight before performing experiments. Not templated hydrogels were subjected to the same protocol. For each of two amounts of photoinitiator concentration, the templated hydrogel had an increased swell ratio relative to the not templated control.

Results suggest that for both not templated and urea-templated hydrogels, increased photoinitiator concentration reduces the swell ratio as displayed in **Figure 5.11**. Additionally, results shown in **Figure 5.12** indicate that increasing urea concentration leads to increased swell ratio. The swell ratio for hydrogels templated with urea crystals is a function of both the extent of crosslinking and the weight percent of photoinitiator. The swell ratio increased with urea-templating at both 0.5% and 1% photoinitiator concentrations. The additional void space from crystal templating may be attributed to the increase in swell ratio. Additionally, the swell ratio decreased with increased photoinitiator concentration for both not templated and urea templated hydrogels. The data suggest that crystal templating does not adversely affect the changes photoinitiator concentration has on hydrogel swelling properties. The trend was conserved for both templated and not templated hydrogel scaffolds.

We have conducted a study to determine the effect of porogen concentration on swelling ratio using urea as a representative porogen; the data collected with urea may provide insight into the behavior of the other crystallizing porogens. The purpose was to evaluate the effect, if any, increased porogen concentration had on the swell ratio. The experiment would identify the role effective void space plays in hydrogel bulk swelling behavior. The swell ratio of urea templated hydrogels increased with increased crystallizing molecule concentration. This is thought to be indicative of the increased effective porosity that results from the crystalline geometry. With increased templating molecule concentration, increased restricted volume results, which allows the hydrogel to absorb increased media and therefore swell to a greater extent.

The not templated control showed a correlation between the SR and UV exposure until 10 minutes. As the UV exposure increased the SR decreased. After 20 minutes of UV, however, the relationship was no longer maintained and the SR increased to a value comparable to the 2 minute UV exposure samples. It is likely that at sufficiently long UV exposure times the polymer begins to degrade and therefore would lead to a lower effective crosslink density and higher swell ratio. Similar behavior was found for urea-templated hydrogels. This suggests as that as far as swell ratio is concerned, the dominating factors remain unchanged between the control and urea-templated samples. Swell ratio values were larger in the control population. Swell ratio behavior was also similar to the control population for the potassium dihydrogen phosphate-templated and glycine-templated samples. These hydrogels displayed a strong relationship between SR and extent of UV exposure. Although the potassium dihydrogen phosphate-templated hydrogel swell ratios tend to plateau after 10 minutes of UV, the overall trend exists.

Guanidine-templated hydrogels were independent of UV exposure until 20 minutes of UV exposure where the SR was reduced. While the mesh size calculations do not give an accurate depiction of the total effective void space, it does give an idea of the crosslink density and how tightly packed the polymer chains are.

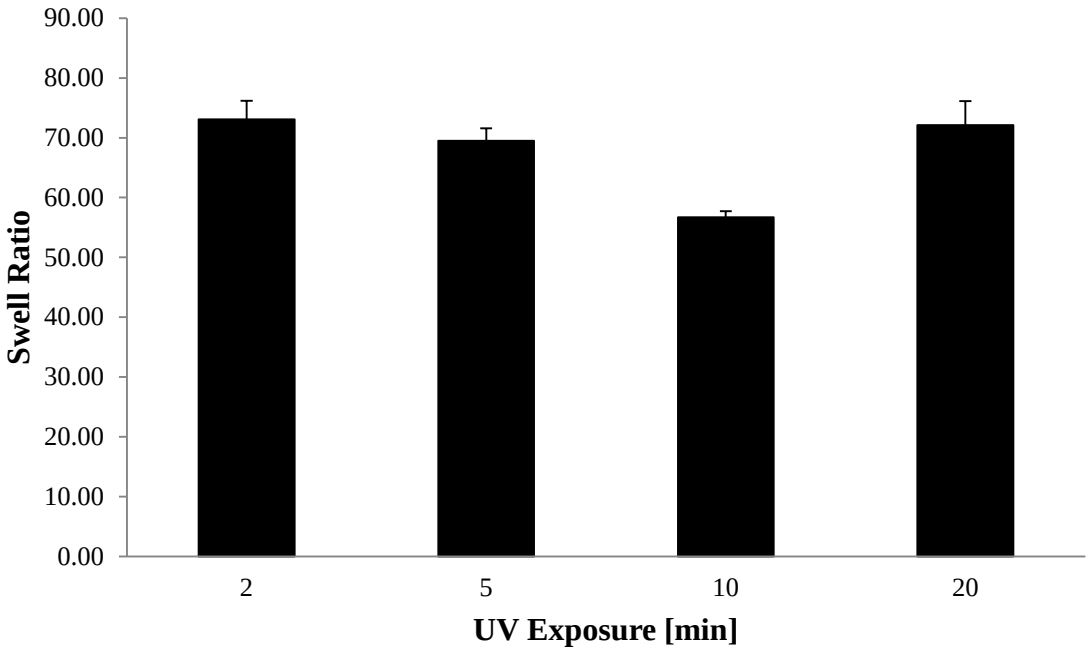

Figure 5.1: Swell ratio of not templated hydrogels as a function of UV exposure. The 20 mg/mL GMHA, 0.3% I2959 samples were crosslinked with 2, 5, 10, and 20 minutes of UV exposure. The samples were first swollen in water, then allowed to equilibrate in PBS. The samples with 2 minutes of UV exposure had the highest SR and the samples with 10 min UV exposure had the lowest. The SR decreased with increasing UV exposure until 10 minutes. At 20 minutes, the SR increased to 72.14. It is likely that this results from UV degrading the GMHA.

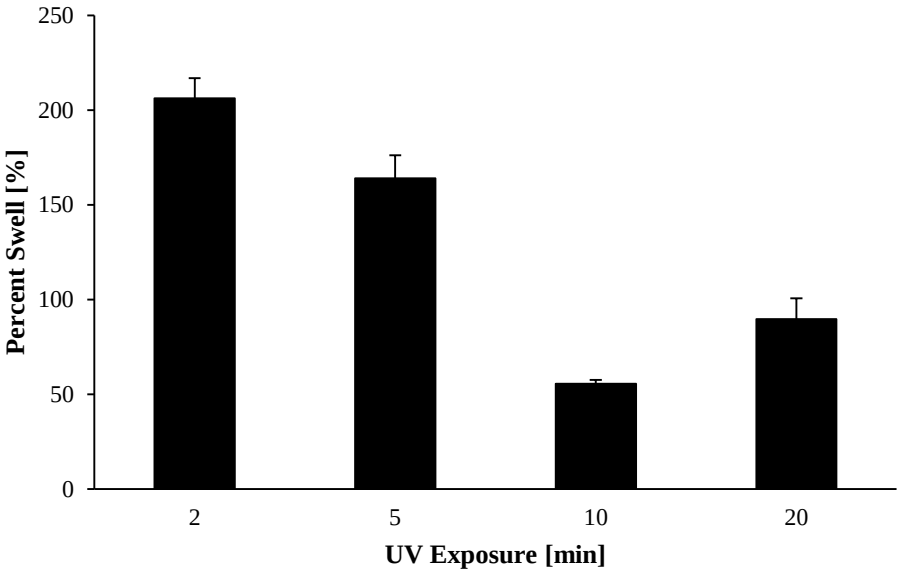

Figure 5.2: Percent swell for not templated hydrogels as a function of UV exposure in minutes. The 20 mg/mL GMHA, 0.3% I2959 samples were crosslinked with 2, 5, 10, and 20 minutes of UV exposure. The samples were first swollen in water, then allowed to equilibrate in PBS. The samples with 2 minutes of UV exposure had the highest SR and the samples with 10 min UV exposure had the lowest. The percent swell decreased with increasing UV exposure until 10 minutes. At 20 minutes, the percent swell increased to 89.75%. It is likely that this results from UV degrading the GMHA. These results mirror the trend for swell ratio.

	Q_M	Q_v	$\overline{M_C}$ (g/mol)	Mesh Size (nm)	υ_e (mol/cm^3)
2	134.3571	164.8959	6520936	2447.74598	1.88E-07
5	140.1617	172.0297	6997872	2571.73125	1.75625E-07
10	124.4056	152.6655	5734931	2237.27386	2.14301E-07
20	188.7139	231.7004	11494892	3640.01206	1.06917E-07

Table 4: Hydrogel characteristics for not templated hydrogels photopolymerized from 2-20 minutes. The degree of mass swelling ranged from 124.4 to 188.7. The Q_M in order from lowest to highest was 10 minutes of UV exposure, 2 minutes, 5 minutes then 20 minutes. The swelling amounts did not follow a trend related to the extent of UV exposure. The calculated mesh sizes ranged from 2.2-3.6 mm. The related crosslink densities ranged from $1.07*10^{-7}$to $2.14*10^{-7}$ mol/cm^3.

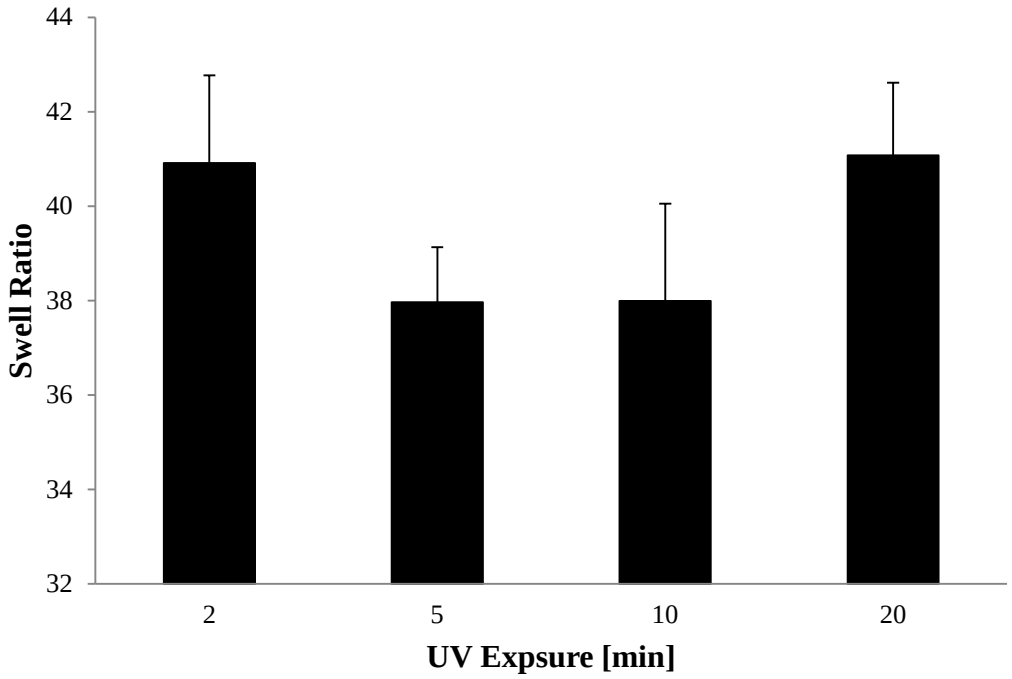

Figure 5.3: Swell ratio of urea-templated hydrogels as function of UV exposure duration. Urea crystals nucleated in the presence of 20 mg/mL GMHA, 0.3% I2959 polymer mixture and the polymer was crosslinked at 2, 5, 10, and 20 minutes of UV exposure. The samples were first swollen in water, then allowed to equilibrate in PBS. The swell ratio decreased as the time of UV exposure increased until 10 minutes. The data suggests that the swell ratio was approximately the same for 5 and 10 minutes of UV exposure. Similar to the not templated control sample results, the swell ratio at 20 minutes UV exposure was similar to that at 2 minutes. The values are presented as the mean ± standard error.

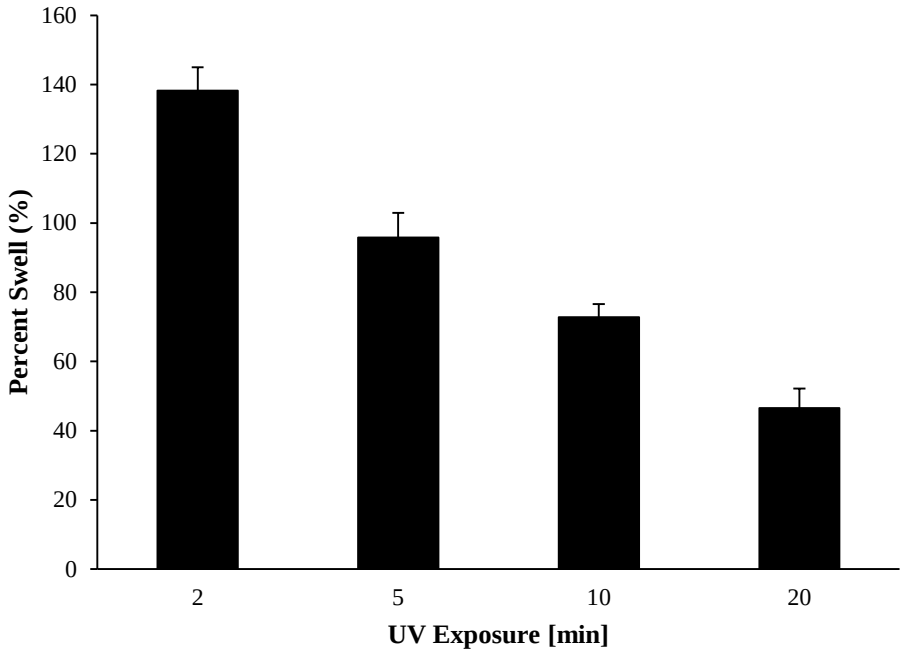

Figure 5.4: Percent swell for urea-templated hydrogels as function of UV exposure duration. Urea crystals nucleated in the presence of 20 mg/mL GMHA, 0.3% I2959 polymer mixture and the polymer was crosslinked at 2, 5, 10, and 20 minutes of UV exposure. The samples were first swollen in water, then allowed to equilibrate in PBS. The percent swell decreased as the time of UV exposure increased. The swell ratio showed similar behavior to the not template controls, however the percent swell is indicative of more overall crosslinking at longer times of UV exposure. The values are presented as the mean ± standard error.

	Q_M	Q_v	$\overline{M_C}$ (g/mol)	υ_e
2	82.40405	101.0456	2882852	4.26E-07
5	79.37741	97.32584	2708156	4.54E-07
10	86.08322	105.5673	3101052	3.96E-07
20	72.35806	88.69906	2320021	5.3E-07

Table 5: Hydrogel characteristics for urea-templated hydrogels photopolymerized from 2-20 minutes. The degree of mass swelling ranged from 124.4 to 188.7. The Q_M in order from lowest to highest were 10 minutes of UV exposure, 2 minutes, 5 minutes, then 20 minutes. The degree of mass swelling values did not follow a trend related to the extent of UV exposure. The related crosslink densities ranged from $1.07*10^{-7}$to $2.14*10^{-7}$ mol/cm^3.

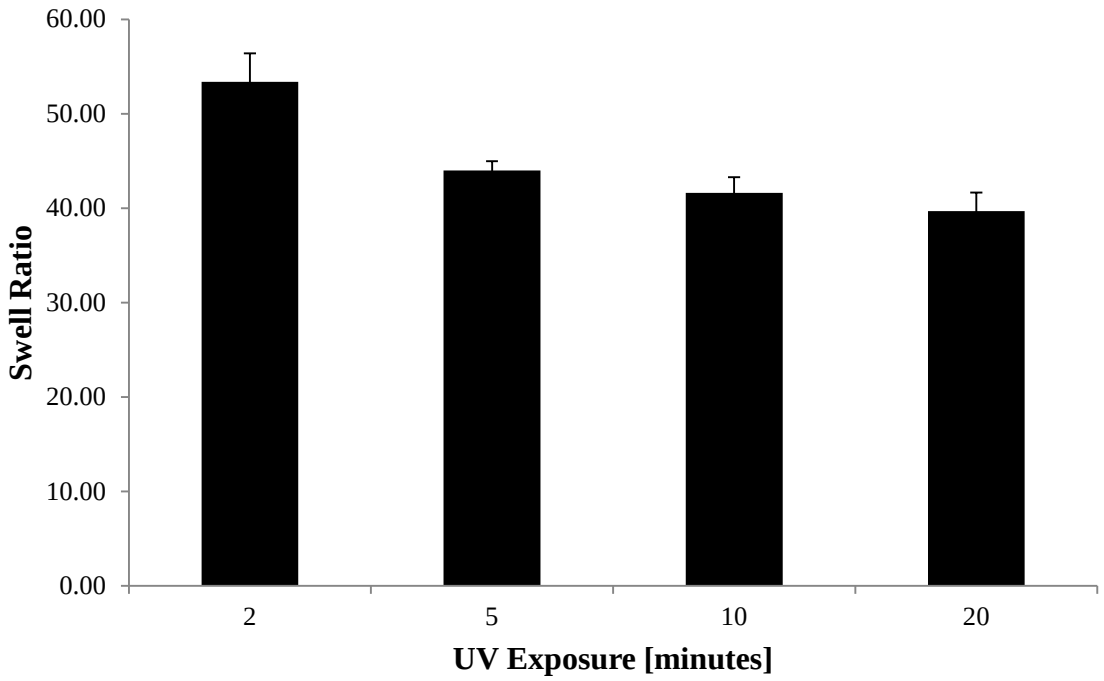

Figure 5.5: Swell ratio of potassium dihydrogen phosphate-templated hydrogels as a function of UV exposure. The hydrogel samples display a swell ratio that decreases with increasing times of photocrosslinking. There is a strong relationship between extent of UV exposure and the swell ratio for these samples. The swell ratios were 53.39 ± 3.01 for 2 minute, 43.99 ±0.99 for 5 minute, 41.63 ± 1.67 for 10 minute and 39.69 ± 1.98 for 20 minutes of UV exposure. These data suggest that the samples reached a maximum degree of crosslinking at 10 minutes; there is not a significant difference between the 10 minute and 20 minute UV exposure samples. The values are presented as the mean ± standard error.

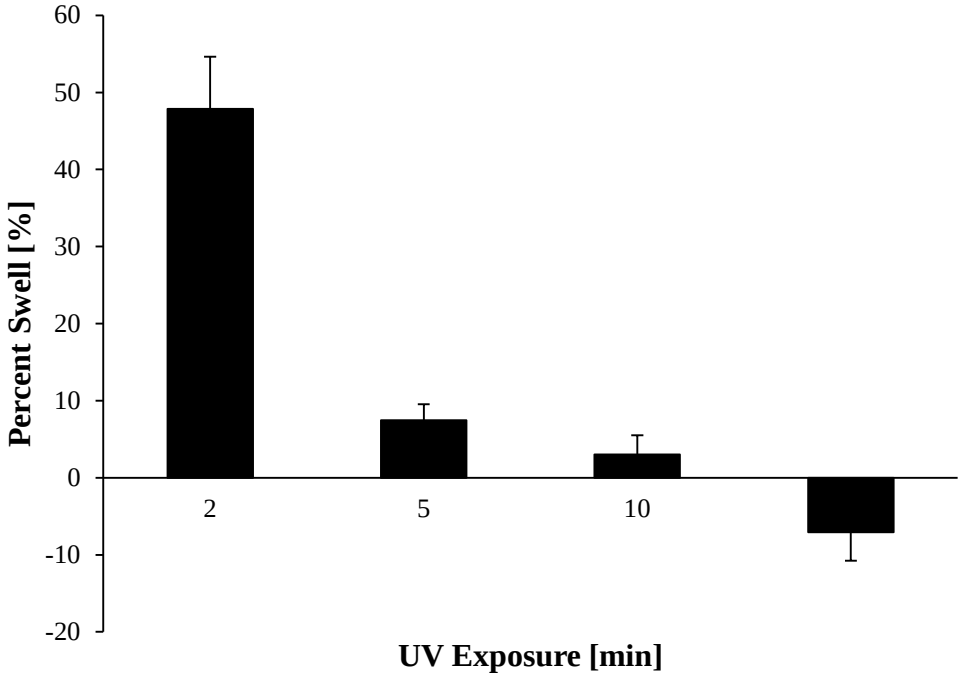

Figure 5.6: Percent swell of potassium dihydrogen phosphate-templated hydrogels as a function of UV exposure. The hydrogel samples display a percent swell that decreases with increasing lengths of photocrosslinking. There is a strong relationship between extent of UV exposure and the percent swell for these samples. These data suggest that the samples saw decreasing amounts of swelling as the UV expsoure increased and after 20 minutes of UV exposure, the samples had a reduction in size relative to the initial sample. The values are presented as the mean ± standard error.

	Q_M	Q_v	$\overline{M_C}$ (g/mol)	υ_e
2	47.74	58.44433	1157526	1.06175E-06
5	37.39	45.72389	768892.2	1.5984E-06
10	34.94	42.7101	686295.4	1.79077E-06
20	34.26	41.87961	664198.4	1.85035E-06

Table 6: Hydrogel characteristics for potassium dihydrogen phosphate-templated hydrogels photopolymerized from 2-20 minutes. The degree of mass swelling ranged from 124.4 to 188.7. The Q_M in order from lowest to highest was 10 minutes of UV exposure, 2 minutes, 5 minutes, then 20 minutes. The degree of mass swelling values did not follow a trend related to the duration of UV exposure. The related crosslink densities ranged from $1.06*10^{-6}$to $1.85*10^{-6}$ mol/cm^3.

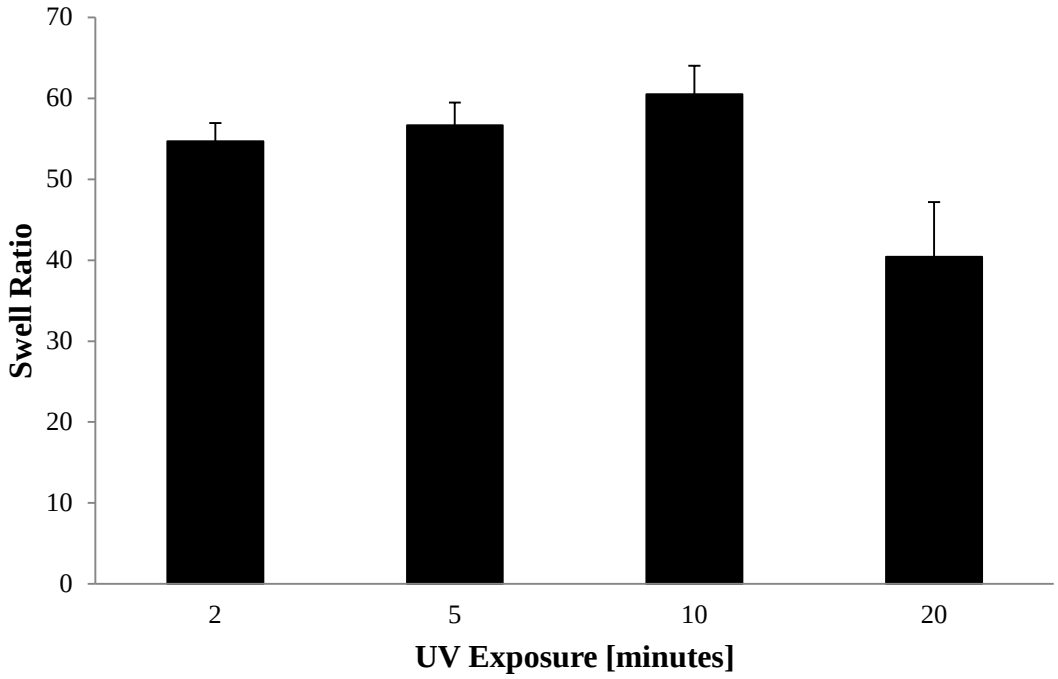

Figure 5.7: Swell ratio of guanidine-templated hydrogels as function of UV exposure. The SR was 54.68 ± 2.23 for 2 minutes, 56.67 ± 2.80 for 5 minute, 60.50 ± 3.5 for 10 minute and 40.4 ± 6.78 for 20 minutes UV exposure. There was not a significant difference in the swell ratio for samples photopolymerized from 2, 5 and 10 minutes, however the SR did increase with increasing UV exposure times. This result is counterintuitive. At 20 minutes, the swell ratio was smaller. Guanidine crystals appear to interfere with the ability to modulate swelling properties using UV exposure. The data is presented as the mean ± standard error.

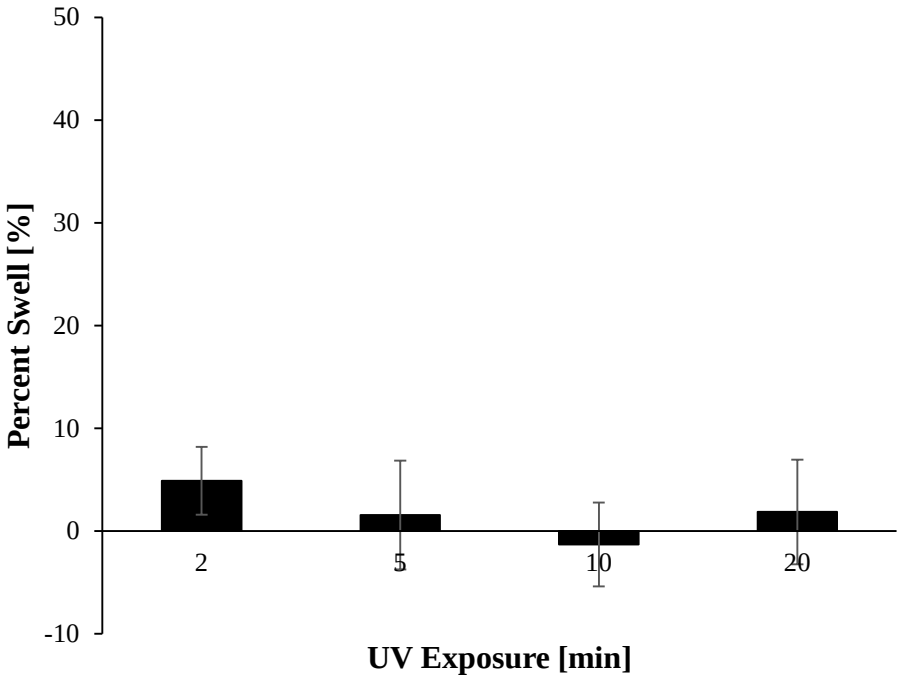

Figure 5.8: Percent swell ratio of guanidine-templated hydrogels as function of UV exposure. The guanidine-templated samples did not swell appreciably. There was not a significant difference in the percent swell for samples photopolymerized at the different time points, however the percent swell did decrease with increasing UV exposure times. This result is intuitive. The percent swell results agree with the swell ratio data that suggests that guanidine crystals appear to interfere with the ability to modulate swelling properties using UV exposure. The data is presented as the mean ± standard error.

	Q_M	Q_v	$\overline{M_C}$ (g/mol)	υ_e
2	49.50253	60.60961	1229880	9.99285E-07
5	82.68271	101.3881	2899155	4.23917E-07
10	60.48219	74.10361	1719330	7.14814E-07
20	42.88533	52.47708	967333.5	1.2705E-06

Table 7: Table of guanidine-templated hydrogel calculated characteristics. The degree of mass swelling did not present a trend with the duration of UV exposure. The degree of mass swelling ranged from 42.89 to 82.68. The hydrogels with Q_M in order from lowest to highest was 20 minutes of UV exposure, 2 minutes, 10 minutes then 5 minutes. The swelling amounts did not follow a trend related to the duration of UV exposure. The related crosslink densities ranged from $1.27*10^{-5}$to $9.99*10^{-7}$ mol/cm^3. No conclusions can be made from these results.

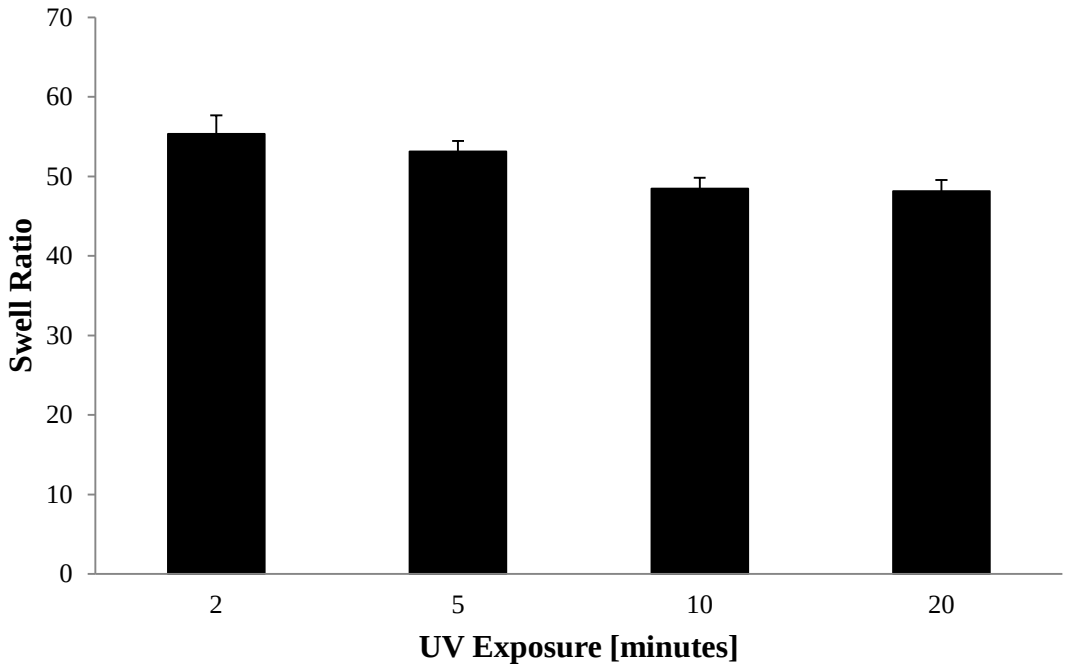

Figure 5.9: Swell ratio of glycine-templated hydrogels as a function of UV duration. The SR at 2 minutes UV exposure was 55.33 ± 2.33, 53.11 ± 1.29 at 5 minutes, 48.44 ± 1.31 at 10 minutes and 48.12 ± 1.4 at 20 minutes. The swell ratio decreased as the extent of UV duration increased. The result is intuitive because as the duration of UV exposure increases, more crosslinks tend to form and the SR tends to decrease. The trends from these samples are most similar to the potassium dihydrogen phosphate-templated samples. Similarly, it is likely that the maximum degree of crosslinking was reached at 10 minutes of UV exposure. The data are presented as the mean ± standard error.

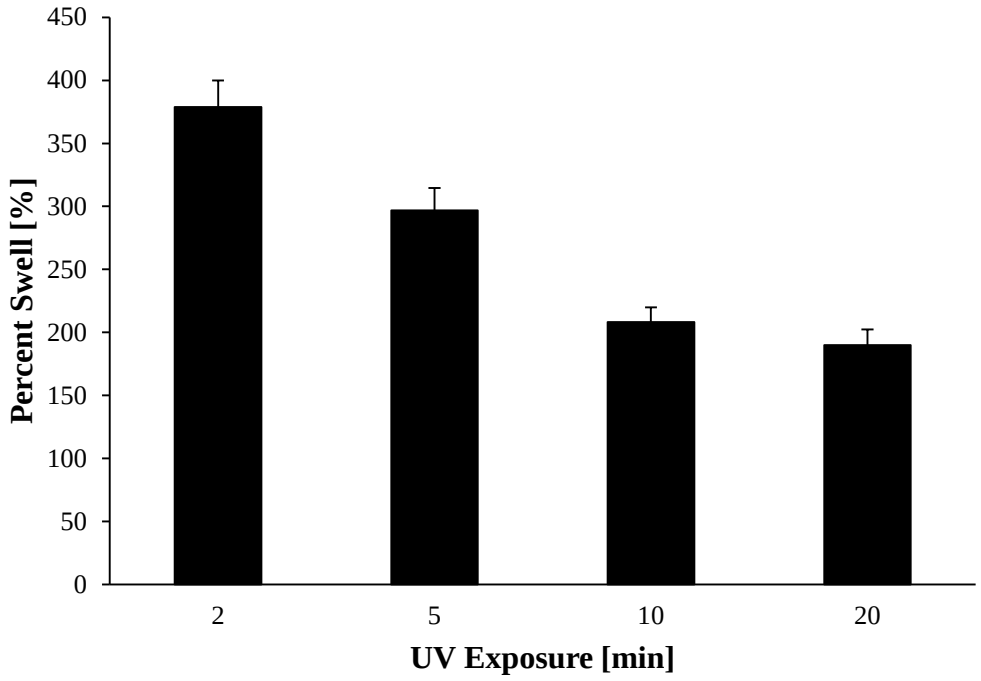

Figure 5.10: Percent swell for glycine-templated hydrogels as a function of UV duration. The percent swell decreased as the extent of UV duration increased. The result is intuitive because as the duration of UV exposure increases, more crosslinks tend to form and the bulk swell tends to decrease. The trends from these samples mirrors that of swell ratio for glycine-templated hydrogels but the trend is more pronounced. The data are presented as the mean ± standard error.

	Q_M	Q_v	$\overline{M_C}$ (g/mol)	υ_e (mol/cm^3)
2	98.29	120.565	3869567	3.17607E-07
5	106.15	130.2321	4400383	2.79294E-07
10	98.62	120.9749	3891515	3.15815E-07
20	109.42	134.248	4628851	2.65509E-07

Table 8: Table of glycine-templated hydrogel calculated characteristics. The degree of mass swelling ranged from 98.29 to 109.42. The Q_M in order from lowest to highest was 2 minutes of UV exposure, 10 minutes, 5 minutes then 20 minutes. The swelling amounts did not follow a trend related to the extent of UV exposure. The related crosslink densities ranged from $2.65*10^{-7}$to $3.17*10^{-7}$ mol/cm^3. The calculated values are independent of UV exposure.

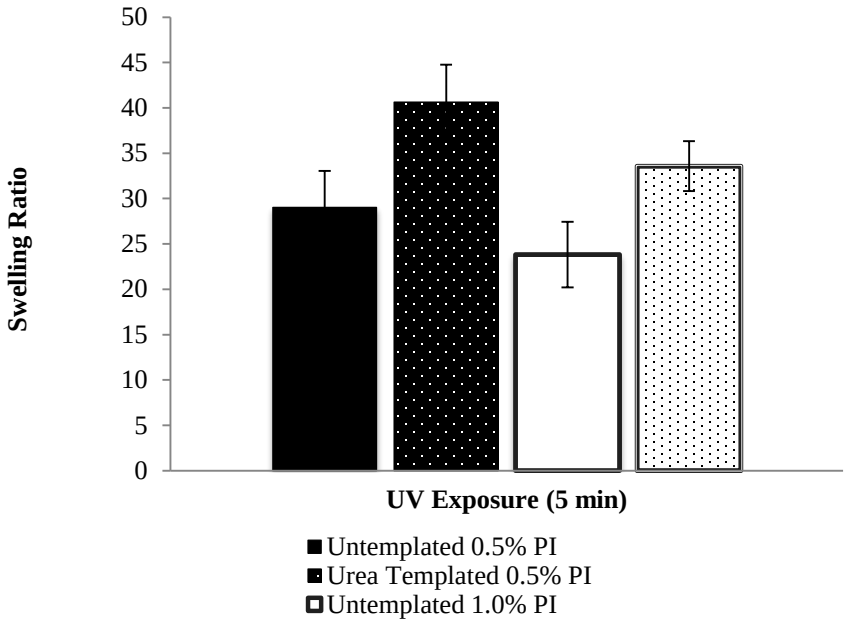

Figure 5.11: The swell ratio of not templated and urea-templated hydrogels was determined at two photoinitiator concentrations. Hydrogels were exposed to 5 minutes of UV exposure. The SR increased for the urea-templated samples as compared to the not templated controls. The SR decreased with increased amount of I2959. The results are intuitive and follow a trend between UV exposures, photoinitiator concentration, and swell ratio in both the not templated and urea-templated samples.

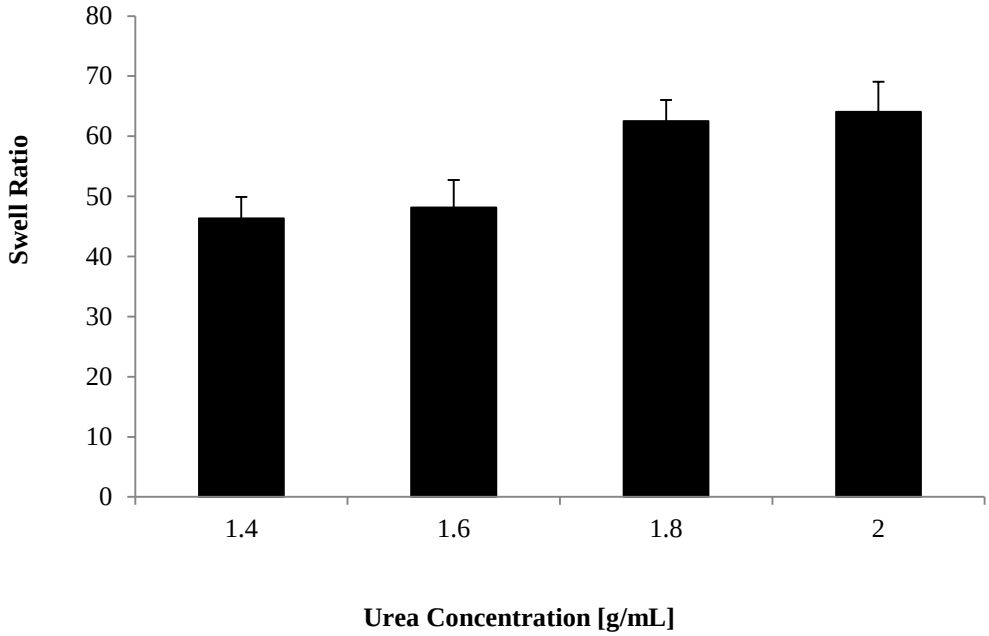

Figure 5.12: Swell ratio was determined for urea-templated hydrogels at increasing urea concentration from 1.4-2.0 g/ml. SR increased with increasing urea concentrations. The increased effective porosity is attributed to longer crystalline formations because of increased molecule concentration. The data are presented as mean ± standard error.

5.3 Viscoelastic Behavior

Hydrogel scaffolds are used for tissue engineering materials because their mechanical properties are similar to native tissue. Mechanically, hydrogels with storage moduli similar to surrounding tissue place less stress on endogenous cells and surrounding tissue because they are able to more closely mimic the native environment [64, 90, 92, 113].

Rheology is the study of deformation and flow in response to applied forces [108]. The rheological properties can be determined for a variety of materials from fluids to asphalt. Mechanical rheology is particularly applicable for bulk sample measurements but there are techniques to measure micro-scale properties. Mechanical rheology is most commonly employed for materials that have both viscous and elastic properties. The viscoelasticity can be dependent on external forces such as stress, strain and temperature. The viscoelastic characterization determines how liquid-like or solid-like a material's behavior is.

Leach et al explain the protocol to synthesize hyaluronic acid at two degrees of methacrylation [4]. Fifty mg/mL concentration solutions of each HA were synthesized with 0.1 and 0.5% Irgacure 2959 photoinitiator. HA was methacrylated at both 11% and 20% methacrylation. The goal was to determine whether photoinitiator concentration or percent methacrylation played a more significant role in hydrogel behavior. **Figure 5.13** plots the rheological behavior of each hydrogel type. Interestingly, two populations are evident from the results. The hydrogels with 0.1% I2959 display moduli of approximately 1 Pa while the 0.5% I2959 hydrogels have moduli of about 8 Pa. The two groups have

very similar behavior despite their differences in percent methacrylation. The influence of percent methacrylation, while important, has been shown to become less evident for high degrees of methacrylation [51]. The results suggest that photoinitiator concentration has a more significant impact on not templated hydrogel behavior than percent polymer methacrylation.

The remaining experiments were all conducted with 20% methacrylated hyaluronic acid, unless otherwise noted. Methacrylated hyaluronic acid hydrogels at 20 mg/mL and 50 mg/mL concentrations were evaluated for the storage modulus from 0.1-10 Hz frequency. The purpose was to determine the effect polymer concentration has on the rheological properties. There was a strong dependence on the polymer concentration as evidenced by **Figure 5.14**. The modulus of the 50 mg/mL hydrogel is almost an order of magnitude larger than the 20 mg/mL concentration. These results show similar behavior to Lutlof et al.'s results where they indicated that an increase in elastic modulus with an increase of precursor concentration [104]. They argue that the molecular weight of the precursor chains determine the molecular weight between the crosslinks. Furthermore, the 50 mg/mL methacrylated hyaluronic samples appears to experience stiffening as the frequency range increases, whereas at 20 mg/mL the samples undergoes slight weakening during the frequency sweep.

The synthesis parameters for hydrogels directly influence hydrogel bulk properties. We hypothesize that the effect of synthesis parameters is more evident in crystal-templated hydrogels because of the large void area. We evaluated how the extent of UV exposure, photoinitiator concentration, and porogen concentration affected hydrogel swelling for each genre of hydrogel independently. This study aimed to

decouple the relative effects of photoinitiator concentration and extent of UV exposure on the hydrogel storage modulus. The 1% I2959, samples with 1 minute of UV exposure had the smallest storage modulus and the 0.7% I2959, with 5 minutes of UV exposure had the highest for not templated hydrogels (**Figure 5.15**). The results from this experiment are not intuitive. The samples with higher duration of UV exposure for consistent amount of photoinitator had higher storage moduli. However, the samples with higher amounts of photoinitator at consistent durations of UV exposure did not have a higher storage moduli. The experimental results are not intuitive because at the same durations of UV exposure there is not a trend between the photoinitiator concentration and the modulus. The 1% I2959, 5 minute UV exposure samples present a lower modulus than both the 0.3% I2959, 5 minute UV exposure and the 0.7% I2959, 5 minute UV exposure samples. This suggests that above a certain concentration, increasing photoinitiator does not increase the modulus for the control population.

Potassium dihydrogen phosphate-templated samples present a strong trend that suggests that both photoinitator concentration and duration of photopolymerization impact the storage modulus (**Figure 5.16**). The modulus increased when UV exposure increased. The 1% I2959 samples with 5 minutes of UV exposure had moduli of approximately 4 Pa while the 2 minute UV exposure samples were only 1 Pa. Similarly, as the amount of I2959 increased so did the modulus. The results show that the trend is mostly conserved from the not templated control population. It appears that the 0.7% I2959 concentration is the optimal concentration to achieve the largest storage modulus. The frequency sweep for 1% I2959 samples with 2 minutes of UV exposure was conducted at 2.5% strain and the 1% I2959, 5 minute UV exposure samples were

conducted at 2% strain. The strain sweeps for each of these sample genres may be found in Appendix A.

Glycine-templated hydrogelsfor 0.3% I2959, 5 minute UV exposure samples had the highest storage modulus and the 0.7% I2959, 5 minute UV exposure samples had the lowest (**Figure 5.17**). The modulus of the 0.3% I2959, 5 minute UV exposure samples was significantly higher than the modulus of the other parameter combinations. There was not trend present between the photoinitator concentrations at consistent levels of UV exposure. At higher frequencies, these samples experience a weakening. The weaking appears to become more pronounced for samples with lower moduli.

The guanidine-templated hydrogels with 0.3% I2959, 5 minute UV exposure had the highest storage modulus and the 1% I2959 samples had the lowest (**Figure 5.18**). There is strong agreement in the moduli of the 1% I2959 samples at both 1 and 5 minutes UV exposure which suggests a more prominent relationship between photoinitiator concentration and storage modulus than duration of UV exposure for guanidine-templated hydrogels. There was not trend present between the photoinitator concentrations at consistent levels of UV exposure. The order of storage modulus from highest to lowest mirrors that of glycine-templated hydrogels, although the differences between the samples are not as pronounced.

The experiment to determine the storage modulus of urea-templated hydrogels as a function of synthesis parameters found that the 0.7% I2959, 5 minute UV exposure samples had the highest storage modulus and the 1% I2959, 1 minute UV exposure samples had the lowest (**Figure 5.19**). The results suggest that the 0.7% I2959 concentration is near the optimal concentration for maximum storage modulus and that

increasing the photoinitiator beyond that amount does not increase the modulus. Additionally, both the photoinitiator concentration and UV expsorure time play a role in the sample storage modulus. The modulus for samples crossliked for 5 minutes of UV exposure each had a larger modulus than the 1 minute UV exposure samples.

Urea-templated hydrogels showed a storage modulus approximately an order of magnitude lower than that of not templated hydrogels in **Figure 5.20**. An amplitude sweep at a strain in the linear range was conducted from 0.1-10 Hz of oscillatory stress at 25˚C. The results suggest that the less effective void volume allows a more solid-like sample. Interestingly both not templated and urea-templated samples exhibit stiffening at higher frequencies.

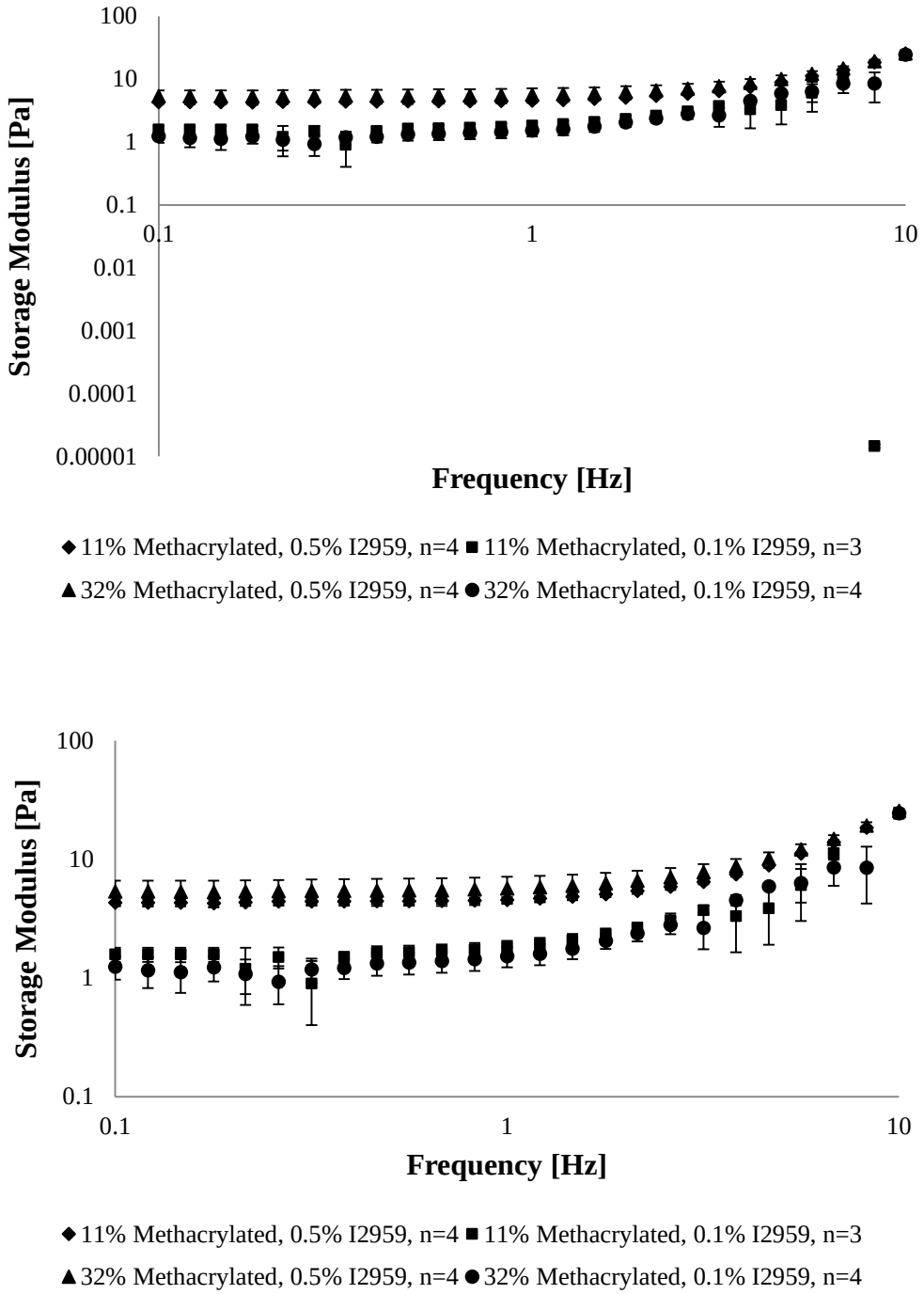

Figure 5.13 Not templated hydrogel storage modulus as a function of percent methacrylation and photoinitiator concentration. 50 mg/ml GMHA was either 11% or 20% methacrylated, and cross-linked for 5 minutes under UV light. The two groups have very similar behavior despite their differences in percent methacrylation. The results suggest that photoinitiator concentration has a more significant impact on not templated hydrogel behavior than percent polymer methacrylation.

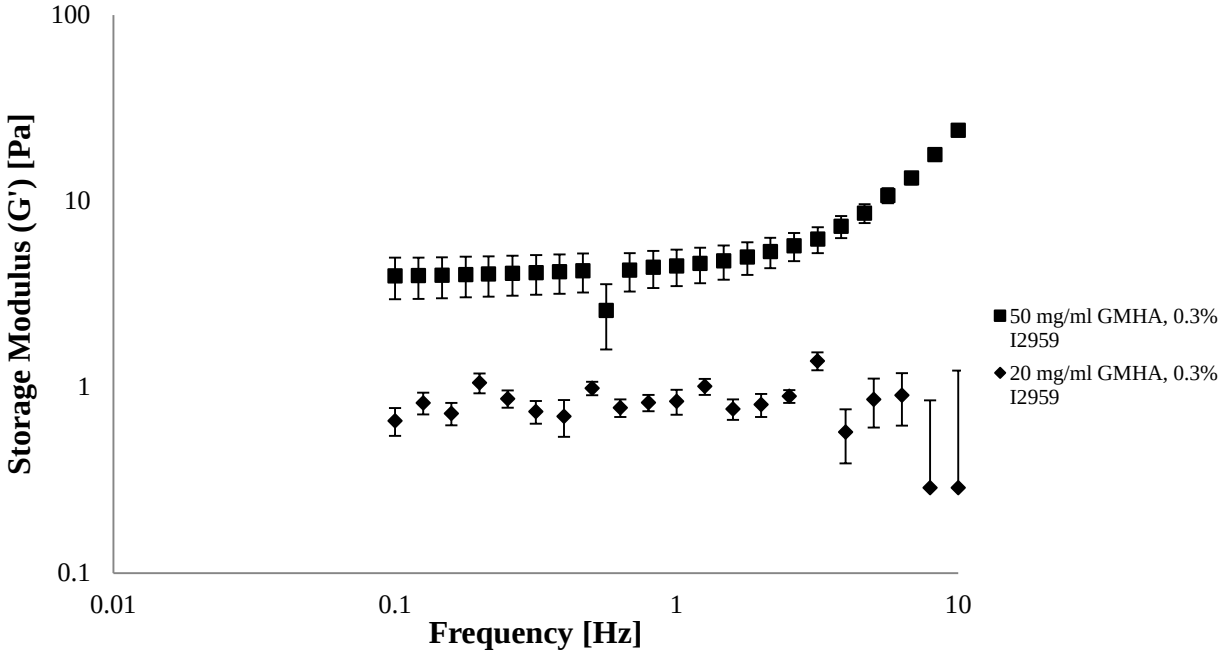

Figure 5.14: Storage modulus of not templated hydrogels as function of methacrylated HA concentration. Hydrogels at 20 mg/mL and 50 mg/mL GMHA synthesized with 0.3% I2959 for 5 minutes under UV. Oscillatory frequency sweep conducted from 0.1-10 Hz. The 50 mg/mL GMHA samples had larger storage moduli than the 20 mg/mL samples. Additionally, the 50 mg/mL samples exhibit stiffening at higher frequencies. The results suggest that higher polymer concentrations lead to higher storage modulus.

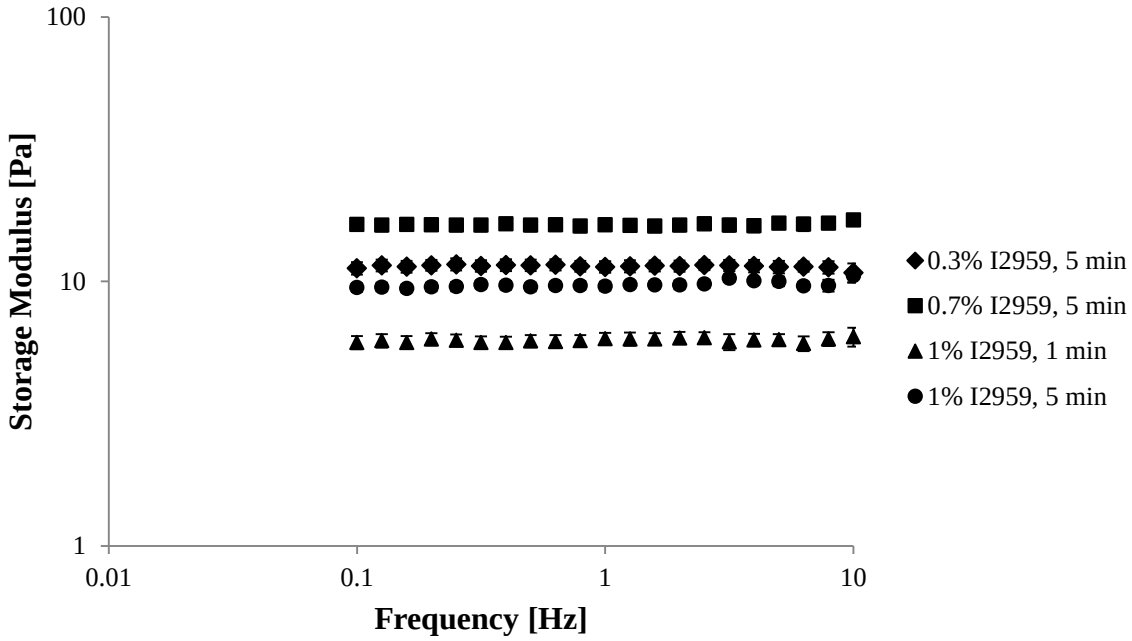

Figure 5.15: Not templated hydrogel storage modulus as a function of synthesis parameters. The study aimed to decouple the relative effects of photoinitiator concentration and duration of UV exposure on the hydrogel storage modulus. The 1% I2959, 1 minute UV exposure samples had the smallest storage modulus and the 0.7% I2959, 5 minute UV exposure samples had the highest. The experimental results are not intuitive because at the same duration of UV exposure there is not a trend between the photoinitiator concentration and the modulus. The 1% I2959, 5 minute UV exposure samples present a lower modulus than both the 0.3% I2959, 5 minute UV expsoure and the 0.7% I2959, 5 minute UV exposure samples. This suggests that above a certain concentration, increasing photoinitiator does not increase the modulus for the control population. The storage modulus is largely frequency independent.

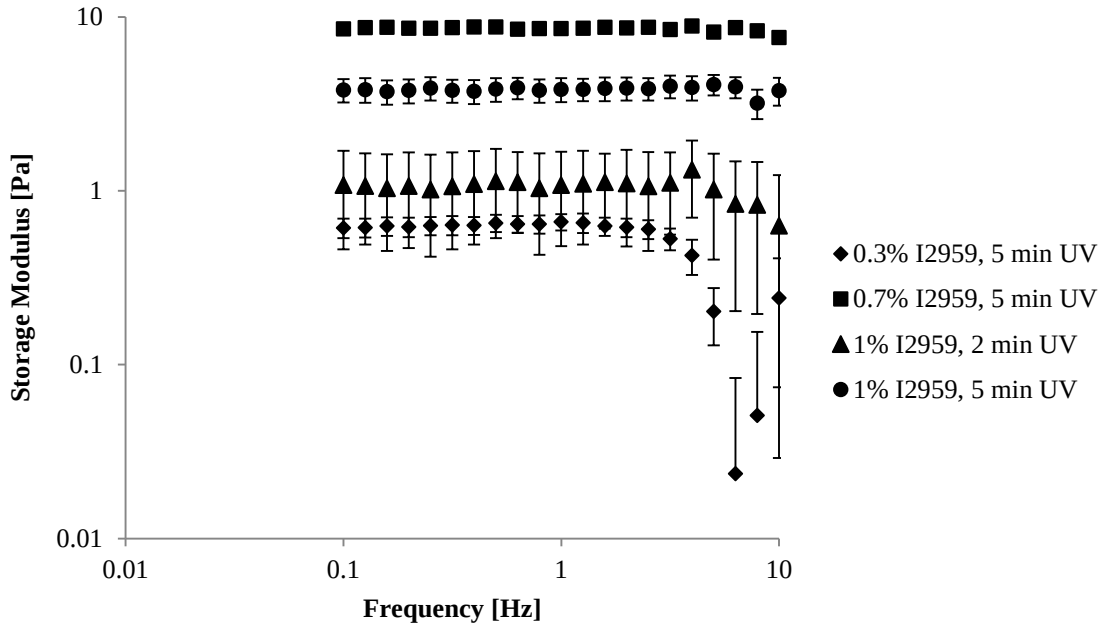

Figure 5.16: Potassium dihydrogen phosphate-templated hydrogel storage modulus as a function of synthesis parameters. This study aimed to decouple the relative effects of photoinitiator concentration and duration of UV exposure on the hydrogel storage modulus. The 0.3% I2959, 5 minute UV exposure samples had the smallest storage modulus and the 0.7% I2959, 5 minute UV exposure samples had the highest. The samples with higher amounts of photoinitator at consistent levels of UV exposure had higher storage moduli. The samples with higher amounts of UV exposure for consistent amount of photoinitator also had higher storage moduli. It appears that the 0.7% I2959 concentration is the optimal concentration to achieve the largest storage modulus. Potassium dihydrogen phosphate-templated samples present a strong trend that suggests that both photoinitator concentration and length of photopolymerization impact the storage modulus. Additionally, there is a weaking effect that occurs at higher frequencies that is more prominent in samples with lower moduli.

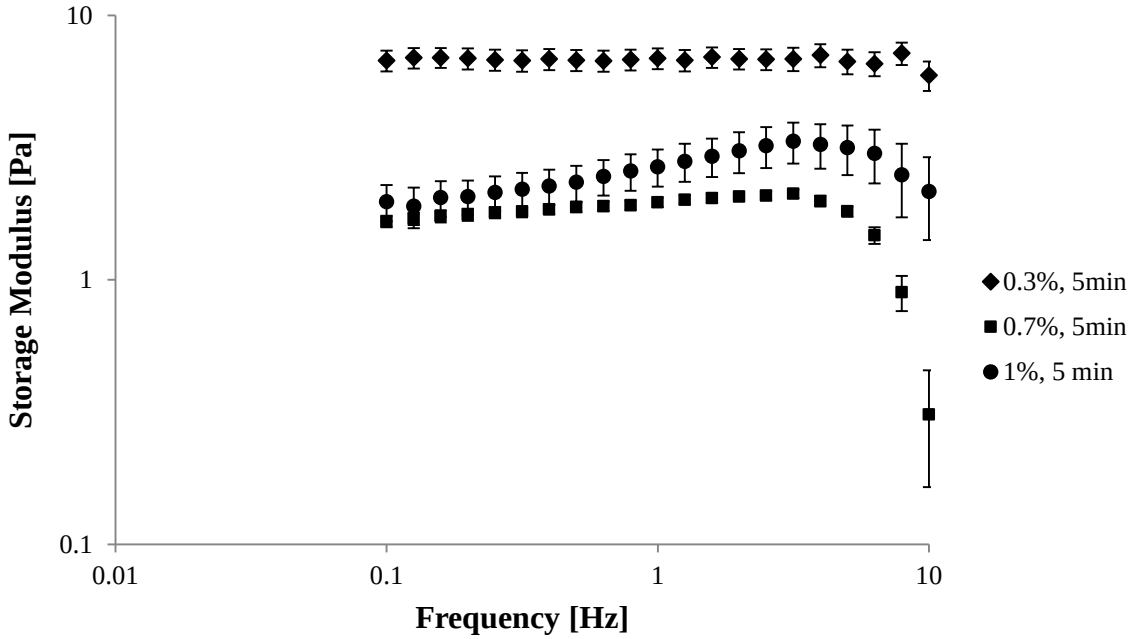

Figure 5.17: Glycine-templated hydrogel storage modulus as a function of synthesis parameters. This study aimed to decouple the relative effects of photoinitiator concentration and duration of UV exposure on the hydrogel storage modulus. The 0.3% I2959, 5 minute UV exposure samples had the highest storage modulus and the 0.7% I2959, 5 minute UV exposure samples had the lowest. There was not trend present between the photoinitator concentrations at consistent levels of UV exposure.

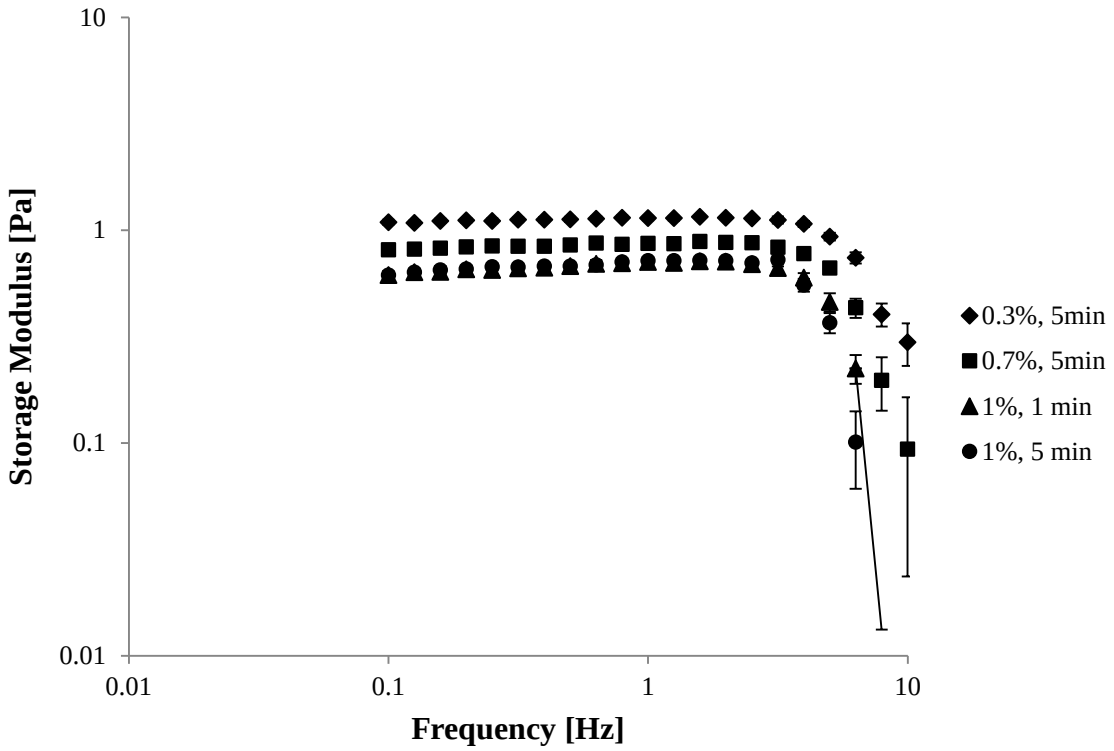

Figure 5.18: Guanidine-templated hydrogel storage modulus as a function of synthesis parameters. This study aimed to decouple the relative effects of photoinitiator concentration and duration of UV exposure on the hydrogel storage modulus. The 0.3% I2959, 5 minute UV exposure samples had the highest storage modulus and the 1% I2959 samples had the lowest. There is strong agreement in the moduli of the 1% I2959 samples at both 1 and 5 minutes UV exposure which suggests a more prominent relationship between photoinitiator concentration and storage modulus than duration of UV exposure for guanidine-templated hydrogels. There was no trend present between the photoinitator concentrations at consistent levels of UV exposure.

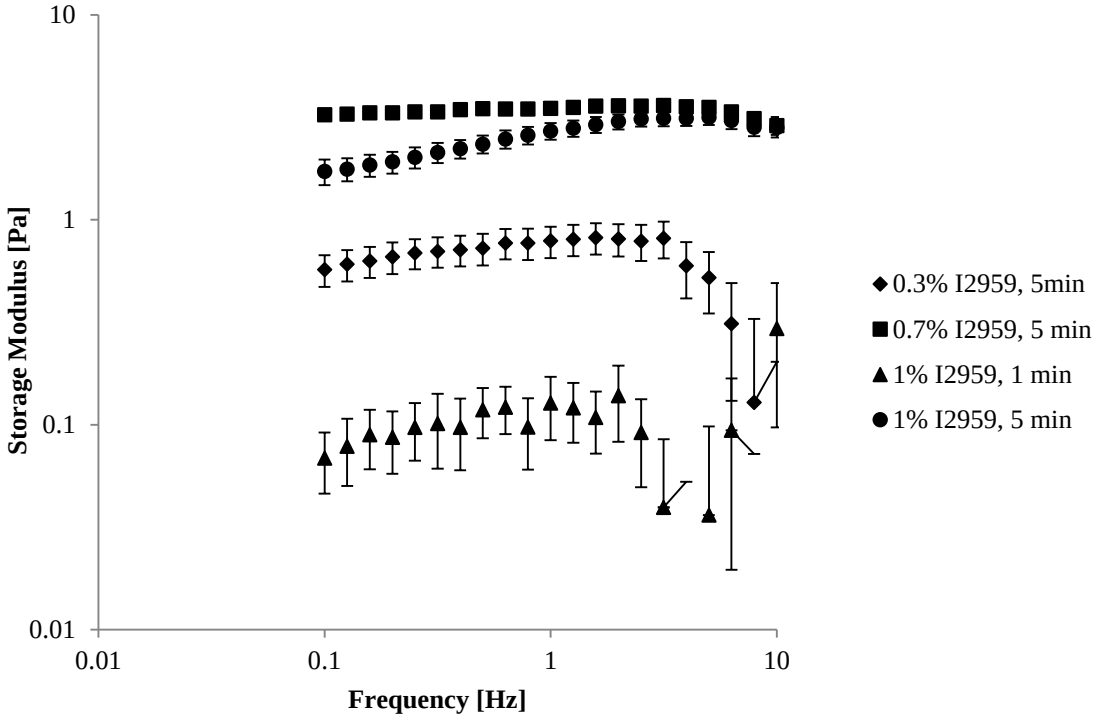

Figure 5.19: Urea-templated hydrogel storage modulus as a function of synthesis parameters. This study aimed to decouple the relative effects of photoinitiator concentration and duration of UV exposure on the hydrogel storage modulus. The 0.7% I2959, 5 minute UV exposure samples had the highest storage modulus and the 1% I2959, 1 minute UV exposure samples had the lowest. The results suggest that the 0.7% I2959 concentration is near the optimal concentration for maximum storage modulus and that increasing the photoinitiator beyond that amount does not increase the modulus. Additionally, both the photoinitiator concentration and UV expsorure time play a role in the sample storage modulus. The modulus for samples crossliked for 5 minutes of UV exposure each had a larger modulus than the 1 minute UV exposure samples.

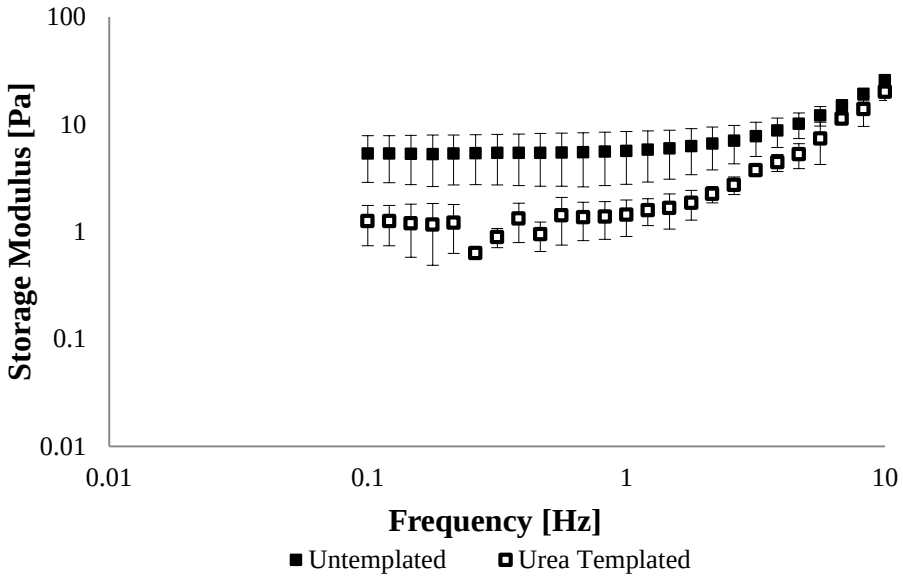

Figure 5.20: The storage modulus of 50 mg/mL not templated and urea templated hydrogels determined over a frequency range of 0.1-10 Hz. Hydrogels had a methacrylated hyaluronic acid concentration of 50 mg/mL and were photocrosslinked for 5 minutes UV exposure, and swollen in 10 mM PBS prior to experiment. All tests were conducted in triplicate. The urea-templated hydrogels had a storage modulus almost an order of magnitude less than the control not template group.

5.4 Degradation Behavior

The following experiments describe the empirical results from the enzymatic degradation of hydrogels templated by each of the small molecules and synthesized at standardized photoinitiator concentrations and UV exposures. The experiments are designed to allow conclusions to be drawn about the relative influences of photoinitiator concentration and UV exposure synthesis parameters and how this varies for hydrogels templated by each crystallizing molecule.

Not templated GMHA hydrogels were the control population for the experiments. **Figure 4.4** showed the effect void spaces created by the different molecules had on the degradation profiles. Similarly, here we take a more focused look at hydrogel response to synthesis parameters in the context of their crystal-induced void spaces. The hydrogels that were not templated did not have crystals in their matrix. The degradation order from slowest to fastest is 0.7% I2959 with 5 minutes UV, 0.3% I2959 with 5 minutes UV, 1% I2959 with 5 minutes UV, and 1% I2959 with 1 minutes UV. The 0.7% I2959 with 5 minutes UV hydrogel was the most resistant to degradation. This suggests that the duration of UV exposure has the largest impact on degradation profile. Even though the 1% I2959 with 5 minutes of UV exposure has a higher photoinitator concentration, 0.7% I2959 still was most resistant by a significant margin. The 0.3% I2959, 5 minutes UV samples experienced slight swelling before degradation. This is within normal hydrogel behavior because as the first polymer chains are enzymatically cleaved, there is an effective increase in the molecular weight between the crosslinks which allows the sample to swell to a larger extent that it was able to before the degradation process began.

Urea templated hydrogel degradation in hyaluronidase behaved similarly to not templated controls in **Figure 5.22**. The degradation order from slowest to fastest is 0.7% I2959 with 5 minute UV, 1% I2959 with 5 minute UV, 0.3% I2959 with 5 minute UV, and 1% I2959 with 1 minute UV. The 0.7% I2959 with 5 minute UV combination remained the most resistant to degradation and the 1% I2959 with 1 minute UV remained the most quick to degrade as compared to the not templated control population. Still, the time of UV exposure appears to take precedence in the resulting behavior. The photoinitiator concentration does not follow a logical trend.

The potassium dihydrogen phosphate-templated hydrogel degradation rates from slowest to fastest: 1% I2959 with 2 minute UV, 0.3% I2959 with 5 min UV, 1% I2959 with 5 min UV, and 0.7% I2959 with 5 minute UV (**Figure 5.23**). These results indicate that both photoinitiator concentration and UV play a role in the degradation profile. For samples with 1% photoinitiator, the 2 minute UV exposure samples degrade more quickly than the comparable 5 minute samples. Among the 5 minutes of UV exposure samples, however, the degradation profile did not follow an intuitive trend. The 1% I2959 with 5 minute UV samples experienced some swelling before they began to show mass loss degradation. The degradation profiles of the 1% I2959 with 5 min UV and 0.7% I2959 with 5 minute UV samples eventually meet and match one another. We hypothesize that the higher photoinitator concentration in the 1% I2959 with 5 min UV lead to additional crosslinks which were initially cleaved and the gel then took on a behavior that was comparable to that of 0.7% I2959 with 5 minute UV for the last 3 experimental hours.

Guanidine-templated hydrogels showed that 0.7% I2959 with 5 minute UV remained the most resistant to degradation as compared to the not templated control group in **Figure 5.24**. Interestingly, though, the relative rates for the remaining samples are different from the control. From the slowest to fastest: 0.7% I2959 with 5 minute UV, 1% I2959 with 5 minute UV, 1% I2959 with 1 minute UV, 0.3% I2959 with 5 minute UV**.** This behavior suggests that the photoinitiator concentration has a dominant role for guanidine-templated hydrogels.

Hydrogels templated by glycine also exhibited reduced degradation for the 0.3% I2959 and 5 minute UV combination. In order of degradation speed from slowest to fastest: 0.7% I2959 and 5 minute UV, 1% I2959 and 1 minute, 1% I2959 and 5 minute and 0.3% I2959 and 5 minute (**Figure 5.25**). Again, the degradation behavior does not follow an intuitive trend. Nevertheless, the two 1% I2959 hydrogel groups have a fairly similar profile so it is plausible that the photoinitator concentration has the most significant impact on the degradation behavior but we cannot definitively make a conclusion without performing additional experiments at times less than 5 minutes.

Interestingly, the 20 mg/mL GMHA samples of 0.3% I2959, 5 minute UV exposure degraded less quickly than the 50 mg/mL samples of the same parameters (**Figure 5.26**). Intuitively, the higher polymer concentrations the samples would be expected to degrade. Similarly, the 20 mg/mL GMHA samples of 0.7% I2959, 5 minute UV exposure samples also degraded less quickly than the 50 mg/mL counterpart. Both time points of 1% I2959 hydrogels showed more rapid degradation for samples with lower polymer concentration.

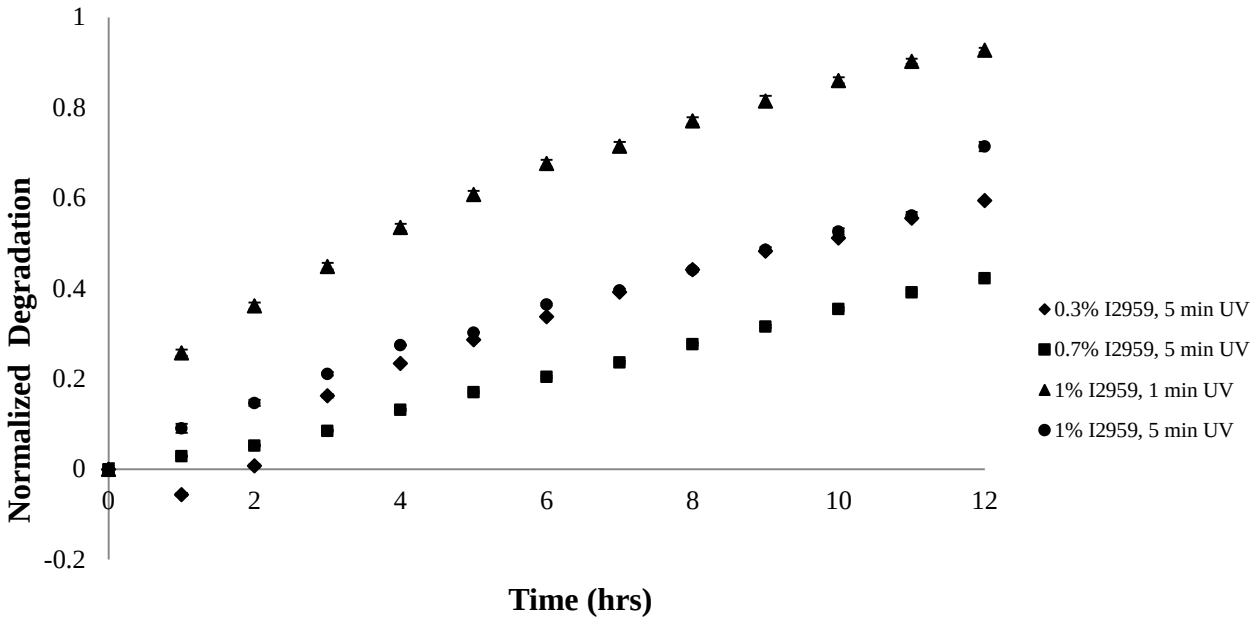

Figure 5.21 The degradation profile of not templated hydrogels examined for 12 hours at room temperature. The accelerated degradation used 50 U/mL of enzyme hyaluronidase in 10 mM phosphate-buffered saline. Samples were examined at a number of photoinitator concentrations and times of UV exposure. The 0.7% I2959 with 5 minutes UV exposure combination is the most resistant to degradation, whereas the 1% I2959 with 1 minutes UV was the most susceptible to degradation by hyaluronidase. All tests were completed in triplicate with a minimum of 12 samples.

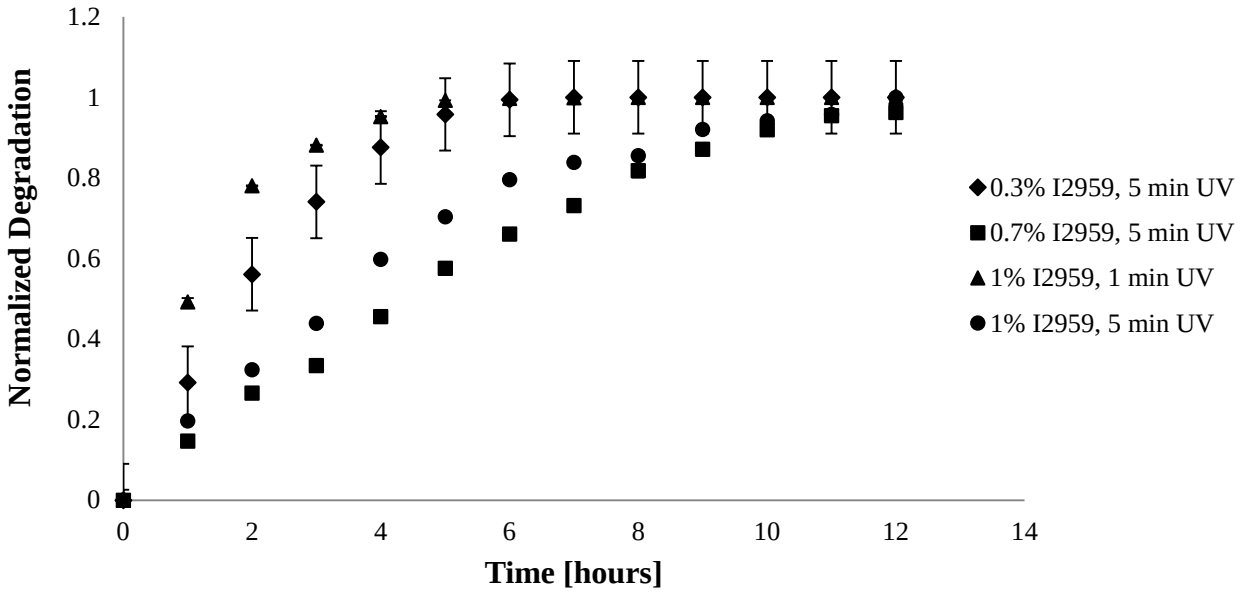

Figure 5.22: The degradation profile of urea-templated hydrogels examined for 12 hours at room temperature. The accelerated degradation used 50 U/mL of enzyme hyaluronidase in 10 mM phosphate-buffered saline. Samples were examined at a number of photoinitiator concentration and times of UV exposure. The 0.7% I2959 with 5 min UV combination is the most resistant to degradation, whereas the 1% I2959 with 1 min UV was the most susceptible to degradation by hyaluronidase. These results are consistent with the not templated control population. All tests were completed in triplicate with a minimum of 12 samples.

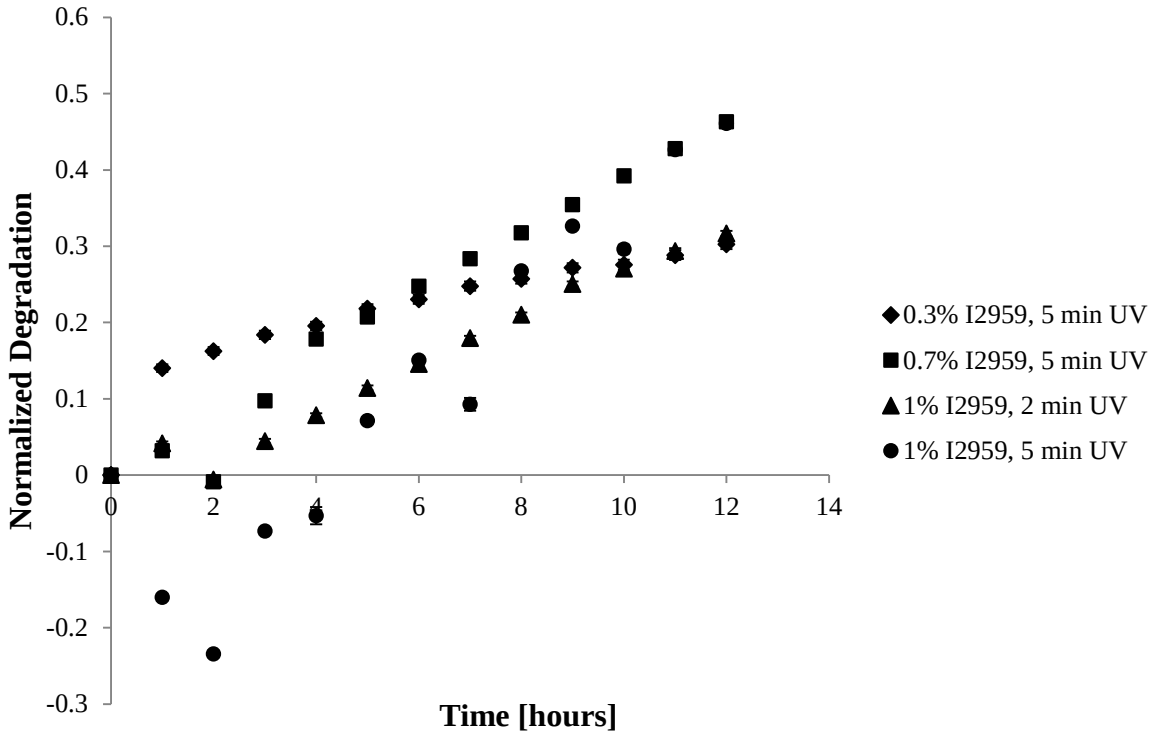

Figure 5.23: The degradation profile of potassium dihydrogen phosphate-templated hydrogels was examined for 12 hours at room temperature. The accelerated degradation used 50 U/mL of enzyme hyaluronidase in 10 mM phosphate-buffered saline. Samples were examined at a number of photoinitiator concentration and times of UV exposure. The 0.3% I2959 with 5 minute UV combination is the most resistant to degradation, whereas the 0.7% I2959 with 5 minute UV was the most susceptible to degradation by hyaluronidase. These results were not consistent with the behavior of the not templated control population. These results suggest that both time of exposure and photoinitiator concentration have an impact on the potassium dihydrogen phosphate-templated hydrogel degradation profile. However, the trend for each is counterintuitive. All tests were completed in triplicate with a minimum of 12 samples.

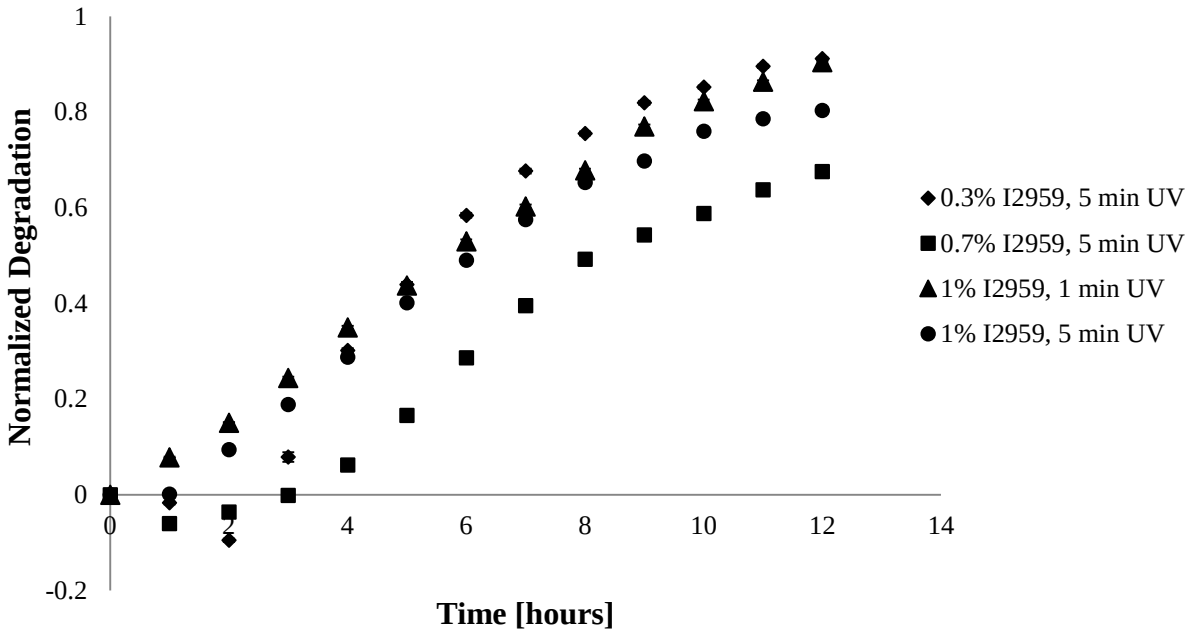

Figure 5.24: The degradation profile of guanidine-templated hydrogels was examined for 12 hours at room temperature. The accelerated degradation used 50 U/mL of enzyme hyaluronidase in 10 mM phosphate-buffered saline. Samples were examined at a number of photoinitator concentration and times of UV exposure. Guanidine-templated hydrogel degradation from the slowest to fastest: 0.7% I2959 with 5 min UV, 1% I2959 with 5 min UV, 1% I2959 with 1 min UV, 0.3% I2959 with 5 min UV. The 0.7% I2959 with 5 min UV combination is the most resistant to degradation, whereas the 0.3% I2959 with 5 min UV was the most susceptible to degradation by hyaluronidase. All tests were completed in triplicate with a minimum of 12 samples.

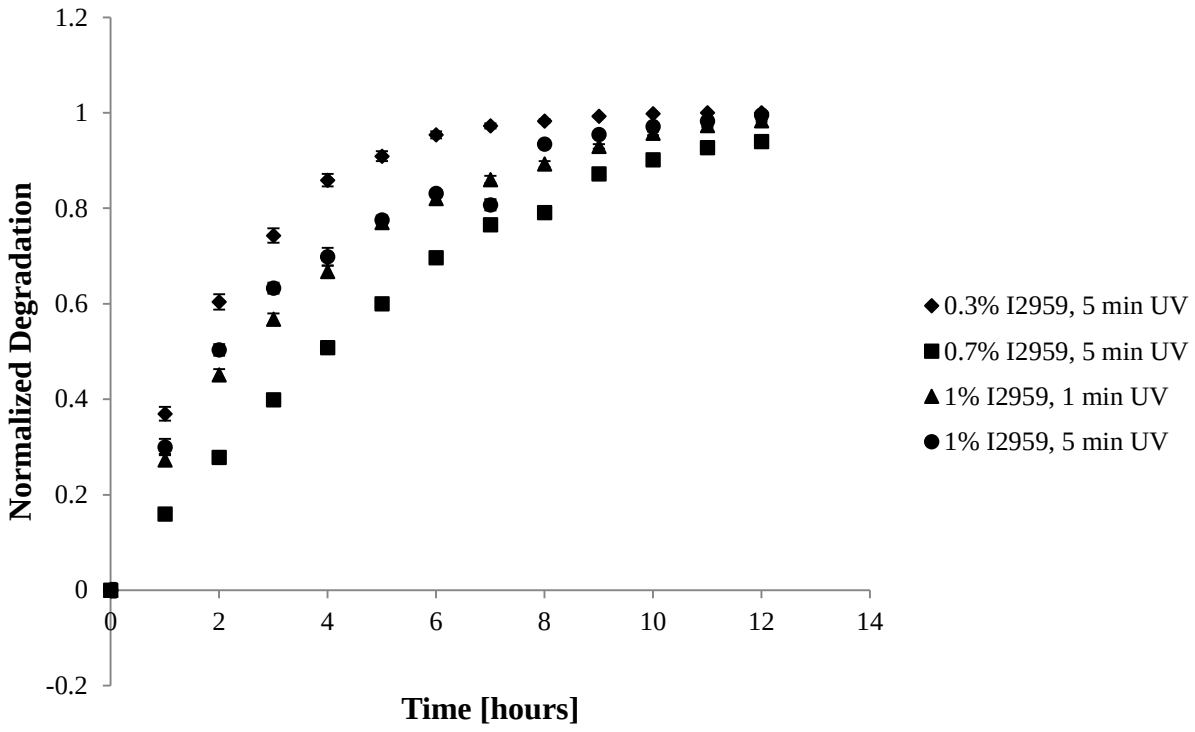

Figure 5.25: The degradation profile of glycine-templated hydrogels was examined for 12 hours at room temperature. The accelerated degradation concentration 50 U/mL of enzyme hyaluronidase in 10 mM phosphate-buffered saline was used. Samples were examined at a number of photoinitiator concentrations and times of UV exposure. The 0.7% I2959 with 5 min UV combination is the most resistant to degradation, whereas the 0.3% I2959 with 5 min UV was the most susceptible to degradation by hyaluronidase. All tests were completed in triplicate with a minimum of 12 samples.

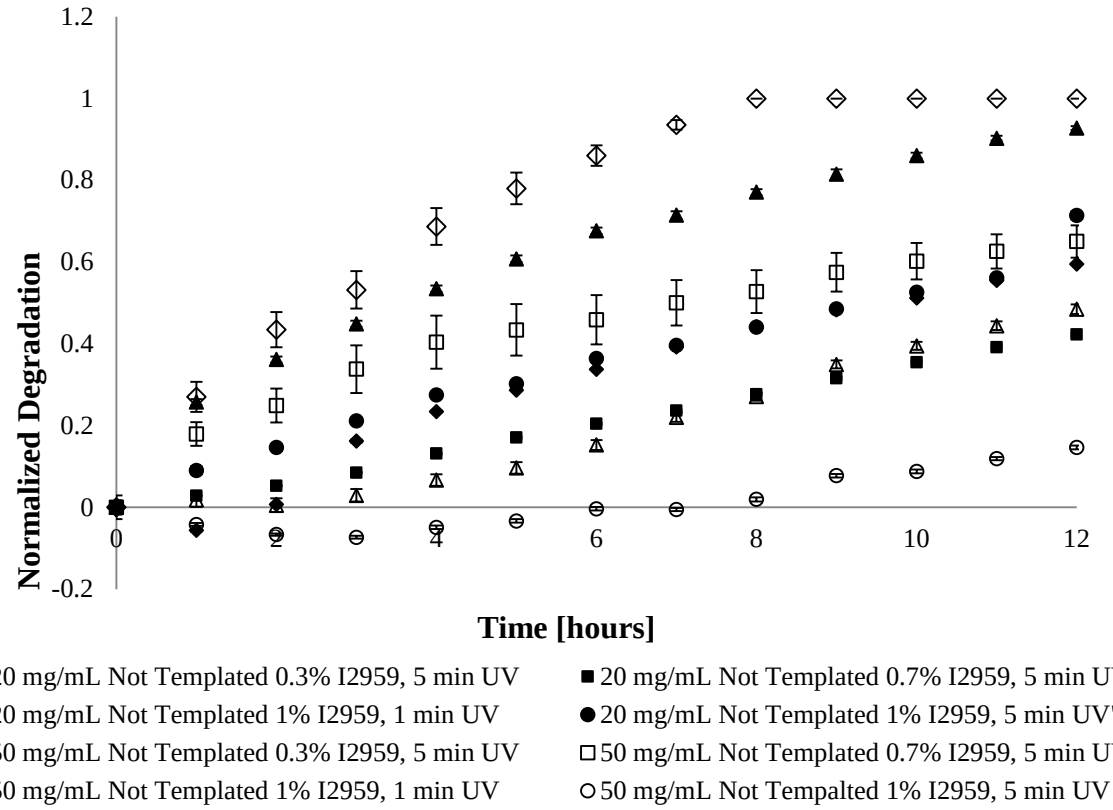

Figure 5.26: The 12 hour enzymatic degradation of not templated hydrogels in 50 U/mL hyaluronidase. Hydrogels were synthesized at 20 and 50 mg/mL GMHA with varying amounts of photoinitiator and extents of UV exposure. Experimental results suggest that urea-templated hydrogels degrade more rapidly than not templated controls. Additionally, data in the appendix supports the degradation profile of templated hydrogels. Interestingly, the 20 mg/mL GMHA samples of 0.3% I2959, 5 minute UV exposure degraded less quickly than the 50 mg/mL samples of the same parameters. Intuitively, the higher the polymer concentration the slower the samples should degrade. Similarly, the 20 mg/mL GMHA samples of 0.7% I2959, 5 minute UV exposure samples also degraded less quickly than the 50 mg/mL counterpart. Both time points of 1% I2959 hydrogels showed more rapid degradation for samples with lower polymer concentration.

5.5 Templated Hydrogel Mass Absorption Profile

The small molecules used in this work are comparable in size to many common therapeutics; therefore their release profiles be reasonably empirically characterized using drug release experimental framework. The hydrogel samples were synthesized with the crystalline small molecules within the matrix. Post synthesis, hydrogels were submerged in water, and both the small molecule began to be released and the polymer began to expand simultaneously. When it comes to investigating small molecule release, these competing phenomena complicate the ability to properly determine behavior. To further identify the problem, the molecules are in a crystalline state during synthesis and must therefore dissolve before they can diffuse out of the scaffold. This dissolving of crystals makes the diffusion not the rate limiting step. Thus, there is a breakdown in theory when discussing the molecule release from the templated hydrogels. The issue of decoupling these simultaneous events proves difficult. To that end, we present empirical behavior of the hydrogels in water and provide theoretical calculations for the purpose of characterizing how the samples deviate from the theoretical paradigm.

5.5.1 Evaluation of Transport properties inside templated hydrogels.

Diffusion can be described by a number of theoretical relationships to characterize the behavior. The Korsmeyer-Peppas equation, the Debra number (De) and the swelling interface number (Sw) may each be used to determine how closely experimental values match Fick's Law [114]. Small molecule or drug release from hydrogels is normally governed by the adsorption of water into the scaffold and simultaneous diffusion of small molecule [6]. Therefore drug release depends on the rate

of polymer relaxation at the glassy-rubbery transition that occurs at the swelling interface. Diffusion is affected by many factors including the molecular shape, molecular size and polymer structure [114, 115]. From a free volume theory perspective for complex structured polymers, diffusion can be viewed as a result of the degree of polymer chain packing , chain mobility and the degree of crosslinking [114, 116]. High molecular symmetry, and the polymer close packing leads to a stronger scaffold. Scaffolds with higher modulus are therefore less permeable; a reduction in polymer chain mobility affects the tortuosity [114]. Unnikrishnan et al. studied mesotransport through polymers with complex internal structures by investigating the effect of fillers on the transport through natural rubber. They found that the permeation decreased when smaller diameter filler particles were used and in polymers with high degree of crystallinity. They argue that solvents primarily penetrate and absorb in the amorphous regions of a polymer. Molecules have a more complicated or an increase in the tortuosity of their path in polymers with a greater degree of cystallinity [114, 117, 118]. The polymer used in this work is not crystalline, but the presence of crystalline molecules within the hydrogel matrix and the potential compaction of the polymer chains could lead the scaffold to have similar behavior.

In a polymer slab, Case I, or Fickian diffusion is proportional to the square root of time. Case II shows a linear time dependence of solute release that diffusion is determined by the rate of polymer relaxation and the diffusion rate [6]. This rate can then be used to determine the transport mechanism. The Korsmeyer-Peppas equation describes solute diffusion in polymers:

$$\frac{M_t}{M_\infty} = kt^n$$

$\mathbf{M_t}$ is the mass of water absorbed or mass of porogen released at time t, $\mathbf{M_\infty}$ is the mass of water absorbed at equilibrium, **k** is a characteristics constant of the hydrogel and **n** is the characteristic exponent of the mode of transport of the penetrating media [6, 12, 17, 119]. The solvent absorption rate is calculated from the ratio of the mass of the hydrogel at time *t*, M_t, and the mass of the hydrogel swollen in pure water, M_∞. The curve from the plot of fractional uptake, $\frac{M_t}{M_\infty}$, versus time yields the solvent absorption rate. It represents the fraction of released drug or fractional media take (depending) and its relation to time. The extent to which a hydrogel swells is indicative of the void space in the polymer and the extent of crosslinks within the network. Equilibrium swelling degree of hydrogels depends on crosslink and charge densities of network and polymer concentration after preparation [120]. Experimental data was averaged and fit to the Korsmeyer-Peppas equation, which accounts for small molecule release from hydrogel systems [16, 119]. Here, we use *n* to determine the transport mechanism and show solvent absorption rate for empirical proof of diffusion behavior. Fickian diffusion in terms of the Korsmeyer-Peppas equation parameters is defined as *n* equal to .5; Case II is the mechanism when *n* equals one and anomalous sorption or non-Fickian diffusion occurs when *n* is between 0.5 and 1. The relationship:

$$De = \frac{\lambda_m}{\theta_D},$$

is used to determine The Deborah number, which predicts whether diffusion in a hydrogel is a relaxation-controlled diffusion process. $\boldsymbol{\lambda_m}$ is the mean relaxation time of hydrogel/solvent system; $\boldsymbol{\theta_D}$ is the ratio of L^2 to D_s, where L is the sample thickness and D_s is the solvent diffusion coefficient. If De>>1 or De<<1 then Fickian diffusion occurs in either a glassy or rubbery state, respectively. If De=1, the system undergoes non-

Fickian diffusion which indicates Case II transport. Similarly, the swelling interface number (Sw), is defined as

$$Sw = V * \frac{\delta(t)}{D},$$

and also determines D determines the mechanism of drug release from a hydrogel. **V** is the velocity of penetrating swelling front, **δ(t)** time dependent thickness of swollen phase and **D** is the drug diffusion coefficient. If the Sw is much less than one, then the system displays Fickian diffusion. If Sw is approximately one then non-Fickian diffusion exists and if Sw is much greater than one, then Case II diffusion occurs. These quantities are summarized in **Table 9**. The fractional uptake is more widely used to determine diffusion behavior, the experimental protocol is more simple to implement and the ratio has greater relation to further theoretical attempts. Therefore this ratio was used for this work.

In these hydrogels, the molecules are crystalline, meaning that there is a non-zero delay in the molecule diffusion where the crystals must first dissolve. Kim et al describes a similar dilemma when attempting to model drug release from a glassy copolymer. Similarly, the behavior they found ranges from Fickian to Case II diffusion. They argue that $\frac{M_t}{M_\infty} = kt^n$is a common equation among Fickian, non-Fickian and Case II [6]. The difficulties come where the variations are dependent on a moving solvent front. This front is dissolving and extracting the molecule, and can dominate experimental parameters and thermodynamic interactions between the solvent and hydrogel. Differences between the polymer behavior and Fickian theory are thought to be a result of polymer chain response to solvents that cause swelling [114, 121].

Porogen release kinetics were determined using mathematical models to evaluate the kinetics and mechanism of porogen release from hydrogels. The model that best fits

the release data, as determined by the R^2 value, was used to fit the data. Hydrogel mass data were plotted on a log-log scale in order to determine the characteristic *n* and characteristic constant *k* according to the Koresmeyer-Peppas equation. Water is the penetrating media in this case. Because the model only suits linear data, only the linear region of the log-log plot was modeled in an effort to gain the swell-release kinetic values. The portion of data that yielded the largest R^2 value was used for these calculations. The linear portion of the log-log plot of the data ranged from 8-25 minutes for hydrogels templated by each of the porogens. Appendix C details the plots to determine *n* and *k* values and the derived parameters are presented in **Table 10**. The *n* value obtained for not templated, glycine- templated, and urea-templated populations was larger than 0.5 and therefore indicates that the release kinetics are non-Fickian [122]. This behavior is expected because Fickian diffusion is principally applicable for tissue engineering applications where the scaffold is completely amorphous; non-Fickian behavior is common in polymer systems [12, 112]. The local, crystal-induced domains within the templated hydrogels were expected to yield a bulk matrix with properties uniquely different from not templated hydrogels. However, results from this experiment suggest that the physical heterogeneity within the templated hydrogels arising from the structural complexity does not lead to water penetration that is different from not templated hydrogel controls. Urea-templated and glycine-templated samples show similar diffusion behavior to the control population. Guanidine and potassium dihydrogen phosphate-templated hydrogels, however, show behaviors that are non-Fickian anomalies. In these two cases, the hydrogels either experienced a reduction in mass or did not show any appreciable swelling. This reduction in mass is likely a result of crystal

dissolve and removal from the sample. While sufficient theory does not exist to fully characterize the unique diffusion behavior, we have been able to identify the non-Fickian behavior and qualitatively characterize them. We hypothesized that this difference would prove advantageous in improving cellular response in the applications explored in Chapter 6.

Genre	$\frac{M_t}{M_\infty}$	De	Sw
Fickian (Case I)	n = 0.5	<<1 or >>1	>>1
Non-Fickian (Anomalous)	n > 0.5	≈1	≈1
Case II Diffusion	n = 1	≈1	<<1

Table 9: Summary of different theoretical characterizations for diffusion behavior [6]. $\frac{M_t}{M_\infty}$ is derived from the Korsmeyer-Peppas equation, which determines solvent absorption rate over time. The Debra number, De, evaluates the relaxation controlled diffusion in a scaffold. Sw is the swelling interface number which identifies the mechanism of drug release.

Porogen	Time until Mass Stability[min]	n	k
Not Templated	90	0.7417	0.02199
Glycine	25	0.6967	0.0689
Guanidine	8	0.2703	0.7686
Potassium Dihydrogen Phosphate	60	-0.4353	0.19306
Urea	9	0.9091	0.06375

Table 10: Swelling kinetics by crystallizing molecule for templated hydrogels. The Koresmeyer-Peppas equation was used to determine *n* and *k* values. Not templated hydrogels have an n of 0.7417 which indicates non-Fickian diffusion behavior. Similarly, glycine-templated and urea-templated hydrogels also have non-Fickian behavior. The experimentally determined values for guanidine-templated and potassium dihydrogen phosphate-templated samples are non-Fickian anomalies. Refer to Appendix C for supplementary plots for determining the n and k values. These results suggest that diffusion in hydrogels templated with urea and glycine crystals does not significantly differ from the control group. Templating with guanidine or potassium dihydrogen phosphate does, however, lead to significant changes in diffusion behavior.

5.5.2 Empirical evaluation of water penetration. Timed swelling experiments were performed in an effort to model the mass change over time for templated hydrogels in deionized water. From this work, the empirical behavior can be shown, however sufficient theory does not exist to fully describe the behavior. Hydrogels templated by each of the small molecules were immersed in deionized water to rinse out the crystalline porogen and weighed at designated time points until equilibrium was reached in an effort to model the simultaneous water absorption and crystalline molecule release kinetics. The porogen release data was normalized by weight after 270 minutes. The weight of the hydrogel samples at various time points was recorded as a function of time in **Figure 5.27** to show the empirical behavior of the simultaneous crystalline molecule release and water absorption profile. The change in mass attributed to water uptake followed this trend (smallest to largest): guanidine-templated hydrogels, potassium dihydrogen phosphate-templated hydrogels, glycine-templated hydrogels, and urea-templated hydrogels.

Molecule diffusion in a scaffold is dependent on both the bulk material, the diffusing molecule properties, and how they interact [15]. To that end, polymers may be characterized as either glassy or rubbery. The glass transition point of a polymer demarcates the reversible transition from a more brittle state into a rubbery like state. No physical transition occurs; rather it occurs over a range of temperatures and other conditions [114]. In viscoelastic polymers such as hydrogels, the liquid-solid transition is more similar to a spectrum that results from the synthesis parameters and relative forces applied. Polymers in rubbery state tend to participate in diffusion action because the larger the initial void space, the more readily accessible it is [114]. Polymers in the

glassy state are more brittle than in the rubbery state and therefore the polymer chains are less mobile and diffusion becomes more complicated. Irons et al. commented on diffusion limitations into and out of a hydrogel matrix caused by hydrogel thickness and density as a distinct drawback of three-dimensional culture environments [19]. Literature suggests that the increased porosity from adding internal structure to a hydrogel scaffold may prove beneficial in increasing efficacy [123]. Theoretically, if the scaffold is patterned then the effective porosity of the scaffold would increase, as would the diffusion capabilities of the scaffold. Indeed, the sorption properties of hydrogels with cylindrical voids were found to absorb more water than the reference hydrogels [124]. These samples, however, were patterned with cylinders that dissolved with organic solvents and therefore did not interfere with the water absorption behavior [124]. Mass transport in polymers typically occurs in three steps. First small solvent molecules absorb to the surface of the polymer, then they diffuse through the polymer and finally they desorb from the polymer [114]. Glassy polymers exhibit anomalous or non-Fickian behavior. In glassy polymers the diffusion behavior cannot be described in concentration-dependent form of Fick's Law with boundary conditions, and Crank points out that this is even more prevalent when the penetrant causes extensive swelling of the polymer [125].

The overall water penetration profile was unique for each molecule. Urea and glycine-templated and not templated control hydrogels each exhibit swelling until equilibrium is reached. The urea-templated samples increased in mass by the greatest amount. Both urea and glycine swell to a larger extent more quickly and reach an equilibrium plateau more quickly than control population. Potassium dihydrogen phosphate-templated hydrogels initially swell then shrink to an equilibrium weight that is

slightly larger than the initial gel mass. Guanidine-templated hydrogels initially decreased in mass then were swollen until equilibrium mass was achieved. Interestingly, the two hydrogel populations with little to no swelling in the empirical experiments were also those with the anomalies in their calculated diffusion parameters. This suggests that diffusion could be hindered in these populations as evidenced by the minor swelling.

The square root relationship describes the solution to the problem of diffusion into a semi-infinite medium having zero initial concentration and the surface of which is maintained constant. This involves only the dimensionless parameter $\frac{x}{2\sqrt{(Dt)}}$. This ratio stems from the equation $C = C_o erfc \frac{x}{2\sqrt{(Dt)}}$ used when solving diffusion into a semi-infinite medium. Boundary is kept constant at concentration C_o and the initial concentration is zero throughout the medium. The fundamental assumptions related to this are that C_o is uniform and that the surface concentration remains constant. This also holds for point or line sources on infinite surfaces within infinite media and also for the case of diffusion in an infinite medium where the diffusing substance is initially confined to a region x<0 [125]. Furthermore, Crank suggests that boundary positions of a liquid penetrant that diffuses into a polymer has sharp boundary conditions or positions that are often proportional to $t^{1/2}$ [125]. There are different classes of non-Fickian sorption [112]. To that end the fractional uptake $\frac{M_t}{M_\infty}$ was plot against square root time to characterize the genre of non-Fickian diffusion qualitatively using **Figure 5.28** as a reference.

The fractional uptake versus square root time plot for the not templated control samples confirms that diffusion in hydrogels is typically non-Fickian as shown in **Figure 5.29**. The data shows a single inflection point and an overall behavior that closely resembles the sigmoidal non-Fickian description found in **Figure 5.28**. These results in

conjunction with the quantitative evaluation of *n* agree with the non-Fickian behavior normally found in hydrogels [6, 114]. Similarly the plot derived from glycine-templated hydrogels showed similar behavior to the control population. **Figure 5.30** confirms the behavior as non-Fickian and further characterizes it as sigmoidal. The data also has a single inflection point and presents a plateau in fractional uptake at longer time points. This suggests that glycine crystal-templating does not significantly affect the diffusion characteristics from not templated controls.

The behavior of guanidine-templated hydrogels shows an initial negative linear region which ends with a sharp transition to an increase in mass until an equilibrium weight is reached. This behavior, shown in **Figure 5.31**, is similar to the two-stage non-Fickian behavior. While an *n* of 0.2703 does not specifically quantitatively designate the samples to display two-stage behavior, it does confirm that the diffusion regime is non-Fickian and an anomaly. These results suggest that guanidine-templating does significantly affect the diffusion regime within hydrogel samples.

The plot of fractional uptake versus square root time for urea-templated hydrogels in **Figure 5.32** reveals a single inflection point and qualitative empirical behavior that resembles sigmoidal characterization. This suggests that urea-templating does not significantly alter the diffusion in hydrogels from the control populations.

The non-Fickian sorption data for potassium dihydrogen phosphate-templated hydrogels in **Figure 5.33** appears as an initial linear portion followed by a sharp transition to a second region where there is a slight increased before decreasing into a plateau region. This behavior is similar to the two-stage non-Fickian behavior presented in **Figure 5.28C** and is also mirrored by guanidine-templated hydrogels. These results

suggest that potassium dihydrogen phosphate-templating does significantly affect the diffusion regime within hydrogel samples.

The viscoelasticity of HA is particularly interesting because it is influenced by its polymeric and polyelectric qualities [48]. HA does have some polyelectrolyte properties, but unlike alginate, does not require divalent cations to crosslink its anionic polymer chains. HA is a weak polyelectrolyte and is incorporated into polyelectrolyte multilayer thin films [126] and polyelectrolyte complexes with other polymers [127]. HA has some natural polyelectric qualities. It is plausible that the differences in potassium dihydrogen phosphate-templated hydrogel behavior stems from its ionic molecular organization as opposed to the hydrogen bonding by the other small molecules, however the potassium dihydrogen phosphate-templated hydrogels do not behave more ionic-like than the control hydrogels (**Figure 5.34**). It is possible that while no actual chemistry took place between the polymer and molecule that any residual potassium dihydrogen phosphate molecules that remain in the scaffold and/or the interaction of the two could lead to the hydrogel displaying ionic-like characteristics. The viscous and mechanical behavior is different in ionic hydrogels. They have viscous moduli that tend to be smaller than the elastic plateau region, and the hydrogel's capacity for swelling tends to increase with increasing number of ionic groups [11]. Ionic hydrogels are highly swollen in water and therefore swelling equilibrium is mainly determined by entropy of mixing of counterions and the hydrogel rubberlike elasticity. The discrepancy between theory and experiment is related to non-Gaussian behavior of fully swollen hydrogels in water. Theory assumes that a polymer network is a collection of Gaussian chains which can be extended to infinity. However the network chains in equilibrium swollen ionic hydrogels are 3-9

times as elongated as they are in the dry state [11]. Okay et al. did a comparison of ideal Flory-Rehner theory swelling to ionic poly(acrylamide-co-sodium acrylate) hydrogels taking the fraction of counterions into account. In their experiment, hydrogel swelling was shown as a function of sodium chloride (NaCl) concentration in external solution. Sodium chloride is a strong electrolyte because it almost completely dissociates in water. Sodium chloride solutions of different concentrations have been used as a monovalent ionic medium to study the effects on hyaluronic acid swelling behavior [55, 101]. They found a decreased swelling ratio with increased salt concentration in external solution that they attribute to a decrease in the difference of counterions inside and outside hydrogel. This trend continued up to 0.1M NaCl in their 0-10M range [120]. The osmotic pressure of a hydrogel during swelling is given as sum of the pressures due to polymer-solvent mix, deformation of the network chains to more elongated state and nonuniform distribution of mobile counterions between hydrogel and external solution $\pi = \pi_{mix} + \pi_{el} + \pi_{ion}$ [120].

To determine if the potassium dihydrogen phosphate-templated hydrogels were displaying traits similar to ionic hydrogels, a similar study was conducted. The SR did decrease as the NaCl concentration increased in the external solution; however this was also the case for the not templated control group. Okay et al. mention the 0.1M NaCl concentration as the point where the relationship between SR and media concentration ends. It is interesting because this concentration shows markedly differing behavior for each of the photoinitiator concentrations used. At 0.3% I2959, the potassium dihydrogen phosphate-templated samples displayed a comparable swell ratio at 0 M NaCl and an increase at 0.1 M NaCl. At 1% I2959, the SR was significantly reduced in the templated

hydrogels. At each concentration and for both genres of samples, the hydrogels exhibited a reduced swell ratio at higher NaCl concentration. These results do not suggest that the potassium dihydrogen phosphate-templated hydrogels display more ionic-like behavior than the not templated controls.

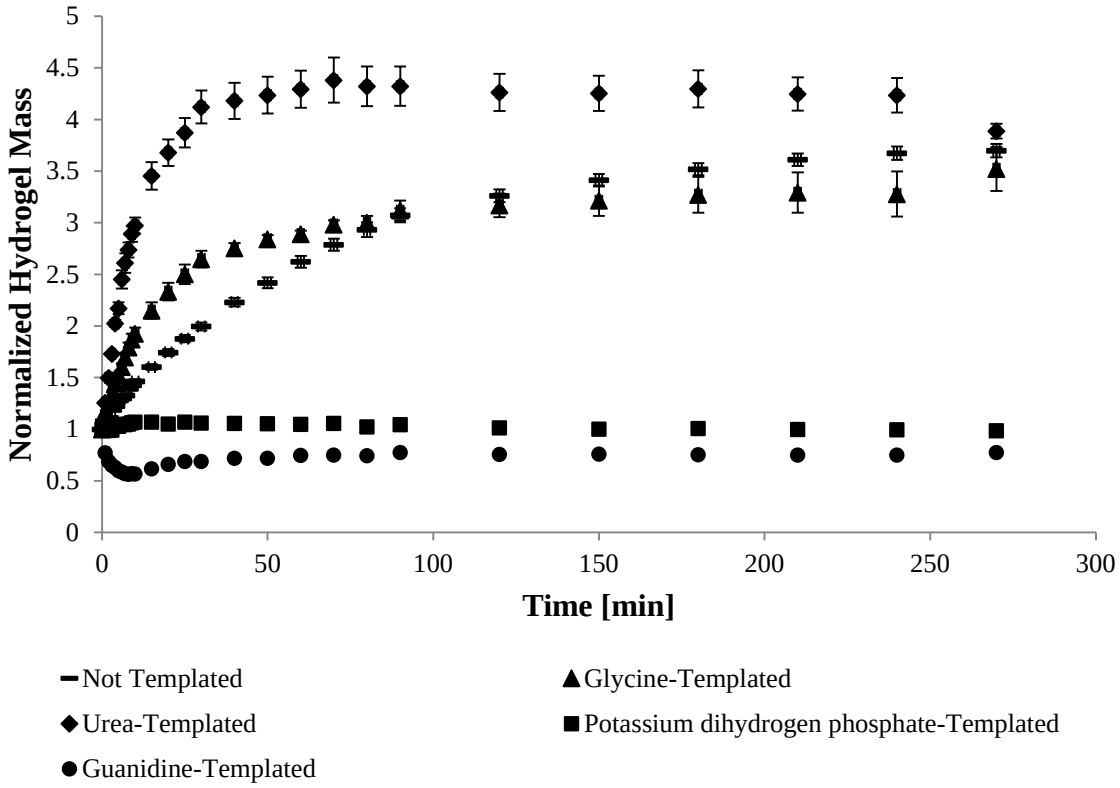

Figure 5.27 : Normalized change in templated hydrogel mass over 270 minutes for the four crystallizing molecules and not templated control. Hydrogels were immersed in deionized water and the weight was recorded until equilibrium weight was achieved. The not templated control samples swell immediately upon water immersion and continue until equilibrium. Glycine-templated and urea-templated samples both swell to a greater extent than the control population and reach their equilibrium more quickly. Potassium dihydrogen phosphate-templated and guanidine-templated samples did not swell significantly in deionized water. Experiments were repeated in triplicate, at least. Values presented as mean ± standard error.

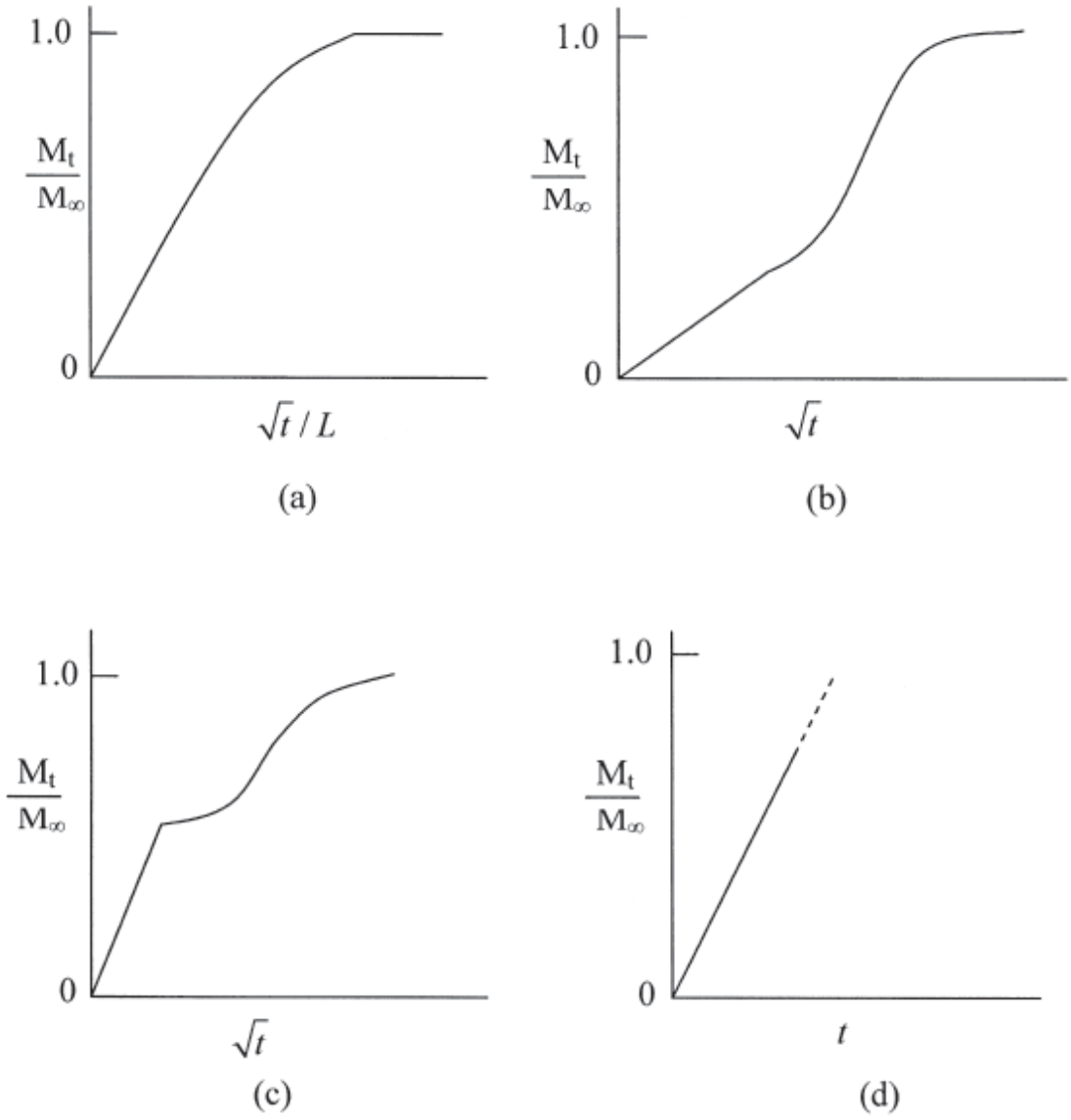

Figure 5.28: Different classes of non-Fickian sorption. The image details (A) classical, (B) sigmoidal, (C) two step, and (D) Case II non-Fickian absorption as qualitative behavior in fractional uptake versus square root time plot. Image courtesy of Kee et al [114].

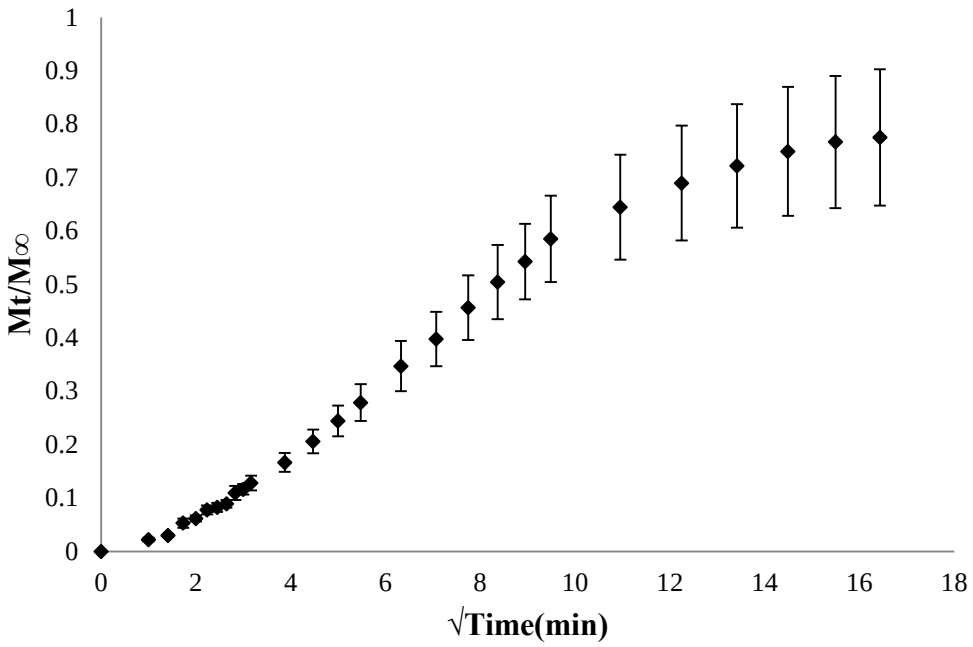

Figure 5.29: Non-Fickian sorption in not templated hydrogel samples shows sigmoid behavior. The plot of fractional uptake versus square root time reveals a single inflection point and qualitative empirical behavior that resembles sigmoidal characterization. These results provide additional information about the non-Fickian quantitative assessment determined by n=0.7417. Samples were weighed at designated time points for 270 minutes and normalized to the ending weight M_∞.

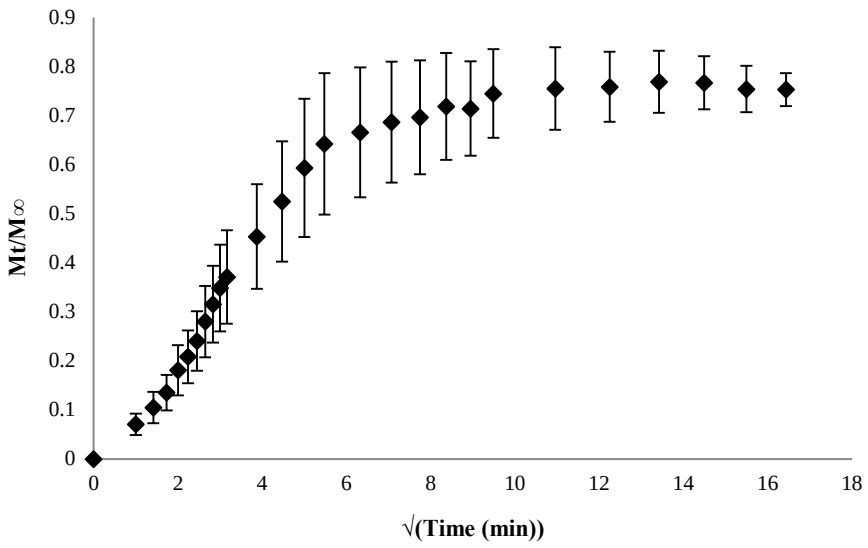

Figure 5.30: Non-Fickian sorption in glycine-templated hydrogel samples shows sigmoid behavior. The plot of fractional uptake versus square root time reveals a single inflection point and qualitative empirical behavior that resembles sigmoidal characterization. These results provide additional information about the specific non-Fickian behavior determined in the quantitative assessment by n=0.6967. Samples were weighed at designated time points for 270 minutes and normalized to the ending weight M_∞.

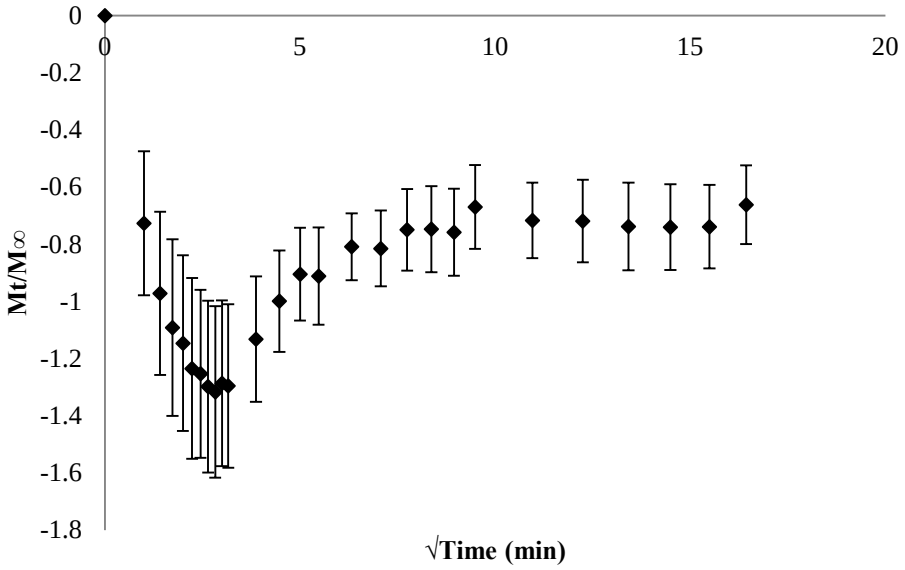

Figure 5.31: Non-Fickian sorption in guanidine-templated hydrogels shows two-stage behavior. The plot of fractional uptake versus the square root time reveals qualitative information. The behavior shows an initial negative linear region which ends with a sharp transition to an increase in mass until an equilibrium weight is reached. This behavior is similar to the two-stage non-Fickian behavior. While an *n* of 0.2703 does not specifically quantitatively designate the samples to display two-stage behavior, it does confirm that the diffusion regime is non-Fickian and an anomaly. These results suggest that guanidine-templating does significantly affect the diffusion regime within hydrogel samples. Samples were weighted at designated time points for 270 minutes to deionized water and normalized to the ending with M_∞.

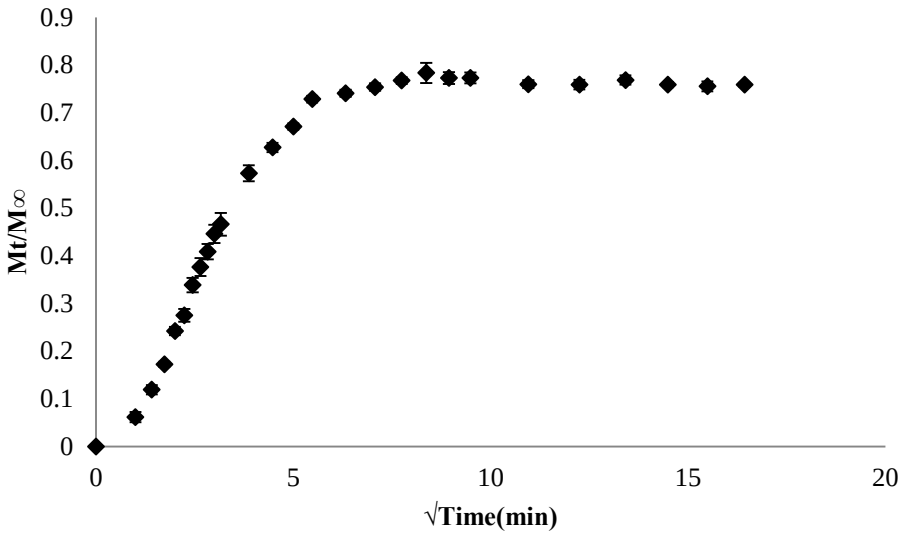

Figure 5.32: Non-Fickian sorption in urea-templated hydrogel samples shows sigmoid behavior. Samples were weighed at designated time points for 270 minutes and normalized to the ending weight M_∞. The plot of fractional uptake versus square root time reveals a single inflection point and qualitative empirical behavior that resembles sigmoidal characterization. This suggests that urea-templating does not significantly alter the diffusion in hydrogels from the control populations.

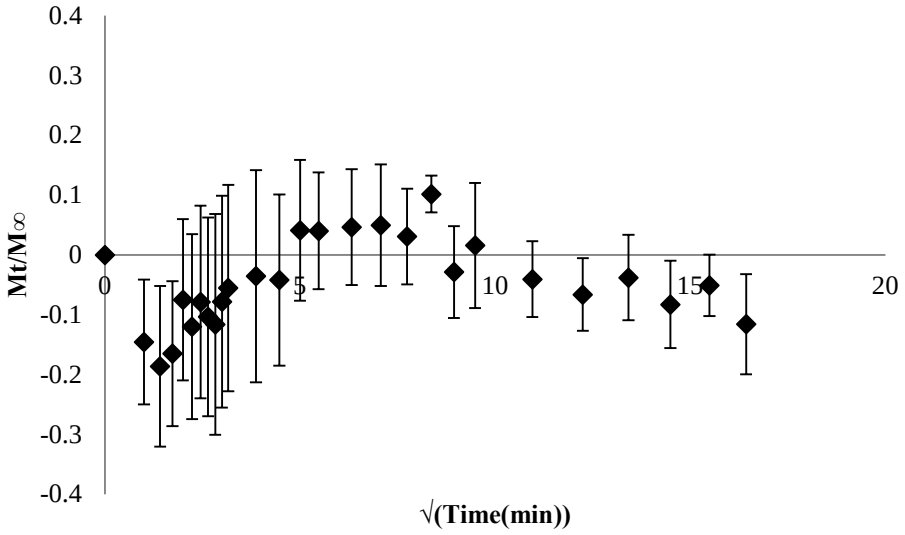

Figure 5.33: Non-Fickian sorption in potassium dihydrogen phosphate-templated hydrogels shows two-stage behavior**.** Samples were weighed at designated time points for 270 minutes and normalized to the ending weight M_∞. The plot of fractional uptake versus the square root time allows qualitative evaluation of the genre of non-Fickian behavior. The data appears as an initial linear portion followed by a sharp transition to a second region where there I a slight increased before decreasing into a plateau region. This behavior is similar to the two-stage non-Fickian behavior. These results suggest that potassium dihydrogen phosphate-templating does significantly affect the diffusion regime within hydrogel samples.

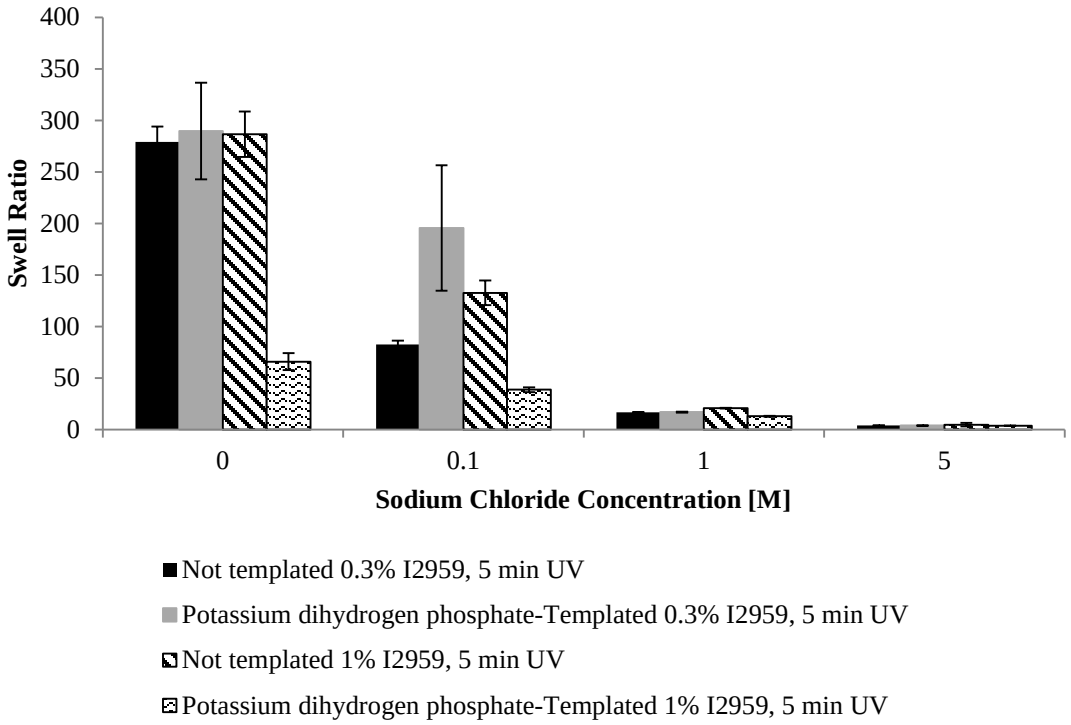

Figure 5.34: Swell ratio of potassium dihydrogen phosphate-templated and control samples as a function of sodium chloride concentration. Potassium dihydrogen phosphate-templated hydrogels were swollen in various concentrations of sodium chloride and compared to not templated control samples. When allowed to equilibrate in water, there was not a significant difference between any of the sample types. For the samples in 0.1M NaCl, the control samples experienced an increase in swell ratio with increased photoinitiator concentration relative to 0M, however the potassium dihydrogen phosphate-templated samples had a reduction in swell ratio under the same conditions. The results suggest that the potassium dihydrogen phosphate-templated samples do not experience large amounts of swelling in water, however at higher concentrations of NaCl postassium dihydrogen phosphate-templated samples do not behave significantly different from the control samples.

5.6 Conclusions

Swelling experiments are a powerful technique for determining effective behaviors in hydrogel scaffolds. In the not templated control population the SR decreased with increasing exposure times to UV light until 10 minutes. At 20 minutes of UV, however, the polymer experienced significant swelling. This behavior was maintained in samples templated with urea crystals. Potassium dihydrogen phosphate-templated and glycine-templated samples decreased until a SR plateau while guanidine held fairly consistent SR values until a significant decrease at 20 minutes. These results suggest that guanidine interferes with the ability to modulate hydrogel swelling behavior by altering UV exposure times. Potassium dihydrogen phosphate-templated and glycine-templated samples, on the other hand, reach a maximum effective degree of crosslinking that is not increased with longer photopolymerization times. The results suggest that urea-templating preserved the swelling behavior of the control population while potassium dihydrogen phosphate and glycine may provide some protection to the polymer from potential UV degradation at long exposure times [128-130]. When taking photoinitiator concentration in to account, the SR increased with increasing photoinitiator concentration at consistent UV exposure times and the urea-templated samples presented a higher SR. In regards to the porogen concentration, as the concentration increased so did the SR. Each of these is indicative of an increased void space. It is important to review the swelling results in the context of the sample and experimental limitations. The swelling protocol swells the hydrogels in PBS prior to oven-drying. Any salts within the scaffold would artificially inflate the recorded dry hydrogel weight. To that end the percent swell of the hydrogels was presented along with swell ratio.

The viscoelastic experiments were able to provide interesting results that help provide a more complete picture of the complex polymer-parameter interplay within hydrogels. Interestingly, photoinitiator has a more significant impact on control sample behavior than the percent polymer methacrylation and an increase in polymer concentration leads to an increased storage modulus. The more apparent significance of photoinitiator concentration led to its role as a varied parameter throughout the subsequent experiments. The 0.7% I2959 hydrogels with 5 minutes of UV exposure had the highest modulus for both the control and potassium dihydrogen phosphate-templated populations. The control population showed no relationship between the photoinitiator concentration and the modulus. This suggests that above a certain concentration further increasing it does not increase the modulus. Potassium dihydrogen phosphate-templated samples, however, show a strong relationship between both the photoinitiator concentration and UV exposure to the modulus. At higher polymer concentrations the modulus was also reduced with urea-templating. Spatial inhomogeneity reduces strength of hydrogels. These inhomogeneities increase with hydrogel crosslink density because there is a simultaneous increase of extent of network imperfections producing regions of more or less rich crosslinks [11]. This could explain the lack of an increase of modulus with higher Irgacure 2959 concentrations.

Enzymatic hydrogel degradation reveals information about hydrogel permeability and the effective crosslink density. The more permeable the scaffold the more effectively the enzyme can enter and cleave the polymer chains. Similarly, the higher the effective crosslink density, the more resistant the scaffold is to degradation. The urea-templated hydrogels degraded significantly more quickly than the not templated hydrogels at

consistent experimental conditions. Hydrogels that were templated with urea porogen retained the ability for their degradation behavior to be modulated via photoinitiator concentration and UV exposure. The 0.7% I2959 and 5 minute was the most resistant to degradation in each of the groups with the exception of potassium dihydrogen phosphate templated samples. Additional studies would have to be conducted to comment on the dominance of photoinitiator versus time for experiments where the data is not clear, such as in the case of glycine-templated hydrogels. Samples that dissolved prior to the experiment were discarded.

In regards to diffusion, the control samples as well as urea-templated and glycine-templated showed sigmoidal, non-Fickian diffusion. Potassium dihydrogen phosphate-templated and guanidine-templated hydrogels, however, did not fall into the normal range of plausible quantities for the Koresmeyer-Peppas derived *n* value. It is interesting that both guanidine-templated and potassium dihydrogen phosphate-templated hydrogels display slipping at higher frequencies and have two-stage non-Fickian diffusion behaviors. There is a need for more in depth investigation of non-Fickian complex polymer behavior. The abnormal quantities result from the samples either showing a mass reduction or little to no mass change upon water immersion. The assumption that polymer-molecule interaction was negligible was proven to not be true in the case of ionic molecules because the normal hydrogel swelling behavior was disrupted.

5.7 Materials and Methods

5.7.1 Materials. High molecular weight sodium hyaluronate from *Streptococcus equi* of molecular weight 1.6 x 10^6 Da (53747-10G), Glycidyl Methacrylate (779342-500ML), Triethylamine (T0886-1L), Urea (U5378), Potassium Phosphate Monobasic (P5655-500G) and dextran-FITC were all purchased from Sigma Aldrich (St Louis, Mo). Irgacure 2959 was purchased from Ciba Specialty Chemicals/ BASF (Basel, Switzerland). Guanidine hydrochloride (BP178-500), Glycine (BP381-500), Acetone (A181), BD PrecisionGlide 25 gauge needles (305122), Luer-Lok syringes (2018-06) were all purchased from Fisher Scientific.

5.7.2 Preparation of Methacrylated Hyaluronic Acid. To attach methacrylate groups to hyaluronic acid polymer backbone to allow for photopolymerization, desiccated hyaluronic acid was dissolved in an equal volume mixture of acetone and water overnight at 1%w/v. The HA was allowed to react with glycidyl methacrylate in the presence of triethylamine as a pH stabilizer and intermediate overnight. The polymer was purified in 20 times excess by volume by slowly adding polymer solution to gently stirred acetone and collecting the sample on a glass stirring rod. The polymer was re-dissolved in 50mL deionized water overnight and the polymer purification in acetone was repeated once more. The final sample was flash-frozen sample with liquid nitrogen and lyophilized for 2-4 days, depending on volume. Polymer was stored at -20C until ready for use.

5.7.3 Synthesis of GMHA not templated and crystal templated hydrogel. A 1%w/v stock solution of I2959 in 10 mM PBS was heat sonicated for 30-45 minutes to

dissolve, taking care to not overly sonicate. Methacrylated HA solution was prepared with desired concentration 1-5%w/v (10-50mg/mL) with final photoinitiator concentration between 0.05-1% w/v. A 1% stock photoinitiator solution was prepared in 10 mM phosphate-buffered saline and added accordingly to the hydrogel solution to obtain the desired final concentration. For templated hydrogels, crystallizing molecules were dissolved in the pre-hydrogel solution slightly in excess of their 25˚C solubility.

Crystallizing molecules were dissolved in sterile water/I2959 for desired end volume in an oven at 40˚C. The desired weight of sterile methacrylated HA was added for 20mg/ml. A hydrogel apparatus was assembled by encasing silicone molds with glass slides and secured with binder clips. Warm hydrogel solution was injected into silicon wells with a sterile syringe needle. The hydrogel apparatus was placed on ice until crystals nucleated within the molds. The apparatus was placed on ice inside a petri dish and crosslinked under UV lamp for desired length of exposure. Finally, hydrogels were individually placed into wells of a 12 well plate with 1ml of water added to each well. The plates were sealed with parafilm and placed on shaker at 4˚C overnight to rinse water. The rinse water was gently removed from each well and replaced with 1ml PBS, after which the hydrogels were stored at 4˚C until ready to use.

The templating protocol illustrated in **Figure 5.35** was developed using HA as the bulk polymer and the specific mechanical attributes that arose from this macroporous templating method were evaluated. Photocrosslinkable three-dimensionally patterned hyaluronic acid hydrogels were synthesized by preparing 2-5% w/v solution of 20% glycidyl methacrylate hyaluronic acid with photoinitiator concentration varied between 0.3-1% Irgacure 2959. A 1 % stock photoinitiator solution was prepared in 10 mM

phosphate-buffered saline and added accordingly to the hydrogel solution to obtain the desired final concentration. The crystallizing molecules were thermally dissolved in the hydrogel solution slightly in excess of their saturation concentration in water at 25°C. The solutions were dissolved at 30-40°C until homogeneous. Warm solutions were injected into silicone molds compressed between two glass slides. Hydrogels were synthesized in 100 µL molds that are 2 mm in depth and 8 mm in diameter. The hydrogels were crosslinked using UV light at 13 mW/cm^2 intensity. Templated hydrogels were soaked in deionized water overnight to remove the porogen, then swollen in 10 mM phosphate-buffered saline.

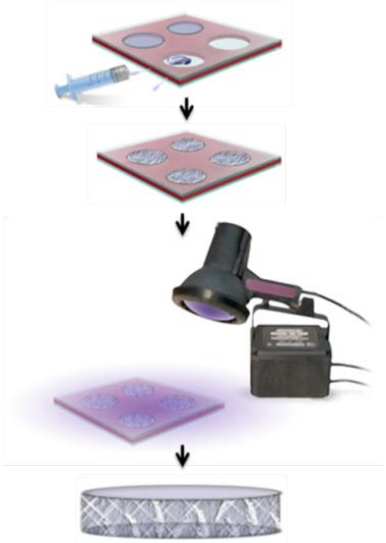

Figure 5.35: Schematic of hydrogel templating protocol. Warm GMHA solution with dissolved porogen is injected into molds. The solution is cooled on ice to encourage nucleation and the polymer is subsequently crosslinked around the crystalline network. Upon rinsing, the hydrogel retains the architecture imparted by the templating method.

5.7.5 Equilibrium Water Content Experiments. The templated hydrogels were first rinsed in deionized water overnight to remove the crystalline molecules. The hydrogel was transferred to fresh deionized water and allowed to reach equilibrium and

the weight recorded. The samples were then dried overnight in an oven to achieve the weight of the polymer component in the hydrogel samples. The dried weight was recorded and used to calculate the equilibrium water content for each templated hydrogel.

5.7.6 Swelling Experiments The swelling of hydrogels was conducted via the gravimetric method. Samples were weighted after they equilibrated in media over night for a constant hydrated weight. An initially weighed hydrogel (relaxed state) was first immersed in deionized water in 10 mM PBS solution at pH=7.4 at room temperature until equilibrium was reached. At equilibrium, excess saline was dried away and the final swollen weight was recorded. Swelling studies were conducted by first weighing gels with porogen inside. The swelling ratio of the hydrogels was evaluated by swelling porogen-free hydrogels in 10mM phosphate-buffered saline overnight and recording the swollen weight. The swollen hydrogels were subsequently dried at 40 ˚C for 48 hours to obtain the dry weight of the polymer.

5.7.7 Rheology. Two rheometers were used in this thesis. The ARES LS1 allows more functionality however the Anton Paar is more user-friendly. The ARES displays the force whereas the Anton Paar only shows contact with the sample. An Anton Paar rheometer with 25 mm parallel plates was used over a frequency sweep of 0.1-10 Hz at constant strain and 2 mm gap size [104]. The ARES was used with an 8mm parallel pate. Samples evaluated on the ARES LS1 with an air pressure of approximately 80 psi on a thermocouple heated stage to maintain 25˚C and 8mm parallel plate. The plate was attached using a balanced pin. The gap was calibrated automatically using normal force then measurements were taken at approximately 0.1N force to exert minimal force on the sample but to ensure contact. Even though different sizes and machines were used, the

data can still be compared to one another because the sample sizes were scaled as appropriate to the plates available. Storage and loss modulus experiments were conducted on swollen hydrogels using gap sizes between 2-2.5mm. The templating was expected to reduce the storage modulus. Twenty mg/ml GMHA hydrogels with 0.3% I2959 exposed to 5 minutes UV were synthesized. The samples were first rinsed overnight in water, then swollen in phosphate-buffered saline. The amplitude sweep was performed to confirm measurements in linear viscoelastic regime [104].

5.7.8 Degradation. For degradation experiments a solution of 50 units per milliliter hyaluronidase in 10mM PBS was prepared. The PBS swollen hydrogels were placed in 1 milliliter of hyaluronidase solution and incubated at 40 ˚C. The initial hydrogel weight was recorded and the weight after incubation with hyaluronidase was subsequently recorded every hour for 12 hours. The 1 mL hyaluronidase was replaced each hour for each hydrogel. The *in vitro* degradation profile of templated hydrogels was evaluated by recording the hydrogel weights after swelling in saline (W_o) and at specific times during hyaluronidase enzymatic degradation (W_t) [4]:

$$\%\, Degradation = \frac{W_o - W_t}{W_o} \times 100\%$$

Chapter Six. Templated hydrogels as three-dimensional culture environments

Hydrogels have the ability to play a dual role of delivery device and tissue engineering construct. To that end, this chapter focuses on using templated hydrogels as a culture environment where cells are encouraged to behave as natively as possible. For this work, urea and potassium dihydrogen phosphate-templated hydrogels were evaluated for their utility as cell culture environments. The increased, organized void region of the templated scaffolds makes them particularly amenable to serving as 3D culture environments. Potassium dihydrogen phosphate-templated hydrogels were used to expand neural progenitor cells in their undifferentiated state for cell therapy applications. Urea-templated hydrogels were used to monitor myelin expression in Schwann cells.

6.1 Connection between templated hydrogels and biological systems

For this work, potassium dihydrogen phosphate crystal-templated hydrogels were evaluated for their ability to retain neural progenitor cells (NPCs) in their undifferentiated state and support increased expansion compared to not templated hydrogels. NPCs have been successfully cultured in three-dimensional hydrogels but not on scaffolds with crystal-templated three-dimensional architecture to our knowledge. Urea-templated hydrogels were used as a three dimensional culture environment for Schwann cells. We hypothesize that the voided domains within the templated hydrogels allow the scaffolds to serve as artificial stem cell niche and peripheral nervous system mimic.

Because NPCs grow as neurospheres, the defined voids within the potassium dihydrogen phosphate-templated hydrogels provide means for the spheres to grow within

the hydrogels. The rationale was to increase the number of progenitor spheres and therefore the number of cells while maintaining them in the undifferentiated state. The urea-templated hydrogels share the needle-like geometry that is similar to the directed alignment found in the peripheral nervous system.

6.3 Role of Architecture in Stem Cell Niches

Interest in stem cell therapy has garnered interest to expand stem cells in their undifferentiated state; NPCs in particular may be useful for vascular and neural cell therapy. Research in this area has focused on directed differentiation but not the maintenance of the undifferentiated state. Hydrogels have the ability to revolutionize the outcome of brain injury and disease by playing a critical role in the space between clinical practice and bench top experimentation. Hydrogel scaffolds can take on a multitude of geometries, length scales and offer a high degree of control over their mechanical and physical properties. Because hydrogels offer control over most physical properties, microarchitecture and the ability to strategically direct cell behavior, they hold great promise to mitigate degeneration and relieve symptoms associated with injury and disease [131]. Additionally, their large water contents cause hydrogel bulk behavior and storage moduli to be very similar to native tissue. Indeed, the brain has 80% water [132, 133], heart tissue has 80% water [134], and lung has 6-7% water [135].

Hyaluronic acid is degraded by hyaluronidase; which is secreted by neurons and some glia. Degradation is imperative because we are interested in harvesting the cells from the hydrogels after culture. Higher molecular weight or higher polymer percentage leads to a more dense hydrogel and therefore a slower degradation rate [136]. Polymer degradation routes have led to an on-going debate over whether biologically derived or

synthetic polymers are better suited for tissue engineering. Scaffold degradation may occur by polymer-compatible enzymes that cleave polymer chains at specific locations, hydrolysable bonds [67], or reversible thiol linkages [137]. Higher water content in scaffolds usually results in higher degradation by hydrolysis. Having biologically familiar polymer-enzyme reactions manage the degradation and clearance of scaffold byproducts makes a strong case for the advantage of biopolymers.

Stem cell niches are localized regions within native tissue that serve as a repository of lineage-specific stem cells. The niche environment provides specific chemical and physical cues to cells within its domain. The cell-cell and cell-substrate interactions provide cues that dictate cell fate based on chemical signals displayed as well as substrate stiffness and topography in both 2D and 3D [138-140]. Advances in stem cell therapy have led to a surge in research on directing progenitor cell fate [141-143] and increasing their survival upon *in vivo* implantation [41]. Research to date has primarily focused on the chemical [144] and bulk mechanical [145-147] properties associated with differentiation in niche environments. ECM components have shown excellent promise in brain tissue engineering. Nevertheless, hyaluronic acid [137], chitosan, gelatin [148], collagen [149-151], alginate, and cellulose have each been used for hydrogel matrices in brain tissue engineering [136]. Synthetic polymers have the advantage of being more mechanically stable and offering superior handling properties to scaffolds comprised of biopolymers. Synthetic polymer scaffolds may elicit a minimal immune response upon implantation, yet that does not mean by conjecture that their precursors and/or degradation subunits would also be bio-inert, therefore there are doubts about the long-

term safety of synthetic polymers [136]. Synthetic polymers such as PEG [137], pHEMA, pMMA, pHPMA are used most often [152] in brain tissue engineering.

Outside of chemistry concerns, physical properties also play a role and can contribute to biocompatibility. The mesh sizes, the presence or absence of pores, surface texture, and roughness/topography each have a significant impact on how the hydrogel behaves and potential cell-material interaction [104]. Fluid flow through the hydrogel and the exchange of nutrients necessary for biocompatibility are all dependent on the mesh size of the hydrogel that result from crosslinking. The distance between crosslink must be large enough to allow free diffusion of gases and fluids and the movement of small molecules. Porosity allows for cell infiltration, uniform cell distribution throughout the matrix, as well as cell growth and proliferation. The pore size of a scaffold directly correlates with its bulk physical attributes, the cell type it would be compatible with, as well as the potential viability of those cells while the scaffolds are in service [123, 153, 154]. The macroporosity is particularly critical in brain tissue engineering because scaffolds must often support the existence or promote the regeneration of an interconnected neural network [131, 153]. The superabsorbent property of the hydrogels is important because it reduces the stress the experimental cells experience in culture. Furthermore, the forces that occur when HA swells are thought to contribute to early neuronal morphogenesis [55]. Cui et al implanted HA and HA-RGD hydrogels in rat cortical defects. The lyophilized samples had uniform pore size diameters that created a large surface area to volume ratio that accommodated a large number of cells and allowed neovascularization of the matrix. The HA-RGD hydrogels provided continuity across the defect. Implants had no visible glial scar formation and were well integrated into the host

tissue at 6 weeks. According to their data, hyaluronic acid alone mitigated glial scar formation, encouraged integration into host tissue, allowed cell infiltration, angiogenesis while RGD conjugation allowed neurite regrowth [155]. These results suggest that HA scaffold with deliberately porous structures can improve cell-substrate interaction in scaffolds.

Neural progenitor cells in particular are multipotent, meaning they have the ability to differentiate into both neurons and glia. They lie in a vascular niche *in vivo* [156]. There are three types of glial cells, astrocytes, microglia and oligodendrocytes. The microglia are the resident immune system cells found in the sub ventricular zone of the lateral ventricles and the subgranular zone of the dentate gyrus in adult brains. These cells have been successfully cultured in three-dimensional scaffolds, however with reduced viability and proliferation. Extracellular matrix scaffolds of HA have been used to create bioartificial stem cell niches for endothelial progenitor cells and to improve NPC survival [41]. In these cases, HA hydrogels were used as a cell delivery medium and did not pertain to phenotype maintenance. There is a need to expand stem and progenitor cell populations in an undifferentiated state for therapeutic applications. Work that has been conducted on undifferentiated expansion has focused on the interplay of immobilized chemical signaling but not the role of substrate properties for cell maintenance in the undifferentiated state. Hydrogels are a very good means of maintaining or differentiating neural progenitor cells and research is on-going to determine if hydrogels can be used as a viable means to deliver stem/progenitor cells [153, 157].

Some recent research has focused on the addition of architectural features to amorphous matrices. The brain is comprised of highly specific regions of intricate architecture, with morphology among the most complicated in the entire body. Scaffolds that mimic the specific and complex organization while providing advantageous chemical cues have the most promise to serve as niche environments. For example, on two-dimensional substrates with nanoscale topography, cell proliferation improved significantly compared to culture on tissue culture polystyrene [158]. Micro- and macrostructure in hydrogel scaffolds have been created by solvent casting/particle leaching [65], freeze drying [150], layer-by-layer [14], and rapid prototyping [159]. Porogen leaching and gas foaming create consistent pore sizes by using sacrificial additions or allowing gas particles to flow through the scaffold. Martinez-Ramos 2012 used poly(ethyl acrylate)-poly (hydroxyl ethyl acrylate) copolymer blend matrices with two different internal geometries for implants into the cortical and subventricular zones (SVZ) of the brain [65]. The *in vitro* experiments proved that neural progenitor cells readily infiltrated into the scaffold and differentiated into neurons and astrocytes regardless of the specific scaffold geometry. *In vivo* implants of both parallel cylindrical channels and those with interconnected voids showed local angiogenesis and neurite extension within scaffolds that were implanted in the SVZ. The different scaffold geometries had a non-significant effect on the scaffold integration or cell penetration. It is likely that scaffolds of both geometries were porous enough to support local regenerative activity. This may mean that the overall effective porosity of the scaffold and pore size takes precedence to the specific geometry of the scaffold.

When designing hydrogels, researchers must keep the function and specific anatomy of site of interest in mind. We argue that the physical properties of scaffolds are almost as important to cell-material compatibility as is the chemical properties. Neural stem cells undergo polarization and contact guidance responses that can be mimicked through complex structuring of the surface. The cellular phenotype, cell survival, extension can be controlled/maximized by varying the culture substrate elastic modulus. Soft tissues in vertebrates maintain mechanical properties which are quantified by elastic modulus within specific ranges. This relationship allows distribution and population sorting to occur based on the mechanical properties of the substrate. Neural cells flourish in softer hydrogels where the mechanical properties more closely match those found in native neural tissue. Using a material whose characteristics are similar to the brain tissue reduces the risk of damaging the surrounding tissue upon implantation. Cortical neurons and astrocytes, for example, respond strongly to changes in matrix rigidity. Modulus of brain tissue is between 0.1-1kPA [160, 161]. The shear modulus G'(w) oscillatory of adult rat brain is about 330 Pa [162]. The storage modulus of potassium dihydrogen phosphate-templated hydrogels were between 0.6-8.5 Pa, depending on parameters as shown in **Figure 5.11**. Neurons survive best at less than 1 kPa while astrocytes are fine at up to 10 kPa. Optimizing the mechanical properties for the cells of interest reduces the contact stresses [136]. Hydrogel swelling is related to hydrogel stiffness and extent of crosslinking which impacts size of distance between crosslinks. Modulus is able to be modulated by the degree of functionality and higher monomer loading.

Hydrogel scaffold integration with cells is particularly sensitive for brain applications both *in vitro* and *in vivo*. For *in vivo* implants in particular, there is concern

of the interaction of the scaffold with tissue surrounding the implant. The Aurand et al review discussed the biocompatibility of materials for implantation into brain or spinal cord. They found that implanting cell replacements provided the most promise for tissue engineering in the brain. Parkinson's research revealed that neurons survived better in host when implanted as a piece of donor neural tissue rather than dissociated cell suspensions. Therefore there is a positive impact from retaining a 3D environment where cell attachments are maintained [136]. Scaffolds with active cellular components that are either pre-loaded or that encourage rapid infiltration of cells have shown the most progress towards successfully replicating the 3D cellular environment. Cells must be seeded on top of the scaffold, injected or encapsulated within the hydrogel and toxicity of each method must be evaluated [153]. Cell encapsulation hinders the ability to create architecture, yet provides the most robust option for optimizing the *in vitro* culture system. With top cell seeding, a lot of cells are lost because of an inability to attach and migrate into the scaffold in the short seeding time frame. Furthermore, depending on the purpose of the biomaterial, a preformed scaffold or an injected hydrogel could be preferred. The three dimensional matrix completely surrounded the cells and allowed them to behave more similarly to how they would in normal physiological conditions. The extent of crosslinking adjusted the effective porosity of the scaffolds [150]. The MSCs were cultured in hydrogels, extracted, and cultured *in vitro* for 3 days to evaluate survival capabilities [163]. The controlled condensation and experimental observations of hydrogels having protective, supportive, quality may be caused by the hydrogel mimicking the environment the ECM cells would expect to find *in vivo* [137].

In order to verify sufficient removal of potassium dihydrogen phosphate from the hydrogels in preparation for cell culture, the samples were rinsed daily for seven days and the effluent water was analyzed for phosphate ion concentration. The concentration was found to be 71380.56 μM on the first day and lower than the detectable range on day seven as shown in Figure 6.1. According to the Manual of Laboratory and Diagnostic Tests, the concentration of phosphate ion in blood for an average adult is 0.87-1.45 mmol/L which equates to 870-1450 μM [164]. Therefore, the potassium dihydrogen phosphate-templated hydrogels released phosphate levels below this threshold after three days of rinsing. Therefore the five days of rinse prior to cell culture release phosphate ions well below systemic levels.

The potassium dihydrogen phosphate-templated samples were effective in allowing progenitor neurospheres to grow within the void spaces (**Figure 6.2**). The progenitor cells in suspension formed spheres after 7 days with some minor evidence of differentiation (**Figure 6.7)**. The control not templated hydrogels maintained nestin expression at 3 days in culture (**Figure 6.4**) and cells cultured in the potassium dihydrogen phosphate-templated hydrogels formed neurospheres after 3 days **Figure 6.5**. At 3 days, cells cultured on not templated hydrogels have higher amounts of nestin expression than cells cultured in suspension. Interestingly, the cells cultured in suspension for 3 days were positive for GFAP (**Figure 6.3**). At both 3 and 7 days the nestin expression in not templated samples is either comparable to (**Figure 6.11**) or slightly higher than the tissue culture controls (**Figure 6.12**). The cell images show evidence of neuronal differentiation after 7 days in both not templated hydrogels (**Figure 6.8**) and potassium dihydrogen phosphate-templated hydrogels (**Figure 6.9**). In regards to

GFAP expression, after 3 days in culture, the not templated samples have the lowest GFAP expression. After 7 days, cells cultured in hydrogels of either genre have more relative GFAP expression, but the negative control samples have the highest. After 3 days, the majority of the population show nestin expression but at 7 days there are higher amounts of GFAP expression in both the not templated and potassium dihydrogen phosphate-templated samples. In the negative control of 10% DMSO, neurospheres formed after 7 days in culture and both neuronal and astrocytic differentiation was evident as shown in **Figure 6.10**. At 3 days in DMSO, however, the progenitor population showed evidence of differentiation in **Figure 6.6** and quantitatively in **Figure 6.11** and **Figure 6.12**.

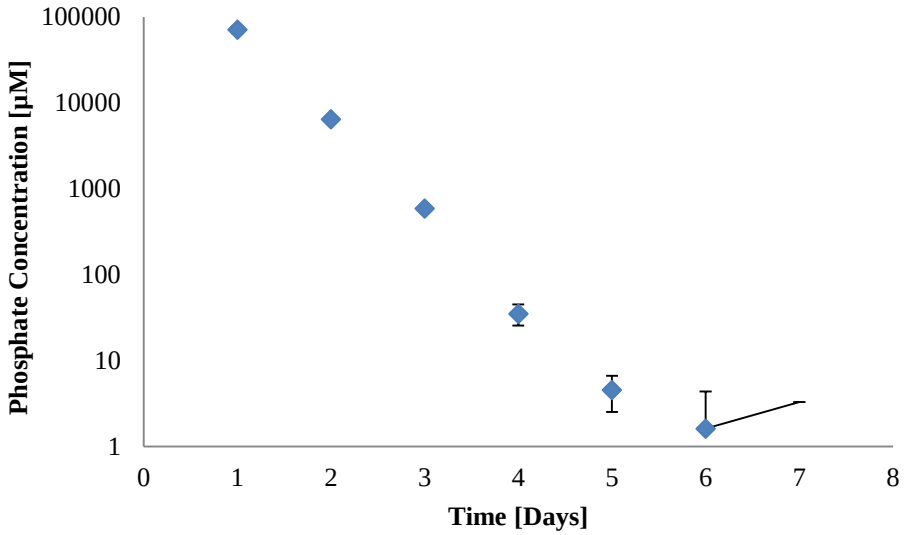

Figure 6.1: Phosphate ion concentration in effluent rinse water from potassium dihydrogen phosphate-templated hydrogels. The phosphate ion concentration was detected in the rinse water using a fluorescence reaction. After three days of rinsing, the concentration of phosphate ions was less than the systemic phosphate levels in adult human blood. These results suggest that hydrogels rinsed for a minimum of three days should not release phosphate ions at a concentration that exceeds the systemic concentration.

Day	Mean Phosphate Concentration [uM]	Std. Error
1	71380.56	6725.51
2	6459.822	372.97
3	589.2922	29.55
4	35.16684	9.71
5	4.568026	2.05
6	1.618485	2.75
7	-0.9384	4.23

Table 11: Phosphate ion concentrations in potassium dihydrogen phosphate-templated hydrogels.

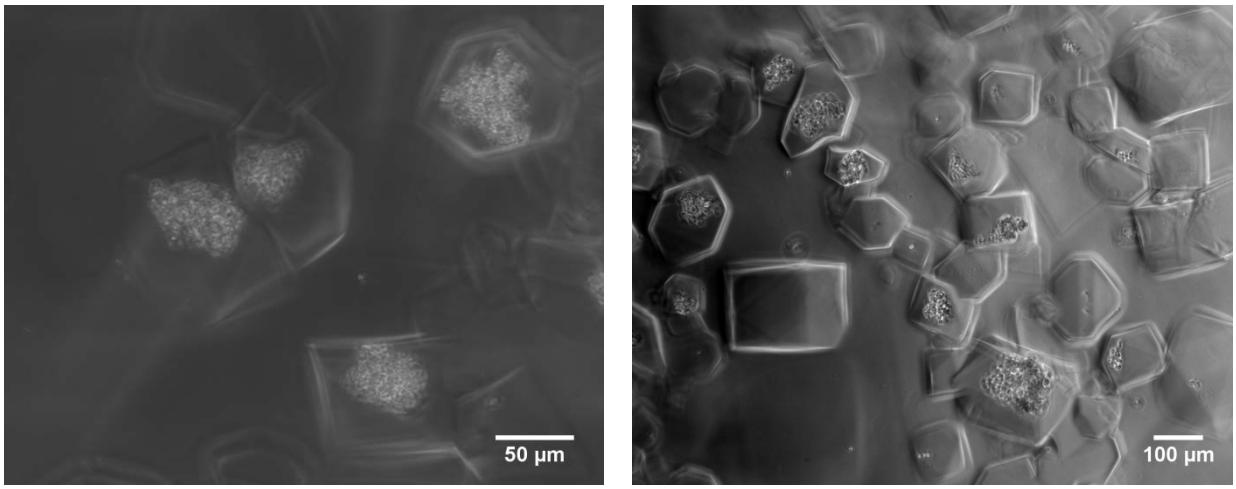

Figure 6.2: Phase contrast images of forebrain progenitor cells cultured in potassium dihydrogen phosphate-templated hydrogels for 7 days. The cells form neurospheres that appear within the voided regions of the templated samples. Void regions appear between 50-100 µm.

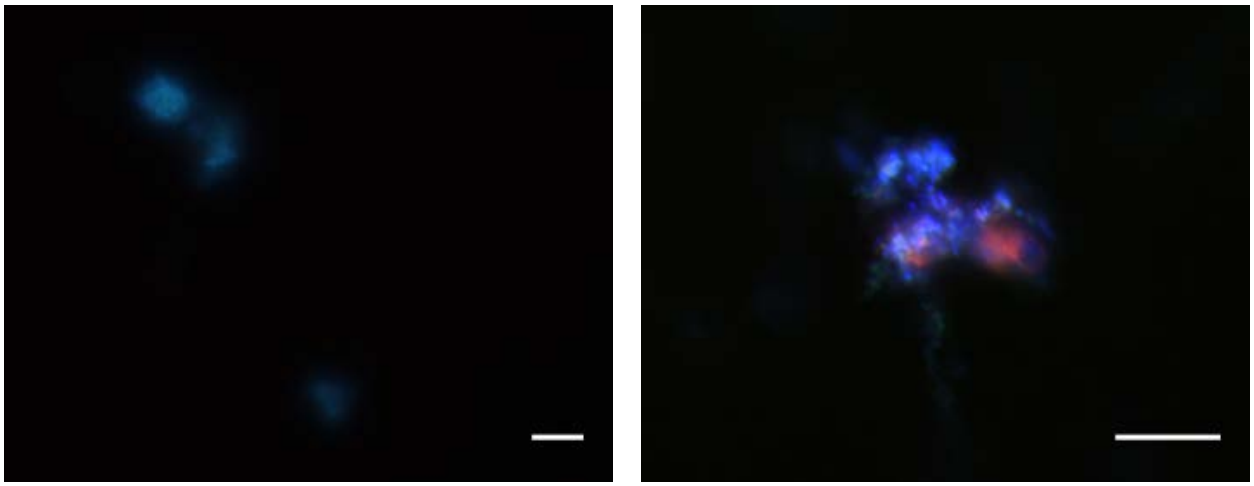

Figure 6.3: Forebrain progenitor cells cultured for 3 days. Stained with DAPI (blue), nestin (green) and either BIII-tubulin (red, left) or GFAP (red, right). The cells show signs of astrocytic differentiation after 3 days in culture. Scale bar 50 µm.

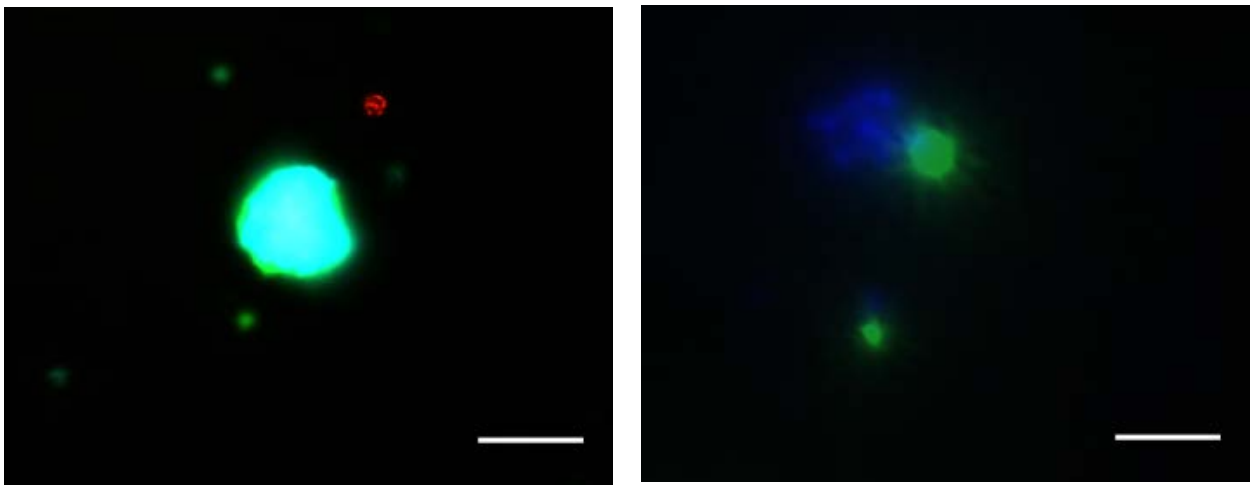

Figure 6.4: Forebrain progenitor cells cultured for 3 days on not templated control hydrogels. Cells were stained with DAPI (blue), nestin (green) and either BIII-tubulin (red, left) or GFAP (red, right). The not templated hydrogels appear to successfully prevent wide-spread differentiation after 3 days in culture. Scale bar 50 μm.

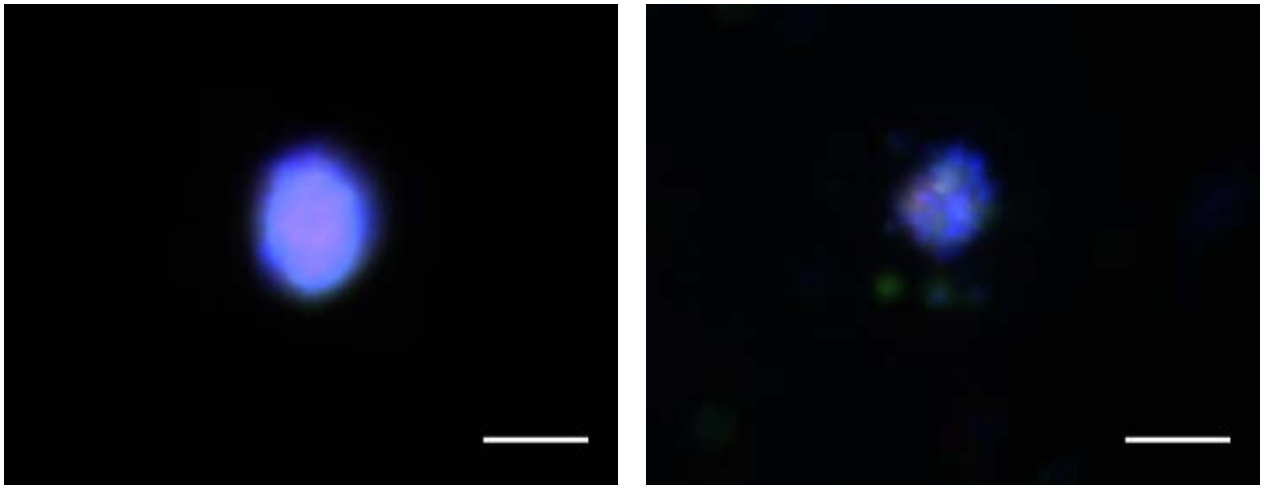

Figure 6.5: Forebrain progenitor cells cultured for 3 days on potassium dihydrogen phosphate-templated hydrogels. Cells were stained with DAPI (blue), nestin (green) and either BIII-tubulin (red, left) or GFAP (red, right). The potassium dihydrogen phosphate-templated hydrogels appear to prevent differentiation after 3 days in culture. Scale bar 50 μm.

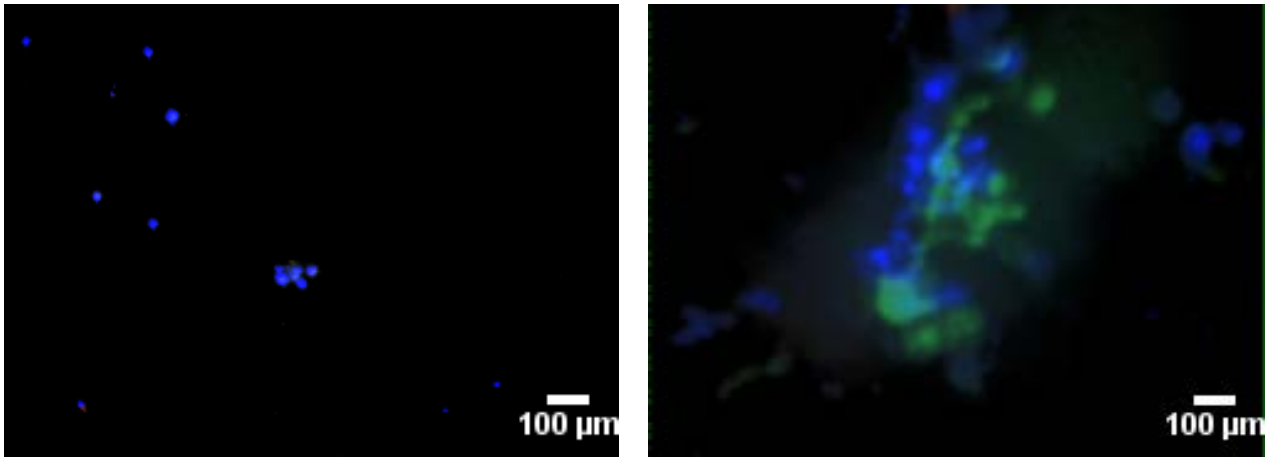

Figure 6.6: Forebrain progenitor cells cultured for 3 days with 10% DMSO. The cells were stained with DAPI (blue), nestin (green) and BIII-tubulin (red, left) or GFAP (red, right). There was minor nuclear differentiation after 3 days in culture, the majority of cells expressed nestin.

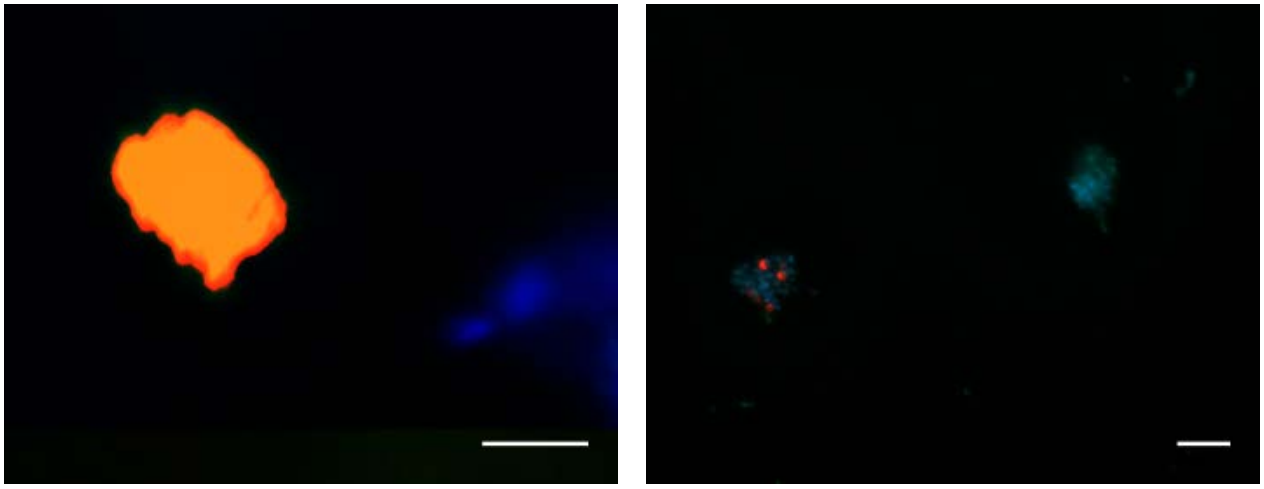

Figure 6.7:Forebrain progenitor cells cultured for 7 days. The cells were stained with DAPI (blue), nestin (green) and BIII-tubulin (red, left) or GFAP (red, right). After 7 days in culture there was some evidence of minor neuronal and astrocytic differentiation. Scale bar 50 µm.

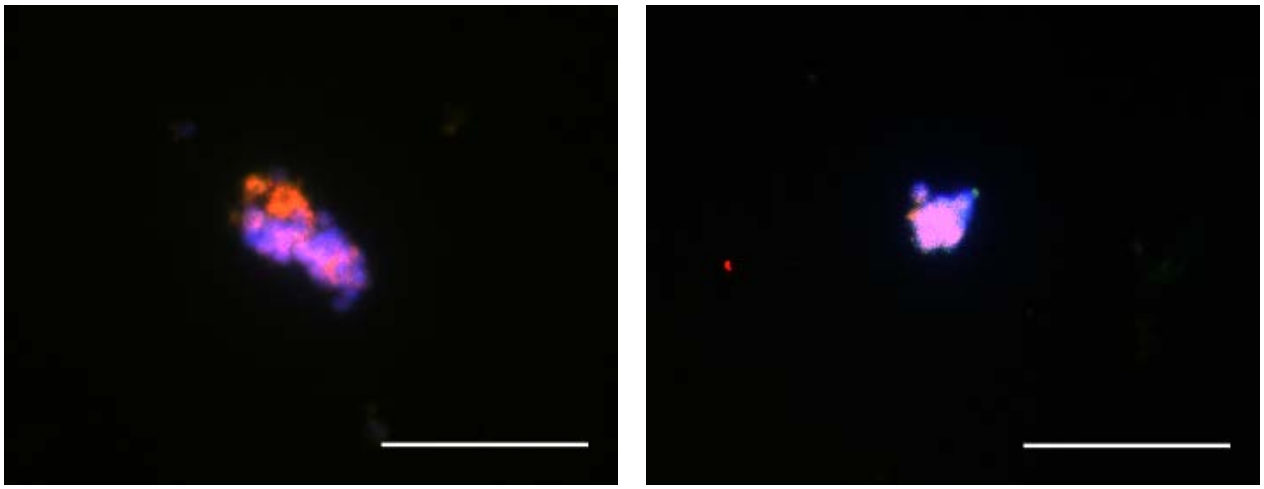

Figure 6.8: Forebrain progenitor cells cultured for 7 days on not templated control hydrogels. The cells were stained with DAPI (blue), nestin (green) and BIII-tubulin (red, left) or GFAP (red, right). Results suggest that cells may not survive well in not templated hydrogels after 7 days in culture. Few neurospheres were present and the ones that existed were smaller in diameter than those found at the other culture conditions. Scale bar 50 µm.

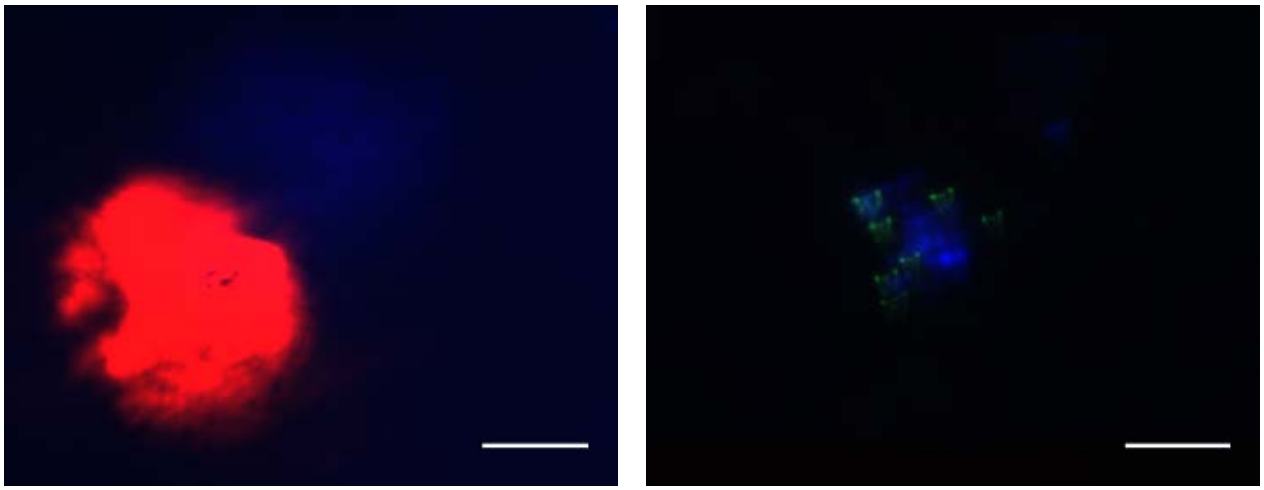

Figure 6.9: Forebrain progenitor cells cultured for 7 days on potassium dihydrogen phosphate-templated hydrogels. The cells were stained with DAPI (blue), nestin (green) and BIII-tubulin (red, left) or GFAP (red, right). The images suggest that the potassium dihydrogen phosphate-templated hydrogels suggest neuronal differentiation. Scale bar 50 µm.

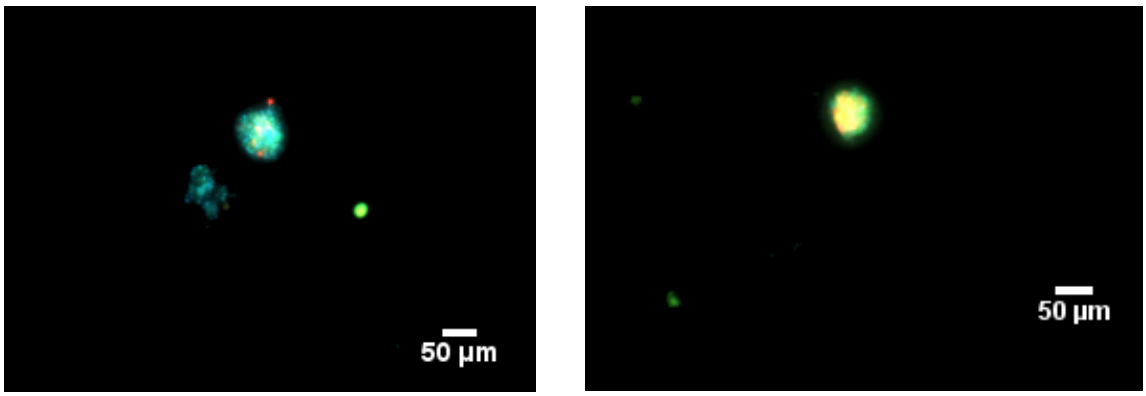

Figure 6.10: Forebrain progenitor cells culture for 7 days with 10% DMSO. The cells were stained with DAPI (blue), nestin (green) and BIII-tubulin (red, left) or GFAP (red, right). Results suggest both neuronal and astrocytic differentiation after 7 days in culture with DMSO.

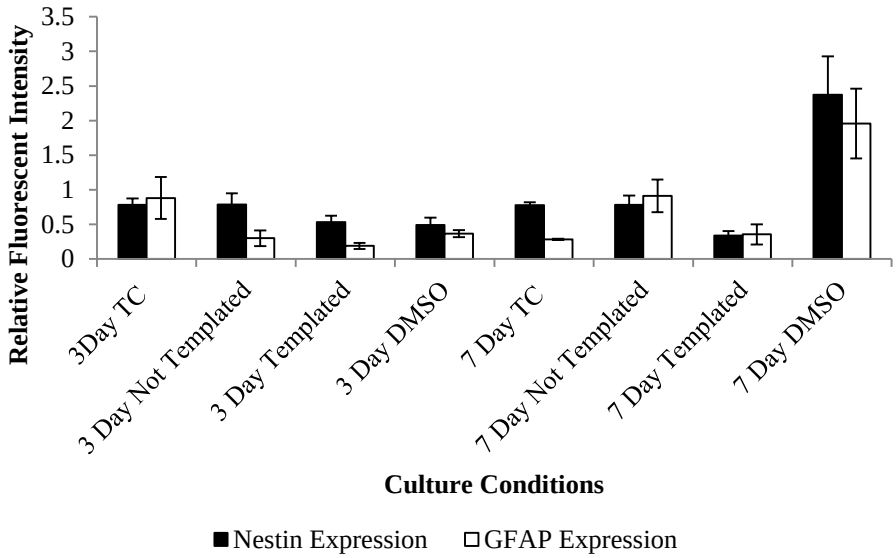

Figure 6.11: Relative fluorescent intensity of nestin and GFAP expression from E11.5 forebrain progenitor cells. Images shown in Figures 6.3-6.10 were analyzed for intensity in each color channel and normalized to the intensity for the number of cells (DAPI staining). The cells cultured in the not templated hydrogels have relative nestin expression that is comparable to the tissue culture control samples. After 3 days in culture, the cells culture on potassium dihydrogen phosphate-templated hydrogels have the lowest amount of GFAP expression. After 7 days in culture, the results show more of the cell population expressing GFAP for celled cultured in hydrogels of either type.

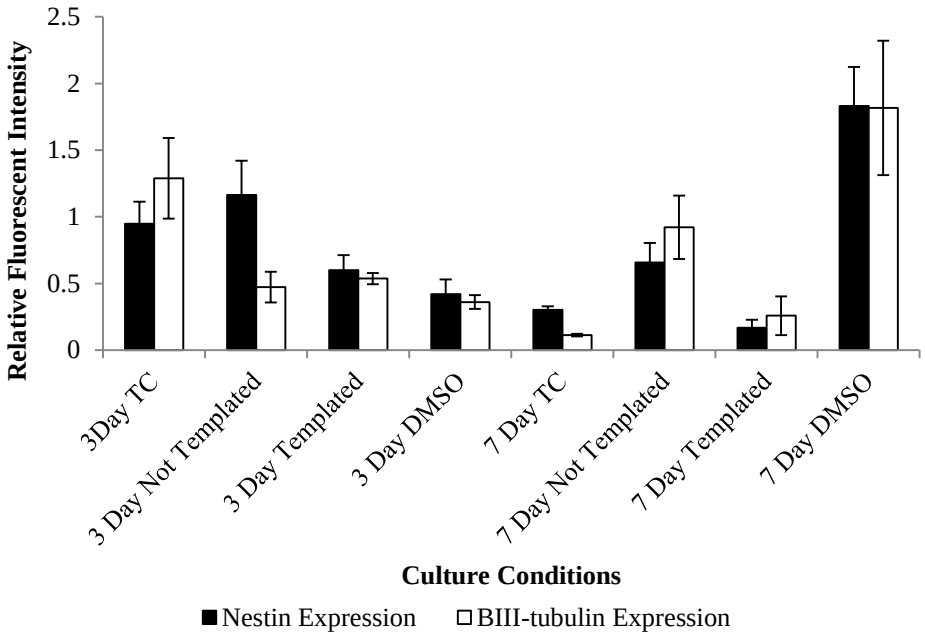

Figure 6.12: Relative fluorescent intensity of nestin and βIII-tubulin expression from E11.5 forebrain progenitor cells. After 3 days in culture, more of the cells were positive for nestin than βIII-tubulin. However, after 7 days in culture, higher amounts of the populations cultured in hydrogels were positive for βIII-tubulin.

6.4 Role of Architecture in Wounds Healing

Wounds are disruptions in the intricately organized tissue structure whose repair involves the resolution of inflammation and restored function. Lumelsky suggests that future tissue engineering therapies should target achieving spatial and temporal control of the inflammatory tissue microenvironment [29]. Materials that "allow creation of tissue-like structures with defined three-dimensional architectures mimicking normal tissue organization" are expected to prove advantageous for altering the tissue microenvironment and immune response [29]. Competing technologies in this area focus on spatially defined growth factor release and layer-by-layer scaffold construction. Approaches that rely on the principles of self-assembly are expected to provide improved biocompatibility and cell-material interaction. HA is reportedly the first macromolecule to appear in the extracellular matrix during wound healing [47, 165]. Therefore HA based scaffolds with complex internal architectures may provide an effective *in vitro* culture environment to mimic the wound healing environment.

In vivo tissues can be viewed as dense, continuous networks with largely interconnected pores. The *in vivo* porous network has hierarchical depth in each dimension that is linked to the role of the tissue. Tissue architecture provides support for cells, and dictates the appropriate morphology. Imposing microscopic architecture within hydrogel scaffolds, was expected to allow improved cellular viability in three-dimensional culture. The enhanced viability was expected to allow *in vitro* experimental models to enable the effective use as a Schwann cell culture environment.

The purpose of this experiment was to determine an appropriate amount of rinsing after hydrogel synthesis that brought urea concentration into a reasonable range prior to

cell seeding. The normal systemic concentration of urea is 29.3 mg/100 cc blood which equates to 4800 μM urea [71]. **Figure 6.13** details the concentration of urea found over seven days of daily rinse water replacement and collection. The experimental results show that the urea-templated hydrogels release a concentration of urea that is below the systemic concentration in the adult human body after four days of rinsing.

For tissue engineering constructs to be truly beneficial they must either make no negative impact or yield a positive cellular response. The cytotoxic effects of urea templated hydrogels were evaluated on fibroblast and Schwann cells and compared with not templated hydrogels and a negative control of 10% dimethylformamide in media. The cell viability of fibroblasts cultured with urea-templated hydrogels was not significantly different from the positive control culture plate or experimental control not templated hydrogels. Cell viability is important to the success of a biomaterial and must be evaluated as a preliminary step. Results presented in **Figure 6.14** indicate that fibroblast and Schwann cell viability was not significantly reduced with urea templated hydrogels as compared to the positive and experimental controls. These results suggest that thorough rinsing with deionized water sufficiently removed the urea molecules from the hydrogels to allow templated hydrogels to have a negligible effect on cell viability relative to not templated hydrogels and tissue culture controls.

Schwann cells do not have a receptor to allow them to attach to HA without the addition of a cell adhesion peptide. Hyaluronic acid was conjugated with a custom RGD peptide to render hydrogels of the polymer cell adhesive. The Gly-Arg-Gly-Asp-Lys(FITC) peptide used has a molecular weight of 921.0 amu and had a 73.9% peptide content. Arg-Gly-Asp or RDG is commonly used to create an adhesive surface on an

ECM protein [15]. RGD has been shown to promote neurite extension in PC12 cells and mediate cell attachment and was therefore conjugated to the polymer [166]. ^{1}H NMR results were used to confirm the presence of the GRGDLys(FITC) peptide on the methacrylated HA as shown in **Figure 6.15**. GRGDLys(FITC)-GMHA was used to facilitate Schwann cell attachment to hydrogels for experimental culture.

Peripheral myelin is synthesized by Schwann cells. These glial cells secrete a sheath that allows for improved conduction along axons in the peripheral nervous system. As immature Schwann cells come in contact with axons, the Schwann cells are activated to wrap around the nerves and form a compact, insulting sheath around the nerve fibers. Myelination in the peripheral nervous system by Schwann cells differs from that of the oligodendrocytes in the central nervous system. Schwann cells wrap around axons in a one to one fashion, however oligodendrocytes myelinate several nerve fibers at once to form a bundle. During the “active myelination period”, which extends through the second, third and fourth weeks after birth, myelin markers such as myelin protein zero and myelin basic protein are expressed [167].

Literature suggests that materials used to shape the microenvironment can also be used to engineer the immune response, by the use of cytokine-releasing scaffolds, for example [29, 168]. The culture of myelinating Schwann cells on urea-templated hydrogels was hypothesized to allow artificially induced cellular behavior or similar to the native environment. Schwann cells were cultured in a pro-myelinating media and phenotype verified with myelin basic protein markers. Cells were evaluated for changes in myelin basic protein after 48 hours using flow cytometry as shown in **Figure 6.17** [169]. The flow cytometry results were used to provide quantitative measures of the

levels of myelin markers present in the culture population. Schwann cell cultures may be contaminated by fibroblasts, therefore a parallel culture of Schwann cells was be maintained and stained for S100 to determine the purity of the culture population. The cells were cultured in media containing varying concentrations of forskolin. Forskolin is a cyclic AMP activator and therefore can be used to artificially induce myelin expression from Schwann cells. The proteins were analyzed independently so the percentages presented are based on the total population. A shortcoming of this experiment is that the populations of interest were not able to be co-localized to only show the population that was both positive for S100 and MBP. Subsequent experiments were conducted with only 0.01µM (standard concentration) and 10µM FSK. Cells were then seeded on templated and not templated scaffolds and again evaluated for phenotype retention after 48 hours in culture with the potential to magnify the effect of forskolin. Fluorescent images of the cells in the 0 µM, 0.01 µM and 10 µM forskolin are shown in **Figure 6.16**. The cell nuclei are stained with DAPI (blue). The cells that express the S100 protein are labeled with FITC (green) and myelin basic protein is labeled with Alexa 568 (red). There appears to be an increase in the myelin basic protein expression in both the 0.01 µM and 10 µM forskolin concentration cells as compared to the 0 µM control. There also appears to be an upregulation of S100 in the cells cultured in 10 µM forskolin as evidenced by the green and red co-localization. **Figure 6.18** confirms the phenomena where a significant increase in both S100 and MBP occur with 10 µM FSK by flow cytometry analysis. The cells were also cultured on not templated controls and urea-templated scaffolds at 0.01 µM and 10 µM forskolin concentrations in media (**Figure 6.18**). In the tissue culture samples, the percent of the population expressing both S100 and MBP increased with

increasing FSK concentration. However, when the cells were cultured in hydrogels, the trend was not sustained. In both the not templated and urea-templated samples the S100 and MBP was reduced both relative to the tissue culture control and from 0.01 to 10 μM FSK. It appears that culture within hydrogels insulates or suppresses the expression of these two proteins.

Wound healing is impaired in diabetic patients and the cellular response to therapeutics has not been adequately investigated. Flow cytometry was used to examine the up/down regulation of myelin markers. Controls for this experiment were Schwann cells cultured on tissue culture polystyrene dishes and untemplated hydrogels. There was an upregulation in cells alone still occurs in plated cells but is not present in those cultured on either form of hydrogel. The not templated hydrogel appears to upregulate 0.01μM. Culture in hydrogels seem to have a suppressive effect on MBP expression.

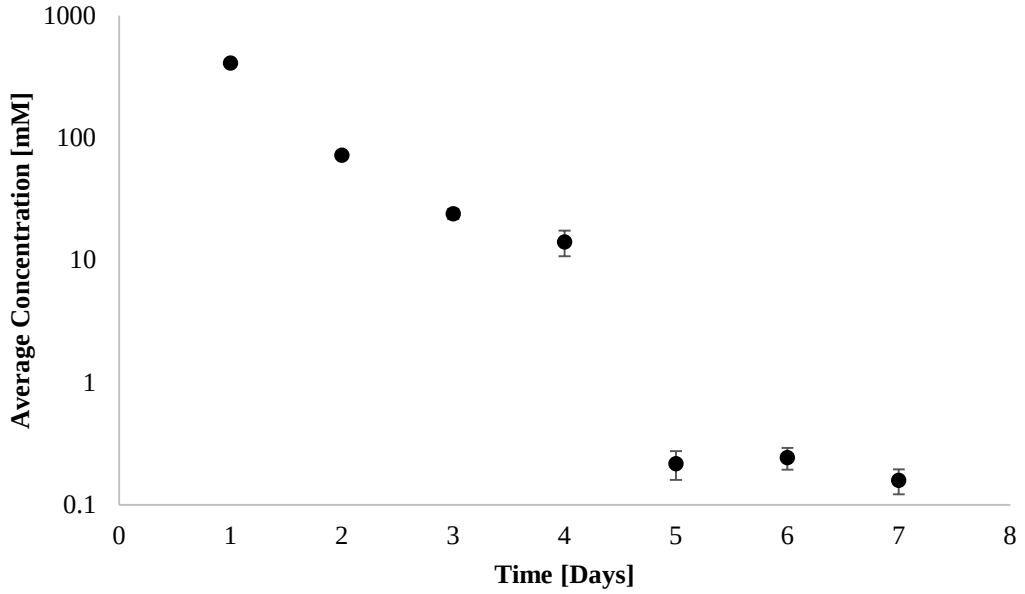

Figure 6.13: Urea concentration in effluent rinse water from urea-templated hydrogels. The urea concentration was indirectly determined using a reaction to convert urea to ammonia which reacts to emit a fluorescent signal. The samples release urea at concentration that is below the systemic urea levels in blood after four days of rinsing.

Days	Mean Urea Concentration [mM]	Std. Error
1	411.074	5.036
2	72.188	2.192
3	23.994	2.330
4	14.117	3.318
5	0.218	0.0579
6	0.244	0.0491
7	0.159	0.0368

Table 12: Mean urea concentrations for effluent media from urea-templated hydrogels that corresponds to Figure 6.13.

	Condition
Positive Control	Cells Only
Experimental Control	GMHA hydrogel in media
Experiment	Templated GMHA hydrogel in media
Negative Control	10 % DMSO in media

Table 13: Experimental conditions for scaffold toxicity in Schwann cell myelination experiments. The cells were cultured in various conditions to determine the effects of three-dimensional complex scaffold on Schwann cell myelin expression.

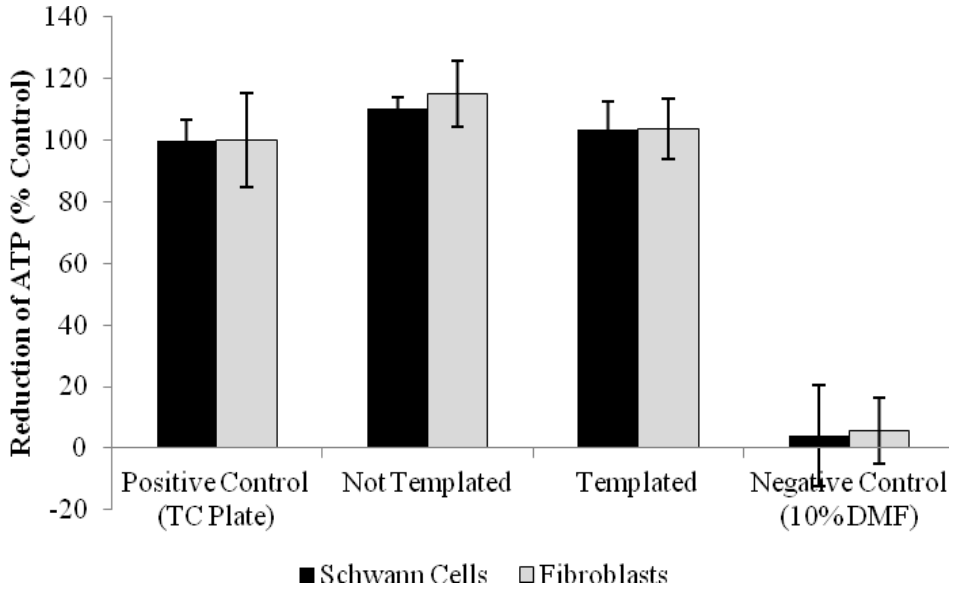

Figure 6.14: Cell Titer Glo Assay of relative cell viability from 48 hours in culture of fibroblasts and Schwann cells with samples suspended in culture media. There was not a significant difference between cell viability from urea-templated and not templated hydrogels.

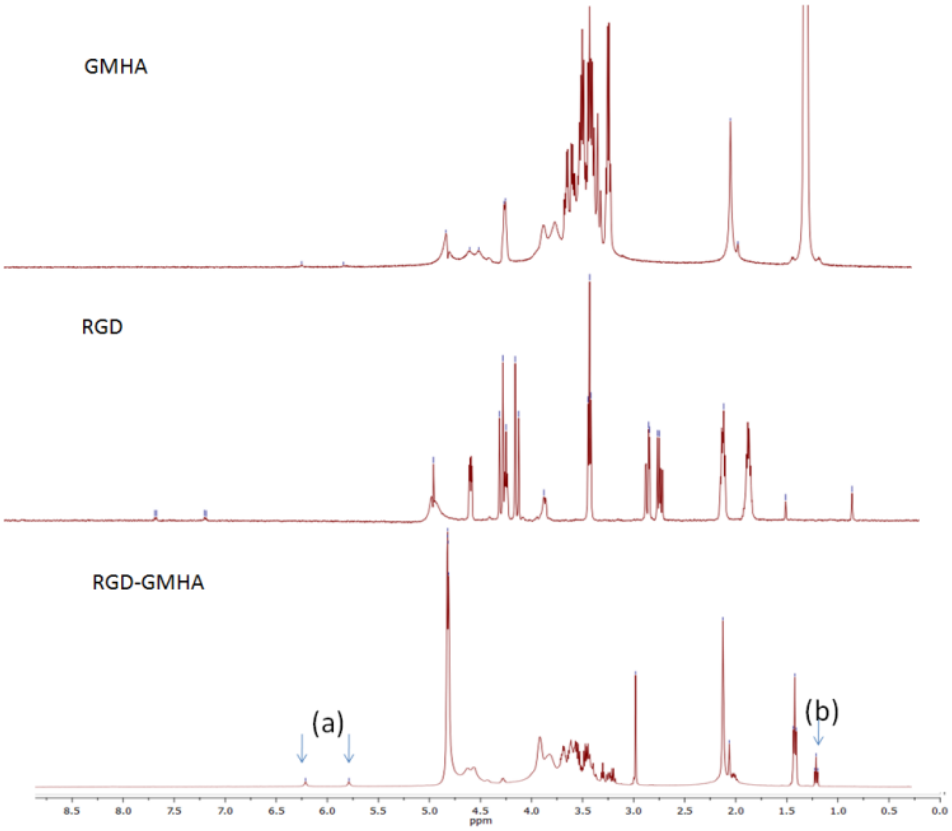

Figure 6.15: H NMR data of methacrylated hyaluronic acid (GMHA), RGD peptide and RGD-GMHA. (a) demarcates peaks that are indicative of the methacrylate groups at approximately 6.1 and 5.6ppm and (b) nitrogen groups of RGD present in the RGD-GMHA polymer**.**

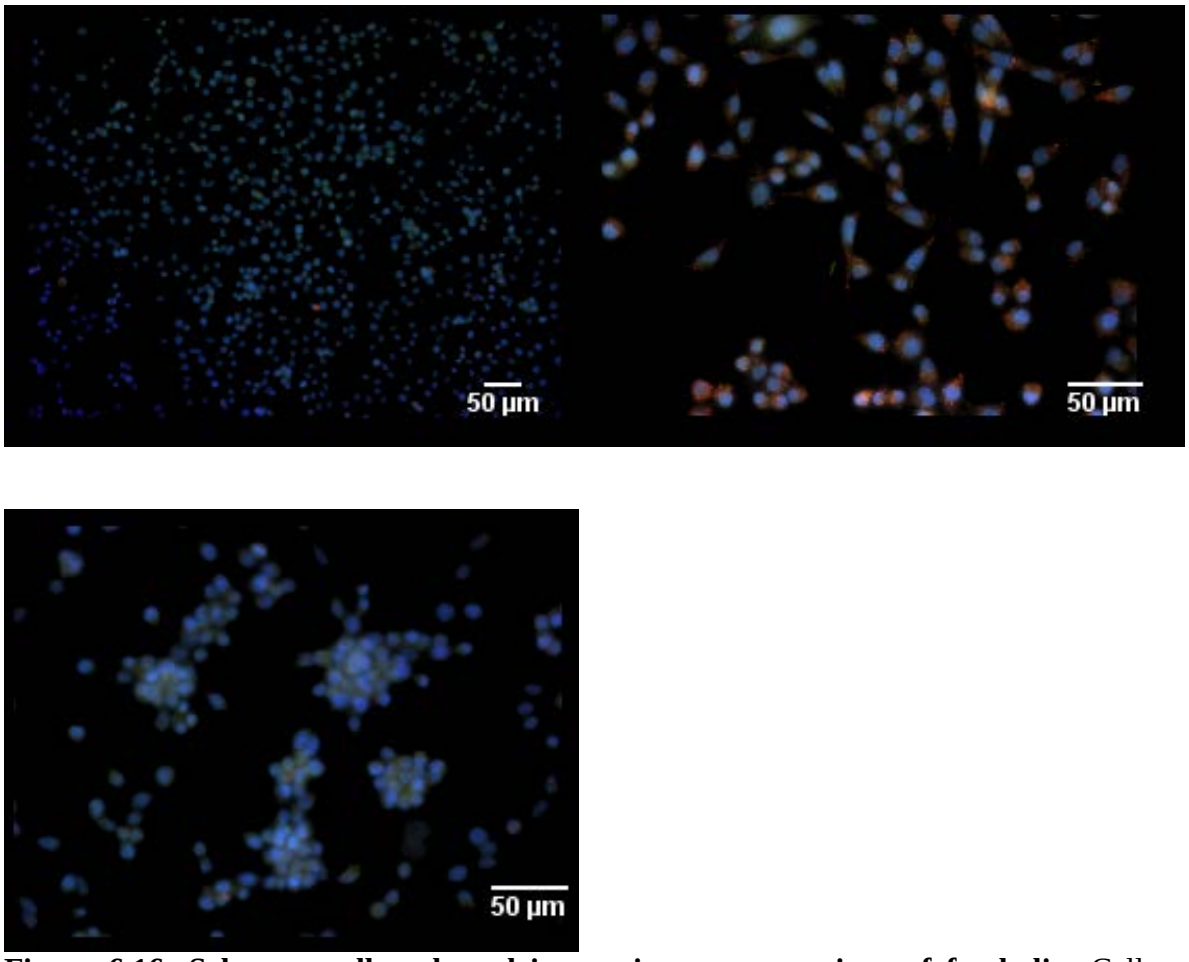

Figure 6.16: Schwann cells cultured in varying concentrations of forskolin. Cells were stained for DAPI (blue), S100 (green), and myelin basic protein (red). Cells were cultured in 0 µM FSK (top left), 0.01 µM FSK (top right) and 10 µM FSK (bottom left). Cells were cultured for 48 hours. The 0 µM FSK cells show evidence of S100 but low amounts of myelin basic protein expression. Cells cultured in 0.01 µM and 10 µM FSK show expression of both S100 and MBP. Cells cultured 10 µM appear to cluster together.

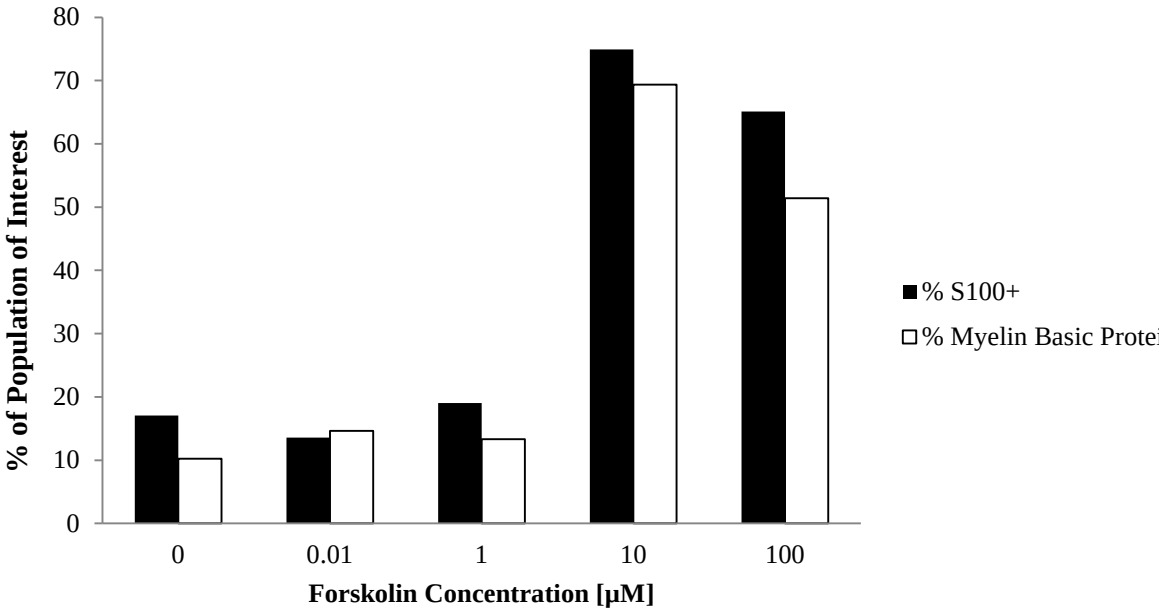

Figure 6.17: Dose-Dependent Myelin Production in Schwann Cells. Schwann cells cultured with varying forskolin concentrations and flow cytometry performed on population. Significant increase occurs at 10µM forskolin where the myelin basic protein increases.

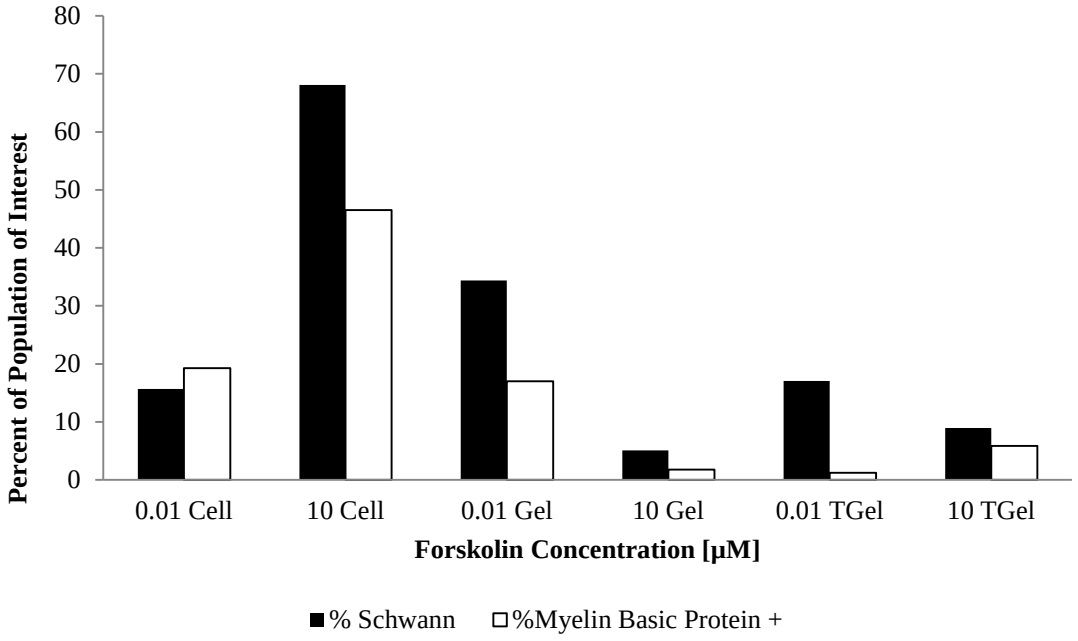

Figure 6.18: Dose-dependent myelin production in Schwann cells cultured within urea-templated hydrogel. Experiment reaffirms the increase that occurs in cell culture however culture within hydrogels appears to depress both the S100 and MBP expression.

6.4.1 Significance and challenges. Diabetes is a global pandemic that is increasingly affecting both the developed and developing world. As countries adapt western lifestyles and eating habits, it is becoming even more important that biomedical technology can compensate for the effects of this disease. High levels of glucose in the blood create an environment where nerves begin to degenerate and wounds in patient lower extremities become prevalent. Poor circulation and high systemic glucose levels contribute to impaired wound healing in diabetic patients. After injury, there is an upregulation of pro-inflammatory cytokine TNF-α [170]. Interestingly, the levels of TNF-α increase over time in diabetic patients, but subside in healthy patients. Research conducted at the Chronic Disease Research Institute at the University of the West Indies, Cave Hill (Barbados) has identified a genetic mutation in a subpopulation of native Barbadians that leads to exorbitant TNF-α production in diabetic wounds. The elevated levels of TNF-α promote sustained inflammation and further hinder wound healing. Schwann cells are responsible for myelinating the axonal trunk and are also adversely affected by the diabetic environment. The levels of myelin markers have been shown to decrease substantially in Schwann cells in the presence of TNF-α [171]. Few studies have been conducted to determine the effect of pro-inflammatory cytokine up regulation for cells cultured *in vitro*. Because inflammation must subside for wound healing to progress, this work investigates the use of anti-inflammatory dosing as a means to promote wound healing *in vitro.* This project addresses the need for an ex vivo culture system to analyze myelin associated protein expression in Schwann cells. The scaffolds with architectural complexity were used to create an *in vitro* replica of the wound environment for therapy

evaluation applications. This work was completed in collaboration with Dr. Clive Landis at the University of the West Indies, Cave Hill in Barbados, West Indies. Experimental supplies were imported to Barbados from the United States.

6.5 Conclusions

The architecturally complex potassium dihydrogen phosphate-templated and urea-templated hydrogels each held great promise for 3D cell culture environments. In both cases hydrogels were successfully rinsed of the templating molecule using deionized water. In each case, this method was effective in achieving molecule concentrations in effluent water that was less than systemic levels in human blood. Experimental results showed that the not templated hydrogels were effective at suppressing differentiation after 3 days in culture. The nestin expression from cells cultured was comparable or slightly higher than the tissue culture controls. The results suggest that after 7 days, culture with hydrogels encourages a relatively higher portion of the population towards differentiation than the cells in suspension.

Cell culture media was be changed every two days to supply the cells with adequate EGF and FGF while in the hydrogels. These growth factors are added to culture media with volumes of 1µL per 10mL of media. The frequency of media changes may have caused more cells to be washed away than would otherwise remain in the scaffold.

Diabetes is a leading cause of neuronal degeneration however few studies have focused on creating an *in vitro* culture system to allow analysis of Schwann cell behavior. Schwann cells are responsible for myelinating the axonal trunk and are affected by the surrounding environment. The purpose of this study is to monitor the in vitro Schwann cell behavior as a result of this therapy. Culture of the Schwann cells with forskolin proved that myelin protein expression could be artificially induced.

6.6 Materials and Methods

6.6.1 Materials. High molecular weight sodium hyaluronate from *Streptococcus equi* of molecular weight 1.6 x 10^6 Da (53747-10G), Glycidyl Methacrylate (779342-500ML), Triethylamine (T0886-1L), Urea (U5378), Potassium Phosphate Monobasic (P5655-500G) and dextran-FITC were all purchased from Sigma Aldrich (St Louis, Mo). Bovine serum albumin (A7906-50G), phosphate buffered saline (P5493-1L), paraformaldehyde, Trion X-100 (X100), Tween 20 and Anti-Myelin Basic Protein (MBP) antibody produced in rabbit (M3821-100UG) were also purchased from Sigma Aldrich (St Louis, MO). Irgacure 2959 was purchased from Ciba Specialty Chemicals/ BASF (Basel, Switzerland). Guanidine hydrochloride (BP178-500), Glycine (BP381-500), Acetone (A181), BD PrecisionGlide 25 gauge needles (305122), Luer-Lok syringes (2018-06) were all purchased from Fisher Scientific. The PhosphoWorks™ Fluorimetric Phosphate Assay Kit *Red Fluorescence (21660) was purchased from AAT Bioquest. The Urea Fluorometric Assay Kit (700620) was purchased from Cayman Chemical. The plate reader used was the BioTek Synergy HT Microplate Reader. Fluval Clearmax (A1348) phosphate remover was purchased from PetCo, Inc. The GRGDLys(FITC) peptide was supplied by American Peptide Company (Product # 316846) with a 96.7% peptide purity. DMEM, high glucose (D1383), fetal bovine serum (16000044) and 0.25% Trypsin-EDTA(1X) Phenol Red (25200114) were purchased from Invitrogen. Flow cytometry was conducted using a Beckman Coulter(R) EPICS XL-MCL Acquisition Flow Cytometer, Class 1 Laser.

6.6.2 Preparation of Methacrylated Hyaluronic Acid. To attach methacrylate groups to hyaluronic acid polymer backbone to allow for photopolymerization, desiccated hyaluronic acid was dissolved in an equal volume mixture of acetone and water overnight at 1%w/v. The HA was allowed to react with glycidyl methacrylate in the presence of triethylamine as a pH stabilizer and intermediate overnight. The polymer was purified in 20 times excess by volume by slowly adding polymer solution to gently stirred acetone and collecting the sample on a glass stirring rod. The polymer was re-dissolved in 50mL deionized water overnight and the polymer purification in acetone was repeated once more. The final sample was flash-frozen sample with liquid nitrogen and lyophilized for 2-4 days, depending on volume. Polymer was stored at -20C until ready for use. For modification with the GRGDLys(FITC) peptide, ECD/NHS chemistry was used to covalently conjugate the peptide to remaining free carboxylic acid groups on the HA. H NMR and RGD-FITC was used to quantify the approximate amount of conjugation.

6.6.3 Synthesis of GMHA not templated and crystal templated hydrogel. A 1%w/v stock solution of I2959 in 10 mM PBS was sonicated for 30-45 minutes to dissolve, taking care to not overly sonicate. Prepare a solution of GMHA of desired concentration 1-5%w/v (10-50mg/mL) with final photoinitiator concentration between 0.05-1% w/v. A 1% stock photoinitiator solution was prepared in 10 mM phosphate-buffered saline and added accordingly to the hydrogel solution to obtain the desired final concentration. The photoinitaitor was heat sonicated for 30-45 minutes to facilitate solubility. For templated hydrogels, crystallizing molecules were dissolved in the pre-hydrogel solution slightly in excess of their 25˚C solubility.

The templating protocol illustrated in **Figure 5.30** was developed using HA as the bulk polymer and the specific mechanical attributes that arose from this macroporous templating method were evaluated. Photocrosslinkable three-dimensionally patterned hyaluronic acid hydrogels were synthesized by preparing 2-5% w/v solution of 20% glycidyl methacrylated hyaluronic acid with photoinitiator concentration varied between 0.3-1% Irgacure 2959. A 1 % stock photoinitiator solution was prepared in 10 mM phosphate-buffered saline and added accordingly to the hydrogel solution to obtain the desired final concentration. The crystallizing molecules were thermally dissolved in the hydrogel solution slightly in excess of their saturation concentration in water at 25^{o}C. The solutions were dissolved at 30-40^{o}C until homogeneous. Warm solutions were injected into silicone molds compressed between two glass slides. Hydrogels were synthesized in 100 µL molds that are 2 mm in depth and 8 mm in diameter. The hydrogels were crosslinked using UV light at 13 mW/cm^2 intensity. Templated hydrogels were soaked in deionized water overnight to remove the porogen, then swollen in 10 mM phosphate-buffered saline. All polymer and hydrogel solutions were filter sterilized using a 0.22µm filter for sterile samples. All additional apparatus were sprayed into a sterile flow hood. Hydrogels were synthesized in sterile conditions and kept sterile until needed for cell culture.

6.6.4 Viability experiments. Hydrogels were suspended in cell culture medium in transwell plates (Corning) to verify the effect of any leaching that may occur from the scaffolds. Schwann cells and fibroblasts were cultured for 48 hours with hydrogels suspended in media and Cell Titer Glo (Invitrogen) assay used to determine viability.

Two luminance readings were taken from each sample and the quantitative values averaged.

6.6.5 Experiment to Determine the Crystal Elution from Templated Hydrogels. The templated hydrogels were individually immersed in 3 mL of deionized water and allowed to equilibrate overnight. The eluted solution was removed and placed in a sealed tube and the water for each hydrogel was replaced with anew 3 mL deionized water, daily for 7 days. For both the urea and potassium dihydrogen phosphate-templated hydrogels, the procedure included with the assay kits were followed. For the urea fluorometric assay kit, the ammonia detector was warmed at 37 C to help its dissolution in ethanol. For urea-templated hydrogels, the dilutions of the eluted solution required to be detected by the assay kit for each day were as follows: Day 1 – $1:10^3$, Day 2 – $1:10^2$, Day 3 – $1:10^2$, Day 4 – $1:10^2$. Days 5-7 were not diluted. For potassium dihydrogen phosphate-templated hydrogels, the required dilutions were as follows: Day 1 – $1:3.5x10^3$, Day 2 – $1:3.5x10^2$, Day 3 – 1:35 (6µL in 210µL). Days 4-7 were not diluted. For the potassium dihydrogen phosphate-templated hydrogels, phosphate free water was created by dialyzing the phosphate remover against approximately 4L of water for a minimum of 7 days. This water was used for the phosphate ion detection. For the potassium dihydrogen phosphate-templated gels, the incubation time used was 1 hour, and the background wells contained 60µL Assay Buffer and 40µL of the sample. A Synergy HT microplate reader was used to analyze the samples

6.6.6 Progenitor cell differentiation and expansion on templated hydrogels. Neural progenitor cells harvested from the forebrain of fetal mice were expanded in neurospheres and used between passage two and five. Not templated hydrogels as well as

those templated with potassium dihydrogen phosphate were seeded with 200,000 cells each. The hydrogels were cultured and imaged at 3 and 7 days. The samples were imaged using confocal microscopy to determine penetration into the gel and viability of the culture population at designated time points. Neural progenitor cells were seeded on potassium dihydrogen phosphate-templated and not templated hydrogel scaffolds and cultured for 3 and 7 days. Cells were cultured in serum-free DMEM F12 HAM media with 1% N2 supplement (Gibco) and 1% penicillin-streptomycin with basic fibroblast growth factor and epidermal growth factor at 1 uL/10 mL media to encourage expansion but not differentiation of the cell population in the experiment. Hydrogels were fixed with 4% paraformaldehyde and stained with primary antibodies against nestin (undifferentiated progenitor cells, Millipore), β-III tubulin (neuronal differentiation, Abcam), GFAP (glial differentiation, Abcam) then fluorescent secondary antibodies prior to imaging. Cells were counterstained with DAPI to label cell nuclei. The cell culture media was gently replaced every two days. Z-stack images were taken using a Zeiss Superscope to visualize the apparent cell types within the hydrogel.

6.6.7 Schwann cell culture at various forskolin concentrations in culture and on hydrogels. Rat Schwann cells were purchased frozen from ATCC (CRL-2765) and cultured in DMEM with 10% (w/v) fetal bovine serum. The cell line was first expanded then cultured in media with bovine pituitary extract and either 0 µM, 0.01 µM or 10 µM forskolin either on tissue culture plastic or on not templated or urea-templated hydrogels at a density of 250,000 cells. The cells were cultured for 48 hours prior to analysis. For imaging, cells were first rinsed in warm PBS then fixed with 4% paraformaldehyde for 15 minutes. The cells were then permeabilized with 0.2% Triton-X100 in PBS for 30

minutes. The cells were then stained with anti-S100 (FITC) at 1:500 for one hour, rinsed three times. Next the cells were incubated with anti-myelin basic protein raised in rabbit at 1:500 for one hour, rinsed three times and incubated with anti-rabbit Alexa 568 for one hour. After rinsing the cell nuclei were stained with DAPI (1:1000). Cells that were in hydrogels were stained at the same concentrations but the antibodies were allowed to incubate overnight followed by 6 hour rinses. For flow cytometry, the cells cultured on tissue culture plastic were incubated with 0.25% Trypsin-ETA to remove the cells. Cells were analyzed at 150,000 cells per vial. The same permeabilization, staining and wash steps took place, however they were conducted on ice and antibodies were incubated for 20 minutes. For flow cytometry, anti-S100(FITC) was used at 1:100, rabbit anti-myelin basic protein primary antibody at 1:100 and anti-rabbit IgG-TRITC produced in goat at 1:100. Hydrogels were digested in hyaluronidase to remove cells prior to flow cytometry.

Chapter Seven. Conclusions

Scaffolds should "facilitate the attachment, migration, proliferation, differentiation and three-dimensional spatial organization of the cell population required for structural and functional replacement of the target organ or tissue" [23]. Hydrogels are no longer comprised of single polymers without architecture. Optimization becomes the most difficult challenge. We are now in a space where we are fine-tuning the optimal morphological layout, length scales and feature sizes along with chemical functionality, desired location and concentration, all with precise expertise. Researchers must ensure transport properties of scaffolds are comparable to native tissue, in order to allow meaningful conclusions to be made. For this reason hydrogels as 3D scaffolds bridge the gap that exists between bench-top experiments of interesting science and practically relevant technology for improved clinical outcome. To this end, sacrificial nucleating crystals were used to create intricate architectures within 3D hydrogel scaffolds.

The original contribution to knowledge was the development of a simple, robust means for allowing substrate driven cellular cues to be translated into a 3D *in vitro* culture environment. The combination of extracellular matrix polymer with geometric architecture allows thorough experimentation of potential therapies. The incorporation of physical architecture into soft polymer scaffolds renders these hydrogels uniquely positioned to be beneficial in a variety of applications. Few other hydrogel systems are able to spatially restrict the polymer component of a hydrogel volume in three dimensions to maximize its effectiveness while remaining gentle enough for use with biopolymers. Hyaluronic acid is a premier substrate because of the relative malleability of its mechanical properties and its natural occurrence in the body. The structure-property

relationship between photoinitiator concentration, UV duration and the mechanical properties has been investigated for the crystal templated samples and the control hydrogels. The system shows promise for a number of applications and this work explores two unique research areas where complex architecture in hydrated polymer networks may prove beneficial, artificial stem cell niches and *in vitro* wound healing.

A limitation of the system is the relative inconsistencies that occur from batch to batch in natural polymers. Indeed this is an attribute because the system possess similar behavior as native tissue, however it can be challenging from an experimental standpoint. Truthfully, most materials demonstrate similar variation; therefore, hydrogel inhomogenieties are an artifact of the nature of the discipline. This is a limitation we cannot overcome. Nevertheless, hydrogels serve as a robust mimic to natural tissue bulk mechanical behavior.

The characterizations of the void regions in the templated hydrogels showed that the polymer portions show agreement with crystal pattern for the urea-templated and potassium dihydrogen phosphate-templated samples. Guanidine-templated and glycine-templated hydrogels, however, only show minor evidence of crystal-templating. These results did confirm that each molecule retained its ability to precipitate crystals in a viscous polymer solution.

While the equilibrium water contents did not change significantly from the not templated control group for the templated hydrogels, except for guanidine, changes in mechanical behavior were evident in both swelling and rheological experiments. The crystal templating was an effective method to restrict the polymer chains in three dimensions. Even more pronounced was the small molecule charge having an effect on

the mesh size. It does make intuitive sense that negatively charged potassium dihydrogen phosphate would have repulsive interactions with HA and therefore highly defined voided regions where the crystals once were. This trend was conserved, largely, in the viscoelastic measurements. The not templated samples had the highest modulus; the modulus for the templated samples followed the same charge-based organization as mesh size. The potassium dihydrogen phosphate-templated samples showed the highest modulus, followed by neutral urea-templated hydrogels and the positive glycine and guanidine-templated hydrogels. The modulus of guanidine-templated hydrogels was higher than that of the zwitterion glycine-templated hydrogels. It was not intuitive that not templated samples had the highest modulus as they had a large mesh size. This is likely attributed to the calculations being for the polymer component and not taking the overall hydrogel void space into consideration. The degradation results showed a different behavior in that while still group by charge, the guanidine-templated and glycine-templated hydrogels degraded slower than the urea-templated samples. It would make sense that the potassium dihydrogen phosphate-templated hydrogels degraded the slowest of all given they had the lowest mesh size.

When investigating structure-property relationships between photoinitiator concentration, duration of UV exposure and mechanical properties as described by swelling, rheological and degradation experiments, there were no trends that were evident among all the sample types. Because each porogen has a unique charge characteristic and crystallizing geometry, these results are not surprising. This is a more fundamental investigation of how well described hydrogel structure-property relationships are either maintained or altered in the presence of small molecules.

Not templated hydrogel controls showed swelling that decreased with increasing UV exposure until 10 minutes, and then increased at 20 minutes. For these samples, data suggests that after an optimal duration of UV exposure, the polymer may begin to degrade as shown by an increase in swell ratio. When comparing photoinitiator concentration and UV duration, the rheological properties indicated that the control group had no relationship between photoinitiator concentration and the storage modulus. Similarly, increasing the photoinitiator concentration did not increase the modulus. It is likely that for these control samples an optimal duration and photoinitiator concentration exists that beyond which the results are negligible or impair the sample mechanical properties.

The uncharged urea molecule did not change the swelling profile from the control group. In both cases the swell ratio decreased until 10 minutes, then increased for samples with 20 minutes of UV exposure. The potassium dihydrogen phosphate-templated and glycine-templated samples both reach a maximum effective crosslinking that does not increase with longer UV durations. Guanidine-templated samples had similar results with swell ratios that were not significantly different for the 2, 5, and 10 minutes then appear to reach a maximum effective crosslinking at 20 minutes UV. The charged species could have potentially provided the polymer with some protection from UV degradation at long exposure times.

Crystal-templating does appear to increase the degradation rate for the hydrogels relative to the control group. The 0.7% I2959 samples with 5 minutes of UV exposure were the most resistant combination to enzymatic degradation for the templated samples, with the exception of potassium dihydrogen phosphate-templated samples.

The diffusion behavior of the samples was crudely characterized as non-Fickian. Current theoretical frameworks do not fully describe the unique collection of simultaneous hydrogel swelling, molecule diffusing and crystal dissolving phenomena in hydrogel samples. To that end, we identified the behaviors as closely as possible to known profiles.

Creating architecture within hydrogel polymer networks has a great deal of potential for a variety of tissue engineering applications. Amorphous hydrogels are useful but fall short of the geometric complexity found in native tissue. This work is a step towards developing scaffolds that specifically replicate the microscopic organization and properties of native tissue. In consideration of future applications, if drug delivery application were of interest, it would be important to determine the effect UV polymerization could potentially have on drug activity. The effect of polymer on hydrocortisone crystallization has already been investigated, however the potential architecture imposed on the polymer and any potential UV-corticosteroid interactions have not been investigated in the system [172].

Stem cell niches are the microenvironments where cells reside in their undifferentiated state. The ability to expand these cultures *in vitro* to create a repository of undifferentiated cells has become an active area of research. Each cell niche has a unique architecture attributed to the tissue in which stem cells reside and thus the microenvironment where these cells may proliferate. To our knowledge, extracellular matrix-derived hydrogels have primarily been used to investigate the influence of microscopic porosity and mechanical signals on cell fate. Complex structured three-dimensional hydrogels have both the three-dimensional culture environment and the

patterned geometry. We hypothesized that the increase in effective bulk porosity and complex microarchitecture would yield an *in vitro* environment that more closely resembles the neural progenitor cell niche. Progenitor cell culture showed neurosphere formation at 7 days as evidenced by the tissue culture control, potassium dihydrogen phosphate-templated hydrogel, and DMSO control results. Templated hydrogels appear to encourage neuronal differentiation, which suggests that the templated hydrogels may support undifferentiated progenitor cells for a length of time shorter than 7 days. In addition, 3 day potassium dihydrogen phosphate-templated hydrogels encourage neurosphere formation sooner than the not templated hydrogels, positive tissue culture control, and the negative DMSO control. As for the not templated gels, insufficient nutrient transport may play a role in the survival of progenitor cells after 7 days.

In considering potential next steps to apply the discussed findings, it would be beneficial to evaluate progenitor cell ability to differentiate after expansion. Progenitor cells must retain their ability to differentiate after expansion for them to be therapeutically relevant. To verify that the cells retain the ability to differentiate after expansion in templated hydrogels, hyaluronidase could be used to digest away the scaffold and recover cells after 7 days in culture. After harvesting, NPCs would then be cultured in a tissue culture polystyrene dish using media with fetal bovine serum (FBS) on tissue culture polystyrene to encourage differentiation and stained to determine phenotype expressions. The templated hydrogels are expected to have increased cell permeability and viability as compared to not templated hydrogels for comparable culture times. Also, because the NPC niche is thought to lie within vascular tissue some research suggests that endothelial cells may provide soluble factors that promote NPC expansion

and prevent differentiation [156, 173]. Therefore, a co-culture system with endothelial cells would be used to encourage further NPC expansion in templated hydrogels. Endothelial cell secretion of soluble factors may enhance the culture environment to more closely imitate the *in vivo* niche.

Appendix A. Supplementary Swell Ratio Data

Table D1: Swell Ratios for Urea Templated and Not Templated Hydrogels [5 mins UV]		
% I 2959	**Architecture**	**Swell Ratio***
0.3	Not Templated	46.71 (3.08, 4)
0.3	Templated	72.92 (9.53, 4)
0.5	Not Templated	31.44 (5.90, 4)
0.5	Templated	51.19 (1.41, 4)
0.7	Not Templated	33.25 (2.87, 4)
0.7	Templated	51.27 (12.40, 4)
1	Not Templated	26.77 (1.53, 4)
1	Templated	47.77 (7.24, 4)
* The first number in parentheses is the standard deviation. The second number is the number of samples.		

Table A1 shows the relationship between the swell ratio urea templated and not templated hydrogels at increasing amounts of photoinitiator concentration. For each concentration, templated hydrogels exhibited a larger swell ratio than not templated hydrogels. This is attributed to the significant increase in void space from crystal templating.

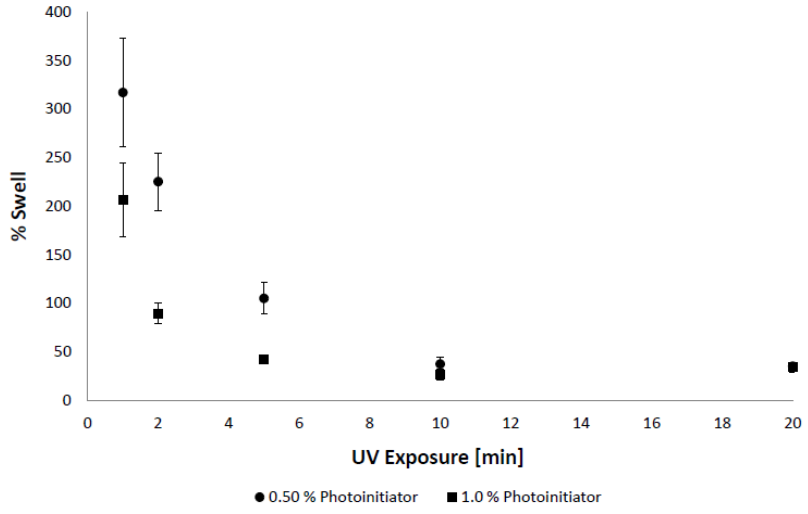

Figure A1: The percent swell of urea-templated hydrogels as a function of UV exposure is shown for two photoinitiator concentrations. Hydrogels were swollen in 10mM PBS.

Urea-templated and not templated hydrogels were compared for the effect the increase in void space as a result of templating has on the swell ratio at increasing UV exposure times as presented in **Figure A1**. The percent swell decreased as UV exposure time increased. The experiment was conducted at two photoinitiator concentrations and the trend was conserved.

Table 14: Percent Swell of Templated Hydrogels

Time	% I2959	% Swell*
1	0.5	316.92 (56.08, 4)
1	1	206.41 (37.65, 4)
2	0.5	225.14 (29.52, 4)
2	1	89.45 (11.10, 4)
5	0.5	104.83 (16.09, 4)
5	1	41.74 (1.10, 4)
10	0.5	37.24 (6.68, 4)
10	1	26.20 (5.20, 4)
20	0.5	34.99 (2.72, 4)
20	1	33.68 (5.37, 4)
The first number in parentheses is the standard deviation. The second number is the number of samples.		

The percent swelling for gels templated with urea porogen is a function of both the extent of crosslinking and the weight percent photoinitiator. The amount of swelling decreases with increased UV exposure and photoinitiator concentration. The templated gels are expected to swell to a higher degree than amorphous hydrogels because of the increase in hydrogel void space. The swell ratio quantity is used to yield an estimate of the void space within the hydrogel.

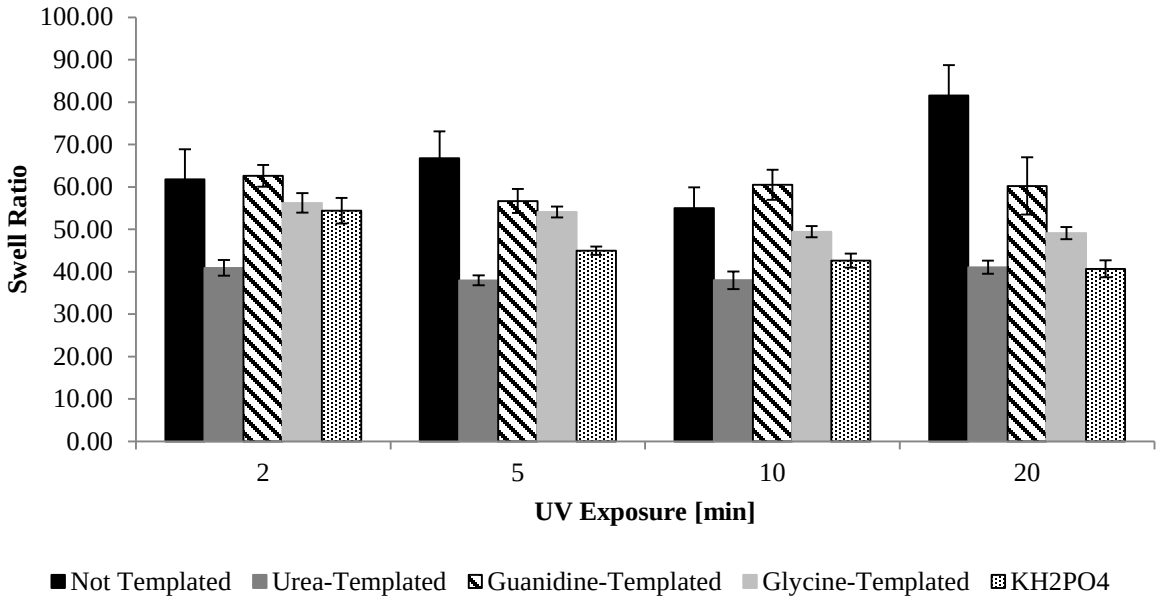

Figure A.1: Effect of UV exposure on templated hydrogels. The figure describes the swell ratio for hydrogels templated by each of the porogens and compared to not templated controls at 2, 5, 10 and 20 minutes.

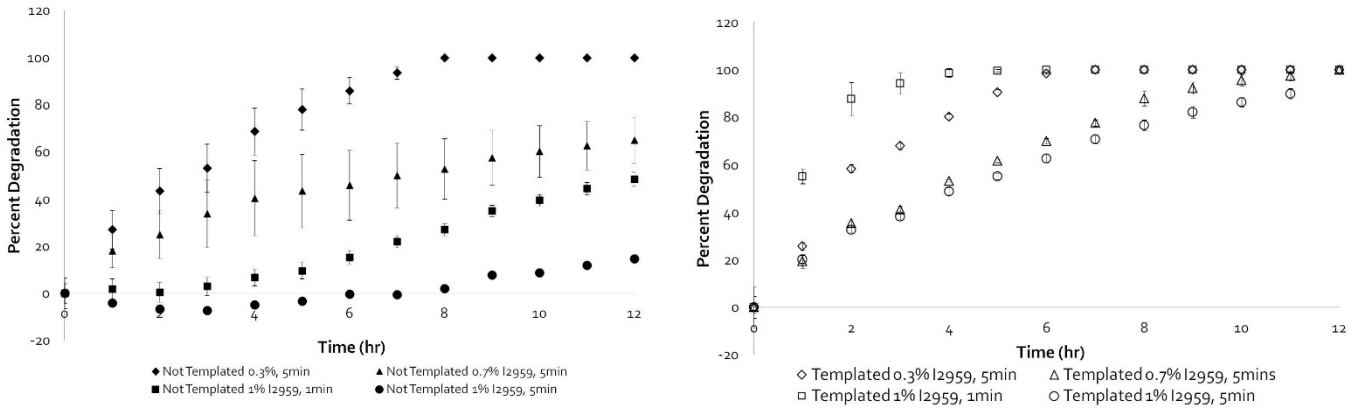

Figure A.2: 12 hour degradation experiment on (A) not templated and (B) template hydrogels at a range of photoinitiator concentrations and UV time exposures. Hydrogels degraded in Hyaluronidase 50 U/ml.

Hydrogels that were templated with urea retained the ability for their degradation behavior to be modulated via photoinitiator concentration and UV exposure. **Figure A3A**

shows the degree of modulation possible with untemplated hydrogels, and **Figure A3B** shows similar results in urea templated hydrogels. The crystal templating does not appear to adversely affect the ability of the polymer component to be modulated. This suggests that crystal templating does not significantly interfere with the photopolymerization process.

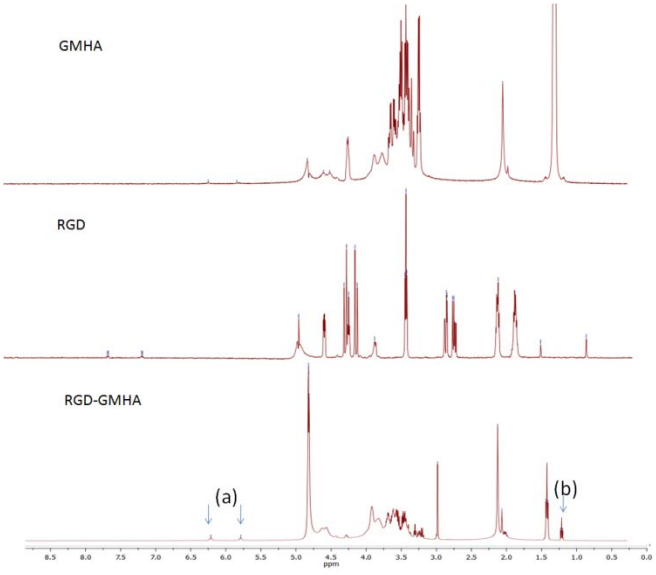

Figure A.3: H NMR data of methacrylated hyaluronic acid (GMHA), RGD peptide and RGD-GMHA. (a) demarcates peaks that are indicative of the –OH and (b) nitrogen groups of RGD present in the RGD-GMHA polymer.

Methacrylated hyaluronic acid was conjugated to an RGD peptide to render the polymer cell adhesive. The ^{1}H NMR results are presented in **Figure A4A.** The doublet at **Figure A4:RGD** at approximately 7.1 and 7.75ppm appears to have shifted to approximately 5.75 and 6.25ppm in **Figure A4:RGD-GMHA** as demarcated by (a).

Appendix B. Strain Sweep Supplementary Data

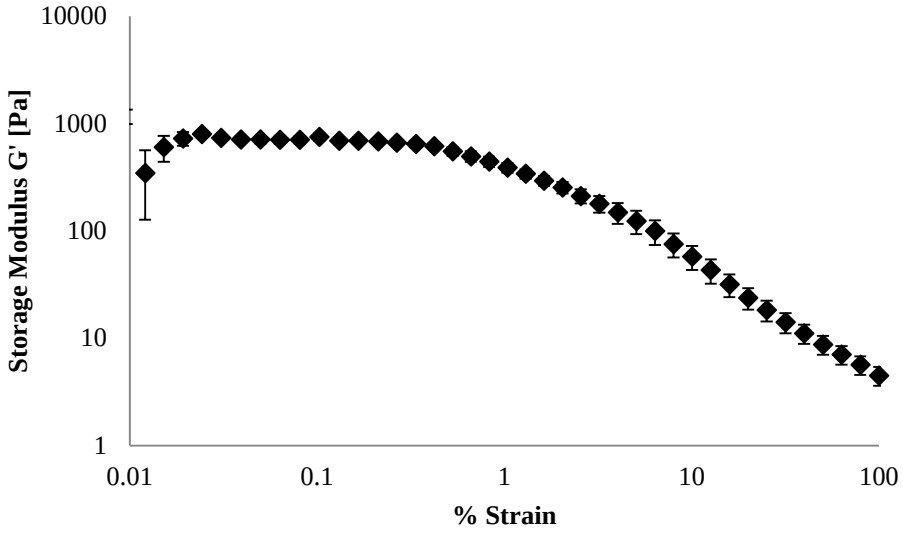

Figure B.1: This strain sweep correlates with frequency sweep in Figure 4.3. Strain sweep for not templated hydrogels synthesized with 0.3% I2959 for 5 minutes of UV exposure. The linear region was approximately 0.03-0.2% strain. Frequency sweeps were conducted at 0.05% strain.

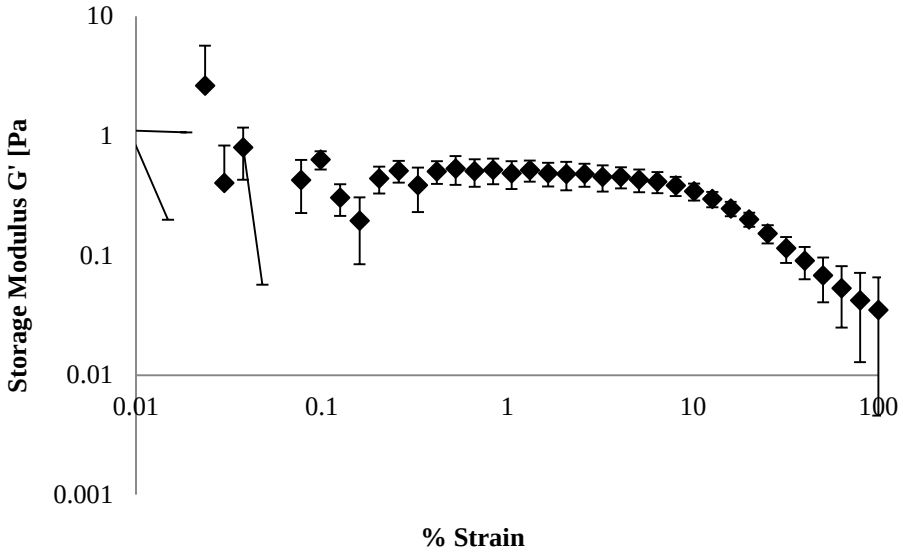

Figure B.2: This strain sweep correlates with frequency sweep in Figure 4.3. Strain sweep for potassium dihydrogen phosphate-templated hydrogels synthesized with 0.3% I2959 for 5 minutes of UV exposure. The linear region was approximately 0.66-4.1% strain. Frequency sweeps were conducted at 0.05% strain.

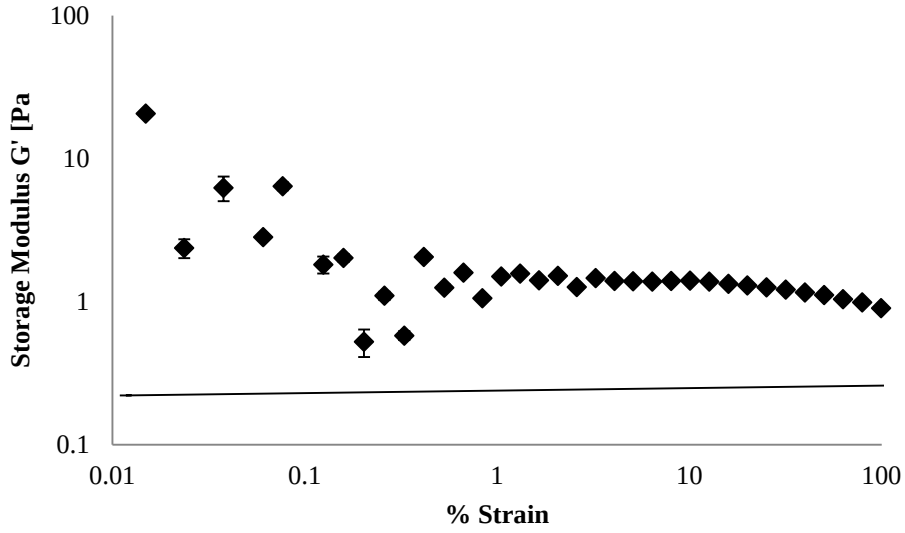

Figure B.3: This strain sweep correlates with frequency sweep in Figure 4.3. Strain sweep for urea-templated hydrogels synthesized with 0.3% I2959 for 5 minutes of UV exposure. The linear region was approximately 3.2-16% strain. Frequency sweeps were conducted at 0.05% strain.

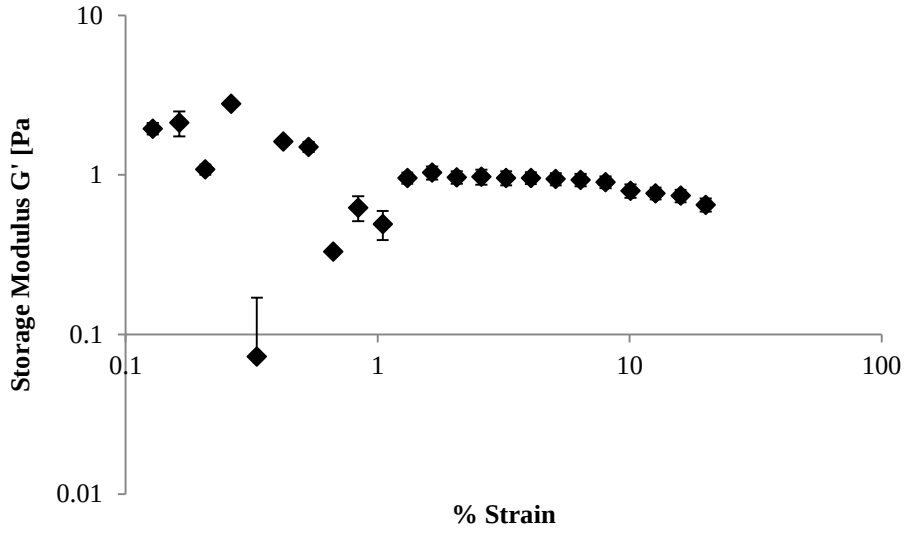

Figure B.4: This strain sweep correlates with frequency sweep in Figure 4.3. Strain sweep for glycine-templated hydrogels synthesized with 0.3% I2959 for 5 minutes of UV exposure. The linear region was approximately 2.1-8.0% strain. Frequency sweeps were conducted at 5% strain.

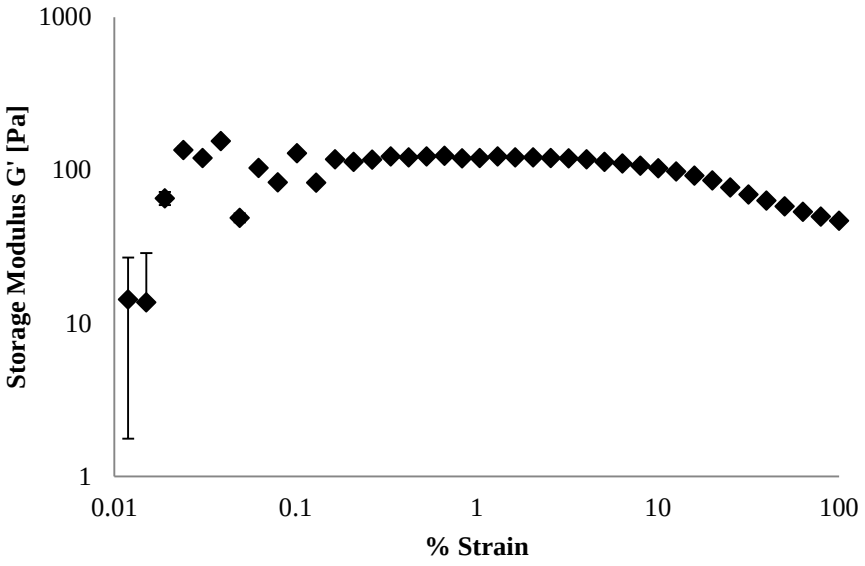

Figure B.5: This not templated hydrogel strain sweep correlates with the frequency sweep in Figure 5.15. Strain sweep for not templated hydrogels synthesized with 0.3% I2959 for 5 minutes of UV exposure. The linear region was approximately 0.83-4.0% strain. Frequency sweeps were conducted at 1% strain.

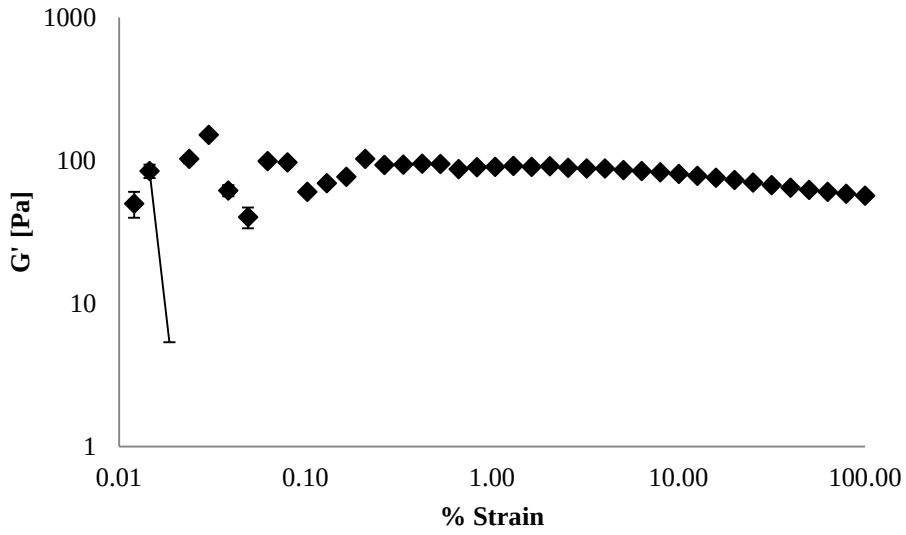

Figure B.6: This not templated hydrogel strain sweep correlates with the frequency sweep in Figure 5.15. Strain sweep for not templated hydrogels synthesized with 1% I2959 for 5 minutes of UV exposure. The linear region was approximately 0.5-3.2% strain. Frequency sweeps were conducted at 0.05% strain.

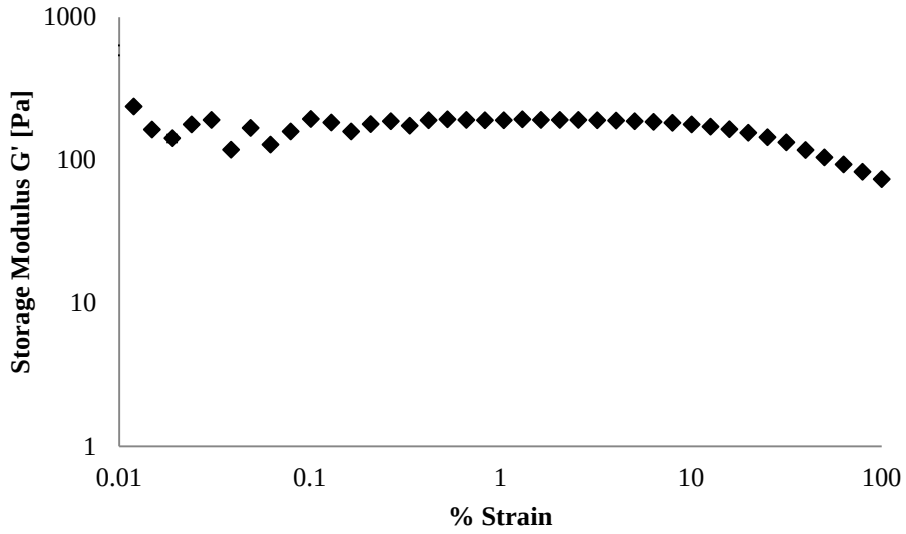

Figure B.7: Strain sweep for not templated hydrogels synthesized with 0.7% I2959 for 5 minutes of UV exposure. The linear region was approximately 0.42-8% strain. Frequency sweeps were conducted at 1% strain.

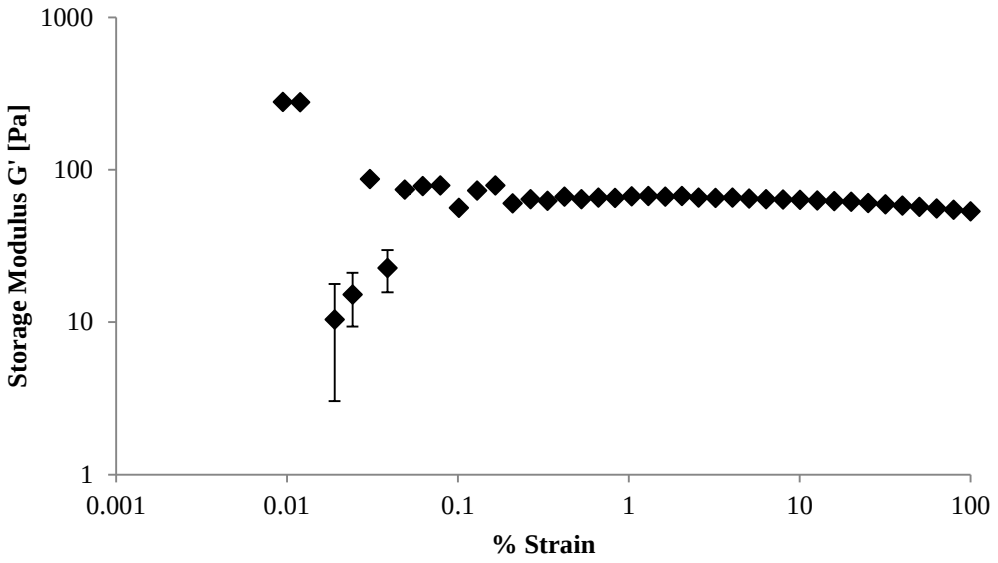

Figure B.8: Strain sweep for not templated hydrogels synthesized with 1% I2959 for 1 minute of UV exposure. The linear region was approximately 0.66-12.6% strain. Frequency sweeps were conducted at 1% strain. This strain sweep relates to **Figure 5.15**.

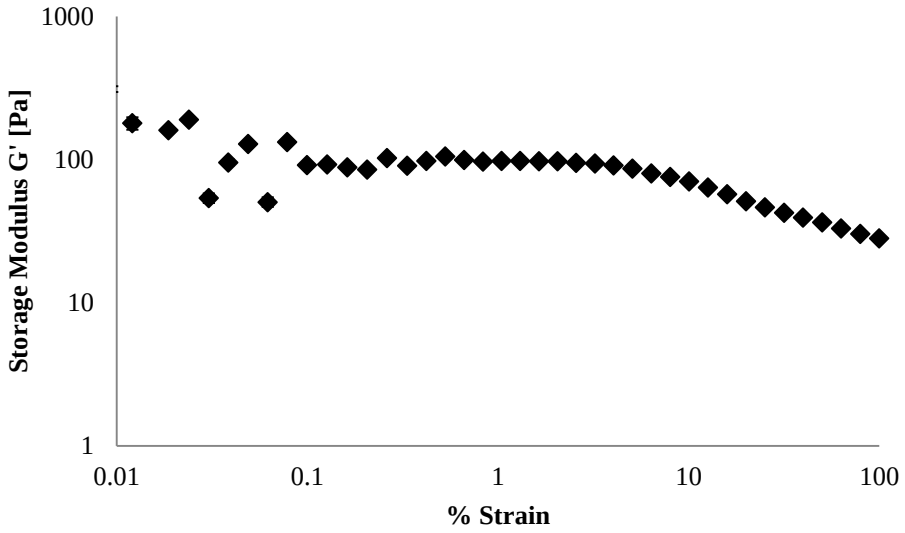

Figure B.9: Strain sweep for potassium dihydrogen phosphate-templated hydrogels. Shows strain sweep for hydrogels synthesized with 0.3% I2959 for 5 minutes of UV exposure. The linear region was approximately 0.8-4.0% strain. Frequency sweeps were conducted at 1% strain. This strain sweep correlates with frequency sweep in **Figure 5.16**.

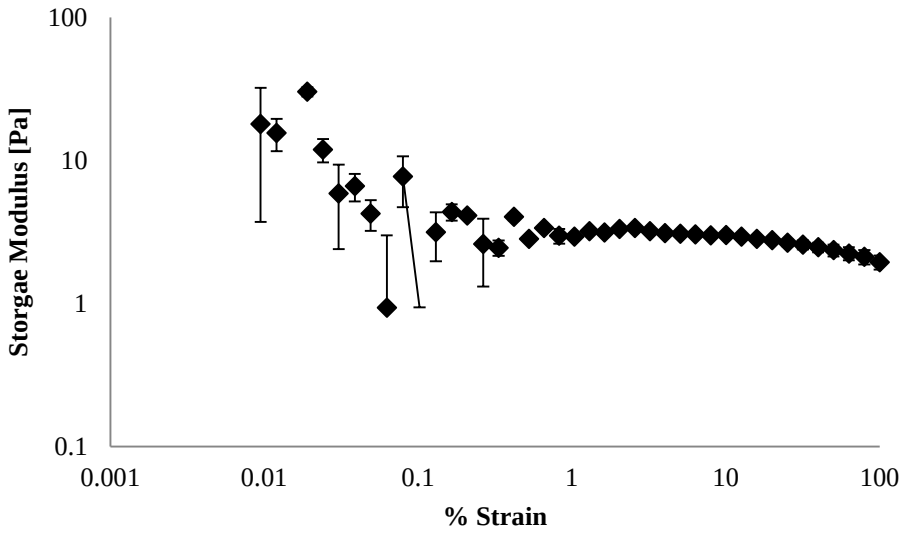

Figure.B.10: Strain sweep for potassium dihydrogen phosphate-templated hydrogels. Strain sweep for 1% I 2959, 2 minute UV exposure. The linear region was approximately 1-8.0 % strain. Frequency sweeps were conducted at 2.5% strain. This strain sweep correlates with frequency sweep in **Figure 5.16**.

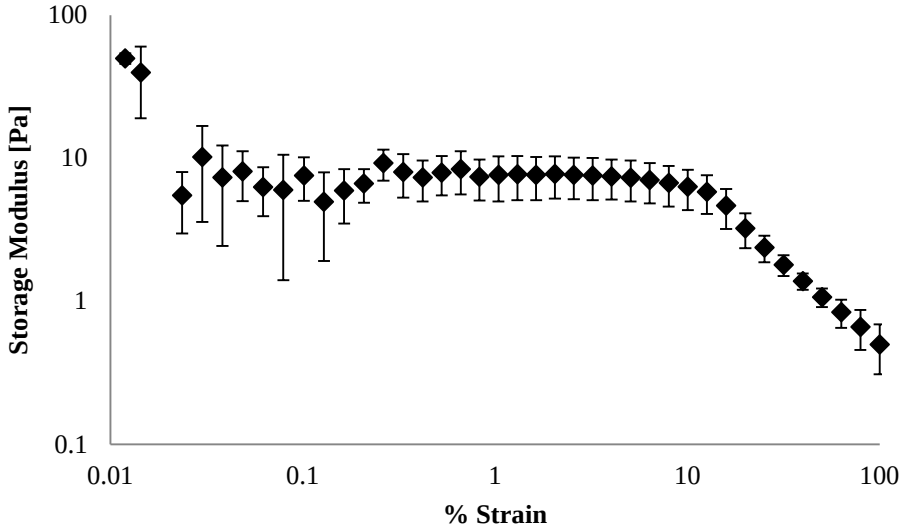

Figure B.11: Strain sweep for potassium dihydrogen phosphate-templated hydrogels. Shows strain sweep for hydrogels synthesized with 1% I2959 for 5 minutes of UV exposure. The linear region was approximately 0.3-8.0% strain. Frequency sweeps were conducted at 2% strain. This strain sweep correlates with frequency sweep in **Figure 5.16**.

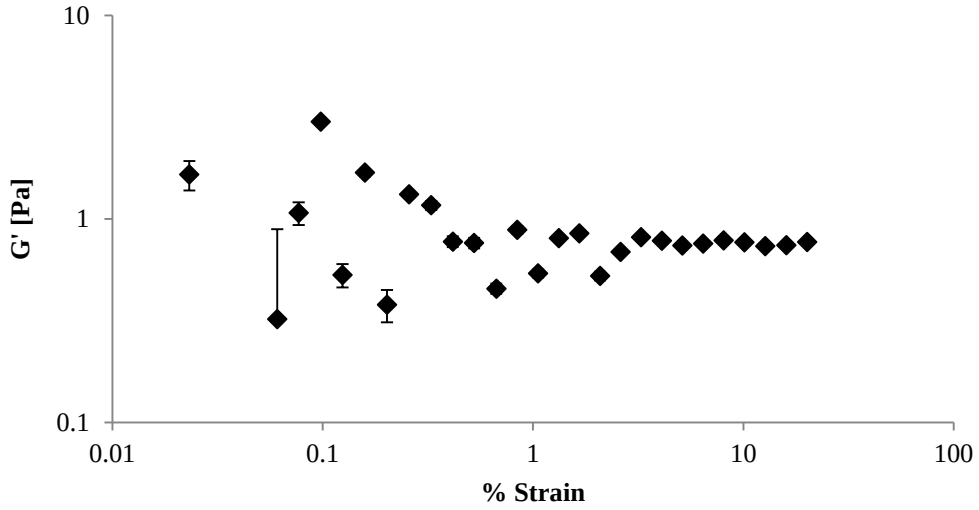

Figure B.12: Strain sweep for guanidine-templated hydrogels synthesized with 0.3% I2959 for 5 minutes of UV exposure. The linear region was approximately 3.3-20% strain. Frequency sweeps were conducted at 0.05% strain. This strain sweep correlates with frequency sweep in **Figure 4.3**.

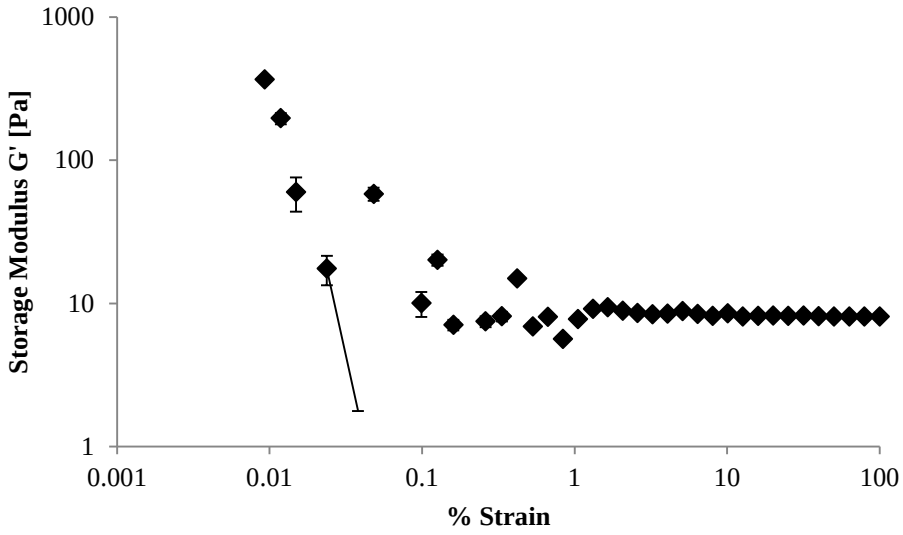

Figure B.13: Strain sweep for guanidine-templated hydrogels synthesized with 0.7% I2959 for 5 minutes of UV exposure. The linear region was approximately 10.1-79.4% strain. Frequency sweeps were conducted at 10% strain. This strain sweep correlates with frequency sweep in **Figure 5.18**.

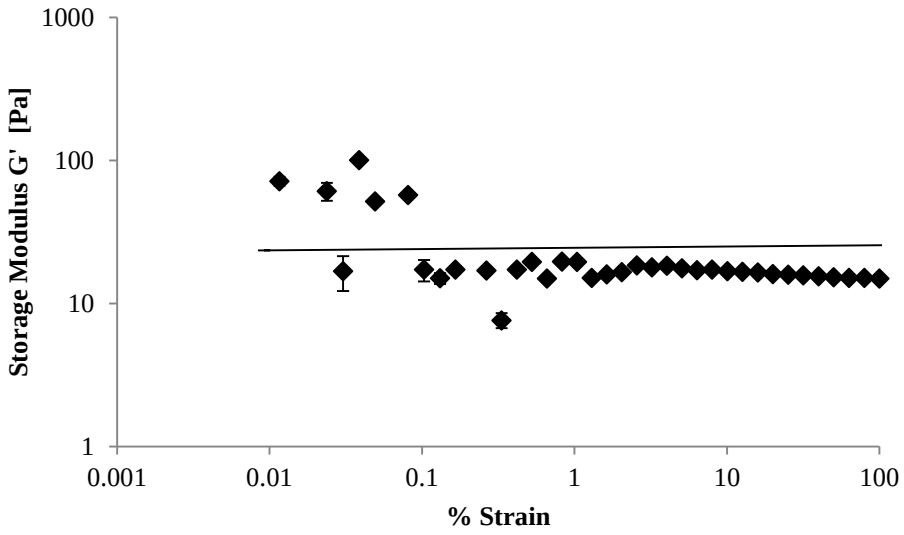

Figure B.14: Strain sweep for glycine-templated hydrogels synthesized with 1% I2959 for 5 minutes of UV exposure. The linear region was approximately 6.4-79.4% strain. Frequency sweeps were conducted at 5% strain. This strain sweep correlates with frequency sweep in **Figure 5.17.**

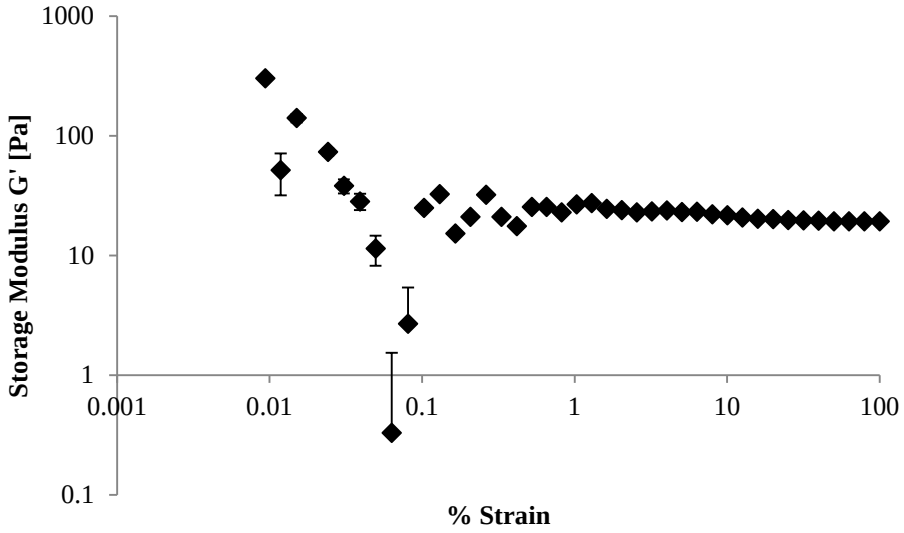

Figure B.15: Strain sweep for glycine-templated hydrogels synthesized with 0.7% I2959 for 1 minute of UV exposure. The linear region was approximately 5.06-20% strain. Frequency sweeps were conducted at 7% strain. This strain sweep correlates with frequency sweep in **Figure 5.17**.

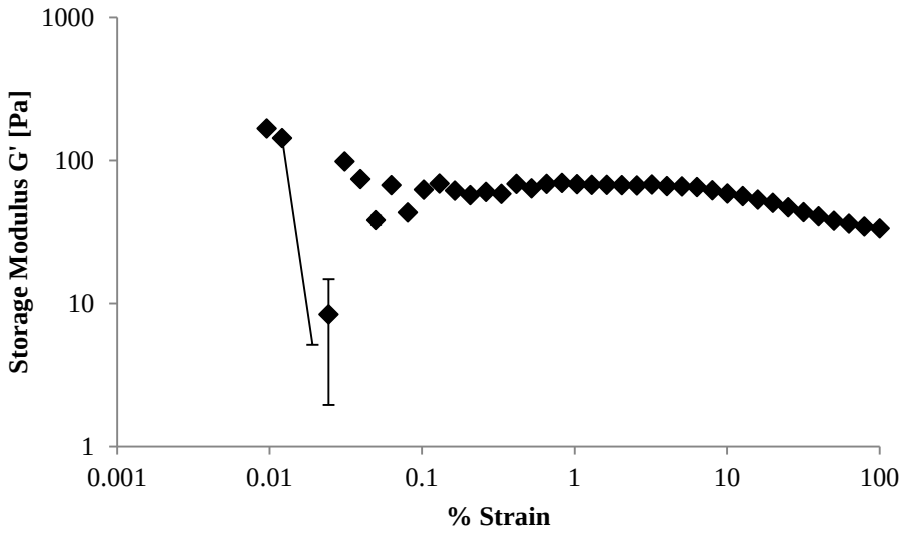

Figure B.16: Strain sweep for glycine-templated hydrogels synthesized with 0.3% I2959 for 5 minutes of UV exposure. The linear region was approximately 1.03-5.06% strain. Frequency sweeps were conducted at 1% strain. This strain sweep correlates with frequency sweep in **Figure 5.17**.

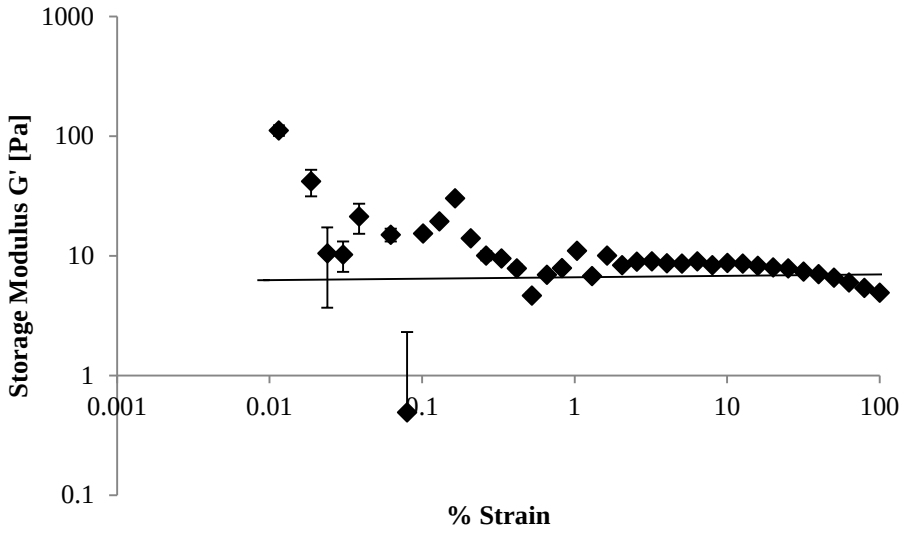

Figure B.17: Strain sweep for urea-templated hydrogels synthesized with 0.3% I2959 for 5 minutes of UV exposure. The linear region was approximately 4.04-6.36% strain. Frequency sweeps were conducted at 7% strain. This strain sweep correlates with frequency sweep in **Figure 4.3.**

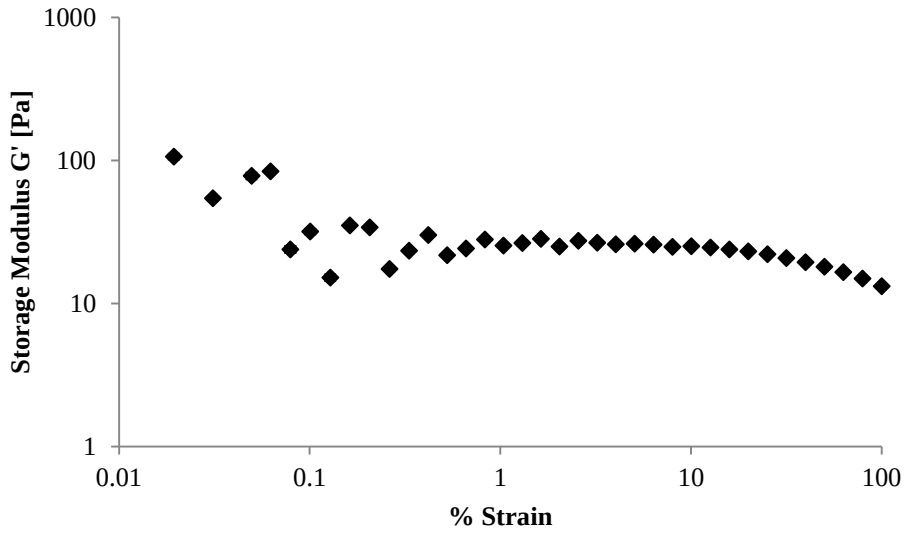

Figure B.18: Strain sweep for urea-templated hydrogels synthesized with 0.7% I2959 for 5 minutes of UV exposure. The linear region was approximately 3.22-5.07% strain. Frequency sweeps were conducted at 3% strain. This strain sweep correlates with frequency sweep in **Figure 5.19.**

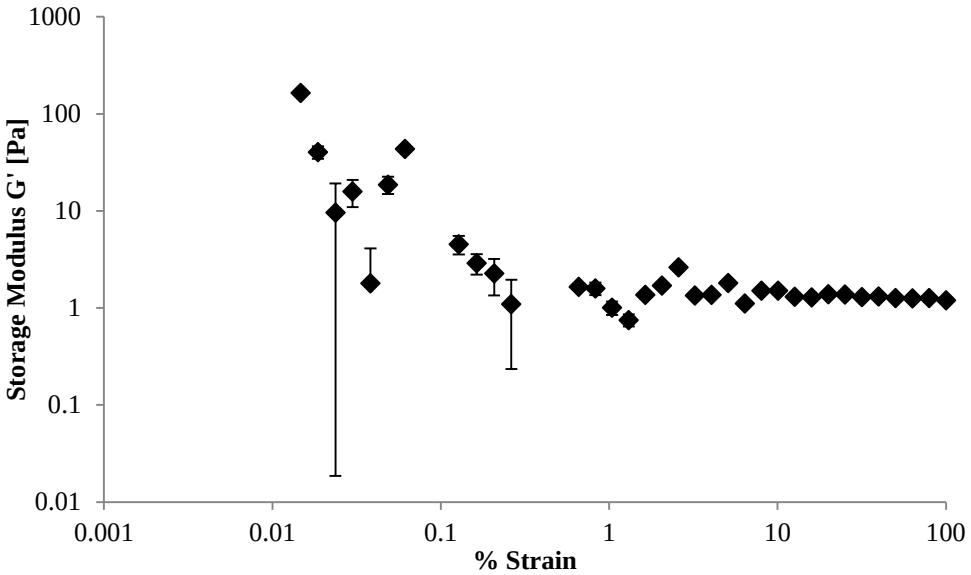

Figure B.19: Strain sweep for urea-templated hydrogels synthesized with 1% I2959 for 1 minute of UV exposure. The linear region was approximately 32-100% strain. Frequency sweeps were conducted at 12% strain. This strain sweep correlates with frequency sweep in **Figure 5.19.**

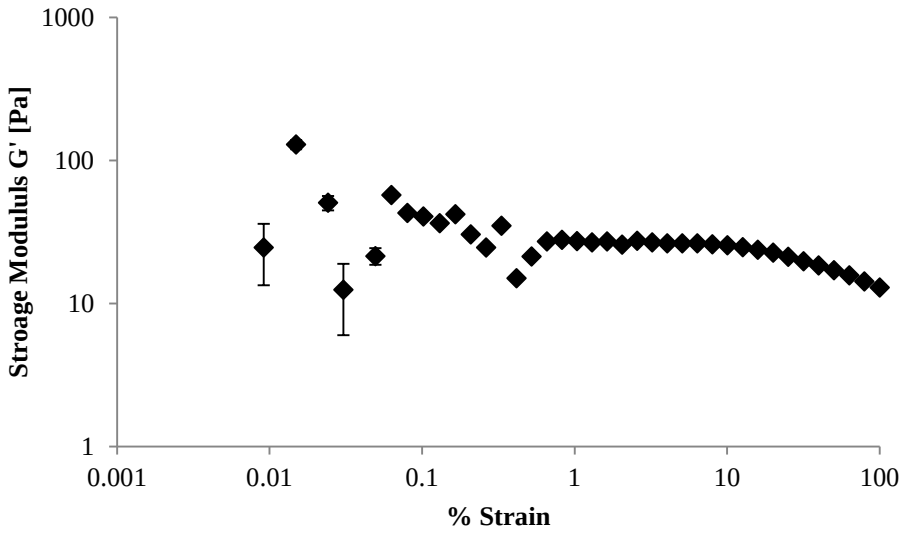

Figure B.20: Strain sweep for urea-templated hydrogels synthesized with 1% I2959 for 5 minutes of UV exposure. The linear region was approximately 4.04-12.6% strain. Frequency sweeps were conducted at 7% strain. This strain sweep correlates with frequency sweep in **Figure 5.19.**

Appendix C. Kinetics Mode of Transport

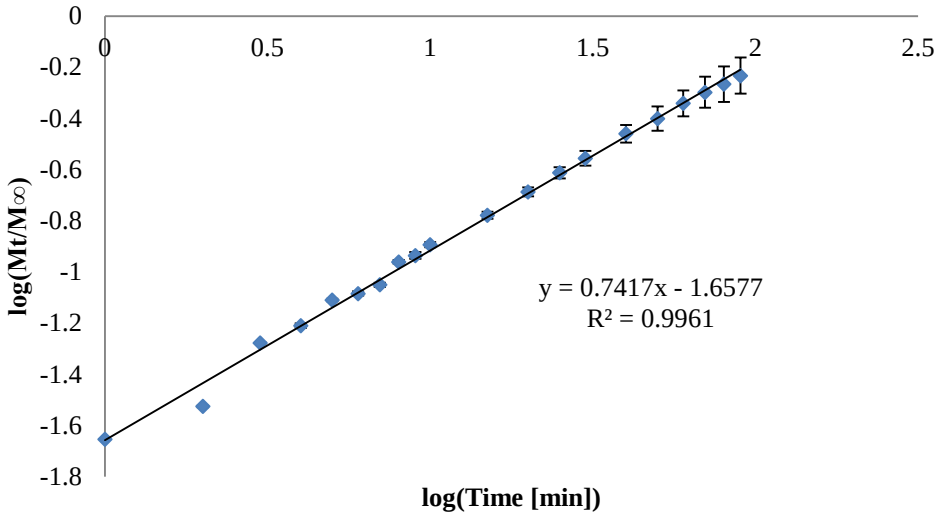

Figure C.1: Mode of transport for not templated hydrogels. Experimental determination of n and k as presented in **Table 10**. n=0.7417 and log k=-1.6577, therefore k=0.02199.

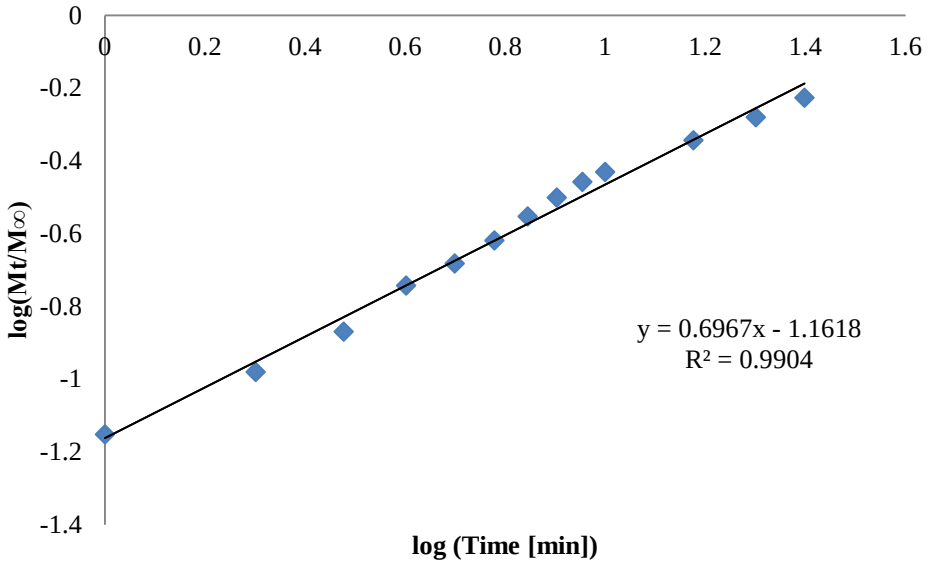

Figure C.2: Mode of transport for glycine-templated hydrogels. Experimental determination of n and k as presented **Table 10**. The n= 0.6967 and log k= -1.1618, therefore k is 0.0689.

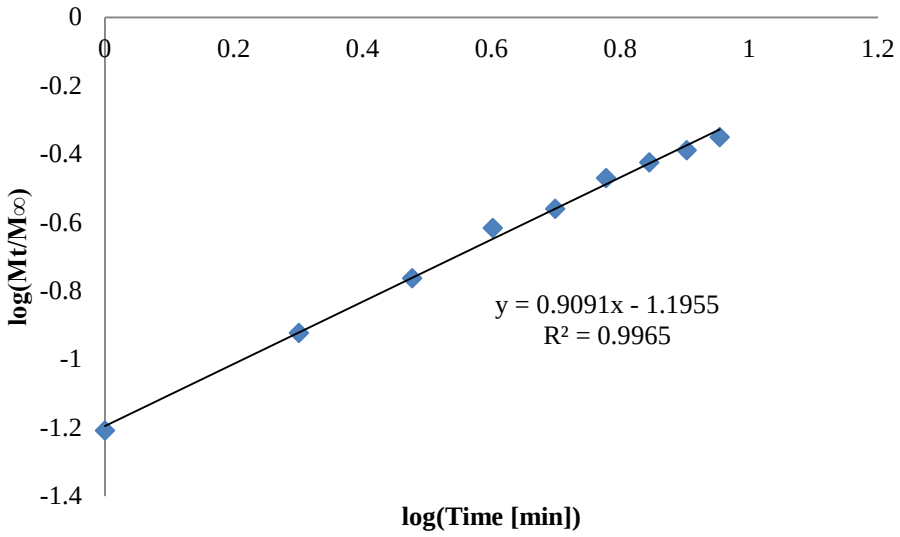

Figure C.3: Mode of transport for urea-templated hydrogels. Experimental determination of n and k as presented in **Table 10**. n= 0.9091 and log k is -1.1955 therefore k is 0.06375.

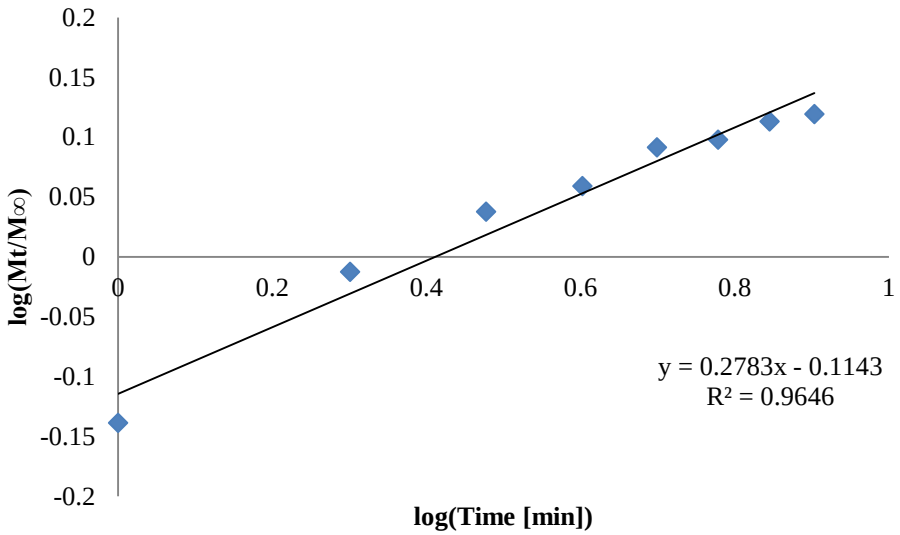

Figure C.4: Mode of transport for guanidine-templated hydrogels. Experimental determination of n and k as presented in **Table 10**. n= 0.2783 and log k is 0.1143 therefore k is 0.7686.

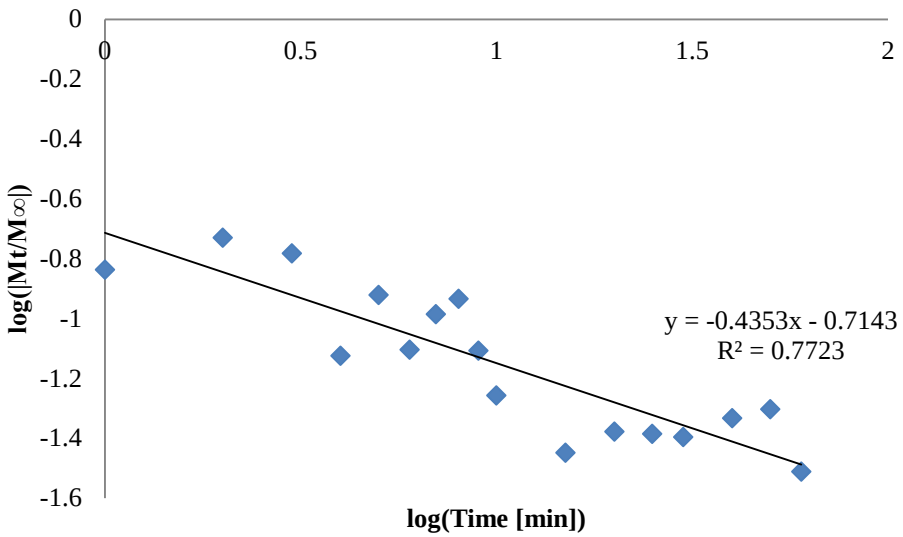

Figure C.5: Mode of transport for potassium dihydrogen phosphate-templated hydrogels. Experimental determination of n and k as presented in **Table 10**. n=-0.4353 and logk=-0.7143, therefore k=0.19306.

Bibliography

1. Zawko, S.A. and C.E. Schmidt, *Crystal templating dendritic pore networks and fibrillar microstructure into hydrogels.* Acta Biomater, 2010. **6**(7): p. 2415-21.
2. Malafaya, P.B., G.A. Silva, and R.L. Reis, *Natural–origin polymers as carriers and scaffolds for biomolecules and cell delivery in tissue engineering applications.* Advanced drug delivery reviews, 2007. **59**(4): p. 207-233.
3. Geckil, H., et al., *Engineering hydrogels as extracellular matrix mimics.* Nanomedicine, 2010. **5**(3): p. 469-484.
4. Baier Leach, J., et al., *Photocrosslinked hyaluronic acid hydrogels: Natural, biodegradable tissue engineering scaffolds.* Biotechnology and Bioengineering, 2003. **82**(5): p. 578-589.
5. Rohindra, D.R., A.V. Nand, and J.R. Khurma, *Swelling properties of chitosan hydrogels.* The South Pacific Journal of Natural and Applied Sciences, 2004. **22**(1): p. 32-35.
6. Kim, S.W., Y.H. Bae, and T. Okano, *Hydrogels: Swelling, Drug Loading, and Release.* Pharmaceutical Research, 1992. **9**(3): p. 283-290.
7. Seo, Y., et al., *Correlation between scaffold in vivo biocompatibility and in vitro cell compatibility using mesenchymal and mononuclear cell cultures.* Cell biology and toxicology, 2009. **25**(5): p. 513-522.
8. Ceballos, D., et al., *Magnetically aligned collagen gel filling a collagen nerve guide improves peripheral nerve regeneration.* Experimental neurology, 1999. **158**(2): p. 290-300.
9. Wong, J.Y., J.B. Leach, and X.Q. Brown, *Balance of chemistry, topography, and mechanics at the cell–biomaterial interface: Issues and challenges for assessing the role of substrate mechanics on cell response.* Surface Science, 2004. **570**(1–2): p. 119-133.
10. Van Vlierberghe, S., P. Dubruel, and E. Schacht, *Biopolymer-Based Hydrogels As Scaffolds for Tissue Engineering Applications: A Review*. Biomacromolecules, 2011. **12**(5): p. 1387-1408.
11. Okay, O., *General properties of hydrogels*, in *Hydrogel Sensors and Actuators*. 2010, Springer. p. 1-14.
12. Slaughter, B.V., et al., *Hydrogels in regenerative medicine.* Advanced Materials, 2009. **21**(32-33): p. 3307-3329.
13. Kim, S.J., S.J. Park, and S.I. Kim, *Swelling behavior of interpenetrating polymer network hydrogels composed of poly (vinyl alcohol) and chitosan.* Reactive and Functional Polymers, 2003. **55**(1): p. 53-59.
14. Zhang, T., et al., *Three-dimensional gelatin and gelatin/hyaluronan hydrogel structures for traumatic brain injury.* Journal of Bioactive and Compatible Polymers, 2007. **22**(1): p. 19-29.
15. Drury, J.L. and D.J. Mooney, *Hydrogels for tissue engineering: scaffold design variables and applications.* Biomaterials, 2003. **24**(24): p. 4337-4351.
16. Stang, F., et al., *Structural parameters of collagen nerve grafts influence peripheral nerve regeneration.* Biomaterials, 2005. **26**(16): p. 3083-91.

17. Ruiz, J., A. Mantecon, and V. Cadiz, *Synthesis and properties of hydrogels from poly (vinyl alcohol) and ethylenediaminetetraacetic dianhydride.* Polymer, 2001. **42**(15): p. 6347-6354.
18. O'Shaughnessy, T.J., H.J. Lin, and W. Ma, *Functional synapse formation among rat cortical neurons grown on three-dimensional collagen gels.* Neuroscience Letters, 2003. **340**(3): p. 169-172.
19. Irons, H.R., et al., *Three-dimensional neural constructs: a novel platform for neurophysiological investigation.* Journal of neural engineering, 2008. **5**(3): p. 333.
20. Souza, G.R., et al., *Three-dimensional tissue culture based on magnetic cell levitation.* Nature nanotechnology, 2010. **5**(4): p. 291-296.
21. Zhang, M. and I.V. Yannas, *Peripheral nerve regeneration*, in *Regenerative Medicine II*. 2005, Springer. p. 67-89.
22. Ratner, B.D., et al., *Biomaterials science: an introduction to materials in medicine.* San Diego, California, 2004: p. 162-164.
23. De Boer, J., et al., *Tissue Engineering*. 2008: Elsevier Science.
24. Manwaring, M.E., J.F. Walsh, and P.A. Tresco, *Contact guidance induced organization of extracellular matrix.* Biomaterials, 2004. **25**(17): p. 3631-8.
25. Ford, M.C., et al., *A macroporous hydrogel for the coculture of neural progenitor and endothelial cells to form functional vascular networks in vivo.* Proc Natl Acad Sci U S A, 2006. **103**(8): p. 2512-7.
26. Burdick, J.A., et al., *An initial investigation of photocurable three-dimensional lactic acid based scaffolds in a critical-sized cranial defect.* Biomaterials, 2003. **24**(9): p. 1613-20.
27. Park, K.M., et al., *RGD-conjugated chitosan-pluronic hydrogels as a cell supported scaffold for articular cartilage regeneration.* Macromolecular Research, 2008. **16**(6): p. 517-523.
28. Gomez, N., et al., *Immobilized nerve growth factor and microtopography have distinct effects on polarization versus axon elongation in hippocampal cells in culture.* Biomaterials, 2007. **28**(2): p. 271-284.
29. Lumelsky, N.L., *Commentary: engineering of tissue healing and regeneration.* Tissue engineering, 2007. **13**(7): p. 1393-1398.
30. Chamberlain, L., et al., *Early peripheral nerve healing in collagen and silicone tube implants: myofibroblasts and the cellular response.* Biomaterials, 1998. **19**(15): p. 1393-1403.
31. *Cross section of one lobe of Mouse Lung. Rotated and Enlarged View of Mouse Lung.* Lung Structure Tour; Available from: http://www.whywasteyourbreath.com/images/4.gif.
32. van Osch, T. ***Measuring capillaries in the brain***. 2006; Available from: http://www.leidenuniv.nl/en/researcharchive/index.php3-c=205.htm.
33. Society, B.R., *Picture Gallery*. 2008.
34. Burdick, J.A. and K.S. Anseth, *Photoencapsulation of osteoblasts in injectable RGD-modified PEG hydrogels for bone tissue engineering.* Biomaterials, 2002. **23**(22): p. 4315-4323.
35. Sannino, A. and M. Madaghiele, *Tuning the porosity of collagen-based scaffolds for use as nerve regenerative templates.* Journal of Cellular Plastics, 2009. **45**(2): p. 137-155.

36. Liao, C.J., et al., *Fabrication of porous biodegradable polymer scaffolds using a solvent merging/particulate leaching method.* Journal of biomedical materials research, 2002. **59**(4): p. 676-681.
37. Nam, Y.S., J.J. Yoon, and T.G. Park, *A novel fabrication method of macroporous biodegradable polymer scaffolds using gas foaming salt as a porogen additive.* Journal of biomedical materials research, 2000. **53**(1): p. 1-7.
38. Nam, Y.S. and T.G. Park, *Biodegradable polymeric microcellular foams by modified thermally induced phase separation method.* Biomaterials, 1999. **20**(19): p. 1783-1790.
39. Nam, Y.S. and T.G. Park, *Porous biodegradable polymeric scaffolds prepared by thermally induced phase separation.* Journal of biomedical materials research, 1999. **47**(1): p. 8-17.
40. Murphy, W.L., et al., *Salt fusion: an approach to improve pore interconnectivity within tissue engineering scaffolds.* Tissue engineering, 2002. **8**(1): p. 43-52.
41. Burdick, J.A. and G.D. Prestwich, *Hyaluronic acid hydrogels for biomedical applications.* Advanced Materials, 2011. **23**(12): p. H41-H56.
42. Cukierman, E., R. Pankov, and K.M. Yamada, *Cell interactions with three-dimensional matrices.* Current Opinion in Cell Biology, 2002. **14**(5): p. 633-640.
43. Cukierman, E., et al., *Taking Cell-Matrix Adhesions to the Third Dimension.* Science, 2001. **294**(5547): p. 1708-1712.
44. Zhang, S., *Beyond the Petri dish.* Nature biotechnology, 2004. **22**(2): p. 151-152.
45. Burdick, J.A., et al., *Controlled degradation and mechanical behavior of photopolymerized hyaluronic acid networks.* Biomacromolecules, 2005. **6**(1): p. 386-391.
46. Langer, R. and N.A. Peppas, *Advances in biomaterials, drug delivery, and bionanotechnology.* AIChE Journal, 2003. **49**(12): p. 2990-3006.
47. Borden, R.C., et al., *Hyaluronic acid hydrogel sustains the delivery of dexamethasone across the round window membrane.* Audiol Neurootol, 2011. **16**(1): p. 1-11.
48. Kogan, G., et al., *Hyaluronic acid: a natural biopolymer with a broad range of biomedical and industrial applications.* Biotechnology letters, 2007. **29**(1): p. 17-25.
49. Ogston, A. and J. Stanier, *The physiological function of hyaluronic acid in synovial fluid; viscous, elastic and lubricant properties.* The Journal of Physiology, 1953. **119**(2-3): p. 244-252.
50. Laurent, T.C., U.B. Laurent, and J.R.E. Fraser, *The structure and function of hyaluronan: an overview.* Immunology and Cell Biology, 1996. **74**(2): p. A1-A7.
51. Bencherif, S.A., et al., *Influence of the degree of methacrylation on hyaluronic acid hydrogels properties.* Biomaterials, 2008. **29**(12): p. 1739-1749.
52. Balazs, E.A., *The Physical Properties of Synovial Fluid and the Special Role~ oi Hyaluronic Acid.* Disorders of the Knee, JB LippincoU Co., Philadelphia, 1974: p. 63-75.
53. Hokputsa, S., et al., *Hydrodynamic characterisation of chemically degraded hyaluronic acid.* Carbohydrate polymers, 2003. **52**(2): p. 111-117.
54. Marković-Housley, Z., et al., *Crystal Structure of Hyaluronidase, a Major Allergen of Bee Venom.* Structure, 2000. **8**(10): p. 1025-1035.
55. Albersdörfer, A. and E. Sackmann, *Swelling behavior and viscoelasticity of ultrathin grafted hyaluronic acid films.* The European Physical Journal B - Condensed Matter and Complex Systems, 1999. **10**(4): p. 663-672.

56. Kim, J., M.J. Yaszemski, and L. Lu, *Three-dimensional porous biodegradable polymeric scaffolds fabricated with biodegradable hydrogel porogens.* Tissue Engineering Part C: Methods, 2009. **15**(4): p. 583-594.
57. Liu, X.Y., et al., *Prediction of crystal growth morphology based on structural analysis of the solid-fluid interface.* Nature, 1995. **374**(6521): p. 342-345.
58. Piana, S., M. Reyhani, and J.D. Gale, *Simulating micrometre-scale crystal growth from solution.* Nature, 2005. **438**(7064): p. 70-73.
59. Ediger, M., P. Harrowell, and L. Yu, *Crystal growth kinetics exhibit a fragility-dependent decoupling from viscosity.* The Journal of chemical physics, 2008. **128**: p. 034709.
60. Lipinski, C.A., *Lead- and drug-like compounds: the rule-of-five revolution.* Drug Discovery Today: Technologies, 2004. **1**(4): p. 337-341.
61. Dougherty, T.J. and M.J. Pucci, *Antibiotic Discovery and Development*. 2012, New York: Springer Science+Business Media, LLC.
62. Joshi, S.C., M.I. Miller, and U. Grenander, *On the geometry and shape of brain sub-manifolds.* International Journal of Pattern Recognition and Artificial Intelligence, 1997. **11**(08): p. 1317-1343.
63. Seidlits, S.K., J.Y. Lee, and C.E. Schmidt, *Nanostructured scaffolds for neural applications.* Nanomedicine (Lond), 2008. **3**(2): p. 183-99.
64. Annabi, N., et al., *Controlling the porosity and microarchitecture of hydrogels for tissue engineering.* Tissue Eng Part B Rev, 2010. **16**(4): p. 371-83.
65. Martinez-Ramos, C., et al., *Channeled scaffolds implanted in adult rat brain.* J Biomed Mater Res A, 2012. **100**(12): p. 3276-86.
66. Wong, D.Y., P.H. Krebsbach, and S.J. Hollister, *Brain cortex regeneration affected by scaffold architectures.* J Neurosurg, 2008. **109**(4): p. 715-22.
67. Tian, W.M., et al., *Hyaluronic acid-poly-D-lysine-based three-dimensional hydrogel for traumatic brain injury.* Tissue Eng, 2005. **11**(3-4): p. 513-25.
68. Friedman, J.A., et al., *Biodegradable polymer grafts for surgical repair of the injured spinal cord.* Neurosurgery, 2002. **51**(3): p. 742-51; discussion 751-2.
69. Stokols, S., et al., *Templated agarose scaffolds support linear axonal regeneration.* Tissue Eng, 2006. **12**(10): p. 2777-87.
70. Wong, D.Y., et al., *Macro-architectures in spinal cord scaffold implants influence regeneration.* J Neurotrauma, 2008. **25**(8): p. 1027-37.
71. MacKay, E.M. and L.L. MacKay, *The concentration of urea in the blood of normal individuals.* Journal of Clinical Investigation, 1927. **4**(2): p. 295.
72. Hendricks, S.B., *The crystal structure of urea and the molecular symmetry of thiourea.* Journal of the American Chemical Society, 1928. **50**(9): p. 2455-2464.
73. Yoshikawa, H.Y., Y. Hosokawa, and H. Masuhara, *Spatial Control of Urea Crystal Growth by Focused Femtosecond Laser Irradiation.* Crystal Growth & Design, 2005. **6**(1): p. 302-305.
74. Francis, P.S., S.W. Lewis, and K.F. Lim, *Analytical methodology for the determination of urea: current practice and future trends.* TrAC trends in analytical chemistry, 2002. **21**(5): p. 389-400.
75. Koncki, R., A. Radomska, and S. Głąb, *Bioanalytical flow-injection system for control of hemodialysis adequacy.* Analytica chimica acta, 2000. **418**(2): p. 213-224.

76. Rho, J.H., *Direct fluorometric determination of urea in urine.* Clinical Chemistry, 1972. **18**(5): p. 476-478.
77. Australia, T.S.o.H.P.o., *Potassium Dihydrogen Phosphate*.
78. Wang, P. and R.W. Giese, *Phosphate-specific fluorescence labeling under aqueous conditions.* Analytical Chemistry, 1993. **65**(23): p. 3518-3520.
79. Velikhov, Y.N., et al., *UV absorption in solutions and crystals of potassium dihydrogen phosphate.* Inorganic materials, 2000. **36**(7): p. 734-738.
80. Gurzadyan, G. and R. Ispiryan, *Two-photon absorption peculiarities of potassium dihydrogen phosphate crystal at 216 nm.* Applied physics letters, 1991. **59**(6): p. 630-631.
81. Albrecht, G. and R.B. Corey, *The crystal structure of glycine.* Journal of the American Chemical Society, 1939. **61**(5): p. 1087-1103.
82. Iitaka, Y., *The crystal structure of [beta]-glycine.* Acta Crystallographica, 1960. **13**(1): p. 35-45.
83. Kayitmazer, A.B., *Effects of polyelectrolyte charge distribution and chain stiffness on polyelectrolyte-protein complex formation and coacervation*. 2007, University of Massachusetts Amherst: Ann Arbor. p. 227.
84. Chandrasekhar, S., M.A. Esterman, and H.A. Hoffman, *Microdetermination of proteoglycans and glycosaminoglycans in the presence of guanidine hydrochloride.* Analytical Biochemistry, 1987. **161**(1): p. 103-108.
85. Hagihara, Y., et al., *Guanidine Hydrochloride-induced Folding of Proteins.* Journal of Molecular Biology, 1993. **231**(2): p. 180-184.
86. Monera, O.D., C.M. Kay, and R.S. Hodges, *Protein denaturation with guanidine hydrochloride or urea provides a different estimate of stability depending on the contributions of electrostatic interactions.* Protein Science, 1994. **3**(11): p. 1984-1991.
87. Horkay, F., A.M. Hecht, and E. Geissler, *Similarities between polyelectrolyte gels and biopolymer solutions.* Journal of Polymer Science Part B: Polymer Physics, 2006. **44**(24): p. 3679-3686.
88. Seidlits, S.K., et al., *The effects of hyaluronic acid hydrogels with tunable mechanical properties on neural progenitor cell differentiation.* Biomaterials, 2010. **31**(14): p. 3930-40.
89. Hersel, U., C. Dahmen, and H. Kessler, *RGD modified polymers: biomaterials for stimulated cell adhesion and beyond.* Biomaterials, 2003. **24**(24): p. 4385-415.
90. Wade, R.J. and J.A. Burdick, *Engineering ECM signals into biomaterials.* Materials Today, 2012. **15**(10): p. 454-459.
91. Calvino-Casilda, V., et al., *Porosity inherent to chemically crosslinked polymers. Poly (N-vinylimidazole) hydrogels.* The Journal of Physical Chemistry B, 2008. **112**(10): p. 2809-2817.
92. Woerly, S., *Hydrogels for neural tissue reconstruction and transplantation.* Biomaterials, 1993. **14**(14): p. 1056-8.
93. Hoffman, A.S., *Hydrogels for biomedical applications.* Advanced Drug Delivery Reviews, 2012. **64, Supplement**(0): p. 18-23.
94. Hoffman, A.S., *Hydrogels for biomedical applications.* Advanced Drug Delivery Reviews, 2002. **54**(1): p. 3-12.

95. Brandl, F., F. Sommer, and A. Goepferich, *Rational design of hydrogels for tissue engineering: Impact of physical factors on cell behavior*. Biomaterials, 2007. **28**(2): p. 134-146.
96. Ananthanarayanan, B., Y. Kim, and S. Kumar, *Elucidating the mechanobiology of malignant brain tumors using a brain matrix-mimetic hyaluronic acid hydrogel platform.* Biomaterials, 2011. **32**(31): p. 7913-7923.
97. Garetz, B.A., et al., *Nonphotochemical, Polarization-Dependent, Laser-Induced Nucleation in Supersaturated Aqueous Urea Solutions.* Physical Review Letters, 1996. **77**(16): p. 3475.
98. Erdemir, D., et al., *Relationship between self-association of glycine molecules in supersaturated solutions and solid state outcome.* Physical review letters, 2007. **99**(11): p. 115702.
99. Lee, F.-M. and L.E. Lahti, *Solubility of urea in water-alcohol mixtures.* Journal of Chemical and Engineering Data, 1972. **17**(3): p. 304-306.
100. Yoshida, H., T. Hatakeyama, and H. Hatakeyama, *Characterization of water in polysaccharide hydrogels by DSC.* Journal of thermal analysis, 1993. **40**(2): p. 483-489.
101. Chan, A.W. and R.J. Neufeld, *Modeling the controllable pH-responsive swelling and pore size of networked alginate based biomaterials.* Biomaterials, 2009. **30**(30): p. 6119-6129.
102. Canal, T. and N.A. Peppas, *Correlation between mesh size and equilibrium degree of swelling of polymeric networks.* Journal of Biomedical Materials Research, 1989. **23**(10): p. 1183-1193.
103. Marsano, E., E. Bianchi, and L. Sciutto, *Microporous thermally sensitive hydrogels based on hydroxypropyl cellulose crosslinked with poly-ethyleneglicol diglycidyl ether.* Polymer, 2003. **44**(22): p. 6835-6841.
104. Lutolf, M. and J. Hubbell, *Synthesis and physicochemical characterization of end-linked poly (ethylene glycol)-co-peptide hydrogels formed by Michael-type addition.* Biomacromolecules, 2003. **4**(3): p. 713-722.
105. Marsano, E., et al., *Behaviour of gels based on (hydroxypropyl) cellulose methacrylate.* Polymer, 2000. **41**(21): p. 7691-7698.
106. Cleland, R.L., *Ionic polysaccharides. IV. Free-rotation dimensions for disaccharide polymers. Comparison with experiment for hyaluronic acid.* Biopolymers, 1970. **9**(7): p. 811-824.
107. Instruments, T., *Understanding Rheology of Structured Fluids*.
108. Instruments, T., *ARES Rheometer: Rheometrics Series User Manual*. 2003, Waters LLC: 109 Lukens Drive, New Castle, DE 19720.
109. Teller, S.S., et al., *High-Frequency Viscoelastic Shear Properties of Vocal Fold Tissues: Implications for Vocal Fold Tissue Engineering.* Tissue Engineering Part A, 2012. **18**(19-20): p. 2008-2019.
110. Basdogan, C., *Dynamic Material Properties of Human and Animal Livers*, in *Soft Tissue Biomechanical Modeling for Computer Assisted Surgery*, Y. Payan, Editor. 2012, Springer Berlin Heidelberg. p. 229-241.
111. Nayar, V.T., et al., *Elastic and viscoelastic characterization of agar.* Journal of the Mechanical Behavior of Biomedical Materials, 2012. **7**(0): p. 60-68.

112. Menzel, E.J. and C. Farr, *Hyaluronidase and its substrate hyaluronan: biochemistry, biological activities and therapeutic uses.* Cancer Letters, 1998. **131**(1): p. 3-11.
113. Whang, K., et al., *Engineering bone regeneration with bioabsorbable scaffolds with novel microarchitecture.* Tissue Eng, 1999. **5**(1): p. 35-51.
114. De Kee, D., Q. Liu, and J. Hinestroza, *Viscoelastic (Non-Fickian) Diffusion.* The Canadian Journal of Chemical Engineering, 2005. **83**(6): p. 913-929.
115. Guo, C., D. De Kee, and B. Harrison, *Effect of molecular structure on diffusion of organic solvents in rubbers.* Chemical engineering science, 1992. **47**(7): p. 1525-1532.
116. Hedenqvist, M., et al., *Diffusion of small-molecule penetrants in polyethylene: free volume and morphology.* Polymer, 1996. **37**(14): p. 2887-2902.
117. Unnikrishnan, G. and S. Thomas, *Molecular transport of benzene and methyl-substituted benzenes into filled natural rubber sheets.* Journal of applied polymer science, 1996. **60**(7): p. 963-970.
118. Gorrasi, G., et al., *Transport properties of organic vapors in nanocomposites of isotactic polypropylene.* Journal of Polymer Science Part B: Polymer Physics, 2003. **41**(15): p. 1798-1805.
119. Beier, B., et al., *Toward a Continuous Intravascular Glucose Monitoring System.* Sensors, 2010. **11**(1): p. 409-424.
120. Okay, O. and S.B. Sariisik, *Swelling behavior of poly (acrylamide-co-sodium acrylate) hydrogels in aqueous salt solutions: theory versus experiments.* European Polymer Journal, 2000. **36**(2): p. 393-399.
121. Khinnavar, R.S. and T.M. Aminabhavi, *Diffusion and sorption of organic liquids through polymer membranes. VI. Polyurethane, neoprene, natural rubber, nitrile butadiene rubber, styrene butadiene rubber, and ethylene propylene diene terpolymer versus organic esters.* Journal of applied polymer science, 1992. **46**(5): p. 909-920.
122. Satish, C., K. Satish, and H. Shivakumar, *Hydrogels as controlled drug delivery systems: Synthesis, crosslinking, water and drug transport mechanism.* Indian journal of pharmaceutical sciences, 2006. **68**(2): p. 133.
123. Annabi, N., et al., *Controlling the porosity and microarchitecture of hydrogels for tissue engineering.* Tissue Engineering Part B: Reviews, 2010. **16**(4): p. 371-383.
124. Vidaurre, A., I. Castilla Cortazar, and J.M. Meseguer. *Water sorption properties of poly (ethyl acrylate-co-hydroxyethyl methacrylate) macroporous hydrogels*. in *Macromolecular Symposia*. 2003. Wiley Online Library.
125. Crank, J., *The mathematics of diffusion*. 1979: Oxford university press.
126. Johansson, J.Å., et al., *Build-up of collagen and hyaluronic acid polyelectrolyte multilayers.* Biomacromolecules, 2005. **6**(3): p. 1353-1359.
127. Lee, S.B., et al., *Preparation and properties of polyelectrolyte complex sponges composed of hyaluronic acid and chitosan and their biological behaviors.* Journal of applied polymer science, 2003. **90**(4): p. 925-932.
128. Shah, A.A., et al., *Biological degradation of plastics: A comprehensive review*. Biotechnology Advances, 2008. **26**(3): p. 246-265.
129. Gijsman, P., G. Meijers, and G. Vitarelli, *Comparison of the UV-degradation chemistry of polypropylene, polyethylene, polyamide 6 and polybutylene terephthalate.* Polymer Degradation and Stability, 1999. **65**(3): p. 433-441.

130. Nagai, N., T. Matsunobe, and T. Imai, *Infrared analysis of depth profiles in UV-photochemical degradation of polymers.* Polymer Degradation and Stability, 2005. **88**(2): p. 224-233.
131. Pettikiriarachchi, J.T., et al., *Biomaterials for brain tissue engineering.* Australian Journal of Chemistry, 2010. **63**(8): p. 1143-1154.
132. De Souza, S.W. and J. Dobbing, *Cerebral edema in developing brain: I. Normal water and cation content in developing rat brain and postmortem changes.* Experimental Neurology, 1971. **32**(3): p. 431-438.
133. Grasso, G., et al., *Does administration of recombinant human erythropoietin attenuate the increase of S-100 protein observed in cerebrospinal fluid after experimental subarachnoid hemorrhage?* Journal of neurosurgery, 2002. **96**(3): p. 565-570.
134. CLARKE, N.E. and R.E. MOSHER, *The water and electrolyte content of the human heart in congestive heart failure with and without digitalization.* Circulation, 1952. **5**(6): p. 907-914.
135. O'Dochartaigh, C., et al., *Lung water content is not increased in chronic cardiac failure.* Heart, 2005. **91**(11): p. 1473-1474.
136. Aurand, E.R., et al., *Building Biocompatible Hydrogels for Tissue Engineering of the Brain and Spinal Cord.* Journal of Functional Biomaterials, 2012. **3**(4): p. 839-863.
137. Zhong, J., et al., *Hydrogel matrix to support stem cell survival after brain transplantation in stroke.* Neurorehabilitation and neural repair, 2010. **24**(7): p. 636-644.
138. Dellatore, S.M., A.S. Garcia, and W.M. Miller, *Mimicking stem cell niches to increase stem cell expansion.* Current opinion in biotechnology, 2008. **19**(5): p. 534-540.
139. Moore, K.A. and I.R. Lemischka, *Stem cells and their niches.* Science, 2006. **311**(5769): p. 1880-1885.
140. Lutolf, M.P. and H.M. Blau, *Artificial stem cell niches.* Advanced Materials, 2009. **21**(32-33): p. 3255-3268.
141. Guilak, F., et al., *Control of stem cell fate by physical interactions with the extracellular matrix.* Cell stem cell, 2009. **5**(1): p. 17.
142. Martínez, E., et al., *Stem cell differentiation by functionalized micro-and nanostructured surfaces.* Nanomedicine, 2009. **4**(1): p. 65-82.
143. Murtuza, B., J.W. Nichol, and A. Khademhosseini, *Micro-and nanoscale control of the cardiac stem cell niche for tissue fabrication.* Tissue Engineering Part B: Reviews, 2009. **15**(4): p. 443-454.
144. Zahir, T., et al., *Neural stem/progenitor cells differentiate in vitro to neurons by the combined action of dibutyryl cAMP and interferon-γ.* Stem cells and development, 2009. **18**(10): p. 1423-1432.
145. Recknor, J.B., D.S. Sakaguchi, and S.K. Mallapragada, *Directed growth and selective differentiation of neural progenitor cells on micropatterned polymer substrates.* Biomaterials, 2006. **27**(22): p. 4098-4108.
146. Seidlits, S.K., et al., *The effects of hyaluronic acid hydrogels with tunable mechanical properties on neural progenitor cell differentiation.* Biomaterials, 2010. **31**(14): p. 3930-3940.
147. Saha, K., et al., *Substrate modulus directs neural stem cell behavior.* Biophysical journal, 2008. **95**(9): p. 4426-4438.

148. Zhang, T., et al., *Three-dimensional gelatin and gelatin/hyaluronan hydrogel structures for traumatic brain injury.* Journal of bioactive and compatible polymers, 2007. **22**(1): p. 19-29.
149. Elias, P.Z. and M. Spector, *Characterization of a bilateral penetrating brain injury in rats and evaluation of a collagen biomaterial for potential treatment.* Journal of Neurotrauma, 2012. **29**(11): p. 2086-2102.
150. Elias, P.Z. and M. Spector, *Treatment of penetrating brain injury in a rat model using collagen scaffolds incorporating soluble Nogo receptor.* Journal of Tissue Engineering and Regenerative Medicine, 2012: p. n/a-n/a.
151. Elias, P.Z. and M. Spector, *Viscoelastic characterization of rat cerebral cortex and type I collagen scaffolds for central nervous system tissue engineering.* Journal of the Mechanical Behavior of Biomedical Materials, 2012. **12**(0): p. 63-73.
152. Nisbet, D.R., et al., *Neural tissue engineering of the CNS using hydrogels.* Journal of Biomedical Materials Research Part B: Applied Biomaterials, 2008. **87**(1): p. 251-263.
153. Woerly, S., *Hydrogels for neural tissue reconstruction and transplantation.* Biomaterials, 1993. **14**(14): p. 1056-1058.
154. Whang, K., et al., *Engineering bone regeneration with bioabsorbable scaffolds with novel microarchitecture.* Tissue engineering, 1999. **5**(1): p. 35-51.
155. Cui, F., et al., *Hyaluronic acid hydrogel immobilized with RGD peptides for brain tissue engineering.* Journal of Materials Science: Materials in Medicine, 2006. **17**(12): p. 1393-1401.
156. Shen, Q., et al., *Endothelial cells stimulate self-renewal and expand neurogenesis of neural stem cells.* Science, 2004. **304**(5675): p. 1338-1340.
157. Ren, Y.-J., et al., *Hyaluronic acid/polylysine hydrogel as a transfer system for transplantation of neural stem cells.* Journal of Bioactive and Compatible Polymers, 2009. **24**(1): p. 56-62.
158. Ahmed, I., et al., *Three-Dimensional Nanofibrillar Surfaces Promote Self-Renewal in Mouse Embryonic Stem Cells.* Stem Cells, 2006. **24**(2): p. 426-433.
159. Billiet, T., et al., *A review of trends and limitations in hydrogel-rapid prototyping for tissue engineering.* Biomaterials, 2012. **33**(26): p. 6020-6041.
160. Engler, A.J., et al., *Matrix Elasticity Directs Stem Cell Lineage Specification.* Cell, 2006. **126**(4): p. 677-689.
161. Toepke, M.W., et al., *Characterization of Thiol-Ene Crosslinked PEG Hydrogels.* Macromolecular Materials and Engineering, 2012.
162. Georges, P.C., et al., *Matrices with compliance comparable to that of brain tissue select neuronal over glial growth in mixed cortical cultures.* Biophysical journal, 2006. **90**(8): p. 3012-3018.
163. Perale, G., et al., *Hydrogel for cell housing in the brain and in the spinal cord.* The International journal of artificial organs, 2011. **34**(3): p. 295.
164. FT, F. and D.M. III, *Manual of Laboratory and Diagnostic Tests*. 2009, Lippincott, Williams and Wilkins: Philadelphia.
165. Doillon, C.J. and F.H. Silver, *Collagen-based wound dressing: Effects of hyaluronic acid and firponectin on wound healing.* Biomaterials, 1986. **7**(1): p. 3-8.
166. Deftereos, J. and B. Mann, *PEG Hydrogels as Nerve Guidance Materials.* Keck Graduate Institute of Applied Life Sciences.

167. Garbay, B., et al., *Myelin synthesis in the peripheral nervous system.* Progress in neurobiology, 2000. **61**(3): p. 267-304.
168. Atala, A., et al., *Wound Healing Versus Regeneration: Role of the Tissue Environment in Regenerative Medicine.* MRS bulletin, 2010. **35**(08): p. 597-606.
169. Biernaskie, J., et al., *Skin-derived precursors generate myelinating Schwann cells that promote remyelination and functional recovery after contusion spinal cord injury.* The Journal of Neuroscience, 2007. **27**(36): p. 9545-9559.
170. Wagner, R. and R.R. Myers, *Schwann cells produce tumor necrosis factor alpha: expression in injured and non-injured nerves.* Neuroscience, 1996. **73**(3): p. 625-629.
171. Chandross, K.J., *Nerve injury and inflammatory cytokines modulate gap junctions in the peripheral nervous system.* Glia, 1998. **24**(1): p. 21-31.
172. Raghavan, S., et al., *Crystallization of hydrocortisone acetate: influence of polymers.* International journal of pharmaceutics, 2001. **212**(2): p. 213-221.
173. Sosa, M.A.G., et al., *Interactions of primary neuroepithelial progenitor and brain endothelial cells: distinct effect on neural progenitor maintenance and differentiation by soluble factors and direct contact.* Cell research, 2007. **17**(7): p. 619-626.

Vita

Richelle Thomas completed her Bachelor's degree in Chemical Engineering from the University of Notre Dame du Lac in Notre Dame, IN, USA in May 2008. During her undergraduate studies, Richelle completed five industry internships. She received several awards during her undergraduate studies, including: the American Chemical Society Scholarship, the American Institute of Chemical Engineers Minority Scholarship Award for Incoming College Freshmen, and the National Society of Black Engineers Fulfilling the Legacy Scholarship. For her doctoral studies at The University of Texas at Austin, Richelle concentrated on the development of photopolymerized scaffolds with complex architectures that mimic the geometry of native tissue. The results of her work were presented at 13 conferences and symposia. She has contributed to two manuscript publications. Richelle was awarded the Virginia & Ernest Cockrell, Jr. Endowed Fellowship from the Cockrell School of Engineering at the University of Texas at Austin upon entry to graduate school in 2008. Additional, she was the recipient the National GEM Consortium Fellowship (2010), the Society of Women Engineers Intel Scholarship (2010), the National Society of Black Engineers 2010 CNA Corporate Scholarship. Professionally, she was a finalist in the 2010 and 2011 Society of Women Engineers Annual Convention Collegiate Poster Competitions and received travel awards from the American Institute for Medical and Biological Engineering (2011), and the University of Texas at Austin Graduate Engineering Council (2011). In 2012, Richelle established a research collaboration with the Edmund Cohen Laboratory for Vascular Research at the University of the West Indies, Cave Hill which was funded by the US Student Fulbright Program, the International Research Fellowship from the International Center for

Materials Research at the University of California Santa Barbara and the Burroughs Wellcome Fund Collaborative Research Travel Grant.

Permanent email address: thomas.richelle@gmail.com

This dissertation was typed by Richelle Thomas.